The University Of Sheffield.

Understanding the threat posed by buried charges in different operating environments

Tommy Lodge MPhys

Thesis submitted to

The University of Sheffield
Department of Civil and Structural Engineering

for the degree of

Doctor of Philosophy

July 2024

Abstract

When an explosive device is buried in soil, it creates a risk to the safe passage of people and vehicles in the area. Buried explosives have been used extensively in warfare for many years, including their use for area denial with minefields, Improvised Explosive Devices (IEDs) and cluster munitions. This work does not consider the doctrine or ethics of the use of explosives in warfare, instead it aims to investigate the impact that the burial conditions of existing explosive remnants of war has on the threat they pose. This has been an active research area for many decades, with numerous teams undertaking research to investigate the impact of different geotechnical parameters. This work extends the existing knowledge to explore new areas of interest both from a geographical and geotechnical point of view. Data has been gathered on three new environments: sub-arctic frozen soil; littoral environment with a varying water table; and carbonate-based soils.

Explosive testing has been conducted at the University of Sheffield's Blast and Impact Dynamics Laboratory, using the Characterisation of Blast Loading test apparatus to measure the specific impulse and total impulse generated by charges buried in different soil conditions. These results have been compared to historical data and conclusions drawn on the risk posed by the newly explored environments.

The results found that the existing standards employed by NATO forces in the design of blast resistant vehicles is likely to be a conservative standard, with all of the testing conducted being of a lower (or equal) threat to that covered by the NATO standards. Of the three environments considered, the variable water table within the soil was found to have the largest impact on the above ground blast loading. Conversely, testing in carbonate sand was found to produce a loading very similar to the historic testing with quartz-based sand. Finally, testing in frozen soil was found to be significantly more variable, with a higher loading than its non-frozen counterpart.

Acknowledgements

Thanks go to my supervisors, 'The Sam's', Prof. Sam Clarke and Dr. Sam Rigby for their guidance with this work. Thanks especially to Sam Clarke who, along with providing academic supervision, provided much needed motivation and encouragement during difficult times. Knowing exactly when to push for progress and updates, and when to let me ramble on about whatever was on my mind at the time (often unrelated).

Also, a special thanks to Prof. Andy Tyas, who has provided a great many late night conversations on different aspects of my work. Thanks also to Andy and Sam (Clarke) for allowing me the freedom to conduct this research alongside managing the research lab, a challenging yet rewarding experience.

This thesis has been funded through an EPSRC CaSE studentship sponsored by Dstl. The new experimental work was funded by Dstl, conducted by myself with help from the team at Blastech Ltd. Historic data collected by Blastech under contract with Dstl and shared with the University research team has also been included. I'd like to express my thanks to the sponsors at Dstl for their support with this thesis.

Finally, thanks to my wife Sarah and daughter Freya. They may not have written this thesis, but they had the harder job of putting up with me while I did, proving much needed distractions when required. This was especially the case during the period in lockdown when my research was at times sidelined by homeschooling, a job I never expected to need to do.

Tommy Lodge - July 2024

Contents

List of Figures

List of Tables

Chapter 1

Introduction

1.1 Background context

> *It is estimated that there are more than 110 million land-mines spread in 64 countries around the world and that between 2 and 5 million more are being laid each year. According to the International Committee of the Red Cross (ICRC), more than 800 people per month are killed by land-mines, most of them innocent civilians, and thousands more are maimed* (United Nations 1994).

There is a wealth of research and activity across the globe to combat the threat posed by landmines. However, the sheer scale of the issue (as identified in the United Nations quote above) means that there are still gaps in the knowledge. Through the improved understanding gained by this work, better models and more informed risk assessments can be produced to assist in demining efforts, potentially saving thousands of lives globally. In the context of this work, a buried charge is an explosive surrounded by soil and is of interest due to the potential to cause significant harm to a vehicle or person when it detonates. Westine et al. (1985) first proposed that in the case of a buried charge, the loading is primarily impulsive due to the material striking the target rather than being due to shock wave loading. This was further verified by others including Ehrgott et al. (2011) who measured both the air shock, and the impulse transferred to a rigid target. They found that the pressure measurements were not able to predict the total impulse including the contribution due to soil throw. Therefore, an understanding of the soil mechanics is vital. The testing reported in this thesis was funded by the Defence Science and Technology Laboratory (Dstl). The author was also funded through an EPSRC CaSE studentship again sponsored by Dstl, indicating the importance of the work conducted to the UK Ministry of Defence.

1.2 Aims

This work aims to investigate the risk posed by buried charges in both littoral and subarctic environments, areas which have yet to be studied. The data collected will be combined with existing data (from both previous University of Sheffield testing and from the literature) to widen our knowledge on **the effect geotechnical conditions have on the loading from a buried charge**.

1.3 Objectives

- Undertake experiments to investigate buried charges in the littoral environment by varying: the water level within a soil; and the presence of water above the soil surface.
- Undertake experiments to investigate buried charges in soil with a different mineralogy but comparable particle size distribution to previous data.
- Develop a system to undertake testing of frozen soil with an emplaced buried charge.
- Undertake experiments to investigate buried charges in the subarctic environment by conducting tests in solid ice, frozen soil and partially frozen soil.

1.4 Thesis outline

This thesis is written in a number of chapters outlined below. The thesis addresses three different, specific, gaps in the knowledge which are discussed in Chapters 6-8. Chapters 1 to 5 present the literature, methodology and structure of the results that are common to all the areas. Additional literature and methodology for a given specific knowledge gap is then included in the relevant chapter before the results are presented.

Chapter 1: Introduction Provides an outline overview of the work to be conducted along with the aims and objectives.

Chapter 2: Literature Review Introduces the main concepts around blast loading and extends this to look at the effect of burial. The chapter also discusses measurement techniques for the output from a buried charge (as due to the presence of soil this is a much more onerous challenge than measuring free-air blast). The chapter then goes on to discuss the sources of errors in buried charge testing as well as describing some of the predictive models which have been made to date.

Chapter 3: Test Plan and Experimental Methodology Based on the literature review, a plan for the geotechnical conditions required for buried charge testing to support this PhD are described along with the rationale where this is not directly contained within the literature review. As the thesis investigates specific but separate burial conditions the broader experimental methodology is described here so as to avoid repetition but to also allow the specifics around frozen, littoral, and carbonate sand testing to be discussed in more detail in subsequent chapters for ease of reading.

Chapter 4: Data Analysis Methodology The testing utilises the CoBL apparatus which requires an understanding of Hopkinson pressure bar theory (covered in the literature review) and also a specific analysis and treatment of the data to allow repeatable analysis. This process is described here in Chapter 4.

Chapter 5: Summary Results Provides the completed test plan along with the structure and format of the results to be discussed in more detail in subsequent chapters.

Chapter 6: Frozen Soils This chapter discusses the specific methodology around preparing frozen soil beds for testing along with initial testing on ice to look at the effects of low temperatures on detonation. The results from charges

buried in frozen soils are then presented and discussed. This work has been published in Lodge et al. (2024).

Chapter 7: Littoral Zone This chapter describes the methodology and presents results for varying the water level both within the soil bed and above the soil surface.

Chapter 8: Carbonate Sand This chapter describes the methodology and presents results from testing to investigate the effect of particle mineralogy on the impulse generated. This work has been published in Lodge et al. (2023).

Chapter 9: Discussion and Conclusions This chapter discusses the overall trends in the data along with conclusions of the work and scope for further work.

Chapter 2

Literature Review

This chapter aims to: provide an introduction to blast with a focus on the effects of burial on the output; outline methodologies for measuring the output from a buried charge; introduce geological properties of soils in the context of blast; and identify gaps in the existing knowledge of buried blast.

2.1 Blast theory

This section describes the fundamentals of blast loading in free-air along with the scaling laws which enable the phenomenon seen in large scale testing to be recreated in a laboratory setting.

For the purpose of this work, a blast wave is taken to mean the pressure wave generated from the detonation of an explosive material. Such materials, when exposed to a sufficient stimulus (e.g. mechanical, electrical, thermal etc.) undergo a rapid chemical decomposition releasing very high amounts of energy. This energy is predominately released as a pressure wave, with some energy released in the form of heat and light. The rate at which the energy is released leads to the formation of a shock wave, whereby there is a discontinuity in pressure in front of and behind the pressure wave. Figure 2.1 shows an idealised representation of a blast wave 10 m from a 1 kg TNT charge, referred to as a Friedlander waveform (Friedlander and Taylor 1946). The waveform shown in Figure 2.1 has a number of distinct features that are of interest, detailed below, which can be characterised and numerically modelled for a given scenario:

- t_a the arrival time of the shock wave at the location of interest;
- t_{pos} the duration of the positive phase of the loading;
- t_{neg} the duration of the negative phase of the loading;
- p_{max} the maximum overpressure at the location of interest; and
- p_{min} the minimum pressure (negative) observed at the location of interest.

It can be seen in Figure 2.1 that there are periods of both positive (red) and negative (blue) pressure due to a blast load, both of which can cause damage to objects and structures via compression (positive) and tensile (negative) failures.

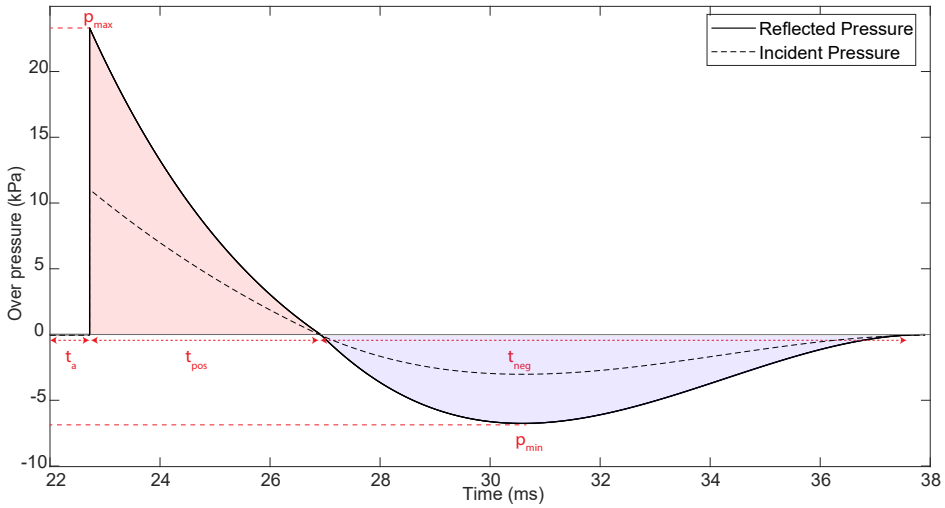

Figure 2.1: An example of the Friedlander waveform, an idealised approximation to the form taken by a blast wave from a 1 kg TNT charge at 10 m distance. Produced using the code published by Rigby and Tyas (2014) showing both the incident (dashed) and reflected (solid) pressures.

The threat posed by explosives depends on not only the magnitude of the pressure loading (p_{max}, p_{min}), but the duration over which it is applied (t_{pos}, t_{neg}). The integral of the pressure with respect to time (i.e. the red and blue areas) gives the impulse which again has both positive and negative phases. Therefore detailed understanding of the damage potential of an explosive event requires knowledge of the pressure time history. This poses issues when designing protective structures and vehicles as the destructive nature of explosives makes them difficult to measure accurately. This is further complicated when designing protective structures or vehicles as validation tests on full-scale systems are inevitably expensive due to their production costs. One common way to lower the cost of testing is to reduce the scale at which they are performed, then scale up the results once completed by appropriate scaling laws as discussed in the next section.

2.1.1 Hopkinson-Cranz scaling

Hopkinson (1915) and Cranz (1926) independently proposed a form of blast scaling commonly referred to as Hopkinson-Cranz scaling. Hopkinson-Cranz scaling is based on the theory that as the radius of a blast wave increases in size by a factor K, the volume within the spherical blast wave scales by a factor K^3. Therefore the energy within the blast wave is reduced by a factor of $\frac{1}{K^3}$ as it is distributed over the larger volume. Consequently, the pressure measured at a distance R from an explosive of mass W is equal to the pressure measured at a distance KR from a sample of the same explosive with a mass K^3W. In both

cases, the energy density is equal, meaning:

$$\frac{WE}{R^3} = \frac{K^3 WE}{(KR)^3} \implies \frac{R}{W^{\frac{1}{3}}} = \frac{KR}{(K^3 W)^{\frac{1}{3}}} \tag{2.1}$$

where E is the energy content of 1 kg of the given explosive.

The scaled distance is then defined as:

$$Z = \frac{R}{W^{\frac{1}{3}}} \left[\frac{m}{kg^{\frac{1}{3}}} \right] \tag{2.2}$$

and is a useful parameter in blast engineering as it is independent of the charge size used. For example, one can estimate the overpressure due to the detonation of 1000 kg of explosive 100 m away by doing a test with a twentieth of the mass, 0.125 kg, $(1000 \times \frac{1}{20^3})$ of the same explosive at a distance of 5 m $(100 \times \frac{1}{20})$. Both of these scenarios are said to be at a scaled distance of 10.

$$Z = \frac{100}{1000^{\frac{1}{3}}} = \frac{\frac{1}{20} \times 100}{\left(\frac{1}{20}^3 \times 1000\right)^{\frac{1}{3}}} = 10 \tag{2.3}$$

As Hopkinson-Cranz scaling is based on geometrical considerations, as the experimental scale is increased by a factor of K for tests at the same scaled distance, key parameters scale as follows:

Scale invariant ($x_{scaled} = x$): Pressure, shock wave velocity

Linear scaling ($x_{scaled} = Kx = W^{\frac{1}{3}} x$): Charge dimensions (length, thickness etc.), stand off distance, shock wave arrival time, shockwave duration, specific impulse

Cubic scaling ($x_{scaled} = K^3 x = Wx$): Charge volume, charge mass, total energy release, total impulse

For more of a detailed review of blast loading, see the works by Cooper (1996), Held (2009), Goel et al. (2012), Fay (2020) and Farrimond (2023).

2.2 Blast measurement techniques

There are a number of ways to measure the output from a free air explosive. These include direct pressure measurements; impulse measurements; and optical techniques, each of which comes with benefits and complications. Modern direct pressure measurements utilise an electronic pressure transducer which converts the physical loading on the sensing element into an electrical signal to be recorded with suitably fast data acquisition hardware (i.e. an oscilloscope). Pressure transducers come in different physical sizes and pressure ratings, with

both piezo-resistive and piezo-electric sensor types. Piezo-resistive gauges have a sensing element whose resistance changes proportional to the loading that is applied, whereas piezo-electric ones have an element that generates a small electric charge proportional to the loading (Carter et al. 2016).

In an idealised situation, an infinitely small transducer would be able to measure the incident pressure at a given location. However, the finite size of pressure transducers and the transient nature of the pressure loading, mean that measuring the pressure causes disturbances and interactions as the wave passes over the transducer. An alternate idealised measurement approach is to utilise an infinite sized reflecting surface normal to the wave propagation, allowing the true reflected pressure to be measured. However, again the real world application of this invariably requires a compromise between the reflecting surface size and the data accuracy.

Impulse measurement techniques observe the effect the blast wave has on physical objects of a known mass. They measure the impulse transferred to an object and can be done with temporal resolution if the objects are tracked using optical or other position transducers. By measuring the displacement (either the total displacement or displacement as a function of time) the impulse driving the object can be determined as in the work of Nansteel et al. (2013) who used high speed imaging of steel plugs impulsively driven by explosive blasts.

Optical techniques, such as Schleiren and shadowgraph imaging (described in detail in the review paper by Settles and Hargather (2017)) aim to observe the shock wave as it passes through a medium (e.g. air). Both shadowgraphs and Schleiren techniques rely on the fact that changes in density of a material result in changes to the refractive index, creating dark and light bands in the images. These can be tracked between frames to determine the shock wave velocity and arrival time at a given distance, both of which are useful parameters as discussed above. Additional information on the use of arrival time as a diagnostic of high explosives can be found in Farrimond et al. (2022).

For buried blasts direct measurement using pressure gauges is not possible, due to the aggressive near-field environment the gauges come into contact with. Hence, buried test diagnostics typically require different techniques to be utilised. Prior to discussing measurement techniques for blasts in soil, it is first important to understand the properties of soil as a material.

2.3 Geotechnical properties of soil

From a geotechnical perspective, soil takes on many forms encompassing a much wider range of materials than the organic 'top soil' known to a layperson. Geotechnic soils range from cohesive clays (particle sizes $<$0.002 mm) through to large boulders (particle sizes $>$630 mm). Table 2.1 shows a common taxonomy used for describing soils.

Table 2.1: Table showing the taxonomy used for categorising soil particle sizes as per BSI5930:2015 (British Standards Institution 2015).

Soil Group	Principle Type	Sub Type	Particle size range (mm)
Very coarse soils	Boulders	Large boulder	$630 < X$
		Boulder	$200 < X \leq 630$
	Cobbles	Cobble	$63 < X \leq 200$
Coarse soils	Gravel	Coarse	$20 < X \leq 63$
		Medium	$6.3 < X \leq 20$
		Fine	$2 < X \leq 6.3$
	Sand	Coarse	$0.63 < X \quad 2$
		Medium	$0.2 < X \leq 0.63$
		Fine	$0.063 < X \leq 0.02$
Fine soils	Silt	Coarse	$0.02 < X \leq 0.063$
		Medium	$0.0063 < X \leq 0.02$
		Fine	$0.002 < X \leq 0.0063$
	Clay		$X \leq 0.002$

Instinctively, it can be said that the type of soil will have a significant effect on the loading due to a buried charge. Therefore, it is vital that the soils are quantitatively described to allow an understanding of how the different properties affect the loading. The primary parameter for categorising a soil is the size of its constituent particles, or more accurately, the distribution of particle sizes, as outlined in Table 2.1. For a given material, a sample with a wide range of particle sizes is likely to have a higher bulk density than one with a uniform distribution; this is due to the different sized particles being able to pack closer together (e.g. smaller particles filling in the voids between the larger ones). A soil sample with a wide range of particle sizes is said to be 'well graded', whereas one with a narrow range of sizes is said to be 'poorly graded' or 'uniformly graded'. There is a third classification for 'gap graded' soils, where there exists one or more groups of particle sizes with little materials sized between the groups.

As soil is a granular material, there exist voids between the individual particles which can be filled with either water or air, as shown in Figure 2.2. The proportion of the voids that are filled by water (as opposed to air) is called the saturation ratio. The ratio of solids to water and air determines the bulk properties of the sample. For example, a higher degree of air voids leads to a more compressible sample than one that is fully saturated. In contrast, a partially saturated sample may have a higher degree of compressibility due to the intra particular moisture effectively acting as a lubricant, allowing the solids

to rearrange more efficiently into the smaller volume (Fox et al. (2014), Grujicic et al. (2007)).

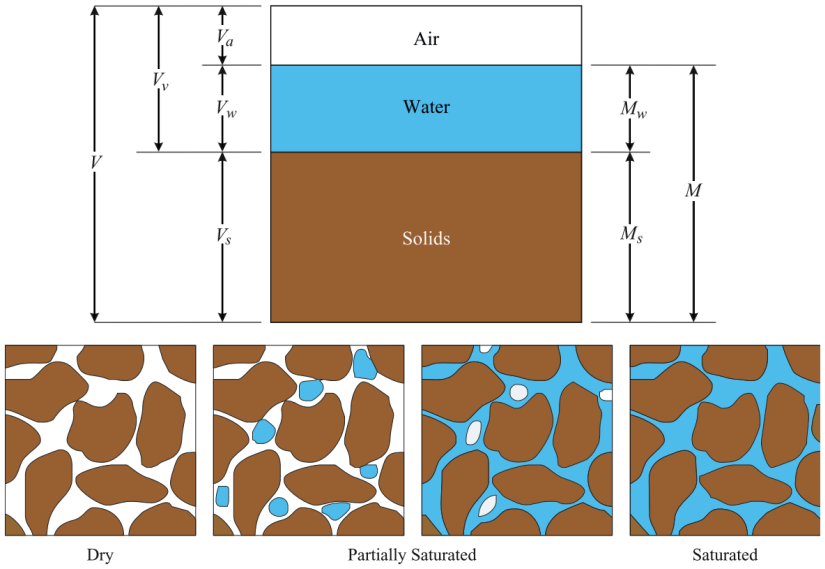

Figure 2.2: Top: diagram showing the three constituent elements of a soil (solids, water and air) of varying volumes (V). Bottom: diagrams showing the voids are present and filled with different amounts of air and water as the saturation level increases (Clarke et al. 2011).

2.4 Blast measurement in soils

Westine et al. (1985) proposed that, in the case of a buried charge, the loading is primarily impulsive due to the material striking the target rather than being due to shock wave loading. This was further verified by others, including Ehrgott et al. (2011) who measured both the air shock and the impulse transferred to a rigid target. They found that the air pressure measurements alone were not able to predict the total impulse, including the contribution due to soil throw. Therefore, an understanding of the mechanisms of confinement is essential for interpreting the comparatively increased loading observed when a charge is buried, which cannot be attributed solely to the effects of air shock and soil mass.

There are a number of different experimental methods to characterise the loading from a buried charge, which have been employed in the literature. Techniques are broadly grouped into a number of categories summarised below along with key findings and the advantages and disadvantages of each technique.

2.4.1 Air blast

Both Bergeron et al. (1998) and Ehrgott et al. (2011) used pressure gauges to measure the incident air shock produced from buried charges. Ehrgott et al. (2011) also conducted experiments taking impulse measurements in a nominally identical experimental setup to that used for the air shock measurements. They found that the pressure measurements were not able to predict the trend in total impulse which was theorised to be because air shock measurements do not take into account the momentum transfer from the soil. It was found that soils with a high incident pressure measurement had a low impulse measurement. The authors postulated that the degree to which the blast products are able to permeate through the soil is linked to the amount of energy/momentum that is deposited in the soil (and subsequently transferred to the target). Therefore they propose that permeability and shear strength are parameters of interest in determining the threat posed by buried charges.

2.4.2 Total impulse based methods

This section discusses data captured using some of these experimental techniques that determine the total impulse transferred to a target of a given size.

Total impulse methods attempt to avoid the issues related to structural response by employing a nominally rigid, non deformable target with a system to capture the momentum transfer due to the detonation of the charge. Similar methods have been employed by: Genson (2006), Anderson et al. (2010), Fourney et al. (2010), Anderson et al. (2011) and Fox et al. (2014) who all measured the vertical travel of a target plate; Hlady (2004), Grujicic et al. (2007), Ehrgott et al. (2011) and Clarke et al. (2017) who used a vertically displaced piston; Heider et al. (2016) who measured the travel of a small scale (150 kg) vehicle shaped target; and Bergeron and Tremblay (2000) who used a horizontal pendulum to measure the impulse.

Anderson et al. (2010) conducted tests using 625 g of Composition B (CompB) explosives in a 3:1 cylinder (3.7×11.3 cm)[1]. CompB has a TNT equivalence of 1.148 (Baker et al. 2012). This corresponds to half scale testing when compared to STANAG threat level M2 as given in AEP-55 (NATO 2014). The charges were buried in sand bins constructed of cardboard tubing, 850 mm tall, 630 mm diameter with a 3 mm wall thickness and a steel reinforcing band at the top and bottom (see the photo in Figure 2.3a). The tests measured the vertical displacement of a 300 kg, 800×800×60 mm steel plate positioned above the charge; the plate was free to travel vertically and held in place pre-test on four timber posts (see Figure 2.3b for a diagram of the setup).

Charges were bottom detonated within the sand bed, with 50 mm of sand above the charge, and a target stand off of 200 mm (as shown in Figure 2.3b). An

[1] Charges were bottom detonated using a 10 g PETN booster and detonator.

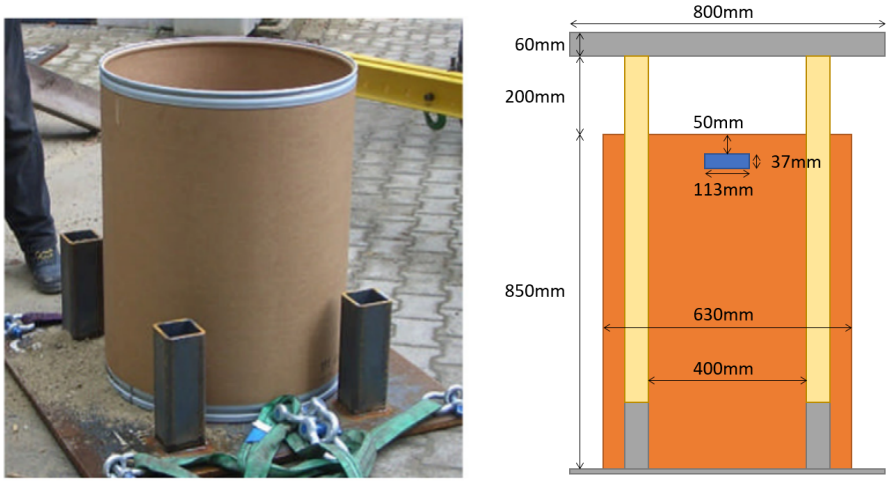

(a) Soil bin **(b)** Test setup

Figure 2.3: Images showing the soil bins and test setup used by Anderson et al. (2011).

Table 2.2: Table showing the properties of the different soils tested by Anderson et al. (2011).

Moisture content (%)	Mean density (g/cm^3)
7	1.37 ± 0.03
14	1.49 ± 0.03
21	1.67 ± 0.03

additional set of tests were conducted with the stand off distance increased to 300 mm. The tests used silica sand with a particle size distribution as shown in Figure 2.4. Tests were conducted at 3 different moisture contents (and therefore bulk densities) which are detailed in Table 2.2. The displacement of the plates post detonation was measured using string pull potentiometers, verified for accuracy using high speed video and an accelerometer. From the peak height of the plate H_{max}, the initial velocity V_i and impulse J can be calculated as follows:

$$V_i = \sqrt{2gH_{max}} \tag{2.4}$$

$$J = MV_i \tag{2.5}$$

where g is the gravitational constant 9.81 m/s^2 and M is the mass of the plate (300 kg).

Based on the experimental results, Anderson et al. (2011) proposed the following equation to determine the impulse imparted to a steel plate as a function of the

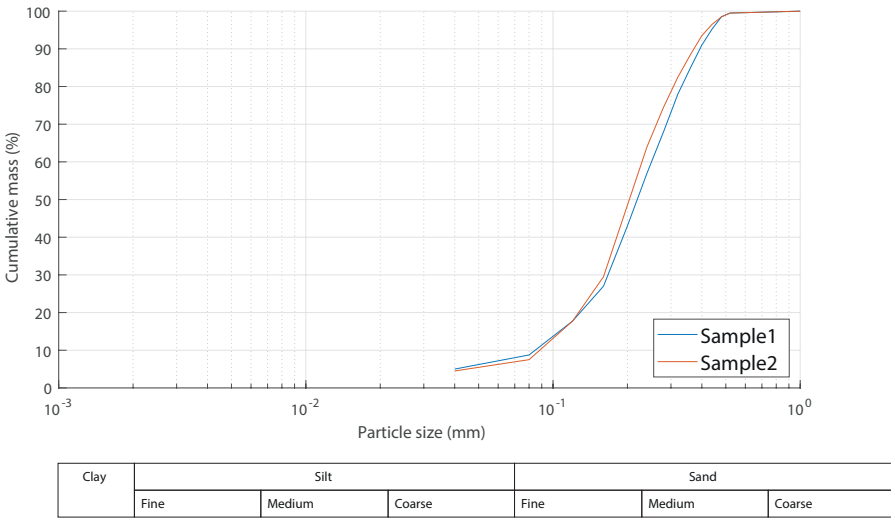

Figure 2.4: Particle size distribution for two samples of the soil used by Anderson et al. (2011).

soil density:

$$J_k = \left(\frac{\rho_k}{\rho_7}\right) J_7 \tag{2.6}$$

where J_n is the impulse imparted by a charge buried in soil with a moisture content n and ρ_n is the bulk density of the soil sample at the given moisture content. It can be seen that this equation effectively utilises the 7% moisture content series as the baseline, with other tests directly scaled up or down from this. From this work, the authors conclude that the increased impulse due to higher moisture content is predominately due to density effects. The total impulse (determined by Equation 2.5) is plotted in Figure 2.5 alongside the experimental results for three different moisture content soils. The dashed line shows an extrapolation of Equation 2.5 beyond the experimental results of Anderson et al. based on a fit to their reported moisture content and density data.

Ehrgott et al. (2011) performed both pressure measurements, and impulse measurements for buried charges using their Impulse Measurement Device (IMD), as shown in Figure 2.6. The IMD has two configurations with the first allowing for total impulse measurements (as shown in the top of Figure 2.6) and the second allowing for the incident pressure to be measured with an array of pressure gauges (as shown in the bottom of Figure 2.6). The impulse measurements used a large piston that is vertically displaced by the detonation of a charge. The target plate of the IMD consisted of a 3 ft (914.4 mm) diameter, 4.5 in (114.3 mm) thick steel plate. This system was able to determine the total impulse transferred to the piston by both the air blast and the momentum transfer due to particle strikes.

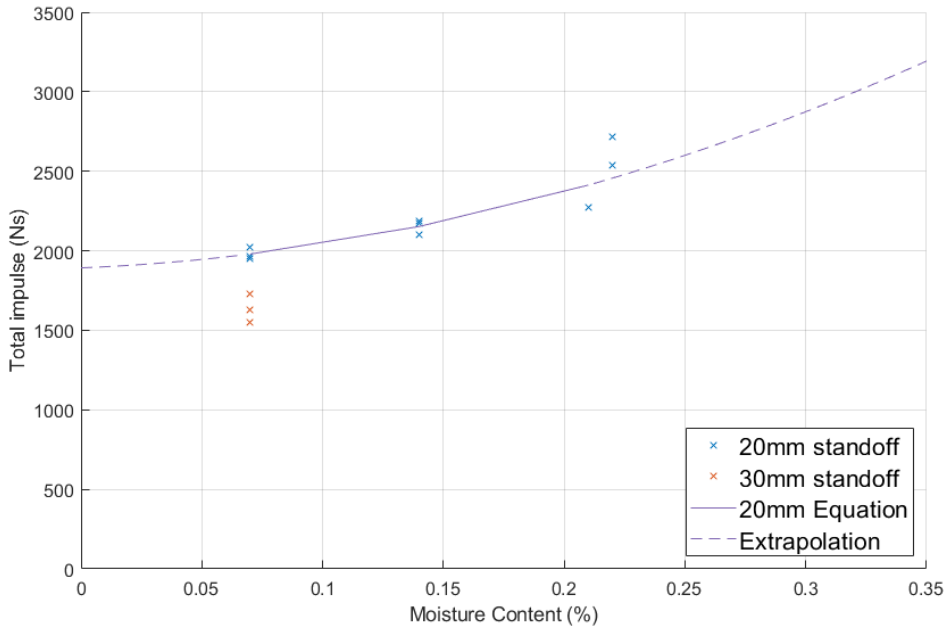

Figure 2.5: Plot showing the total measured impulse vs moisture content of the sand. The line shows Equation 2.5 proposed by Anderson et al. (2011) with the dashed sections representing an extrapolation of the function outside the region interrogated by the experiments.

Ehrgott et al. (2011) found that the pressure measurements were not able to predict the total impulse measurements as they do not take into account the momentum transfer from the soil. Soils with a high pressure measurement led to a low impulse measurement, as noted in the previous section on air blast. The authors theorised that this shows how the degree with which the blast products are able to permeate through the soil is linked to the amount of energy/momentum that is deposed in the soil (and subsequently transferred to the target). Therefore they proposed that permeability and shear strength are parameters of interest in determining the risk from buried charges.

Ehrgott et al. used three different soils for the tests to represent different levels of moisture content and air voids; each soil type was tested using the IMD with a buried charge and one flush with the surface. The PSDs for the three soils are shown in Figure 2.7. For all the tests the total stand off between the top of the charge and the test rig was kept constant (i.e. the buried charges had a smaller air gap between the soil surface and the IMD than the top of the flush charges had with the IMD.) For all tests, the charges were 5 lb (2.27 kg) 3:1 cylinders of C4. In addition to the total impulse and pressure measurement, Ehrgott et al. (2011) also compared the size of the crater produced by an explosive charge to the total impulse measured in the three different soils. It was found that as the crater size increased, so did the total impulse imparted to a target. Similar analysis was also conducted by Bergeron et al. (1998) who, alongside crater size

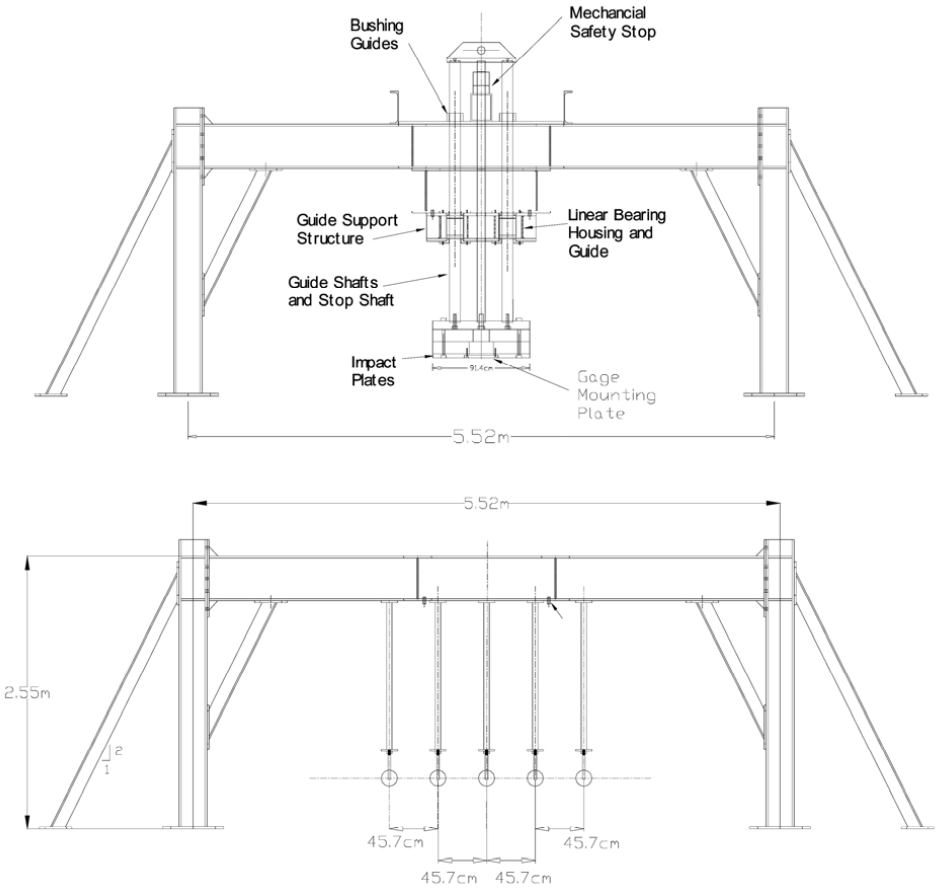

Figure 2.6: Diagram showing the IMD in the impulse measuring arrangement (top) and pressure measuring arrangement (bottom) (Ehrgott et al. 2011).

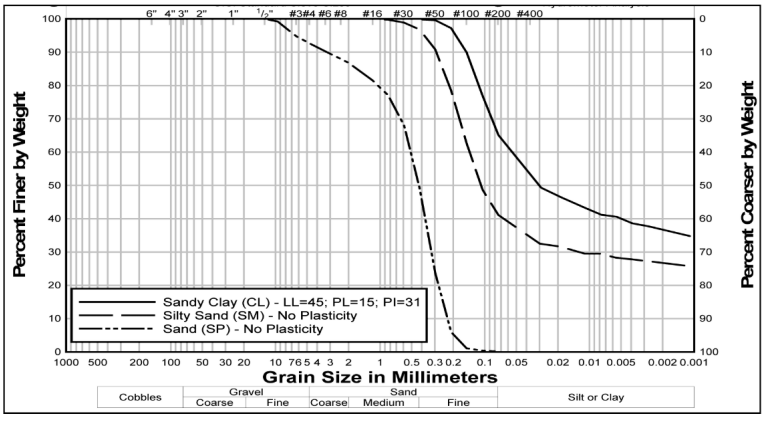

Figure 2.7: Particle size distribution for samples of the soil used by Ehrgott et al. (2011).

Table 2.3: Table showing the measured peak impulse for 3 soil types (Ehrgott et al. 2011).

Sand type	Peak impulse (kN·S) Surface	Buried
Poorly graded (dry sand, SP)	2.753	7.273
Intermediate (silty sand, SM)	2.424	8.363
Wet sandy clay (CL)	2.891	11.61

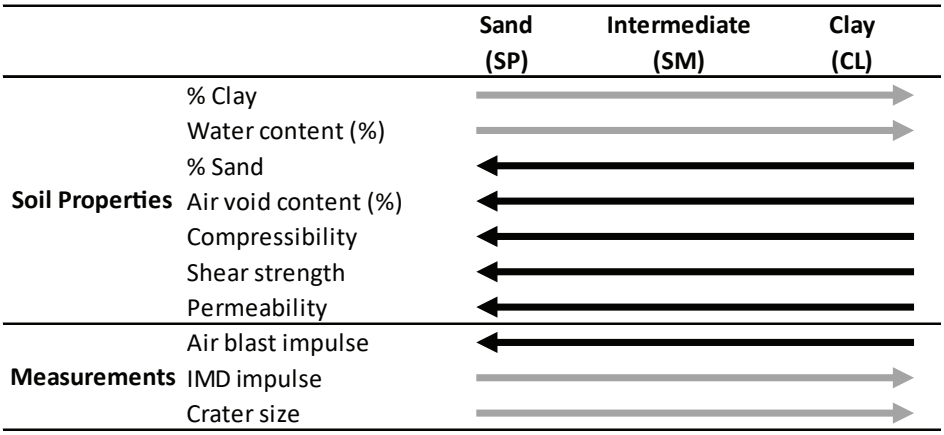

Figure 2.8: Table showing the trends identified by Ehrgott et al. (2011); the arrows show how the parameters increase between the three sand types.

analysis, also used x-rays to measure the soil deformation and throw, however this was not equated to the impulse on a target. Results from Ehrgott et al.'s testing are shown in Table 2.3 and the trends between different parameters of the soil and the results are included in Table 2.8. They found that increasing the clay content and increasing the water content increased the total impulse transferred when using the IMD apparatus, but reduce the impulse derived from pressure measurements. Conversely they found the opposite trend for increases in: sand content;. air void content; compressibility; shear strength and permeability. However, these properties are interdependent variables and the testing did not isolate one factor at a time, making it difficult to draw firm conclusions on which is the driving factor.

Clarke et al. (2017) conducted testing at half the scale of the STANAG threat level M2 as given in AEP-55 (NATO 2014). This equated to a charge size of 625 g PE4 in a 3:1 cylinder with a TNT equivalence of 1.2 (Rigby and Sielicki 2014). Tests were conducted on five different soils detailed in Table 2.4 with the particle size distributions plotted in Figure 2.9.

Charges were buried at a depth of 50 mm with a stand off distance of 137.5 mm. There were three test series conducted with LB sand, (a, b and c) where the

Table 2.4: Table showing the properties of the different soils tested by Clarke et al. (2017).

ID	Description	Particle Size Distribution	Water content $w(\%)$	Bulk dry density $\rho(Mg/m^3)$
LB	Leighton Buzzard 14/25	Uniform (0.6–1.18 mm)	0–25	1.5–2.0
2LB	Leighton Buzzard 6/14	Uniform (1.18–2.8 mm)	0–25	1.6–2.0
LBF	Leighton Buzzard 25B grit	Well graded (0.5–5.0 mm)	0–25	1.6–2.0
STANAG	Sandy gravel AEP 55 (NATO 2014)	Well graded (0–20 mm)	0–14	1.9–2.2
Clay	Brown laminated silty clay	66% $<$ 0.002 mm	∼27	1.93

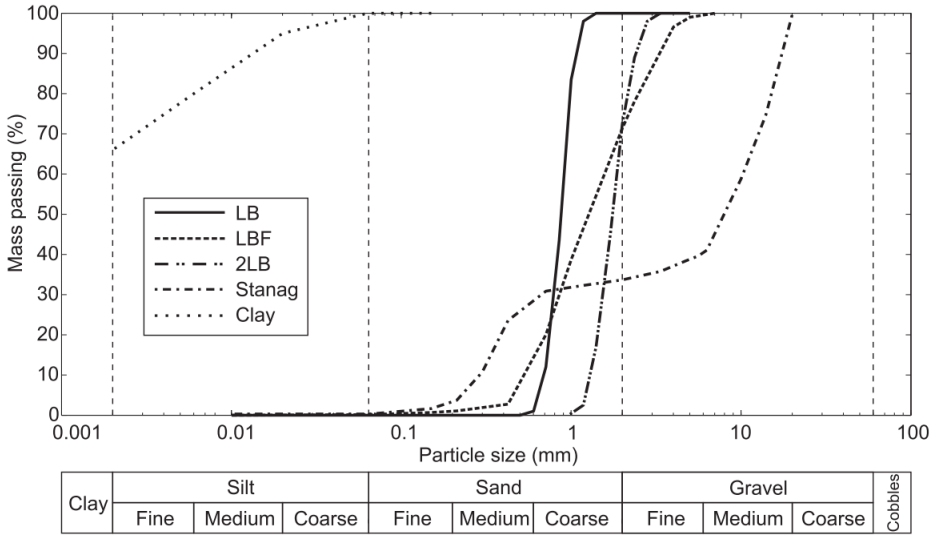

Figure 2.9: Particle size distribution for two samples of the soil used by Clarke et al. (2017).

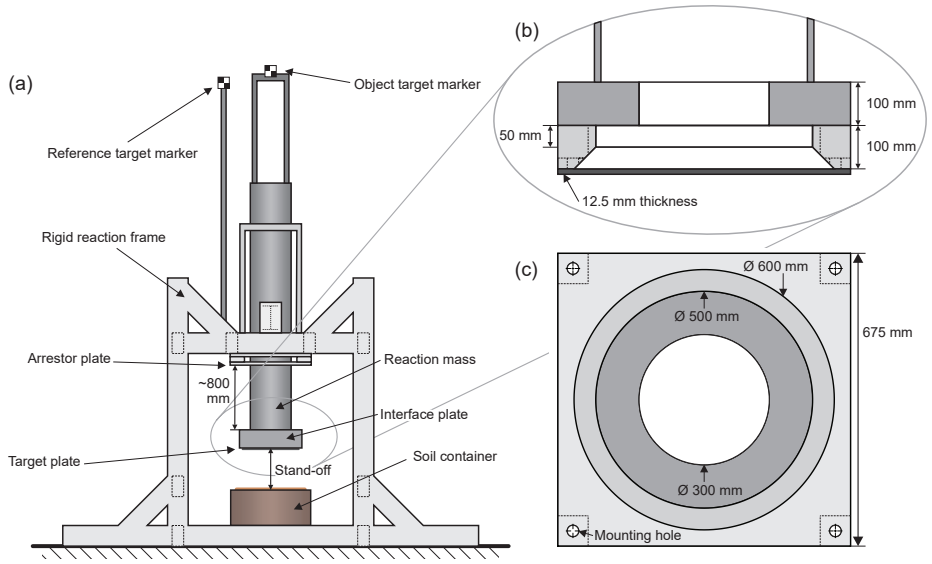

Figure 2.10: Diagram of the test setup used by Clarke et al. (2017) showing a) the whole rig, b) the target detail and c) a plan view of the target detail.

bulk density, dry density, and air void ratio were kept constant respectively. For each test, the impulse was determined by measuring the vertical displacement of a 1574 kg reaction mass. The target face was a 675×675×12.5 mm mild steel target plate attached to a 675×675×100 mm reaction frame with a circular free span of 500 mm in the centre of the target plate. Figure 2.10 shows a diagram of the test setup.

The results of series 'b' of Clarke et al. (2017) (Figure 2.11b) are in agreement with the findings of Anderson et al. (2011) and Ehrgott et al. (2011), that is as the moisture content increases so does the impulse. However, series 'a' showed that in tests of sands at the same bulk density but different moisture contents, the loading increased with the moisture content (Figure 2.11a). This finding is in contrast to the conclusions of Anderson et al. (2011) who determined that the increased loading due to increased moisture content was predominately due to the higher bulk density. Fourney et al. (2005) also had similar findings to Clarke et al. (2017), in that the increase in loading was not predominantly due to the soil density. Fourney et al. conducted tests in a test bed of saturated lead shot (with a soil bulk density over 7 Mg/m^3) and found that the measured impulse was comparable to their test in saturated sand (bulk density around $2Mg/m^3$).

The results of (Clarke et al. 2017)'s testing led to their development of a modification factor I_{mod} to be applied to the output from the Westine model (discussed below in § 2.5.1) to determine the loading from a buried charge. In short, the Westine model quantifies the soil based on its bulk density and wave speed alone, whereas the use of I_{mod} extends this to include moisture content. Equa-

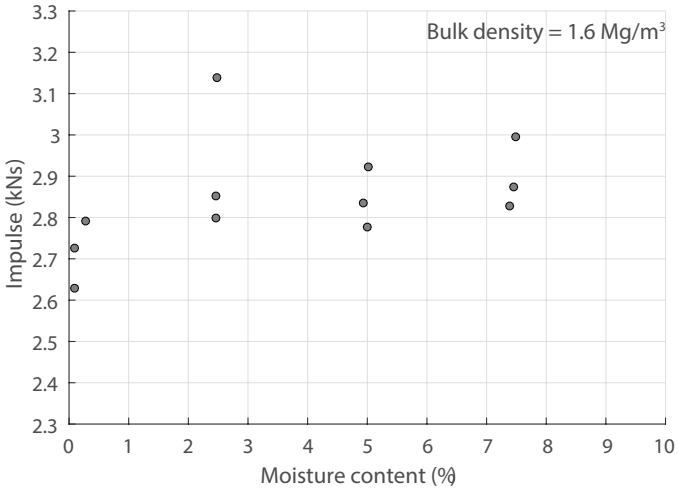

(a) Results at constant bulk density

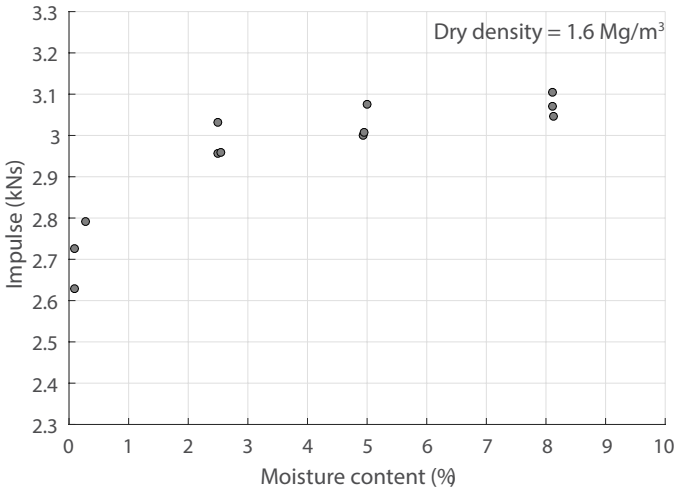

(b) Results at constant dry density

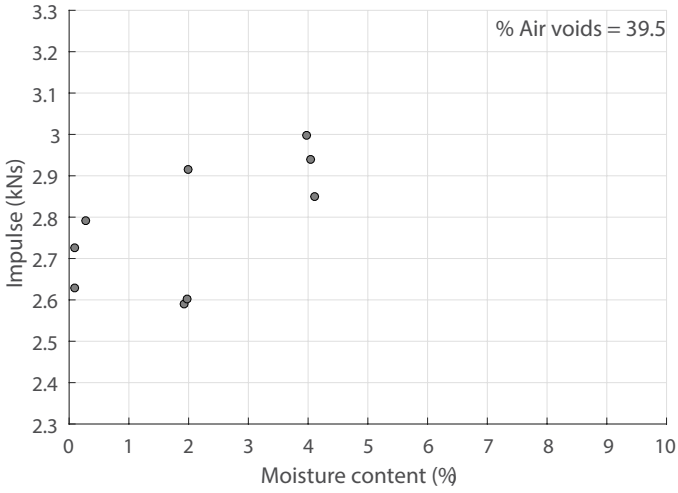

(c) Results at constant air voids

Figure 2.11: Impulse as a function of moisture content for the three series, isolating the effect of moisture content from bulk density (Clarke et al. 2017).

tion 2.7 gives the formulation of I_{mod} as defined in Clarke et al. 2017, which determines the impulse relative to a baseline condition of dry (w=0%) quartz sand at a bulk density of 1.6 Mg/m^3.

$$I_{mod} = 0.9 - 0.096w + 0.033\rho + 0.078w\rho \tag{2.7}$$

where w is the gravimetric moisture content (%) and ρ is the soil bulk density (Mg/m^3). Equation 2.7 has been rounded to 2 significant figures here as the extra precision makes no practical difference to predictions.

One key limitation of total impulse based methods is that they do not generate information on the spatial distribution of the loading, and therefore cannot accurately predict how a deformable target will respond to the loading. Methods to generate this data are covered in the following sections.

2.4.3 Target deformation tests

Tests have historically been conducted wherein a target plate is placed above an explosive charge e.g. Neuberger et al. (2007), Pickering et al. (2012), Curry (2017) and Fuller et al. (2015). The dynamic deformation, residual deformation or both are then measured and used to infer the loading on the target plate. The key advantage of this method is that it is a simple test to conduct (especially when only looking at the residual deformation) as the diagnostic systems are simple to design. This allows a wide range of test to be conducted and results compared. The main disadvantage is that plate deformation is an effect, rather than a cause and so accurate knowledge of the target plate material is required to calculate the loading imparted to the target. In addition to this, the spatial distribution of the loading is unknown. These factors combined lead to issues when attempting to apply the results from a given test to other scenarios as structural response of the target plate does not necessarily follow the same scaling laws as the explosive loading does.

To combat these issues, Pickering et al. (2012) conducted testing with deformable target plates mounted in a vertical pendulum setup. This allowed for comparisons to be made between the impulse transferred to a rigid target and a deformable one, as shown in Figure 2.12. The measured impulse for the deformable targets was also compared to the peak mid-point deformation of the plates, shown in Figure 2.13.

Pickering et al. (2012)'s results showed good correlation between the measured impulse and the target plate deflection across a range of charge sizes and burial depths, as seen by the coloured lines on Figure 2.13. Their results did show a difference in the impulse measured with rigid and deformable targets, as is to be expected, but this was not a consistent factor, with some tests showing a larger difference than others. For example, Figure 2.12 shows a difference of more than 50 Ns was observed for the tests with 21+1 g charges at a 10 mm burial depth, and a difference of less than 10 Ns at 40 and 50 mm. The work of Curry (2017)

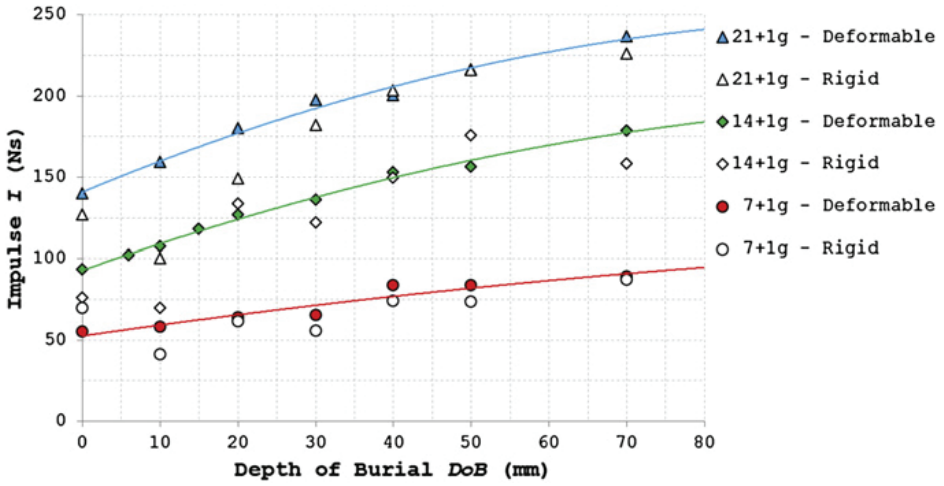

Figure 2.12: Results of testing by Pickering et al. (2012) who undertook testing with both rigid and deformable target plates at different burial depths and charge sizes.

built on the target deformation tests and utilised Digital Image Correlation techniques to measure the spatial and temporal distribution of loading on a deformable target plate mounted on the lower face of a ballistic pendulum. The use of DIC allowed the velocity distribution of the rear face of the loaded plate to be inferred and, subsequently, the specific impulse distribution on the front face required to generate this velocity distribution. This reduces the dependance on the properties of the target material, but does not remove it entirely.

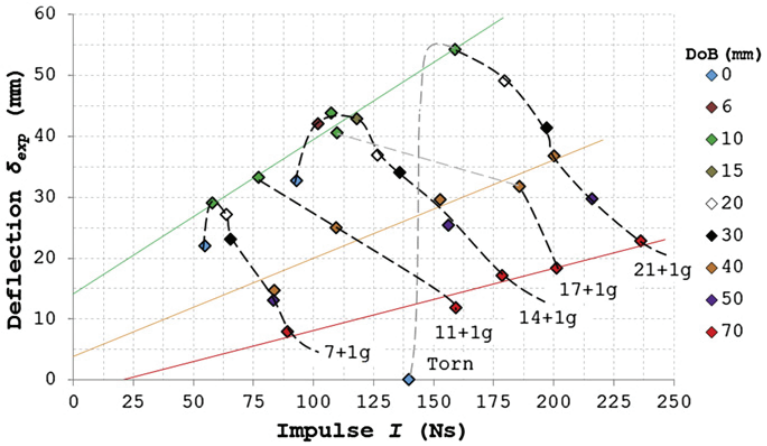

Figure 2.13: Results of testing by Pickering et al. (2012) who compared the peak mid-plate deflection with the impulse measured with a vertical pendulum at different burial depths and charge sizes.

2.4.4 Specific impulse based methods

In contrast to other impulse methods that only capture the total impulse, Denefeld et al. (2017) used an experimental rig consisting of concentric steel rings to measure the spatial distribution of the momentum imparted by a buried explosive charge. Eight concentric rings, each 20 mm thick of varying heights were used and the initial velocity of the rings was used to calculate the specific impulse imparted on each annulus. A photo and cross sectional view of the test rig are included in Figure 2.14. A combination of x-ray, and high speed, imagery was used to determine independent measures of the initial velocity with a high degree of consistency between the two. This technique is an improvement on the total impulse techniques discussed previously and produces information on how the loading is distributed across the target.

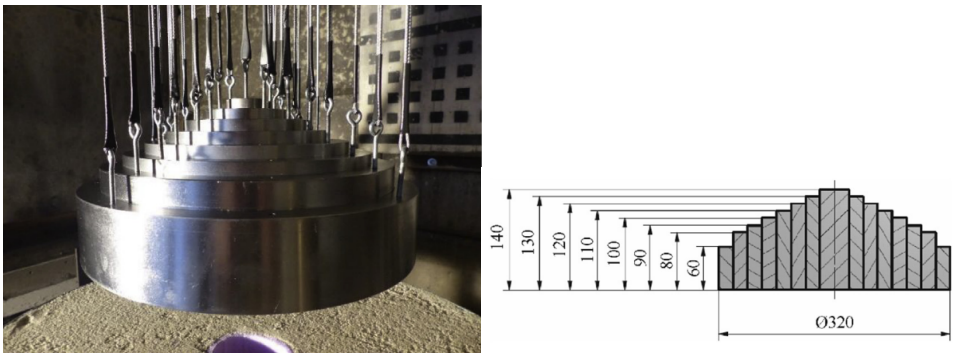

(a) Photo **(b)** Cross sectional view

Figure 2.14: Images showing the steel ring arrangement used by Denefeld et al. (2017).

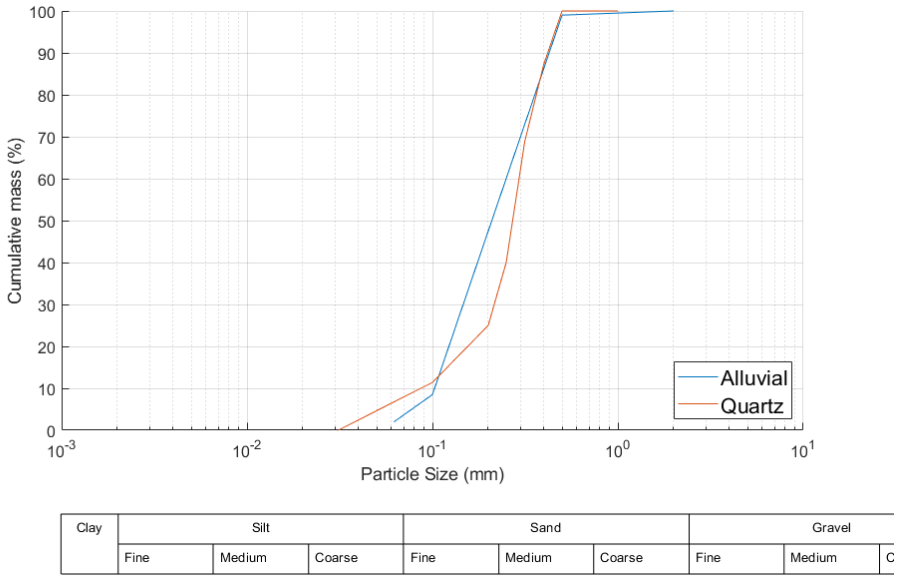

Figure 2.15: Particle size distribution for two samples of the soil used by Denefeld et al. (2017).

The test setup was used to investigate the effect of moisture content, burial depth and soil type on the measured impulse. Tests were conducted using 3:1 cylindrical, 84 g PETN charges. Two types of sand were tested, 'alluvial sand' and 'quartz sand', the PSDs of which are included below in Figure 2.15. Further details on the geotechnical properties of the soils used for the tests is included in Table 2.5 which shows the degree of consistency that was achieved in the soil preparation. Samples were prepared in barrels which were 630 mm diameter by 800 mm tall.

The results from alluvial sand (Figure 2.16a & c) show that the spatial distribution of the specific impulse is more concentrated for a charge buried at 116 mm when compared to one at 46.4 mm. This trend extends out to between 70 mm and 90 mm from the centre at which point the shallower burial depth gives a higher specific impulse. Despite the different distribution of the loading, the total impulse across all rings for the charges at two different burial depths are the same (within experimental variation).

The results for the quartz sand (Figure 2.16b & d) show that the dry sample produces a much larger specific impulse in the central regions than the two wet samples, with the two wet samples showing little difference outside the experimental variation. The cumulative impulse for the dry sand is also higher than for the wet sand, however the difference between the two reduces as the distance from the centre increases (as seen in Figure 2.16d). There is no observed difference between the two wet sands, from which the authors draw the conclusion that the degree of saturation does not result in a difference in the loading

Table 2.5: Table showing the properties of the different soils tested by Denefeld et al. (2017).

Test number	Soil type	Depth of burial [mm]	Wet density [Mg/m^3]	Water content %	Saturation %
1	Alluvial	116.0	1.59	3.8	8.8
2	Alluvial	116.0	1.25	5.5	9.5
3	Alluvial	46.4	1.27	3.8	6.7
4	Alluvial	46.4	1.25	7.2	12.0
5	Quartz	46.4	1.60	0.0	0.0
6	Quartz	46.4	1.60	0.0	0.0
7	Quartz	46.4	1.59	10.0	31.6
8	Quartz	46.4	1.59	10.0	31.6
9	Quartz	46.4	1.77	20.0	66.8
10	Quartz	46.4	1.80	17.8	64.7

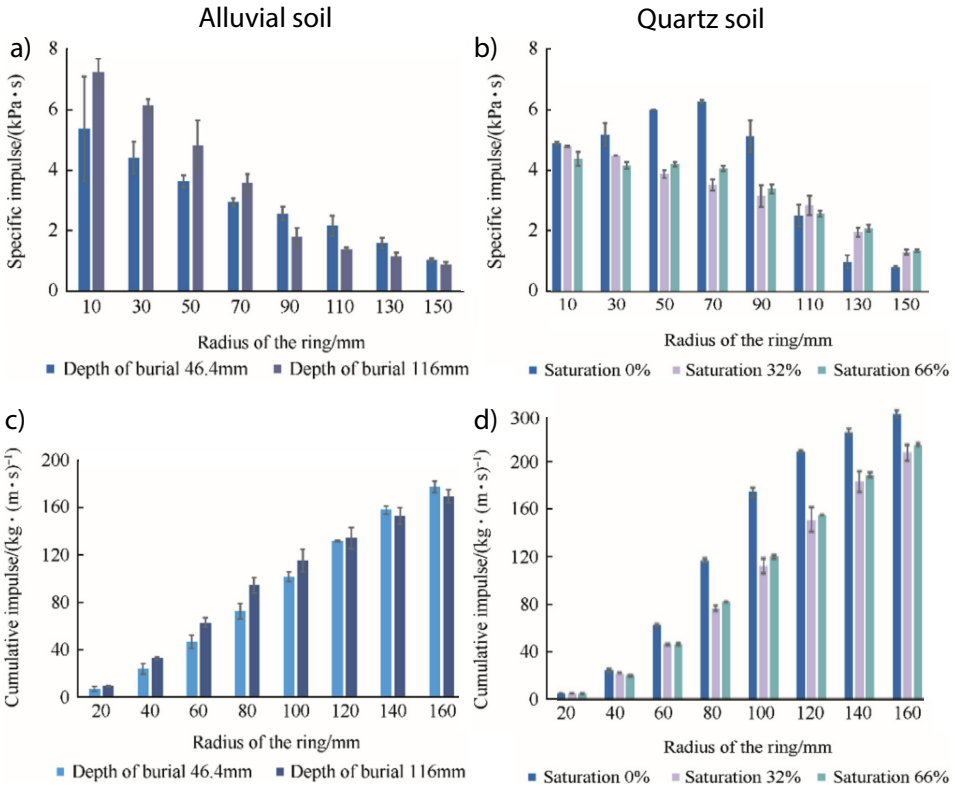

Figure 2.16: Specific impulse (top) and cumulative impulse (bottom) distributions for alluvial sand at two different burial depths (left) and quartz sand at three different moisture contents (0%, 10% and 20%) (right) (Denefeld et al. 2017).

above a given point. This point was not identified within the work but would appear to be below 32% saturation, which corresponds to 10% water content for quartz sand. These results are in direct contrast to those of Anderson et al. (2011), Ehrgott et al. (2011) and Clarke et al. (2017) discussed previously.

Denefeld et al. (2017)'s comparisons to modelling they performed show differences between the simulations and experimental results. For example, the experimental results show a more centralised loading from a charge buried at 116 mm when compared to one at 46.4 mm (as shown in Figure 2.16). In contrast, the modelling shows the inverse, with the 46.4 mm charge showing a more centralised loading. The experimental and simulation results are also compared to those of Westine et al. (1985), with the Westine model predicting impulses approximately 50% higher.

Both Clarke et al. (2020) and Leiste (2012) utilised Hopkinson bars to measure the spatial and temporal loading due to a buried charge. This method measures the stress pulse travelling in a long rod which can be used to calculate the load applied to the end of the bar, a system based on the work of Hopkinson in 1914. The small size allows for high resolution spatial measurement to be taken with multiple Hopkinson bars arranged in a small area. Similarly, the use of strain gauges to record the stress pulse in the bar allows for high temporal resolution. Further details on Hopkinson pressure bars is below in § 2.4.5. By interpolating between multiple measurements from a single buried charge test, it is possible to calculate the distribution of impulse across the whole target area.

Leiste (2012) utilised an array of eight Hopkinson Pressure Bars (HPBs) to measure the loading from small (4.4 g) explosive charges buried in dry and saturated sands. Figure 2.17 shows photos of the experimental setup in two arrangements. The top shows the Hopkinson Bars arranged in a line across the centre with a) being a wide view and b) being a detailed view. The bottom images show an arrangement where the bars are all at the same radial distance from the charge centre with a wide angle c) and a detail view d).

Leiste (2012) found that the loading from saturated sands and water was higher than that from dry sands. They hypothesised this was due to the ratio of air voids within the sample, with the dry soil containing 30% air voids and saturated sand containing 3%. Despite the higher overall loading from saturated sands, Leiste (2012) found the loading to be over a wider area than with dry sands. This can be seen in Figure 2.18 where the saturated sand shows a lower central loading and a higher loading at larger distances.

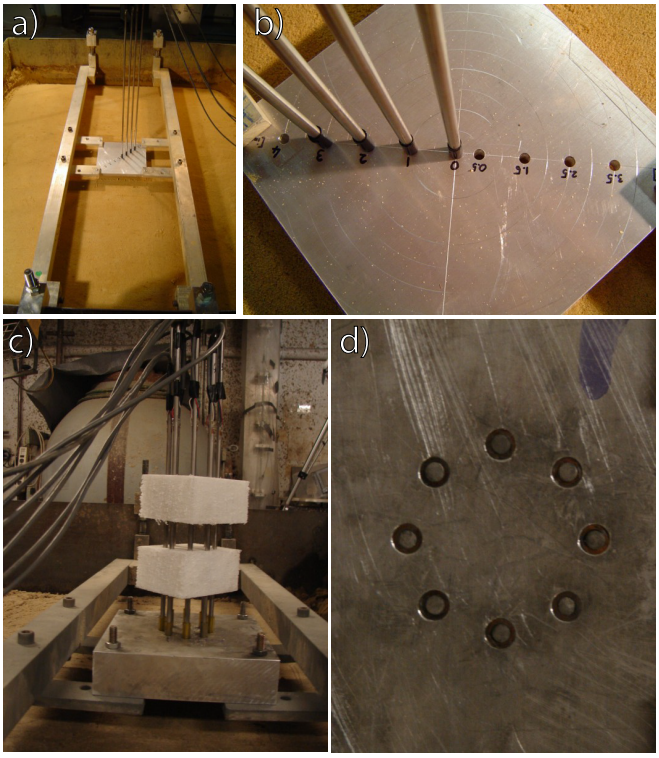

Figure 2.17: Images showing the test setup of Leiste (2012) with a linear array of Hopkinson pressure bars (top) and a circular array (bottom).

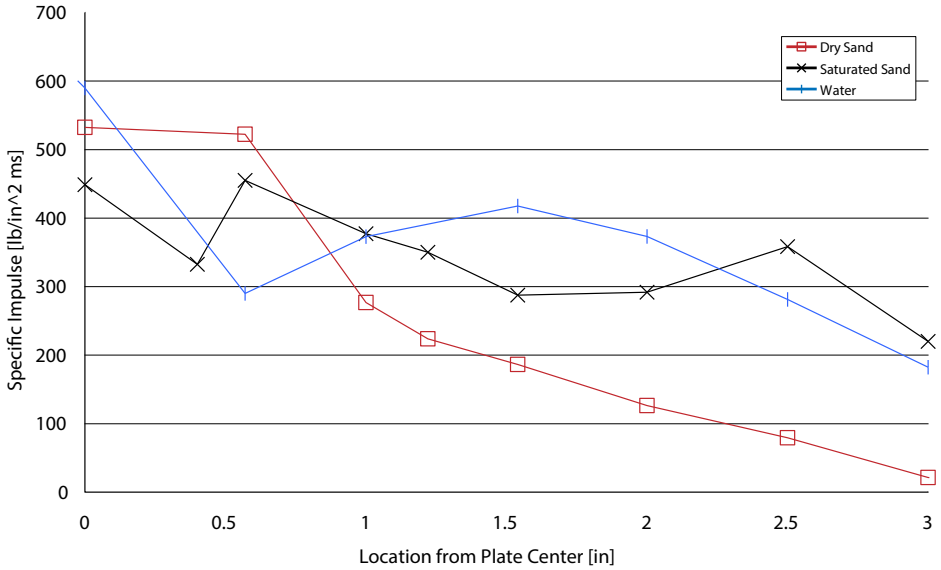

Figure 2.18: Spatial specific impulse distribution for charges buried in dry sand, saturated sand and water with a burial depth of 0.396" (Leiste 2012).

Clarke et al. (2020) used an array of 17 Hopkinson pressure bars to measure the specific impulse generated from shallow buried charges in a range of soil conditions. They investigated the effect of the following parameters: the degree of confinement around the charge; the influence of moisture content; the influence of burial conditions; and the influence of confining material. Figures 2.19 & 2.20 show the results presented as total impulse and specific impulse respectively. The results are grouped to allow ease of comparison of the different parameters investigated.

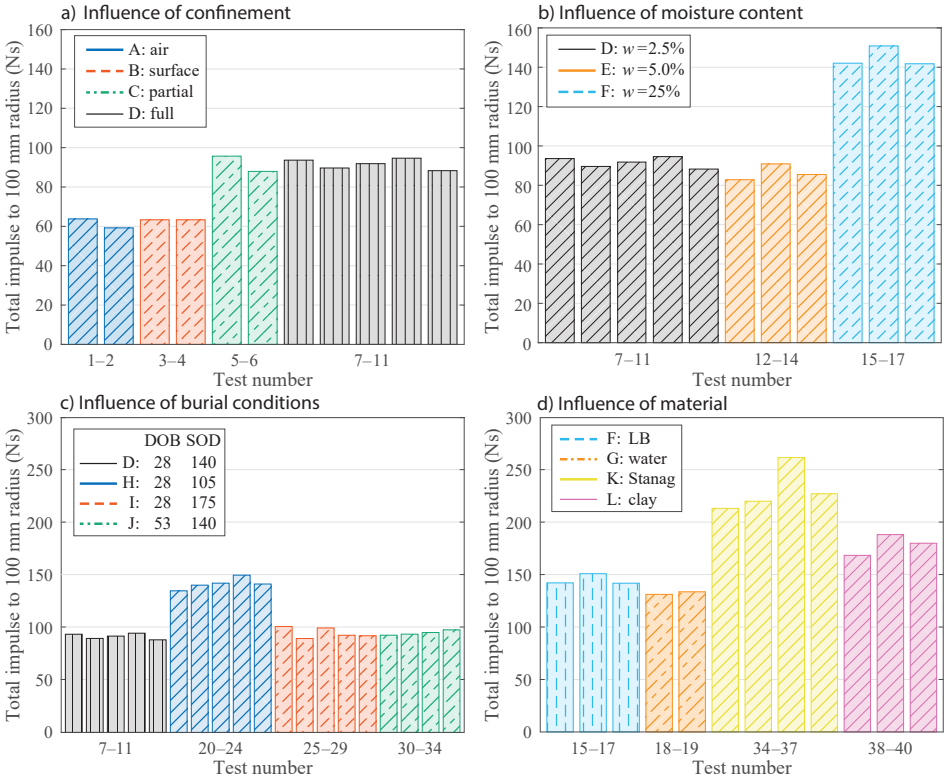

Figure 2.19: Total impulse within the 100 mm radius instrumented region in testing by Clarke et al. (2020), investigating four different parameters.

Clarke et al.'s findings on the effect of confinement showed that the material behind a buried charge had little effect on the loading i.e. charges placed on the surface had a similar loading magnitude and distribution as ones suspended in free air (Figure 2.19a & 2.20a). They also found that the total impulse for the fully and partially buried cases was similar (Figure 2.19b) despite them having different loading profiles (Figure 2.20b). This difference in loading profile, with a more centralised loading for the partially buried case, is interpreted as being due to the lateral confinement of material around the charge leading to a more directional loading.

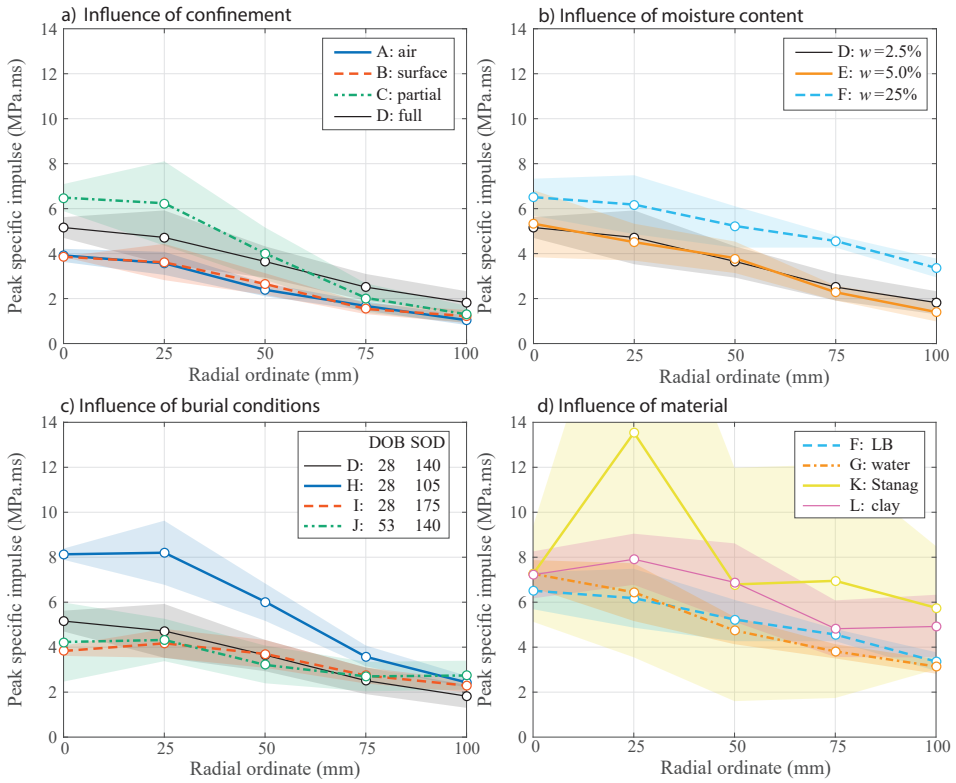

Figure 2.20: Specific impulse distribution in testing by Clarke et al. (2020), investigating four different parameters.

Clarke et al.'s findings on moisture content showed that for small changes in moisture content (2.5% to 5%) there was no observable change in loading, however, large changes (e.g. compared to full saturation at 25%) resulted in significant differences in loading (Figure 2.19b & 2.20b). This is in line with previous work of Clarke et al. (2017) that measured total impulse (as discussed in § 2.4.2). What Clarke et al. (2020) found, however, was that not only is the total impulse greater for saturated soils, but the loading profile is significantly different too. They hypothesised that the loading for a dry/low moisture content soil is similar to an air shock with discrete particle strikes creating an approximately uniform loading on the target face. In contrast, they found the loading from a saturated materials is more akin to the loading from a fluid droplet interacting with a rigid surface, with a non-uniform loading taking the form of an expanding annulus on the target.

Clarke et al.'s findings on the influence of burial conditions (Figure 2.19c & 2.20c) are in line with previous results of Westine et al. (1985) (discussed in § 2.5), showing that for a given burial depth, decreasing the stand off distance increases the imparted loading. The results of different materials Figure 2.19d & 2.20d) showed that the non-uniform STANAG soil to be the worse case scenario with

a higher total impulse, higher average specific impulse at all distances and a higher degree of experimental variation. Though this increase is possibly due to individual large soil particles hitting the HPBs and skewing the interpolations Waddoups et al. (2023). This indicates that additional knowledge of the soil composition is required to accurately predict the loading that is to be expected. Tests comparing water to saturated soil (series F and G in the (Figures 2.19 & 2.20)) confirms the findings of that the saturated sand results in a fluid like interaction with the target plate.

2.4.5 Hopkinson pressure bars

Hopkinson (1914) first proposed a test apparatus, commonly known as the Hopkinson Pressure Bar (HPB), for measuring the pressure from a bullet impact or explosive detonation. Hopkinson's apparatus consisted of two cylindrical bars of the same materials and diameter, which he referred to as the rod and the end piece. A strike on one end will result in a compressive wave travelling down the rod. The length of the compressive wave is determined by the duration of the loading. If the two parts are in firm contact, this wave will be transmitted into the end piece with minimal losses or reflection. As the compression wave reaches the distant, free face of the end piece it will be reflected back as a tension wave. If the forward travelling compression wave has already passed the join when the backwards travelling tension wave reaches it, it will cause the end piece to fly off, taking some of the imparted momentum with it. By varying the length of the end piece, the duration of the loading event can be determined. When the end piece is half the length of the compressive wave both the compressive and tension waves will be entirely within the end piece when it is ejected, leaving the main rod at rest. The duration of the loading event is therefore $2\times$ the time taken for the compression wave to travel the length of the end piece. If the sound speed of the material is known, the duration of the loading can be determined.

If a bullet is fired into the end of the rod, or an explosive is detonated close to it[2] in the case where the main rod remains at rest after the ejection of the end piece, measurements of the end piece size and momentum can be used to determine the duration and magnitude of the initial loading respectively.

A modern adaptation of the HPB is to use strain gauges to measure the axial strain caused by the stress pulse as it travels down the bar, negating the need to use the end piece for measurement Davies (1948). In this sense, a modern HPB is a single instrumented bar. A strain gauge mounted on the exterior surface of the bar will be sensitive to small deformations in the bar length due to the propagating stress wave. As the bar deforms, the strain gauge also deforms with a resultant change in its resistance. This change in resistance is measured via a Wheatstone bridge circuit. The recorded voltage-time data

[2]The detonation event needs to be far enough from the end of the rod to avoid plastic (permanent) deformation.

is then converted into a strain-time data set using the gauge factor. As the Young's Modulus modulus (E) of the HPB material is known, the strain data can be easily converted into stress data using the relationship $E = \frac{\sigma}{\varepsilon}$ which is valid in the regime of elastic deformation.

Special attention is being given to the conversion from the loading event to pressure/stress-time history for the Hopkinson pressure bars as this will inform much of the original testing which forms part of this thesis. Below is a summary of the loading and analysis process using the HPBs in this work:

1. initiation of the loading event;
2. stress wave is generated within the bar;
3. elastic deformation/elongation pulse travels down the bar;
4. strain gauge resistance changes due to the deformation;
5. a Wheatstone bridge is used to measure this small change in resistance;
6. measured strain is converted into stress using the Young's modulus of the bar; and
7. the total impulse is calculated by integrating the stress-time history.

This process assumes that the elastic stress pulse travels as a single wave down the bar at the wave speed determined by the bar's material. In reality, this stress wave travels as a series of waves generated by a process known as dispersion. For free air blast, this can be corrected by allowing the original form of the stress-time history to be recreated (Rigby et al. (2016b) and Barr et al. (2020)). For buried blast events, the smoothing caused by the presence of the soil particles means that anything beyond a first mode correction is likely not required and even first mode correction is likely to have minor differences to the pressure-time history. In either case, the total impulse is the same due to the nature of the dispersion correction.

2.4.5.1 Wheatstone bridge

The Wheatstone bridge, invented by Wheatstone (1843), allows the resistance of an element (unknown resistor or other electrical component) to be measured to a high degree of accuracy. This is achieved by balancing the resistance of each side of a bridge circuit until no current flows between them. By measuring the current flow between the two legs of the bridge, it also allows the unknown/variable resistance to be measured. Figure 2.21 shows a diagram of a Wheatstone bridge. A known voltage is applied across nodes 2 and 3 and the voltage across nodes 1 and 4 is measured, which depends on the values of the four resistors. The ratio of the output voltage to the input voltage is given by equation 2.8 below (Hoffmann 1974):

$$\frac{V_{out}}{V_{in}} = \frac{R_1}{R_1 + R_2} - \frac{R_4}{R_3 + R_4} = \frac{R_1 \cdot R_3 - R_2 \cdot R_4}{(R_1 + R_2)\left(R_3 + R_4\right)} \tag{2.8}$$

The bridge circuit can be constructed where one of the resistors is substituted for a variable element (i.e. a sensing element which outputs a change in resistance).

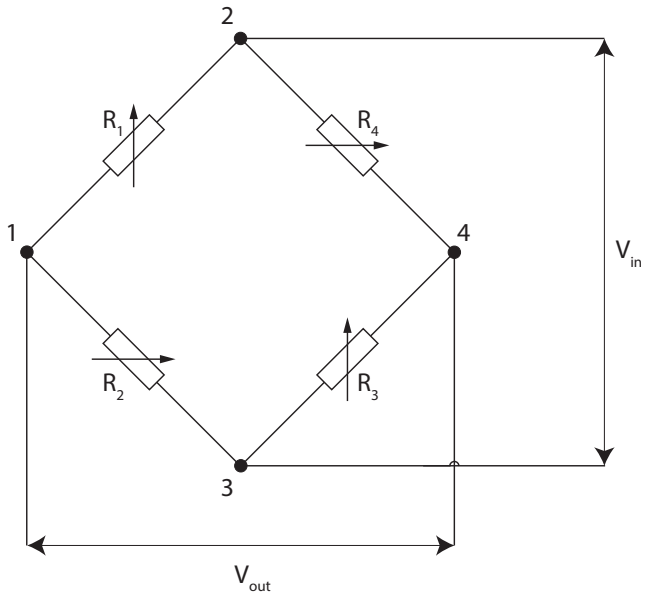

Figure 2.21: Diagram showing a Wheatstone bridge circuit with four resistors (R_1 to R_4) connected at four nodes (labelled 1-4), an input voltage V_{in} and an output voltage V_{out}.

If the paired resistor is also replaced with a variable resistor, the bridge can be balanced such that the output voltage is zero. Any subsequent change to the resistance of the sensing element (e.g. a stimulus is applied to the sensor) will result in an output voltage proportional to the change in resistance.

2.5 Numerical tools for estimating buried charge loading

Research into the threat posed by buried charges has been ongoing for many years using both experimental and numerical methods. Figure 2.22 shows the naming convention used by Westine et al. (1985), which is also used within this work. The target structure is assumed to be a rigid, non-deformable plate and hence predicts the worst case scenario.

2.5.1 The Westine model

Westine et al. (1985) used dimensional analysis to determine the form of the equation required to predict the specific impulse at a given point due to the detonation of a buried charge. They then conducted experimental work to empirically determine the coefficients for each term in their equation, giving the following:

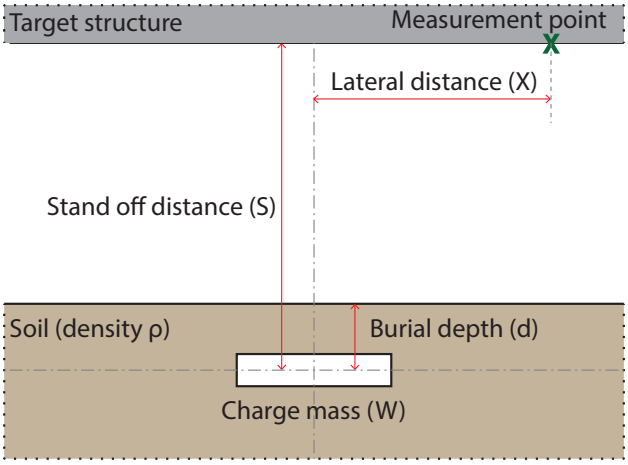

Figure 2.22: Diagram showing a geometry and naming convention used for the models discussed, using the name convention proposed by Westine et al. (1985).

$$i = 0.1352\left(1+\frac{7d}{9S}\right)\left(\frac{\rho W}{S}\right)^{\frac{1}{2}}\left(\frac{\tanh(0.9589\zeta X)}{\zeta X}\right)^{3.25} \tag{2.9}$$

where:

$$\zeta = \frac{d}{S^{\frac{5}{4}}A^{\frac{3}{8}}\tanh\left(\left(2.2\frac{d}{S}\right)^{\frac{3}{2}}\right)} \tag{2.10}$$

and
i = specific impulse [Pa·s]
W = energy released by the explosive[3] [J]
ρ = density of soil [kg m^{-3}]
S = stand off distance from centre of the charge to the face of the target [m]
d = burial depth from the centre of the charge to the soil surface [m]
A = cross-sectional area of charge [m^2]
X = lateral distance to location of impulse prediction [m]
$Z = \zeta X$ = scaled position [dimensionless]

Note: Equation 2.10 is undefined when $\zeta = 0$. However, using the small angle approximation, $tanh(\theta) \approx \theta$, the last bracket of Equation 2.9 reduces down to $0.9589^{3.25} = 0.8724$, and Equation 2.9 can then be rewritten as

$$i = 0.1180\left(1+\frac{7d}{9S}\right)\left(\frac{\rho W}{S}\right)^{\frac{1}{2}} \tag{2.11}$$

[3]This can be calculated based on a TNT equivalency, with TNT having an energy release of 4.516 MJ/kg (Tremblay 1998).

Due to the empirical nature of Westine et al.'s work, their predictions are only valid within limits defined by the experimental results. These limits can be expressed as follows:

$$0.106 \leq \frac{d}{S} \leq 1.00 \tag{2.12}$$

$$6.35 \leq \frac{W/A}{\rho c^2 S} \leq 150.0 \tag{2.13}$$

where c is the wave speed in the soil

$$0.154 \leq \frac{A^{\frac{1}{2}}}{S} \leq 4.48 \tag{2.14}$$

$$0.00 \leq \frac{X}{S} \leq 19.3 \tag{2.15}$$

Westine et al. also defined the scaled impulse (Y) as follows:

$$Y = i\left(\frac{S}{\rho W}\right)^{\frac{1}{2}}\left(\frac{1}{1+\frac{7d}{9S}}\right) \tag{2.16}$$

which is plotted against the scaled position (Z) in Figure 2.23. It can be seen that when plotting the scaled impulse against the scaled position, Westine et al.'s experimental data points are clustered within the region of $Y \times 1.8$ and $Y \div 1.8$.

It can be seen from Equation 2.9 that Westine et al.'s model only requires a single parameter to characterise the soil (namely its density), making it a powerful tool for predicting the loading. This, however, has been shown from the literature to be an oversimplification. For example, Clarke et al. (2017) found that the loading was not consistent between soils with a fixed bulk density, but different moisture content. Ehrgott et al. (2011) also found a difference between 'silty sand' and 'sandy clay' which had similar densities and proposed the parameter of interest is the air void ratio and permeability.

2.5.2 Total impulse in the Westine model and the development of the Tremblay model

To translate the specific impulse at a given point into the total impulse, Equation 2.9 needs to be integrated over the full area of the target plate. i.e.

$$i_{tot} = 0.1352\left(1+\frac{7d}{9S}\right)\left(\frac{\rho W}{S}\right)^{\frac{1}{2}}\int_{x_{min}}^{x_{max}}\int_{y_{min}}^{y_{max}}\left(\frac{\tanh(0.9589\zeta X)}{\zeta X}\right)^{3.25} dydx$$

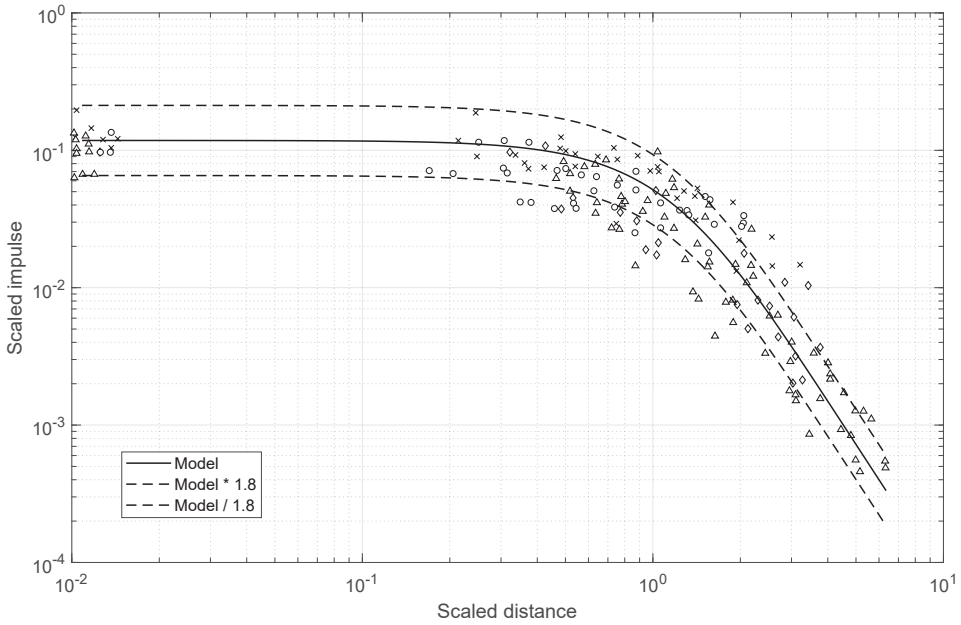

Figure 2.23: Plot showing how the majority of Westine et al.'s experimental data lies in the region bounded by the two lines which represent $Y \times 1.8$ and $Y \div 1.8$.

(2.17)

However, the form of the red section of equation 2.17 means it can only be solved numerically. Therefore, Tremblay proposed the following approximation to Westine et al.'s impulse equation:

$$i = 0.1352\left(1+\frac{7d}{9S}\right)\left(\frac{\rho W}{S}\right)^{\frac{1}{2}}\left(\kappa_1\left(1+\kappa_2(\zeta X)^6\right)e^{-\kappa_3(\zeta X)^2}\right) \tag{2.18}$$

where
$\kappa_1 = 0.8725$
$\kappa_2 = 0.04837$
$\kappa_3 = 0.8917$

The red part of Westine et al.'s and Tremblay's equations are plotted in Figure 2.24 for $0 < \zeta X < 3$[4] to demonstrate their similarity.

[4]this represents a wide range of realistic scenarios where the stand off distance, burial depth and measurement distance are all the same order of magnitude.

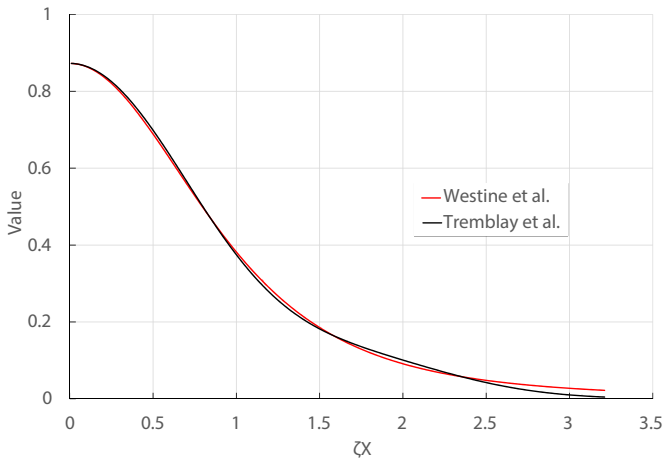

Figure 2.24: The difference between Westine et al.'s equation and the approximation proposed by Tremblay; the plot shows the value of the red part of Equations 2.18 & 2.17.

Tremblay's approximation leads to an algebraically solvable form when integrated to determine the total impulse, namely:

$$\begin{aligned} i_{tot} &= 0.1352\left(1+\frac{7d}{9S}\right)\left(\frac{\rho W}{S}\right)^{\frac{1}{2}}\int_{x_{min}}^{x_{max}}\int_{y_{min}}^{y_{max}}\left(\kappa_1\left(1+\kappa_2(\zeta X)^6\right)e^{-\kappa_3(\zeta X)^2}\right)dxdy \\ &= \kappa_0\left(1+\frac{7d}{9S}\right)\left(\frac{\rho W}{S}\right)^{\frac{1}{2}}(S_1+S_2) \end{aligned} \tag{2.19}$$

where

$$\begin{aligned} \kappa_0 &= 0.1352\kappa_1 = 0.1180 \\ S_1 &= \int_{x_{min}}^{x_{max}}\int_{y_{min}}^{y_{max}}\left(e^{-\kappa_3(\zeta X)^2}\right)dxdy \\ S_2 &= \int_{x_{min}}^{x_{max}}\int_{y_{min}}^{y_{max}}\left(\kappa_2(\zeta X)^6 e^{-\kappa_3(\zeta X)^2}\right)dxdy \end{aligned}$$

The strength of Tremblay's model is that it is applicable, and remains solvable, for target plates that are at an angle to the soil surface. However, for the purpose of this work, the target plates remain parallel to the soil surface and the total impulse is calculated through numerical integration. Therefore, while an important development, the Tremblay modifications to the Westine model are not required.

2.5.2.1 Special case of a square plate centred above the target

Tremblay's equation for the total impulse, while algebraically integrable, is still non trivial to compute due to the e^{x^2} terms in both S_1 and S_2 which, when integrated return error functions (erf). The full version of these integrals can be found in Tremblay (1998). For the purposes of this work, the special case of a square deflector of length l centred above the charge is used. For this case Tremblay shows that the S_1 and S_2 terms are given by:

$$S_1 = \frac{\pi}{\kappa_3 \zeta^2} erf^2\left(\frac{\sqrt{\kappa_3} l \zeta}{2}\right) \tag{2.20}$$

$$\begin{aligned} S_2 = \frac{\kappa_2}{16\kappa_3^4\zeta^2}\Bigg[& \\ & \left(36\kappa_3 l^2\zeta^2 + 6\kappa_3^2 l^4\zeta^4\right) e^{\frac{-\kappa_3 l^2\zeta^2}{2}} \\ & + 96\pi \mathrm{erf}^2\left(\frac{\sqrt{\kappa_3} l\zeta}{2}\right) \\ & - l\zeta\sqrt{\kappa_3\pi}\left(132 + 16\kappa_3 l^2\zeta^2 + \kappa_3^2 l^4\zeta^4\right)\mathrm{erf}\left(\frac{\sqrt{\kappa_3}\zeta l}{2}\right) e^{\frac{-\kappa_3 l^2\zeta^2}{4}}\Bigg] \end{aligned} \tag{2.21}$$

Again taking the square plate case, the total impulse transferred to an infinite sized plate can be calculated using the identities

$$\lim_{x\to\infty} e^{-x} = 0 \qquad\qquad \lim_{x\to\infty} \mathrm{erf}(x) = 1$$

$$\lim_{l\to\infty} S_1 = \frac{\pi}{\kappa_3\zeta^2} \tag{2.22}$$

$$\lim_{l\to\infty} S_2 = \frac{6\pi\kappa_2}{\kappa_3^4\zeta^2} \tag{2.23}$$

$$
\begin{aligned}
\lim_{l\to\infty} i_{tot} &= \kappa_0\left(1+\frac{7d}{9S}\right)\left(\frac{\rho W}{S}\right)^{\frac{1}{2}}\left(\frac{\pi}{\kappa_3\zeta^2}+\frac{6\pi\kappa_2}{\kappa_3^4\zeta^2}\right)\\
&= \kappa_0\left(1+\frac{7d}{9S}\right)\left(\frac{\rho W}{S}\right)^{\frac{1}{2}}\left(\frac{\pi}{\kappa_3\zeta^2}\right)\left(1+\frac{6\kappa_2}{\kappa_3^3}\right)\\
&= \frac{1}{\zeta^2}\left(\frac{\kappa_0\pi}{\kappa_3}\right)\left(1+\frac{6\kappa_2}{\kappa_3^3}\right)\left(1+\frac{7d}{9S}\right)\left(\frac{\rho W}{S}\right)^{\frac{1}{2}}\\
&= \frac{\kappa_4}{\zeta^2}\left(1+\frac{7d}{9S}\right)\left(\frac{\rho W}{S}\right)^{\frac{1}{2}}
\end{aligned}
\tag{2.24}
$$

where

$$
\kappa_4 = \frac{\kappa_0\pi}{\kappa_3}\left(1+\frac{6\kappa_2}{\kappa_3^3}\right) = 0.5857 \tag{2.25}
$$

Equation 2.24 gives a maximum impulse for the given burial conditions that does not require any integrations to be performed. As shown in Figure 2.25 this maximum is reached for a relatively manageable plate size (0.7 m in the example used).

2.5.3 The truncated Westine model

As discussed above, an advantage of the Tremblay model is that it has a numerically calculable maximum whereas the Westine model asymptotes to a maximum at infinite target size. This makes it difficult to determine the efficiency[5] of a given experiment as there is no maximum. To combat this, a third model is proposed which imposes a maximum based on the limits of data used to compile the model. In the original work, Westine et al.'s data had a maximum scaled position (ζX) of 6.35. In the truncated Westine model, any positions on the target plate greater than this have been suppressed, resulting in the model reaching a maximum value at a manageable plate size. The Westine, Tremblay and trucated Westine models are plotted in Figure 2.25.

2.5.4 Exploration of the Westine model

The following section explores how the different variables in the model influence both the total impulse and specific impulse distribution. Table 2.6 shows the default values for the different parameters used in the modelling. For the purposes of this exploration, the charge is taken as a 3:1 cylinder (115 mm diam, 38 mm thick) in line with the threat definition in AEP-55 (NATO 2014).

[5] i.e. the percentage of the total impulse due to the buried charge that is captured by the target.

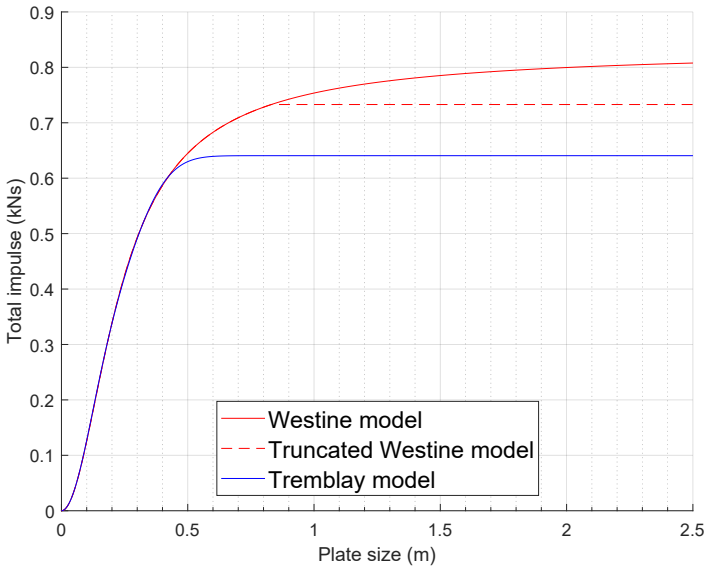

Figure 2.25: Plot showing how the total impulse for a given target plate size compares in the three different models discussed.

Table 2.6: Parameters used within this section when exploring the Westine et al. model.

Variable		**Value**	**Units**	**Comment**
Energy Release	W	3,387,000	J	625 g of PE4 assuming a TNT equivalence of 1.2 and an energy release for TNT of 4.516 MJ/kg Tremblay (1998)
Lateral distance	X	-337.5 to 337.5	mm	Based on the setup used by Clarke et al. (2017)
Stand off distance	S	0.2065	m	
Burial depth	d	0.0690	m	
Charge area	A	0.01039	m^2	
Charge mass	M	0.625	kg	
Soil density	ρ	1.633	Mg/m^3	Based on dry LB sand used by Clarke et al. (2017)

Soil density Figure 2.26 shows how varying the soil density affects the specific impulse distribution (2.26a) and the total impulse (2.26b). As expected from Equation 2.9, the specific impulse at a given point is proportional to the square root of the soil density. This equates to a difference in the total impulse of approximately 30% for the given geometry for soil densities ranging from 1200 kg/m^3 to 2000 kg/m^3 (which extends beyond the typical range observed in natural soils).

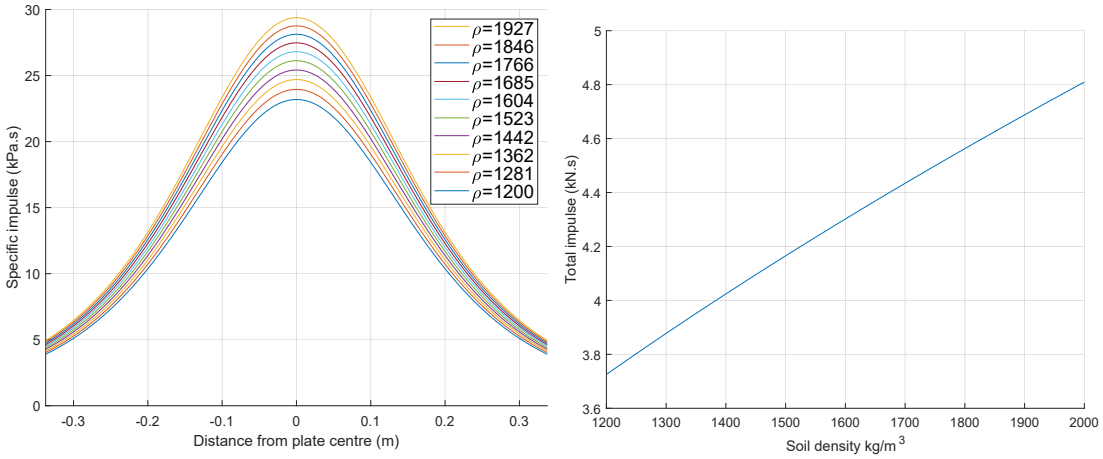

(a) Specific impulse distribution **(b)** Total impulse

Figure 2.26: Influence of soil density in the Westine et al. (1985) model.

Charge area Figure 2.27 shows how varying the charge area affects the specific impulse distribution (2.27a) and the total impulse (2.27b). The vertical red lines on Figure 2.27b indicate the limits imposed on the charge area by Equation 2.14. Further to this, assuming the charge volume is constant, the pink line represents the lower limit on the area of a 3:1 cylindrical C4 charge based on its critical diameter (5.2 mm (Dobratz and Crawford 1985)) and the dark blue line is the lower limit for a pure RDX charge (critical diameter 3 mm (Dobratz and Crawford 1985)). This demonstrates that the limits imposed in the model by Equation 2.14 span a range significantly beyond what is experimentally practical. The pink line also highlights that a 3:1 cylinder charge (as per (NATO 2014)) is in the region where small changes in the charge area have a significant affect on the output of a buried charge.

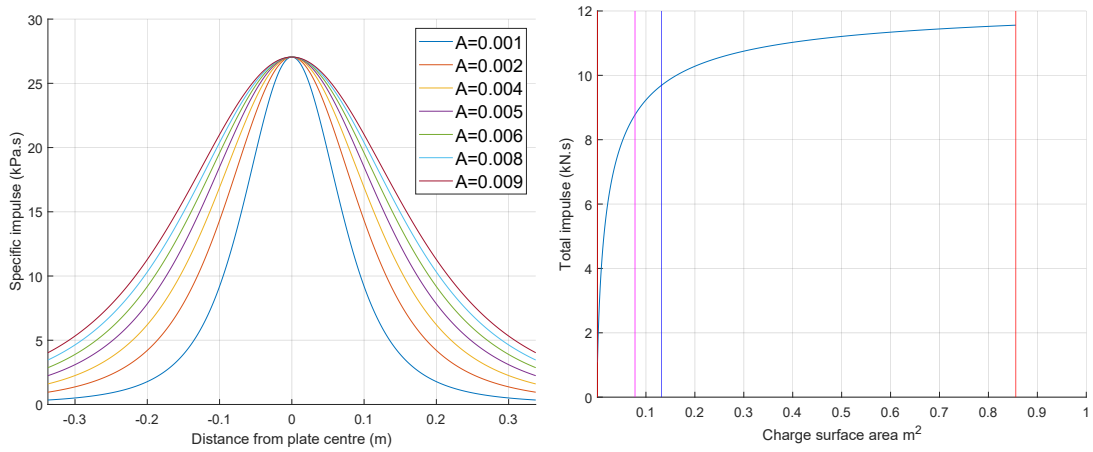

(a) Specific impulse distribution **(b)** Total impulse

Figure 2.27: Influence of charge area in the Westine et al. (1985) model.

Burial depth Figure 2.28 shows how varying the burial depth for a fixed stand off affects the specific impulse distribution (2.28a) and the total impulse (2.28b). As the burial depth increases, so does the specific impulse at the centre of the target plate. Initially, as the burial depth increases, the distribution shows a similar shape up to a given depth, above which the specific impulse distribution begins to become more centrally weighted. This point is shown in Figure 2.28a as the purple dotted line. The point where the trend changes coincides with the peak of the total impulse vs burial depth curve (Figure 2.28b), indicating that there is an 'optimal' burial depth (for a given parameter set) to deliver the maximum impulse to a target. This depth also corresponds to the burial condition where the soil depth and air gap are equal, or alternatively where the burial depth is half of the stand off distance.

The vertical red line on Figure 2.28b indicates the limits imposed on the burial depth by Equation 2.12, and the pink line represents the burial depth used by Clarke et al. (2017) based on the definitions in NATO (2014). Also shown on the right hand axis is the burial conditions i.e. the depth of soil and air gap between the surface of the soil and the target plate for the given stand off (0.2065 m),

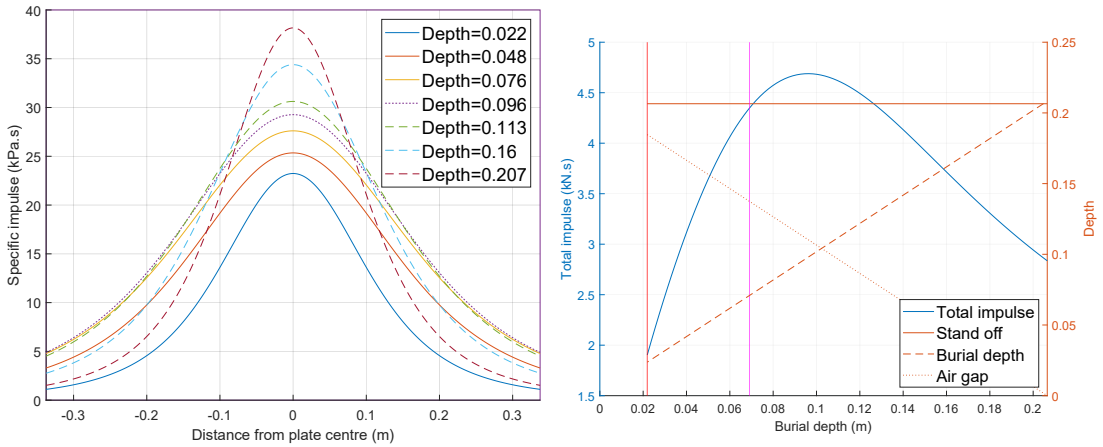

(a) Specific impulse distribution **(b)** Total impulse

Figure 2.28: Influence of burial depth in the Westine et al. model.

2.6 Identification of knowledge gaps

Geotechnical properties that effect the loading from a buried charge that have been discussed in the existing literature include: bulk density, particle size distribution, moisture content (defined as M_w/M_s), saturation, air void ratio and permeability. There has, however, been very little work investigating the effects of mineralogy on the loading. Where different soils have been analysed and compared, this has predominantly been silica based soils of different particle sizes/distributions. However, other granular soils may respond differently if they have inherently different particle geometries and material strengths. Work of Safinus et al. (2013) on the bearing strength of carbonate sands in the context of offshore structure stability has shown that applying models developed for silica based sediments can lead to significant discrepancies.Therefore, is it proposed that testing is undertaken using soils with different particle mineralogies, this will be explored further in the next chapter.

As discussed above in section 2.5.1, the Westine model only contains a single parameter to characterise the soil. It has already been proven by Clarke et al. (2017) and Ehrgott et al. (2011) that this is an over simplification. Clarke et al. have shown that the moisture content of the soil is an important factor when characterising the loading and the authors have therefore proposed the addition of an extra term in the Westine equation to account for the moisture content of the soil.

The testing of both Clarke et al. (2017) and Clarke et al. (2020) was conducted with soil samples of a uniform moisture content throughout the sample. However, in the littoral environment of interest to Dstl, it is probable that there could be situations where the soil is fully saturated below a given depth (e.g. if it is within the inter tidal zone of a beach). Therefore, it is proposed that addi-

tional testing is undertaken into the effect of the water level in fully saturated soils, including soils with a layer of water above the surface (e.g. representing the threat posed by a buried charge to a vehicle driving in shallow water).

Finally it is also clear from the literature that no buried charge testing has been conducted looking at temperature effects, specifically the threat posed by charges buried in frozen ground (and to address Dstl's interest in soils of subarctic regions). It is proposed that testing is conducted with soils that are frozen. This presents a challenging research goal as again, the prepared soil sample may not be of uniform construction (e.g. it may be frozen or thawed to a given depth from the surface). The development of the research questions and test plans are discussed in the next chapter.

2.7 Scoping the problem

As the funder for this work, Dstl suggested that investigations should focus on expanding the knowledge to incorporate information on charges buried in littoral and subarctic regions. From the literature review it is clear that these regions have not been specifically investigated (§ 2.6). Given that neither area have been previously studied in the context of buried charges, this work aims to define the areas to be investigated along with a clear test plan to explore the issues raised.

Firstly, it is useful to define the scope of littoral and subarctic environments.

2.7.1 Littoral environment

The littoral environment is defined in UK military doctrine as follows:

> *Those land areas (and their adjacent areas and associated air space) that are susceptible to engagement and influence from the sea* (Ministry of Defence 2017).

Alternative definitions from the field of marine biology define the littoral zone as being:

> *A marine ecological realm that experiences the effects of tidal and longshore currents and breaking waves to a depth of 5–10 metres below the low-tide level, depending on the intensity of storm waves. The zone is characterized by abundant dissolved oxygen, sunlight, nutrients, generally high wave energies and water motion, and, in the intertidal subzone, alternating submergence and exposure.* (The Editors of Encyclopaedia Britannica 2019).

The shore area or intertidal zone, where periodic exposure and submersion by tides is normal (Allaby 2010).

The definitions incorporate a wide variety of geological environments, ranging from fully submerged coastal waters to inland areas within the range of sea based military effects. Modern naval guns have a range in the region of 25 km (United States Navy 2019) and carrier based aircraft have combat ranges in excess of 800 km (RAF 2020), therefore, in the context of modern military technology this definition covers a vast portion of the earth's surface, as shown in Figure 2.29.

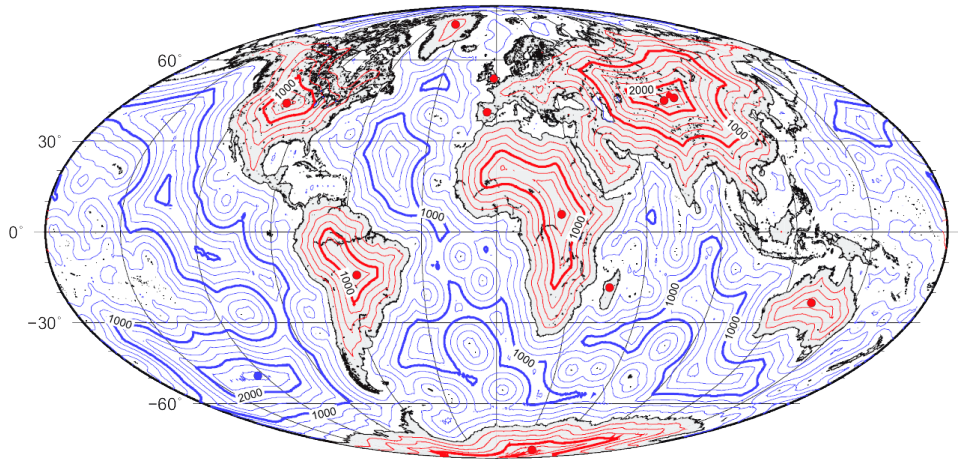

Figure 2.29: Map showing the distance from the nearest coastline. Contours are plotted at 250 km intervals (Garcia-Castellanos and Lombardo 2007).

For the purposes of this study, the definition of Allaby (2010) has been used as this represents a more manageable and less geologically varied environment where changes are likely to be dominated by the local level of the water table. This narrower definition of the littoral zone is consistent with the other definitions above and significantly increases the focus of the study. Specifically, all the testing in the literature has focussed on soils with a consistent moisture content throughout the whole sample. In the definition employed here, littoral soils will have a water table within the sample leading to a step change in the moisture content of the soil. It is also highly likely that there will be occasions in the littoral environment where the water level will be above the surface of the soil, e.g. when the tide is coming in, hence, this section of the study will focus on the effect the level of the water table has on the output from a buried charge.

2.7.2 Subarctic conditions

The subarctic region is defined as follows:

> *The continental subarctic climate is a major climate type of the Köppen classification dominated by the winter season, a long, bitterly cold period with short, clear days, relatively little precipitation (mostly in the form of snow), and low humidity. It is located north of the humid continental climate, from about 50° to70° N* (The Editors of Encyclopaedia Britannica 2016).

> *Regions immediately outside of the arctic circle or regions similar to these in climate or conditions of life* (Merriam-Webster n.d.).

Based on the definition of The Editors of Encyclopaedia Britannica (2016), the subarctic region covers the region between the two red lines in Figure 2.30. The ground conditions are typified by significant amounts of permafrost of varying extent. For the purposes of this work, the subarctic region has been taken to mean the regions with frozen ground (either seasonally or permafrost) as this presents a different environment to those previously studied.

Work of Åkerman and Johansson (2008) found that the thickness of the active layer[6] across nine sites in Sweden is in the region 60–70 cm. This measurement was taken during September at the time when the thawed layer is thickest, meaning that for the given sample sites, the depth of thawed material is no more than 70 cm. The Level 2 threat definition in NATO (2014) specifies a 10 cm burial depth meaning for the purposes of this work, a Level 2 threat will be buried within the active layer of the subarctic region and, depending on the time of year, may be either above or within the frozen section of the soil.

With there being no buried charge work done in frozen soils in the literature, initial testing will need to be conducted to both ensure the function of a high explosive charge when frozen and to also explore the methods to prepare frozen soils (both partially and totally frozen).

2.8 Previous work

It is useful to briefly describe the previous work done both in established measurement techniques and the soil preparation techniques before the specifics around the littoral and subarctic testing are described. Previous work conducted by the University of Sheffield's Blast Group (Clarke et al. (2015a), Clarke et al. (2017), Rigby et al. (2018a), Fay (2020) and Clarke et al. (2020)) has investigated a range of different soils including clay, quartz-based sands (Leighton Buzzard) and a sandy gravel representative of the standardized soil defined in AEP-55, Volume 2 (NATO 2014). These soils have been tested at a range of moisture contents and bulk densities.

[6] The layer of soil that undergoes seasonal freeze-thawing above the permafrost.

Figure 2.30: Map showing the location of permafrost in the region around The North Pole (International Permafrost Association Standing Committee on Data Information and Communication 2003). The red lines indicate the lines of 70° and 50° latitude.

2.8.1 Threat definition and scale

As well as being used to design an experiment, Hopkinson-Cranz scaling can also be used to compare the results of two different experiments that were conducted at different scales. In this application, the mass of the charge in each experiment can be used to scale up/down the results to compare them to other experiments of interest. To allow conclusions to be made from existing data in the literature, the results first need to be scaled to a common baseline. AEP-55, Volume 2 (NATO 2014) defines a range of threat levels to be used in the assessment of protection systems against buried charges/mines. Previous work using the Characterisation of Blast Loading (CoBL) apparatus were conducted at quarter scale with a 78 g PE4 charge corresponding to a 5 kg full-scale charge using

Hopkinson-Cranz scaling (Clarke et al. (2015a)). Given the TNT equivalence of PE4 is 1.2 (Rigby and Sielicki 2014) this equates to AEP-55 Threat Level 2 of 6 kg TNT. Clarke et al. (2018) showed that testing at quarter-scale is representative of full-scale testing with no loss in fidelity.

For the purposes of this work, this same scale has been chosen, a quarter scale with respect to the definition in AEP-55 Threat Level 2. As per Clarke et al. (2016a), 78 g PE4 charges with a diameter of 57.33 mm and a thickness of 19.11 mm will be used. This baseline has been selected as the CoBL apparatus was designed to work at this scale so there is a wealth of comparable historic data, allowing direct comparisons. This is also the largest charge size that could be used in the current apparatus without leading to permanent deformation of the soil containers.

Chapter 3

Experimental Design and Justification

3.1 Experimental apparatus

As discussed in § 2.4.4, the Characterisation of Blast Loading (CoBL) apparatus is a custom built test frame, detailed in the paper by Clarke et al. (2015a) and a schematic of which is included in Figure 3.1. The CoBL apparatus consists of a large mild steel target plate (1400 mm diameter, 100 mm thick) mounted on a reinforced concrete frame under which an explosive charge can be detonated. The charge can be either suspended in free air or buried within a soil container depending on the nature of the testing. CoBL soil containers are mild steel cylinders 500 mm diameter, 375 mm tall with 30 mm thick walls and a 25 mm base plate (Fay et al. 2013). Data from each test is recorded via an array of 10 mm diameter, 3.25 m long Hopkinson pressure bars (HPBs), made of EN24(T) steel, which pass through the target plate. The ends of the bars sit flush with the lower target plate surface and are exposed to the blast event. AS discussed in § 2.4.5, the length of the HPBs determines the duration of the loading event that can be recorded. The HPBs are instrumented 0.25 m away from the loaded face (i.e. behind the target plate). This offset from the loaded face of the bar is to protect the strain gauges from the detonation pressure/debris. For the given experiment, taking a sound speed in the bars of 5000 ms^{-1}, this gives a maximum recording time of 1.2ms before the reflected signal from the distal end interferes with the transmitted signal at the gauge location.

The signal from each HPB can be analysed to give the pressure-time history at that point on the target face. Through a process of interpolation, the overall loading on the target can be determined both spatially and temporally. This is discussed further in the following chapter which details the analysis methodology.

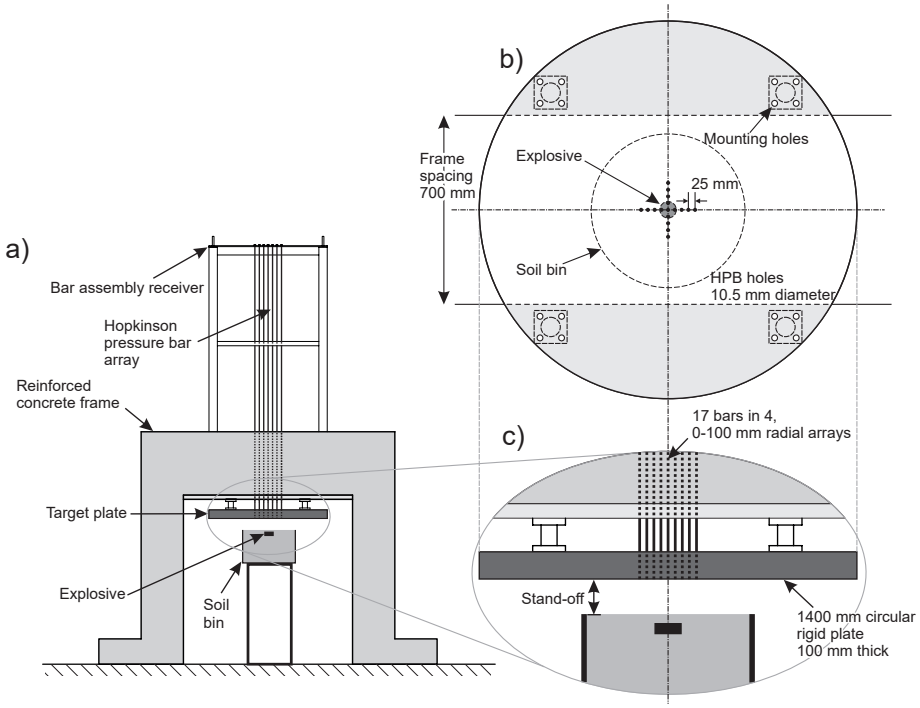

Figure 3.1: a) Diagrammatic representation of the CoBL apparatus showing the soil container, target plate, and array of Hopkinson pressure bars. b) Plan view of the target plate showing the arrangement of the bars in relation to the explosive charge and soil container. c) Detail view of the target plate (Lodge et al. 2023).

3.1.1 Instrumentation

Each of the 17 bars used in the apparatus has two strain with Kyowa KSPB-2-120-E4 semiconductor strain gauges attached to it in a balanced Half Wheatstone Bridge configuration allowing the strain to be recorded by a high-speed USB oscilloscope. The instrumentation settings used for this work are summarised in Table 3.1. The naming convention used for identifying the bars is included in Figure 3.2. Each array of locations is given a number and each radial distance a letter, meaning bars with the same letter designation are at the same radius, and bars with the same numerical designation are in the same array.

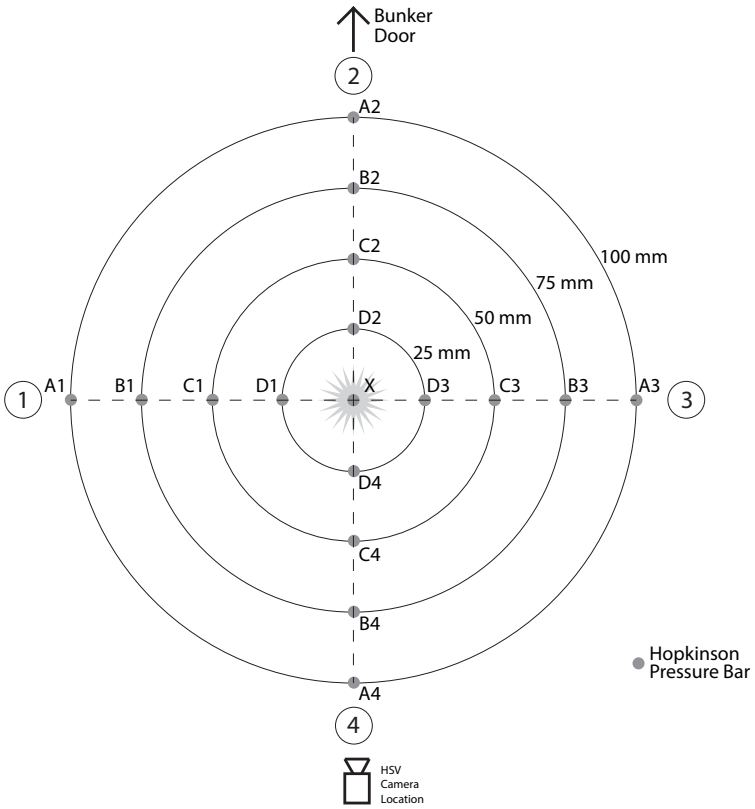

Figure 3.2: Diagram showing the naming convention used for the CoBL apparatus in this work.

Table 3.1: Table outlining the oscilloscope settings to be used for this work.

Parameter	**Value**
Make	TiePie
Model	Handyscope HS4
Resolution	14 Bit
Frequency	3.125 MHz
Number of samples	131.072 kSa
Pre-trigger	10%
Trigger type	5 V break wire
Hopkinson bar voltage	10 V

3.1.2 Charge preparation

In line with the previous work of Clarke et al. (2016a), charges for this work will be 78g PE4 cylinder 115 mm diameter 38 mm thick (forming a 3:1 cylinder as per the standard in AEP55, (NATO 2014) and used for the work of Anderson et al. (2010), Ehrgott et al. (2011), and Clarke et al. (2017)). The charges were housed in a 3D printed ABS plastic case with a 3 mm wall thickness and detonated from the centre of the bottom face using a Euronel 2 Non-Electric detonator. As per the testing of Clarke et al. (2016a), the charge cases were open on the top face to improve repeatability.

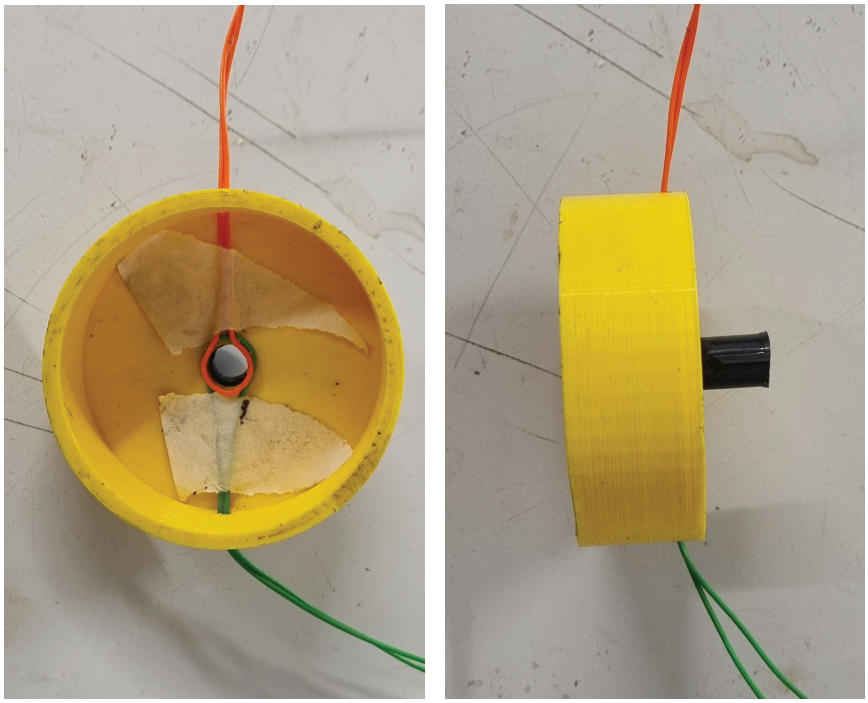

Figure 3.3: Photos showing the 3D printed ABS charge case, with two break-wires installed prior to adding the charge. Note the break-wires are superglued in place (held by tape whole the glue dries) to prevent their movement during charge preparation.

Figure 3.3 shows two photos of the charge case prior to being filled with the explosive. In the photo, two wires can be seen entering the case and passing around the detonator hole. These wires were used as break-wires to trigger the high speed camera and oscilloscope. The camera break-wire was set to trigger on a break in continuity (as monitored by the camera's internal triggering system) and the oscilloscope break-wire set to trigger on a falling edge trigger with the wire running as a 5 V closed circuit prior to testing. The break-wires were only connected to the camera and oscilloscope and the soil container was in place ready for testing to avoid the risk of a premature initiation by stray electrical connection.

Once the charge case was prepared, the pre-weight amount of PE4 was stemmed into the mould in small amounts (approximately 10 g at a time) to ensure no voids were present. The case was designed in such a way that adding the full 78g into the void with a the top surface level with the sides created a charge with a consistent bulk density.

3.1.3 Soil compaction and saturation

Previous work on saturated soils at the University of Sheffield has been conducted through a process of first preparing a soil bin to a given bulk density and moisture content before then saturating it. The soil samples are filled in multiple lifts of approximately 1/3 of the total volume, with each being compacted to the desired level prior to adding the next lift. This matches the procedure presented by Baker (1976) who suggests multiple lifts are used to prepare frozen soil samples.

Once the full sample is prepared, a hose embedded in the base of the soil container is used to saturate it from the bottom up (Clarke et al. 2014). Figure 3.4 shows photos of this process with the hose embedded at the bottom of the sand bin. It is proposed that a similar technique is used in the preparation of samples for this work. Baker's procedure requires the samples to be saturated slowly so as not to cause localised changes to the soil density/compaction and inefficient evacuation of air from between the solid particles. Baker also proposes that a vacuum is applied to the top of the sample to achieve saturation levels close to 100%. However, this is only feasible at the smaller lab scale and is both not practical for the size of samples required for this work (approximately 500 mm diameter) or required if the samples are not intended to be fully saturated.

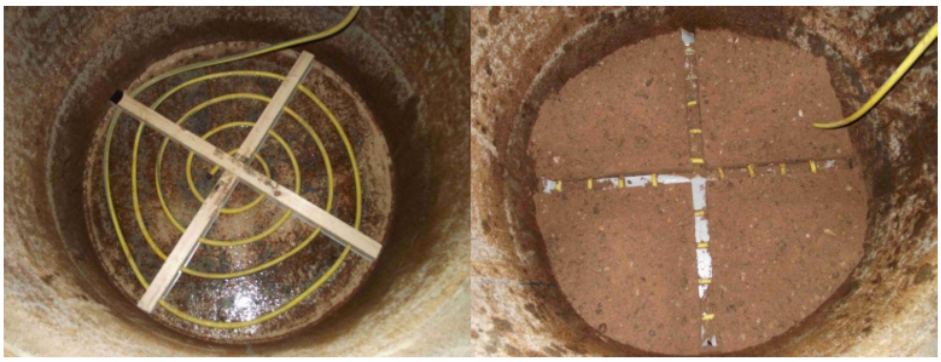

Figure 3.4: Photos showing the position of the saturation hose at the base of a soil bin. The bin is filled and compacted prior to saturation (Clarke et al. 2014).

Figure 3.5: Photos showing the method for placing a charge in a pre-prepared sand bin whilst minimising the degree of disruption to the geotechnical parameters.

3.1.4 Charge placement

Previously, Clarke et al. (2014) determined a methodology for placing the charge in a highly controlled sand bin for buried charge testing (further details can be found in Rigby et al. (2016) and Fay (2020)). Their method involves the following steps, as illustrated by the photos in Figure 3.5:

1. The sand bin is prepared and filled according to the test requirement (§ 3.1.3).
2. A former is used to create a void in the centre of the sand bin to house the charge. The removed material is stored in a plastic bag to maintain the set moisture content.
3. A channel is made for the detonator lead and trigger wire.
4. The charge is placed in the cavity with a detonator attached.
5. The excavated material is replaced and tamped down to the required density.
6. The end result is a buried charge within a sand bin which is as consistent as possible.

3.2 Experimental justification

Previous parametric testing has focussed on using well characterised quartz sand when looking at geometric and geotechnical variations. With the research focussing on littoral soils, the next logical question is *what sort of geological conditions make up the majority of the world's intertidal zones?* The analysis of Luijendijk et al. (2018) determined that 31% of the world's ice-free shoreline consists of sandy beaches, with the remainder being a range of types such as barrier islands, sea cliffs, tidal flats, and river deltas. Figure 3.6 shows how the sandy beaches identified by Luijendijk et al. (2018) are distributed globally. Sandy soils provide an ideal test bed as, with careful, well controlled preparation, they have been shown to give consistent results (Clarke et al. (2015a)). Therefore, sandy soils will form the basis of this research.

Reise (2012) states that tidal sediments are predominantly composed of a combination of quartz and carbonate minerals, with quartz based materials usually dominating due to their increased hardness (which grinds down weaker carbonates). The exception to this is in warm seas where there is a higher rate of carbonate production, in which case calcareous minerals dominate. For the purposes of this study, we define carbonate sand as having greater than 50% calcium carbonate content and soils with less than 50% calcium carbonate as calcareous soils. As previous work has already examined the effects of the moisture content of quartz-based Leighton Buzzard (LB) sand on the loading using the CoBL apparatus, extending this to cover varying water table levels and frozen soils are logical steps. Therefore, testing will begin with LB to allow direct comparison to previous work. The next stage would be to look at the effects of soil mineralogy (i.e. carbonate versus quartz-based soils), extending the applicability of the research to wider littoral settings. In geotechnical testing there also exists a well characterised carbonate sand, Dog's Bay sand (from Ireland), which would form an ideal baseline soil for non-quartz based littoral soils testing (White (2003) and Bowman et al. (2001)).

3.2.1 Littoral testing - water table

To allow the water table level to be controlled in the current testing, it is proposed to use a similar technique to previous work (§ 3.1.3). An external clear tube connected to the base of the soil bin can be used to measure the water level within the soil sample (for coarse grained soils where capillary rise is minimal). For one series of proposed tests (detailed later in Figure 3.10c), the sample will need to be prepared with a head of water above the surface of the charge, meaning the water level in the soil bin will need to be raised after the charge is placed. It is proposed that this set of tests utilises a frangible collar extending above the edge of the soil bin to contain a depth of water, in effect replacing some of the air gap between the soil and the target with water. This

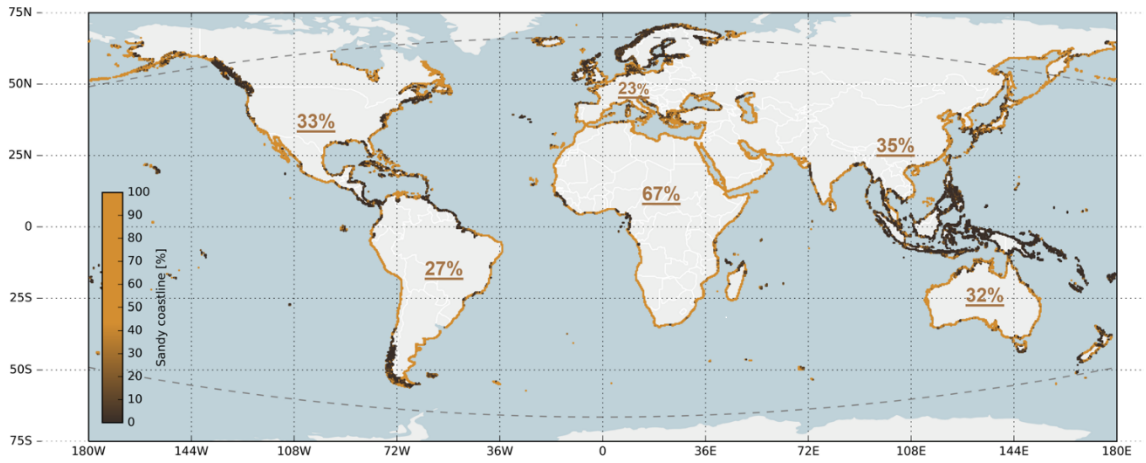

Figure 3.6: Plot showing the proportion of the world's ice free coastline that is made up of sandy beaches. The curved dashed lines at the top and bottom represent the boundary of the regions that were deemed predominantly icy shorelines and were therefore excluded from the study (Luijendijk et al. 2018).

arrangement will allow direct comparison to previous CoBL tests with a charge at the same burial depth and stand off.

It is believed that the worst case scenario for a land mine in the littoral environment would be where the vehicle is partially submerged up to the floor plate, i.e. there is no air gap between the surface of the water and the underbelly of the vehicle. This is due to the incompressible nature of water, when compared to air, allowing a better transmission of the shock wave into the vehicle. This worst case scenario to be likely to result in damage to the HPBs if the water is forced down the side of the bars, potentially scouring off the gauges. Therefore, an alternate arrangement will be tested wherein there is still an air gap between the target plate and the water surface. Representing a vehicle being partially submerged without the belly plate entering the water.

Figure 3.7 shows how the water table will be varied for the LB tests. The first series will perform tests with the water level with the base of the charge and compared to the results of Clarke et al. (2020). If, as in the results of Clarke et al., the properties of the material below the charge lead to no significant difference in the measured load, then for the second series of tests, the water table will be set to the top surface of the charge (shown on the left hand side of Figure 3.7, labelled 'Charge top'). This will be to assess conditions similar to those of Series C in Figure 3.11, i.e. partial confinement of the charge by the heightened water table. If, however, there is a difference between the results of the tests with water at the base of the charge and the results of Clarke et al.'s testing on saturated sand, then a water table below the surface of the charge will be used for the second series (shown on the right hand side of Figure 3.7, labelled 'Below charge'). The final test series to investigate the water table will

be conducted with water abvoe the surface of the soil, as shown in Figure 3.7 and labelled 'Above surface'.

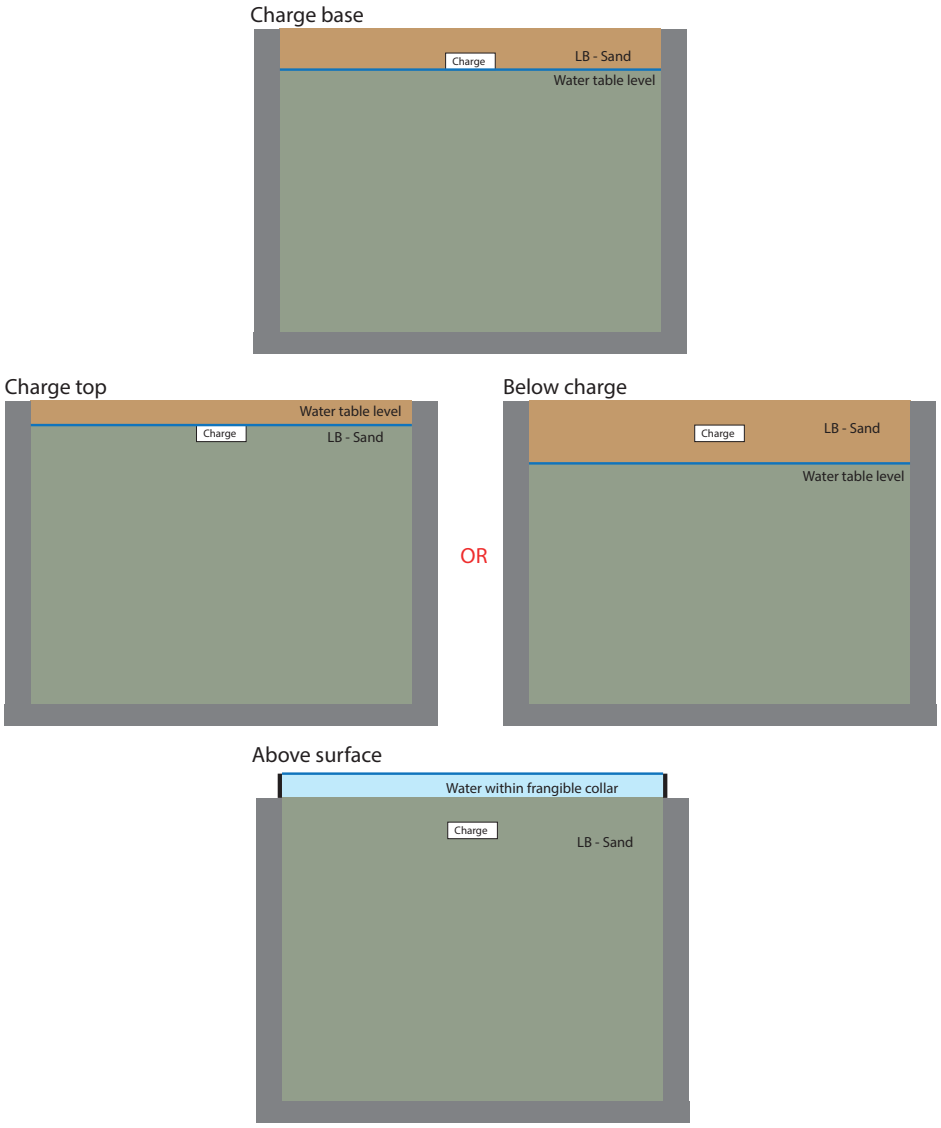

Figure 3.7: Diagrams showing the test arrangements for the littoral tests on LB.

3.2.2 Littoral testing - mineralogy

The particle size distributions (PSD) of Dog's Bay sand (DB) and three fractions of LB are included in Figure 3.8. The PSDs in the plot show that DB sand is composed of smaller particles (D_{50}=0.44 mm) than the LB fraction B sand (D_{50}=0.87 mm) used by Clarke et al. (2017). Results comparing LB fraction B and LB fraction A, which is twice the size of LBB (D_{50}=1.76 mm), showed

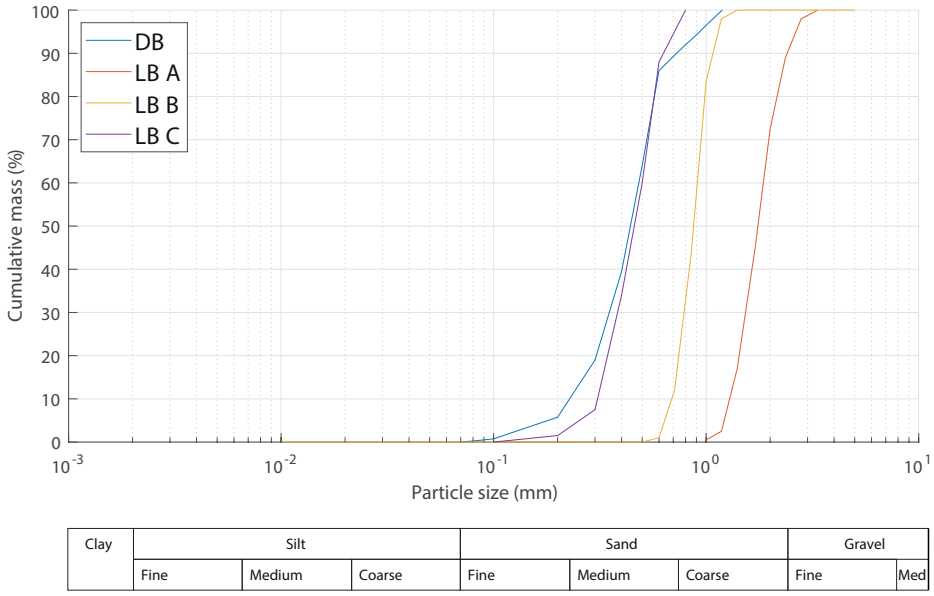

Figure 3.8: PSD for two grades of quartz sand used by Clarke et al. (2017), one grade of quartz sand from Bowman et al. (2001) and Dogs Bay (DB) sand from White (2003).

that there was no systematic difference in the impulse loading between the two materials. This indicates that a variation in D_{50} by a factor of two should not affect the impulse, which can be extrapolated to say LB fraction B and DB should not display any differences due to particle sizes. To allow direct comparison to existing geotechnical literature, testing with DB sand would be ideal. However, the large quantities of sand required for blast testing present difficulties. Therefore, an appropriate, sustainable surrogate will be sought out and used for the testing. This will be selected to be as close to the mineralogy of DB, and as close to the PSD of LBB as possible. Further details of the materials selected can be found in Chapter 8.

Although the PSDs of LBC and DB are similar, the particle shape/morphology is significantly different. Figure 3.9 shows how closely the grains of three different sands match a given shape through use of complex Fourier descriptors (Bowman et al. 2001). A higher shape coefficient corresponds to a grain that more closely resembles the descriptor shape. The plot shows aggregated data for each sand type based on sample sizes of LBC: 91, LBE: 488 and DB: 128. The results show that DB sand is more square, more elongate, more triangular and more asymmetric than the two LB sands[1]. However, the right hand plot shows that,

[1]The statistical nature of the results explains how a single sand type can be both 'more square' and 'more triangular' at the same time. e.g. the values plotted show that over the grains sampled, both the average 'squareness' score, and the average 'triangularity' score are higher for DB than the two other sands.

for a given descriptor DB has a similar distribution of values around the mean, i.e. DB is not inherently any more variable than the other sands. The conclusion to be drawn from the data is that DB sand is consistently different to the two LB sands tested.

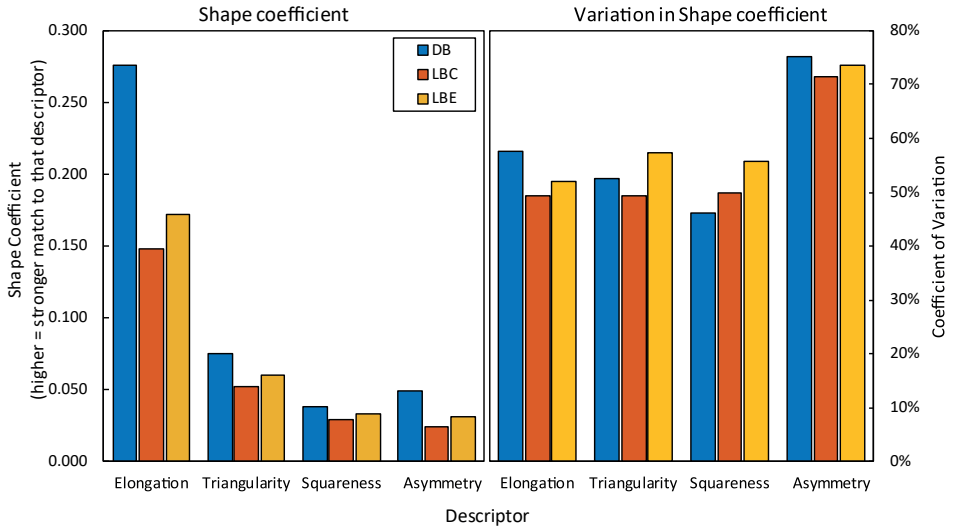

Figure 3.9: Left: Shape coefficients for three different sand types, showing that DB sand is more varied in its grain shape than LBC and LBE. Right: Coefficient of variation for the shape coefficients, showing that DB has a similar distribution around the mean as the other samples (Bowman et al. 2001).

3.2.3 Frozen soils

Figure 3.10, shows schematic representation so the frozen soil scenarios to be tested. These arragnements are designed to investigate conditions where: the charge is frozen in a solid water ice, Figure 3.10a; the charge is frozen in a monolithic structure of frozen soil, Figure 3.10b; the charge is buried where the surface is thawed and the subsoil frozen (e.g. a permafrost environment), Figure 3.10c; and the charge is buried where only the surface soil is frozen (resembling the climate of a winter in the UK, for example), Figure 3.10d.

3.2.3.1 Baseline testing

The first set of tests will be conducted with the charge inside a soil bin filled with a block of water ice (prepared using the most suitable method as determined by the preliminary testing). This will be discussed later in § 6.2.7. These tests will produce data which can be compared against previous work of Clarke et al. (2020) using the CoBL rig with the charge suspended in water . The aim of this is to understand if there is an underlying difference in the loading due to the water being frozen.

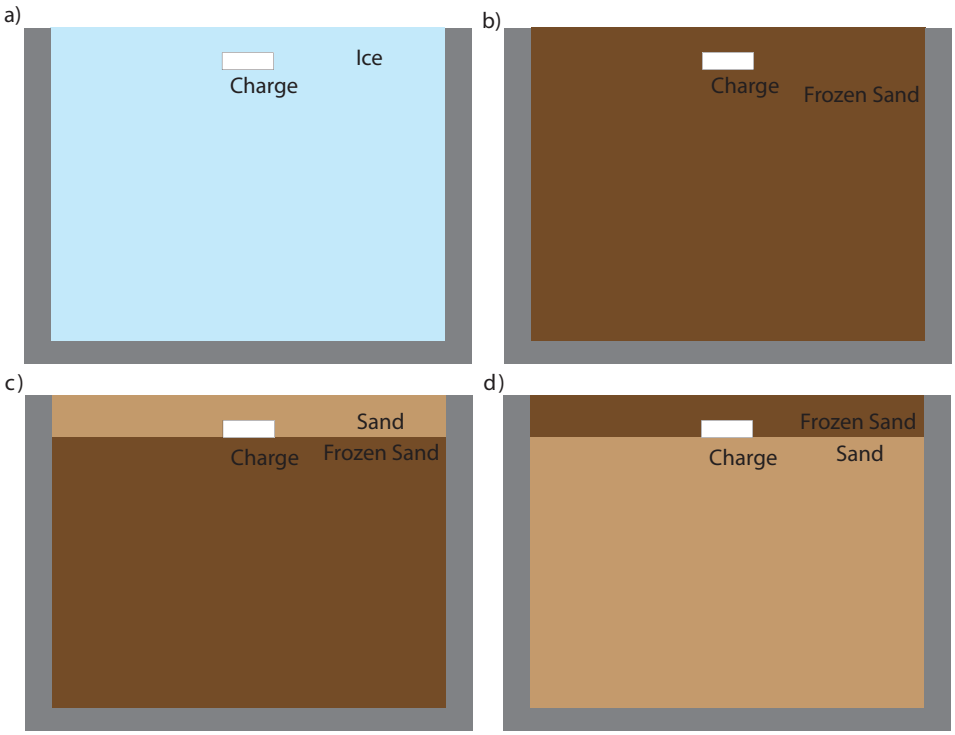

Figure 3.10: Diagrams showing six of the different setups referenced in Table 3.2. a), b) and c) show tests where the water table is varied until it is above the surface of the sand; d) shows the test with the charge in ice; e) shows the charge buried in a fully frozen sample; and f) shows the charge buried in partially frozen soil up to the base of the charge.

There are potentially a number of different factors at play here that may affect either the magnitude, distribution or both elements of the loading:

- Losses due to the energy required to break up the ice (this may be on a comparable scale to the energy losses in atomising the water).
- Channelling/focusing of the loading due to the solid mass surrounding the charge, as observed by Clarke et al. (2020) .
- Changes in the degree of back tamping below the charge between water and ice. This factor is assessed to be unlikely based on the results of Clarke et al. (2020), who found that a charged backed by air (Series A) resulted in a comparable output to charges backed by sand (Series B), as shown in Figure 3.11.

3.2.3.2 Impact of soil geometry

Previous work of Clarke et al. (2020) found that the geometry of the soil around the charge has a large impact on both the magnitude and distribution of the loading. This is highlighted in Figure 3.11, which shows the loading recorded by

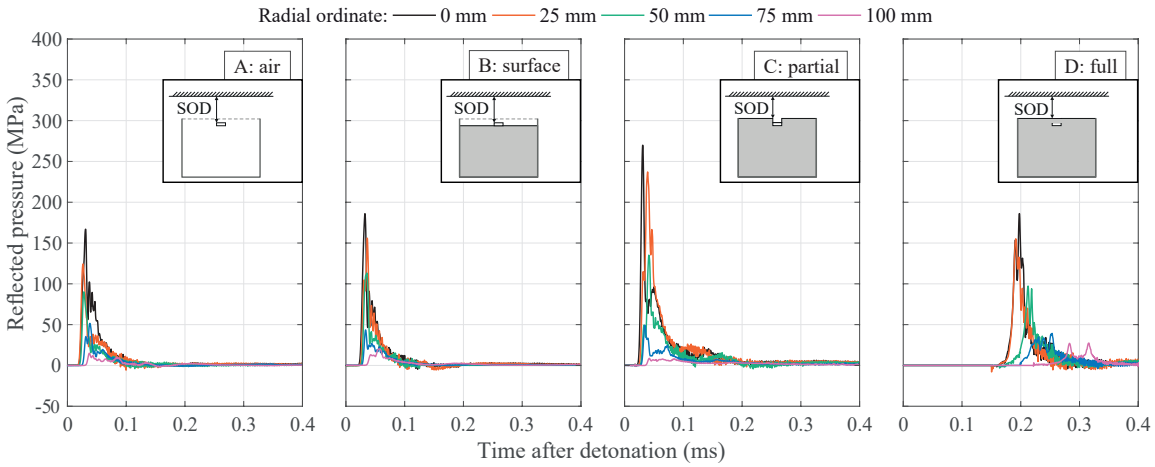

Figure 3.11: Results from Clarke et al. (2020) showing how the arrangement of soil around the charge affects the loading as measured by HPBs at five different lateral distances from the charge. The inlaid diagrams show the arrangement of soil around the charge.

HPBs at five different horizontal distances from the charge centre for four different charge arrangements: free air; surface; partially buried; and fully buried. The results show that the presence of material below the charge (A vs B) has a lower impact on the recorded loading than a partial backfill (C vs D). It is therefore hypothesised that a horizontal discontinuity below the charge will have a lower effect than a vertical ring around the charge. This will need to be taken into account when looking at methods for producing frozen soils. It can also be seen that in the case of partial backfill (C), this has the effect of channelling the blast and increasing the pressure in the central regions of the target.

3.2.3.3 Frozen soil testing - LB

The next series of tests will be with frozen LB as there is already a wealth of CoBL data to compare it to (as discussed above). This will look to assess if the trends identified between ice/water also transfer over to soil. The two different tests on LB look to replicate how a charge may be buried in a threat environment. The first arrangement is representative of a charge that has been dug in and placed in soil before it has frozen (e.g. due to seasonal variations in soil temperature). The second arrangement is that of a charge dug in and placed onto of a layer of existing ice (e.g. buried as deep as possible without breaking ice). The results shown in Figure 3.11 (Clarke et al. 2020), indicate that the soil below the charge being frozen should not lead to a significant change to the measured loading (plots A vs B).

3.2.4 Test matrix

Overall, there are 35 tests planned, of which 30 are CoBL tests. The shot plan is summarised in Table 3.2 and Figure 3.12 with each test described in more detail in the following sections.

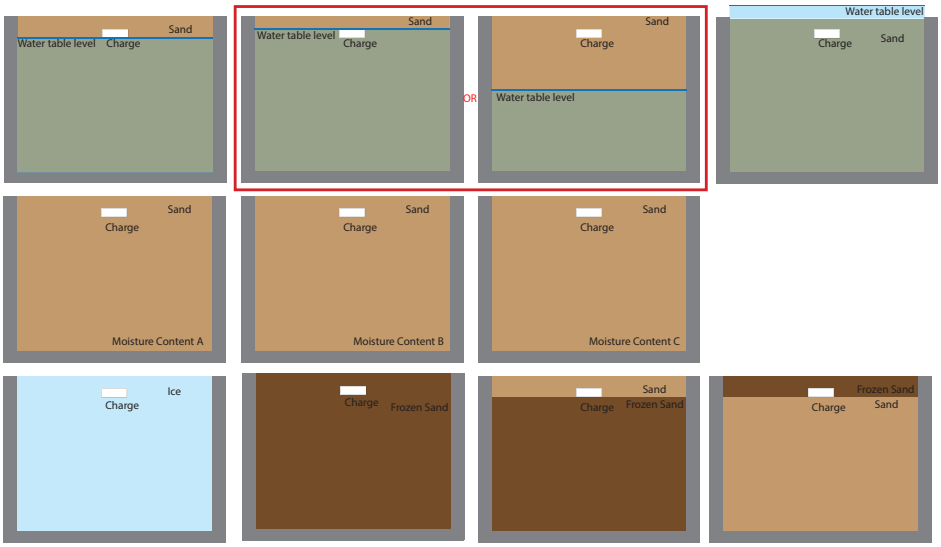

Figure 3.12: Diagrams showing the ten different setups referenced in Table 3.2. The top row show tests where the water table is varied until it is above the surface of the sand; the middle row show tests with carbonate sand at three different moisture contents; and the bottom row shows test in frozen conditions. The red box indicates the two potential options for the water table testing, with the decision which to perform based on the results of the previous test

3.2.5 Test constants

Throughout the testing, the following parameters were maintained as constants. These were selected to align with the bulk of the testing of Clarke et al. (2020) to allow for direct comparisons to be made between the new data and old data. This will enable any newly developed analytical techniques from this work to be applied to the historic dataset, furthering the information available to the wider community.

Table 3.2: Table outlining the shot plan.

Set	Subset	Description	Repeats
Preliminary	Preliminary	Frozen far field reflected pressure	3
		High speed video of ice	2
Littoral	Water table	Water Level A	3
		Water Level B	3
		Water Level C	3
	Carbonate sand	Moisture content A	3
		Moisture content B	3
		Moisture content C	3
Frozen	Ice	Charge in ice	3
	Frozen soil	Fully frozen	3
		Top frozen	3
		Base frozen	3
		Total	**35**

Table 3.3: Table of experimental constants.

Parameter	Value	Units	Notes
Charge mass	78	g	
Burial depth	28	mm	Measured to the top surface of the charge
Stand off distance	140	mm	Measured to the top surface of the soil
Charge material	PE4		
Detonator type	Euronel2 non-electric detonator		
Charge geometry	115 $\times$ 38 mm cylinder		
Charge casing	3 mm thick, 3D printed PLA open topped case		
Soil container	Steel, 375 mm tall, 500 mm ID, 30 mm wall thickness		
HPB locations	17$\times$10 mm bars at 25 mm spacings in 4$\times$radial arrays		
HPB material	EN24T Steel		

Chapter 4

Data Analysis Methodology

This section aims to detail how the data generated from the tests is processed and analysed to produce outputs that can be used to compare different test sereis. For the hopkinson bars, this chapter includes details on: how the raw data traces are processed into pressure, how the pressure is then integrated to give specific impulse; and how the specific impulse is then interpolated across multiple; measurement points to determine the total impulse. For the high speed video this section details: how the videos were used to validate the shape of the interpolated impulse; and how the videos were analysed to track the shock wave and ejecta clouds from the buried charge.

4.1 Hopkinson bars

4.1.1 Zeroing

While every attempt is made to balance the Wheatstone bridge prior to testing, the data recorded for each bar does contain a "zero offset". This is caused when the Wheatstone bridge isnt perfectly balanced during the test, meaning a voltage across the two measurement points is record. Prior to testing, the bridge was balanced by adjusting a variable resistor to bring the signal as close to zero volts as possible. However, changes in the temperature of the gauges (e.g. due to Ohmic heating with them, or due to environmental change changing the temperature of the bars) between configuring the bridge can lead to small changes in the resistances of the strain gauges resulting in a change in the output signal. One approach to correct for temperature effects is ot utilise an extra strain gauge of the same type attached to a section of bar of the same type used for the experiment, but not exposed to the loading. This 'dummy gauge' will have the same level of resistance change due to thermal effects as the loaded ones and, if placed on the opposing side of the Wheatstone bridge, will cancel out, resulting in no change in voltage due to temperature changes. This approach, which technically appealing is expensive to implement as it requires double the number of strain gauges. Therefore it was not financially viable for

this work, and manual zeroing was determined to be appropriate as changes due to temperature are unlikely to occur over the timescales of interest, so any zero offset can be removed in post processing.

To account for this, the first step of data analysis is to remove this from the traces. To do so, the average reading over a period of recording before the signal arrives is used and subtracted from all future values. If the zeroing region is chosen correctly, then the plotted data (discussed below) will start at zero and not "drift" once the loading event has been completed. A poorly zeroed data trace can lead to spuriously high impulse readings, as any small zero offset is compounded during the temporal integration.

For this analysis, a period of 90 data points after the trigger signal is used. The first 10 data points after the trigger signal were discounted to rule out any electrical noise or cross talk on the channels of the digital oscilloscopes. The 100 point range was selected as a suitable zeroing period as it represents a time frame of 32 μs; this corresponds to a travel distance of the detonation wave *inside* an explosive charge of 256 mm[1]. This is a significant overestimate of the distance the signal could travel in the period as the wave speed in sand, air and steel will be significantly lower than the detonation velocity. In the experimental setup, the total distance between the break wire point (at the base of the charge by the detonator) and the gauge points on the Hopkinson bars is more than 300 mm, indicating there is no physical mechanism by which the signal from the explosive could arrive at the gauge station in this time frame and any signal is spurious noise that can be removed. A longer zeroing period could be used, however, analysis showed that there was no benefit in doing so. In contrast, shorter zeroing periods were found to be reliable in the majority of cases, but were susceptible to being skewed by significant noise signals[2].

Therefore, the zeroed voltage can be calculated as follows:

$$V_{\text{zeroed}} = V_{\text{recorded}} - \frac{\sum_{n=10}^{n=100} V_n}{90} \tag{4.1}$$

where:
V_{zeroed} is the zeroed voltage
V_{recorded} is the recorded voltage
V_n is the voltage of the n$^{\text{th}}$ data point after the trigger signal.

[1] Assuming a detonation velocity for PE4 of 8000 ms^{-1}.

[2] For example a typical long wave radio broadcast at 148.05 kHz would correspond to approximately 21 samples so longer zeroing periods are required to avoid such interference.

4.1.2 Voltage to pressure

The zeroed voltages are then converted into pressure readings using a "bar factor". This factor is calculated as follows:

$$B_{\text{Factor}} = \frac{2E}{V_0 GF} \qquad \left[\text{Pa V}^{-1}\right] \tag{4.2}$$

where:
E is the Young's modulus of the steel bars (200 GPa)
V_0 is the voltage powering the gauges (10 V for this work)
GF is the strain gauge factor[3] (120).

4.1.3 Pressure to specific impulse

Once the pressure-time history has been generated for each bar, the specific impulse for each bar can then be calculated by cumulatively integrating the pressure signal with respect to time. This gives a reading for the specific impulse at the bar location as a function of time. Theoretically, the maximum of this is then the specific impulse at the given location. However, due to second order effects, the signals are not perfect and, even after zeroing, do include a degree of "drift" after the event. This is likely due to thermal effects and reflections/oscillations within the experimental apparatus, which while minimised as far as is practical are still present. In addition drift can be caused if any element of the experimental apparatus (such as power supplies or data recorders) are of poor quality or damaged such that they fail to isolate noise form mains voltage, a 60hz sine wave may be detected by the oscilloscope. A 60 Hz sine wave has a period of 16.6 ms so, if present could cause a signal to drift significantly from zero if not removed. Another source of potential electrical noise comes when using generators for powering equipment, where changes to the load on the generator may cause small dips or spikes in voltage. To avoid these types of spurious noise signals, effort was taken to ensure the equipment was of suitable quality and running on battery power where possible. Prior to testing, the readings from the oscilloscope was observed and checked for any noise or drift.

Further to the experimental design, effort was undertaken to avoid including these drift elements in the analysis by calculating the specific impulse is over a fixed duration. Work by Clarke et al. (2020) calculated the total specific impulse by finding the maximum value within a fixed time window (approx. 0.5–0.55 ms after detonation), as shown by the solid red lines in Figure 4.1.

One difficulty with this approach is that it requires the time of detonation to be accurately known/recorded to ensure a consistent approach. However, during

[3]The strain gauge factor is quoted by the gauge manufacturer. It is the fractional change in resistance divided by the fractional change in length (strain) for the gauges used in the CoBL apparatus.

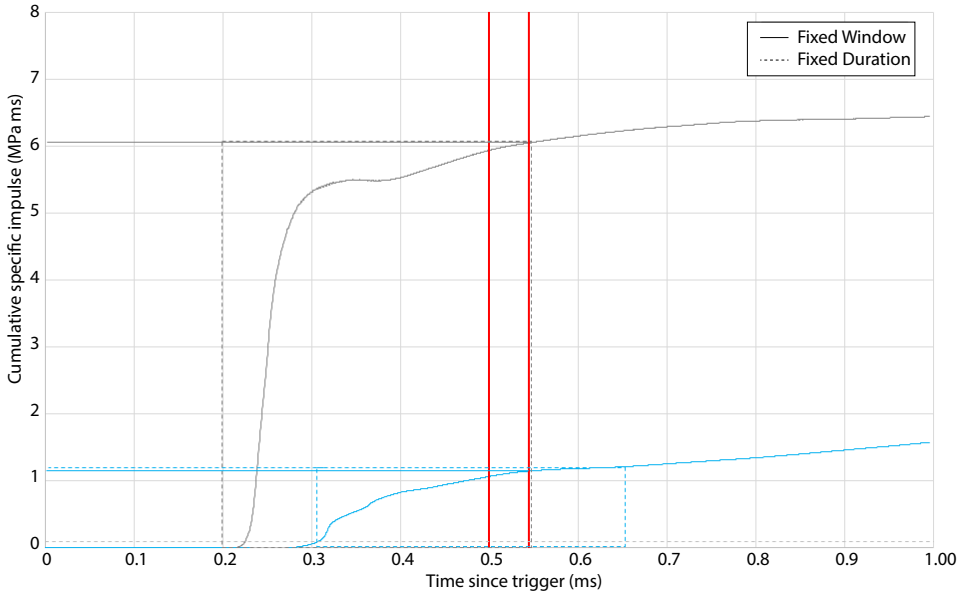

Figure 4.1: Plot showing the window in which Clarke et al. (2020) calculated the total specific impulse overlaid on test data from their work (solid red lines) compared to the window used in this work (dashed blue lines). As can be seen, the calculated values are very similar for the data presented.

the analysis of work for this project, it was found that the break wire can, on some occasions break 'slowly', leading to an apparent reduction in the arrival time of the shockwave. It is theorised that these rare events could be caused by the break wire elongating before breaking the circuit, or being contained within a conductive gas/plasma cloud. Without knowing the exact cause of these delays, it is difficult to use a system that relies on the detonation time. Therefore, for this work, an approach has been developed where the specific impulse has instead been calculated over a period of fixed duration from the arrival of the signal at the given bar. To reduce the risk of noise leading to a prematurely determined arrival time, the arrival time at a given bar was calculated as the time which cumulative specific impulse first reaches 0.1 MPa.ms ($T_{0.1\ \mathrm{MPa.ms}}$). The bar specific impulse was then found as the maximum within 0.35 ms after this point. To further avoid any spurious noise contributing to the cumulative specific impulse, the calculated values before $T_{0.1\ \mathrm{MPa.ms}}$ have been omitted from future analysis and the cumulative specific impulse starts at 0.1 MPa.ms.

During the analysis of the data from the second round of testing, it was discovered that this approach was no longer suitable due to the frozen soils producing much more variable data traces (e.g. the raw voltage time data trace which is then converted into the pressure time data) and increased noised within the experimental apparatus. The reason for the increase in noise has not been established, but does not appear to be a systemic instrumentation issue, as much cleaner signals were obtained in recent work using identical settings with free

air charges. Instead, a manual approach was used where the author of this work set the end of the period over which to calculate the specific impulse by interpreting the pressure time trace. The following general rules were applied:

- Expected loading duration of approx. 0.35 ms – integration should end around here in absence of any other factors (e.g. Figure 4.2).
- If a large post-shock zero drift/offset is detected, integrate the signal up to the point where it drops to the new baseline (e.g. Figure 4.3).
- If multiple clear loading events are seen, include these in the integration (e.g. Figure 4.4).
- If a spurious signal is detected outside of the expected loading duration, exclude it from the analysis (e.g. Figure 4.5)
- If the signal is indecipherable from noise or shows an instrument failure, discount it from the analysis (e.g. Figure 4.6).
- If no other rules apply, and the signal is still changing after the 0.35 ms period, integrate the signal upto the point where it falls back to zero after the 0.35 ms window (e.g. Figure 4.7).

This approach required the user to take a consistent approach and is based on experience of what the pressure time history is expected to look like. Example pressure time histories are included and discussed below to highlight some of the issues/decisions that are required for the analysis. Note, these pressure time were selected to best highlight the points discussed in this section and are not intended to be representative of the typical variability of the experimental results (e.g. these are shown as examples of where additional consideration to their analysis is required). Sensitivity analysis was conducted where the rules were applied in a stricter and more lenient fashion and it was found that this did not impact on any of the trends/conclusions as the relative difference between data series was unchanged. For example, applying stricter interpretation of the rules above resulted in an approximately 25% reduction in the total impulse over the 100 mm area across all shots and data series.

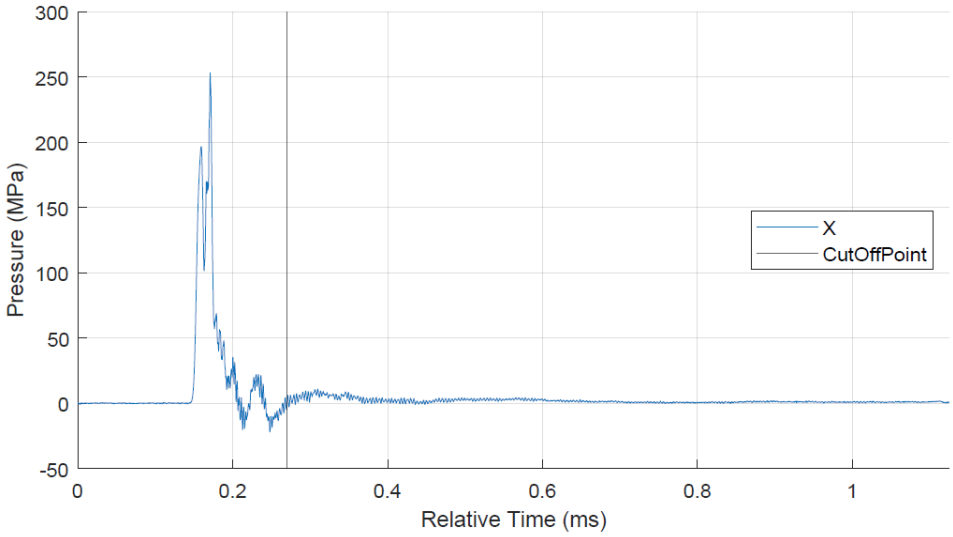

Figure 4.2: An example of a trace where the cut off point is easy to determine, as the signal returns to zero with little subsequent noise.

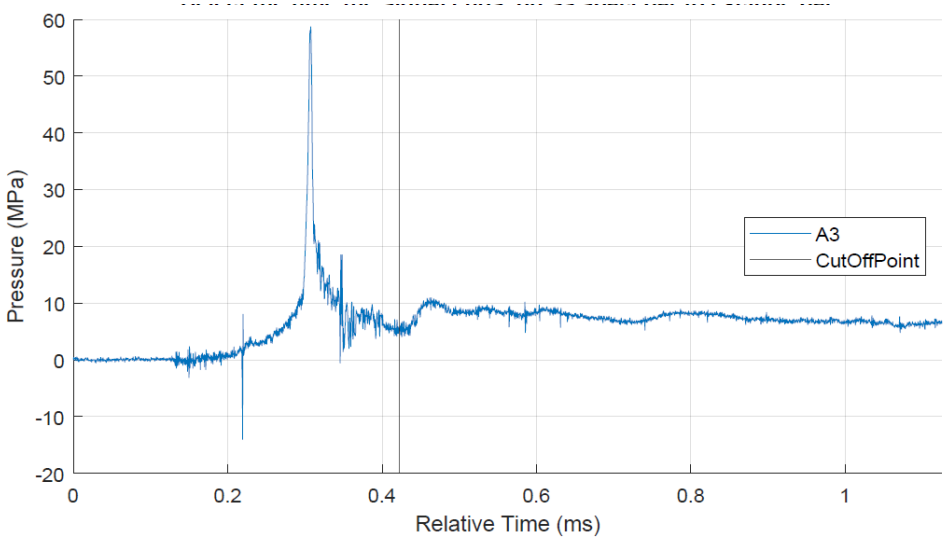

Figure 4.3: Example trace showing a zero drift is present. Here the integration has been taken by interpreting where the end of the first spike would occur (assuming a similar shape to other traces) in the absence of the zero drift.

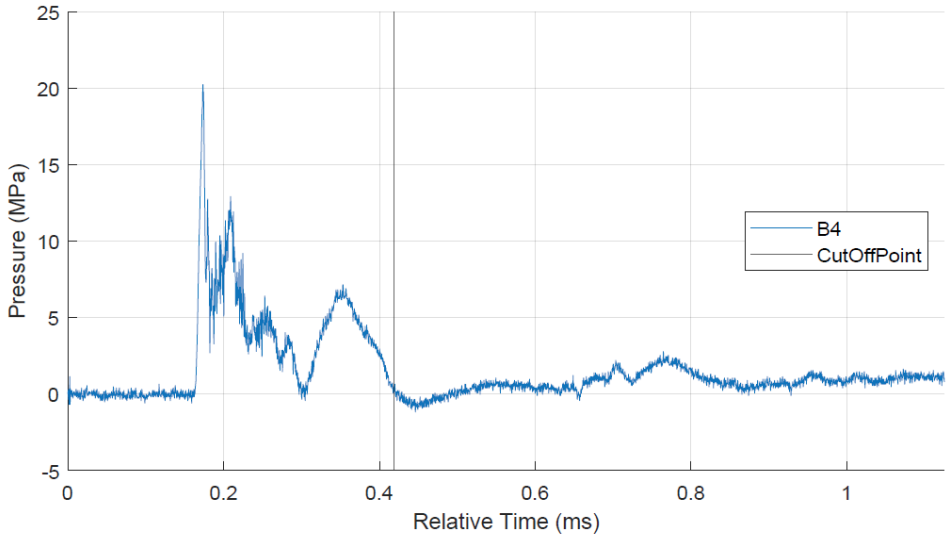

Figure 4.4: This plot shows a trace with a clear second peak. This is likely caused by ejecta impacting the target plate separately to the pressure wave. The trace also shows the late time drift on the signal, which while low, impacts on the specific impulse as it is present over a long duration.

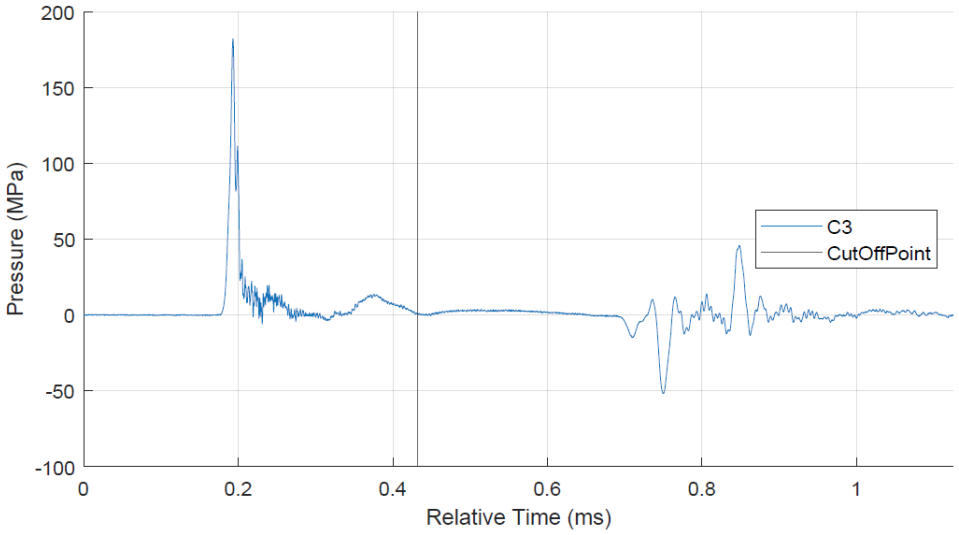

Figure 4.5: The features on the trace between 0.75 ms and 0.85 ms are spurious and not caused by a loading. They are potentially caused by the bar striking one of the guides as it moves up. These signals are 'real' stress waves travelling in the given bar and can be seen reflecting off the free surfaces with the correct timing when plotting over a longer timebase. However, there are no known mechanisms that could cause a negative pressure 0.5 ms after the initial pulse in the given experimental setup.

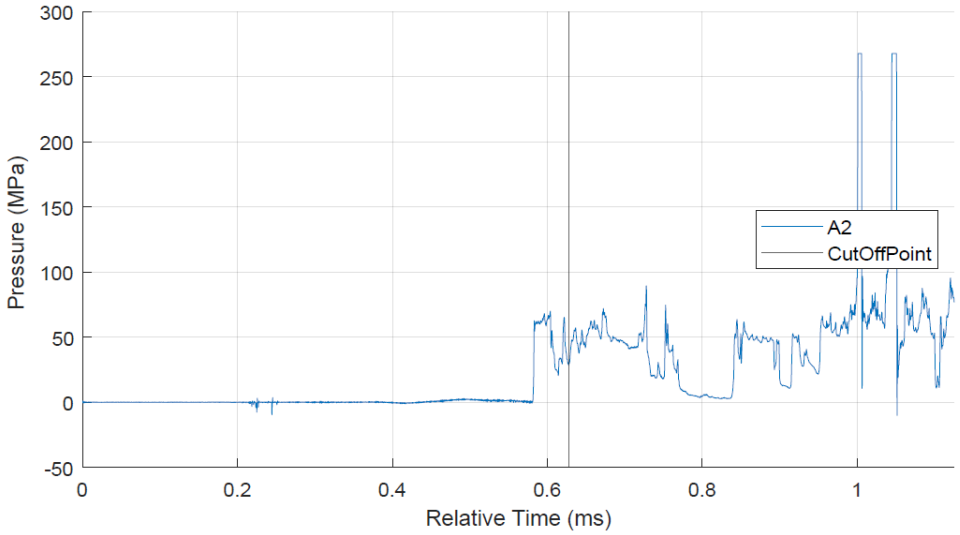

Figure 4.6: An example where the pressure signal is indiscernible from the noise and does not have the expected shape. This data would be excluded from subsequent analysis.

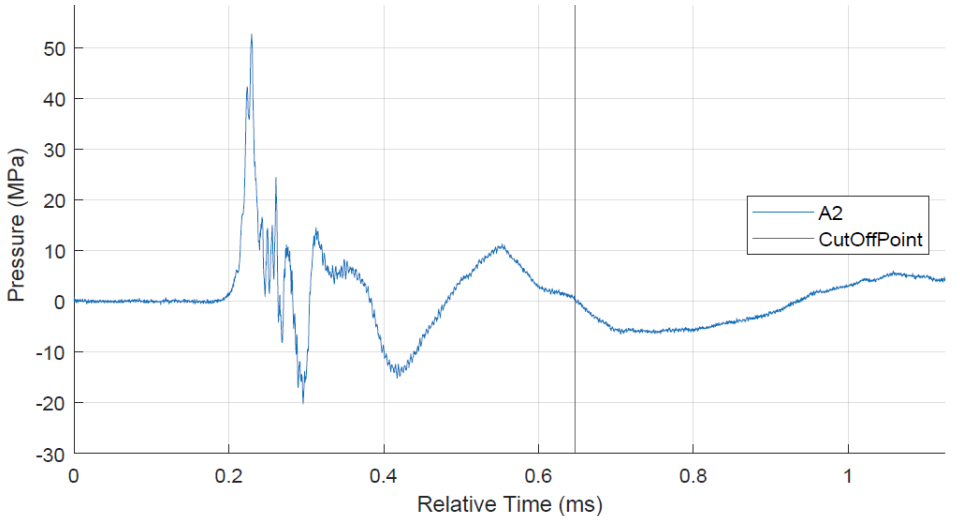

Figure 4.7: This plot shows a pressure trace that is harder to interpret, as there is not a clear end. This is often the case for bars further from the centre of the loading as the magnitude is lower, so any noise of second order effects are more noticeable.

4.1.4 Data smoothing

To aid in visual comparison of the data from different shots, the pressure data was filtered using an Savitzky-Golay filter, which applies a quadratic fit over a rolling five point data window and is typically applied when the underlying data has rapid changes. Figure 4.8a shows the pressure and specific impulse for a given shot before the filtering is applied, and Figure 4.8b shows the results of applying the filter to the data before the rest of the analysis. The total calculated specific impulse for each trace in the filtered analysis is within 1% of the corresponding value for the unfiltered data, with an average difference of 0.25%, indicating that the filter does not fundamentally change the results. All subsequent analysis was therefore performed on the filtered dataset. Comparing Figures 4.8a and 4.8b, it can be seen that the peak pressure is reduced when the filter is applied, however, Figures 4.9a and 4.9b show that the cumulative specific impulse is not.

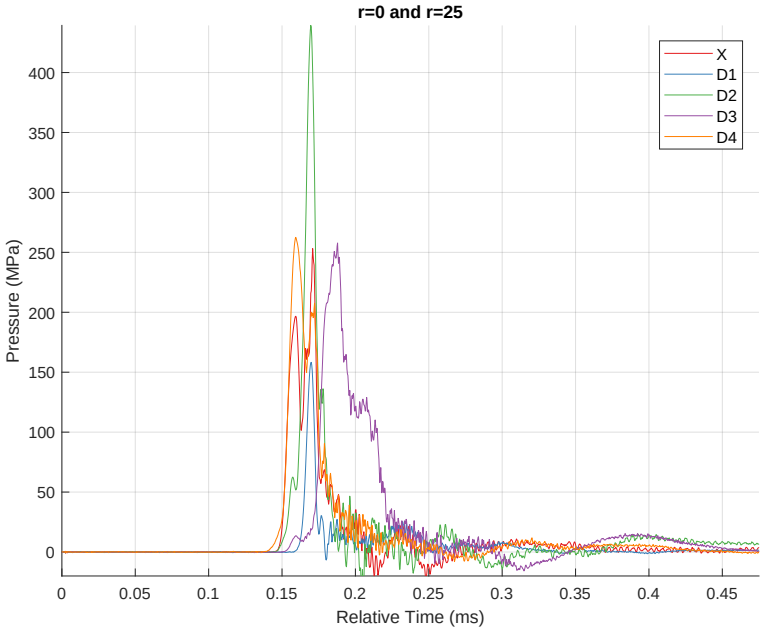

(a) Unfiltered

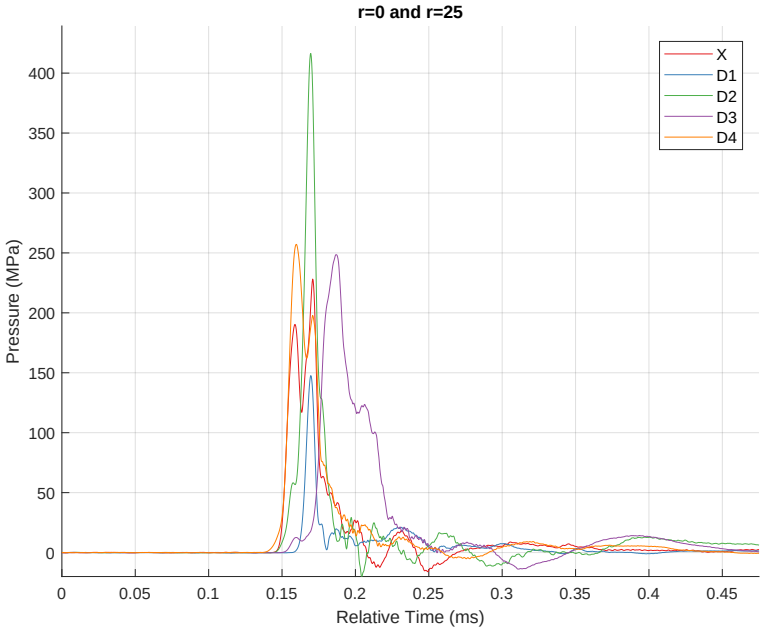

(b) Filtered

Figure 4.8: Shot 025 filtered and unfiltered pressure traces for the r=0 mm and r=25 mm bars, showing how applying a filter allows the shape of the pressure pulse for each bar to be more easily discerned.

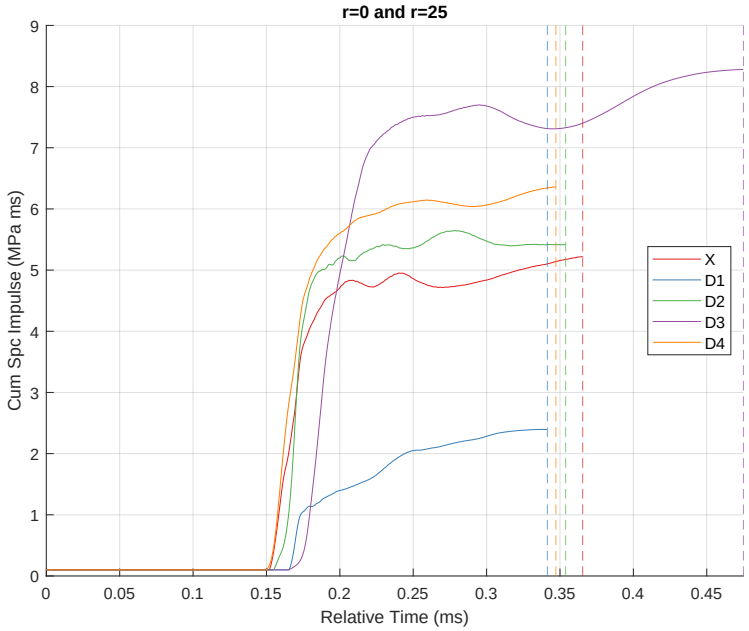

(a) Unfiltered

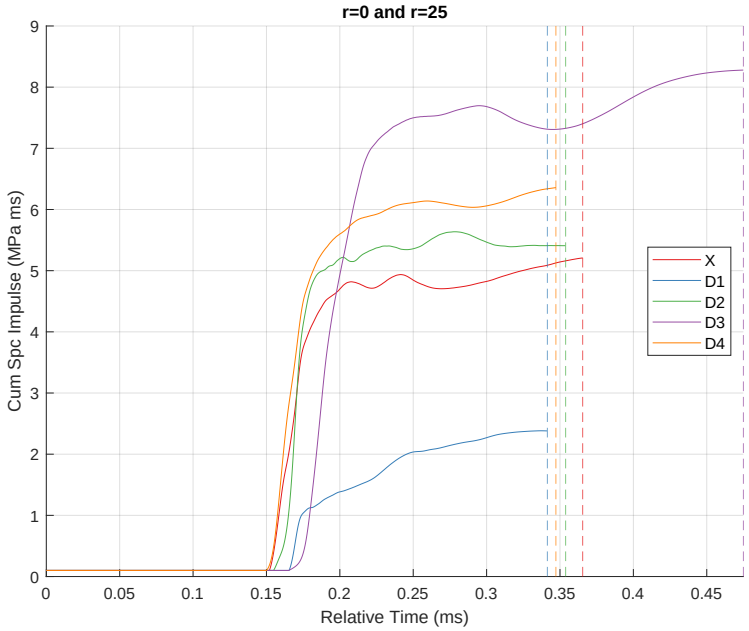

(b) Filtered

Figure 4.9: Shot 025 filtered and unfiltered pressure traces for the r=0 mm and r=25 mm bars, showing how applying a filter allows the shape of the pressure pulse for each bar to be more easily discerned.

4.1.5 Total impulse

The total impulse as a function of distance can be calculated in two ways:

4.1.5.1 Linear interpolation

This method uses as an area-weighted integration of the specific impulse distribution. The circular target area is split into 1000 concentric annuli, and the area of each annulus is calculated along with the radius of the areal bisector of the annulus[4]. The specific impulse at this radius is then calculated by linear interpolation and multiplied by the area of the annulus to give the impulse in the given area. By summing the impulse for all annuli, the total impulse measured within the 100 mm radius target plate is determined. This approach is a fast running approach that does not take into account the different measurement axes, and is only a suitable approach when there are multiple measurements at the same radial distance.

4.1.5.2 2D interpolation

This method, proposed by Clarke et al. 2015a, was developed to be applicable to any arrangement of HPBs. It is best described by first considering a 1D interpolation of the data along a single array of measurement points (radial interpolation) and then performing a second 1D interpolation along the angular co-ordinate (angular interpolation). In polar co-ordinates, this is simply an interpolation in R and then θ.

Radial interpolation: Figure 4.10a shows a contour plot of the pressure record along a single radial axis. The plot shows how the loading radiates outwards, with the signal arriving at more distant points later. The discontinuous nature of the data does not enable a 2D (space and time) interpolation to be conducted. Therefore, the first step in the radial interpolation is to time shift the signals based on the arrival time of the peak pressure and aligning it to the central bar (which is common to all radial arrays). This creates a one dimensional dataset that can be interpolated to generate a continuum of data across the full radial scale. The results of this are shown in Figure 4.10b. Figure 4.10c shows the measured arrival times, and a cubic fit to the data. This fitted function is then used to re-shift the 1D interpolated pressure array to generate a continuous data set of pressure data as a function of distance and time. The results of the radial interpolation are shown in Figure 4.10d.

[4]The circle which splits the annulus into two annuli of equal area.

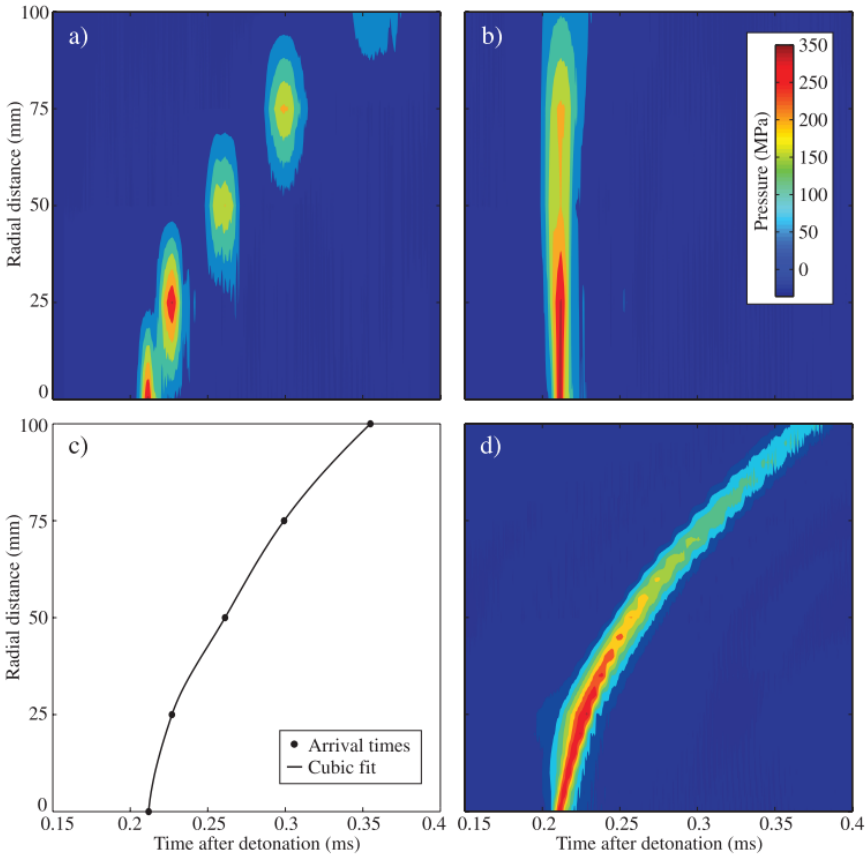

Figure 4.10: Plots showing the four stages of the radial interpolation for a given angle: a) the raw data; b) the time shifted data; c) the position time data and fit; and d) the final interpolated data after applying the time shift (Clarke et al. (2015a)).

Angular interpolation: A similar interpolation is then conducted along the angular dimension, angularly interpolating between the radially interpolated pressure signals (i.e. the pressures in Figure 4.10d) corresponding to the two closest experimental measurement arrays.

Combined 2D interpolation: By subdividing the instrumented area into discrete cells and running the two interpolations above, the pressure distribution across the whole surface can be inferred and plotted for each time step, as shown in Figure 4.11. This shows how the peak pressure radiates outwards, which is expected when examining the raw pressure traces. It can also be seen in the t=0.22 ms and t=0.23 ms that the 2D interpolation method retains non-uniformities in the loading that are lost in the simple linear interpolation. However, this means any tests that are not centrally aligned may result in a lower total impulse using the 2D interpolation technique when compared to the linear interpolation.

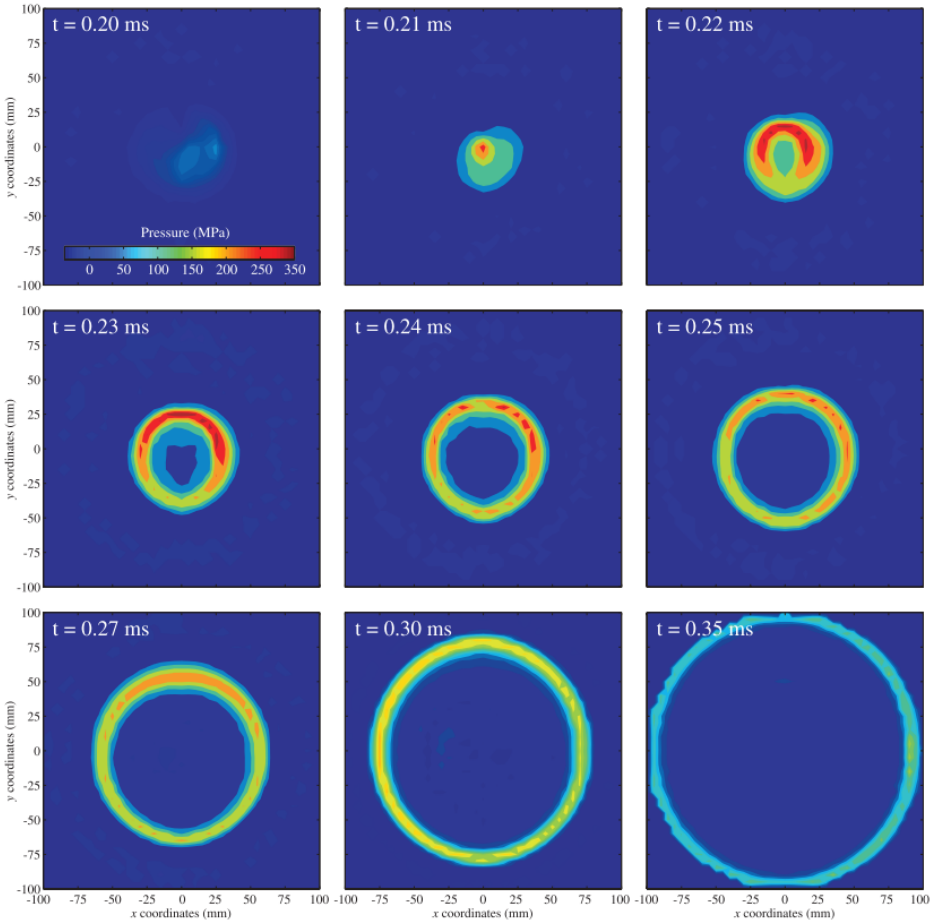

Figure 4.11: Plots showing the 2D interpolated pressure for nine different time steps (Clarke et al. (2015a)).

4.1.5.3 Approach taken

For this work, the 2D interpolation will be used as this accounts for variation in the loading in different measurement axis to be represented in the data. The interpolation routine was coded into a MATLAB script that allowed the user to set the cut off points for the integration for each data channel in a given test (as per § 4.1.3) before conducting the 2D interpolation.

4.2 High speed video

4.2.1 Comparison to 2D interpolation

To validate the results of the 2D interpolation, the results can be compared to the high speed imaging of the same tests. Figure 4.12 shows examples of this, comparing the high speed video frames (centre) to the interpolated pressure in the X-Z plane (top) and the X-Y plane (bottom). The video frames are aligned and scaled to the interpolated pressure plots so features can be compared. In the example in Figure 4.12, it can be seen from the video that the ejecta struck the target plate off centre, a result that is also present in the interpolated pressure data.

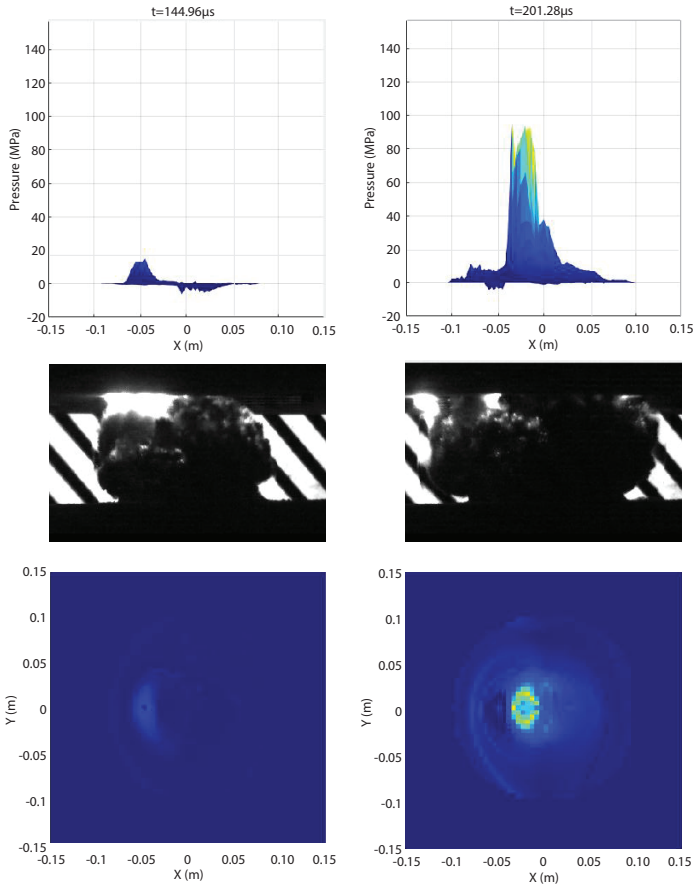

Figure 4.12: Screenshot from dynamically generated 2D interpolated pressure, aligned with the high speed video of the tests for two different times during a test.

4.2.2 Shock wave and ejecta tracking

The high speed videos were analysed in MATLAB using an edge detection method modified from Farrimond et al. (2022), which itself was modified from Rigby et al. (2020). Previously, Rigby et al. and Farrimond et al. (2022) used this technique to detect the shockwave from an explosive charge detonated in a free field environment against a high contrast background For this work, the method was modified to track both the shockwave from a buried charge and the shape of the ejecta cloud produced. This required significant modification to the procedure to work in a different environment much closer to the charge The method applied uses frame subtraction to identify changes at a pixel level. The modified process, as applied to this work is illustrated in Figure 4.13, is as follows:

- Perform image subtraction on a frame by frame basis, to identify changes between sequential frames.
- Divide the frame into 5°radial segments (Figure 4.13a).
- For each segment in each frame:
  - Identify the largest radial distance at which a change is detected, and record this as the position of the shock front[5] (purple points in Figure 4.13b).
  - Identify the smallest radial distance at which a change is detected, and record this as the position of the ejecta cloud[6] (yellow points in Figure 4.13b).
- For each frame:
  - Apply a negative quadratic fit to the shock wave data[7] (purple fit in Figure 4.13c).
  - Apply a Savitzky-Golay filter to the ejecta data[8] (yellow fit in Figure 4.13c).
- Plot the fitted shock wave and filtered ejecta data for each frame (Figure 4.14).

[5] This is based on the observations that the shockwave is outside of the ejecta cloud and is the fastest moving element.

[6] This utilises the fact the images were backlit, so the ejecta cloud forms an opaque shadow. Therefore, the outer edge of the shadow can be used to determine the extent of the ejecta cloud.

[7] A quadratic fit is used to approximate the shape of the shockwave which is known to be smooth at this scale

[8] As discussed above, a Savitzky-Golay filter applies a quadratic fit over a rolling five point data window, and is typically applied when the underlying data has rapid changes, as was observed with the ejecta cloud. Applying this smoothing filter allowed for easier interpretation of the data

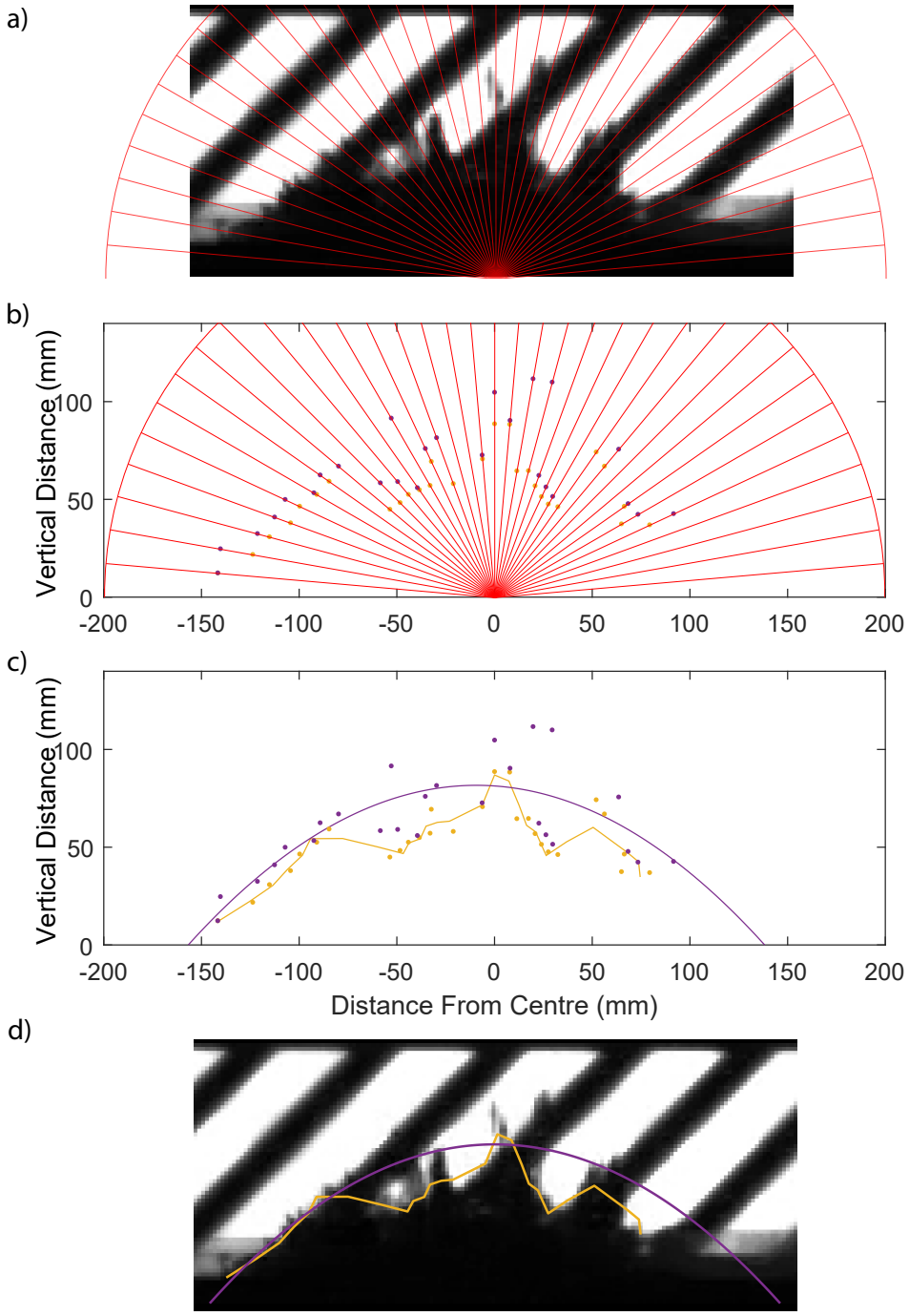

Figure 4.13: Images illustrating the process by which the shock wave and ejecta cloud are tracked in the high speed video.

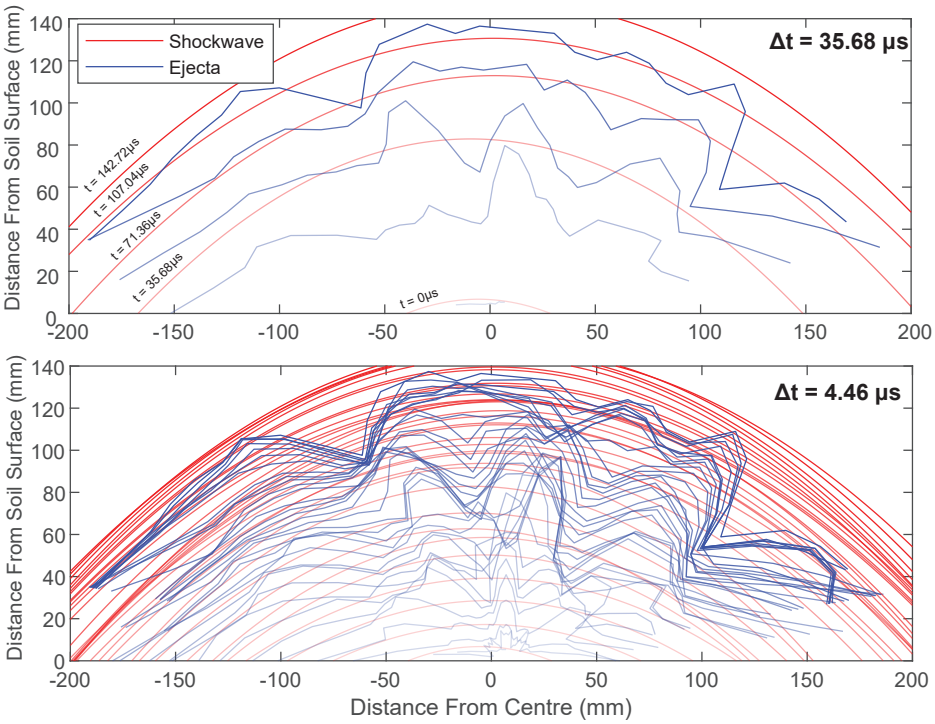

Figure 4.14: Plots showing the tracked shock wave (red) and ejecta (blue) for a given test. The top chart shows a subset of the data with a plot every eight frames and the bottom the data for every frame.

Chapter 5

Summary Results

This section details the tests that were conducted, and the format of the results that have been generated for each of the different test environments.

Table 5.1 summarises the shots completed using the CoBL apparatus for this work, how they are split into series, and provides details of the experimental conditions for each shot. Table 5.2 summarises the shots from historic data that have been re-analysed for comparison to those conducted in this work, how they are split into series and provides details of the experimental conditions for each shot.

Table 5.1: Table outlining the shots conducted.

Shot name	Series name	Soil type	Bulk density† [Mg/m^3]	Moisture content‡	Burial conditions
Shot001 Shot002	Preliminary testing/commissioning - no data to report				
Shot003 Shot004 Shot005	Charge base	LB	1.662 1.634 1.574	2.50% 2.50% 2.68%	Soil saturated to the base of the charge
Shot006 Shot007 Shot008	35 mm above	LB	1.609 1.565 1.561	2.62% 2.51% 2.50%	Fully saturated with 35 mm of water on the surface of the soil
Shot009 Shot010 Shot011 Shot012	Charge top	LB	1.566 1.558 1.558 1.576	2.55% 2.56% 2.59% 2.49%	Soil saturated to the top of the charge
Shot013 Shot015 Shot016	Carb 2.5%	Carbonate	1.290 1.247 1.240	2.15% 2.39% 2.40%	Carbonate sand at 2.5% moisture content
Shot014 Shot017 Shot018	Carb 5%	Carbonate	1.281 1.252 1.263	4.95% 4.80% 4.80%	Carbonate sand at 5% moisture content
Shot019 Shot020 Shot021	Carb 7.5%	Carbonate	1.335 1.285 1.295	7.50% 7.49% 7.48%	Carbonate sand at 7.5% moisture content
Shot022	Frozen top and bottom unconfined	LB	1.600	2.50%	LB sand frozen above and below charge (no radial confinement during the test)
Shot023 Shot024 Shot028	Frozen top and bottom	LB	1.604 1.620 1.592	5.00% 5.00% 5.00%	LB sand frozen above and below charge
Shot025 Shot026 Shot027 Shot037 Shot038	Ice	Ice	1.000	N/A	Water ice
Shot029 Shot030 Shot031	Frozen bottom	LB	1.660 1.629 1.616	5.00% 5.00% 5.00%	LB sand frozen below charge
Shot032 Shot033 Shot034	Frozen top	LB	1.645 1.593 1.589	5.00% 5.00% 5.00%	LB sand frozen above charge

†Bulk density is taken prior to freezing where applicable

‡Moisture content is the geotechnical moisture content, that is the mass of water divided by the mass of solids and is taken prior to freezing or saturation where applicable

Table 5.2: Table outlining the historic test data from Clarke et al. (2020) that has been re-analysed and compared to the new data.

Shot name	Series name	Soil type	Bulk density [Mg/m^3]	Moisture content‡	Burial conditions
Hist041 Hist042 Hist043 Hist044 Hist045	LB saturated	LB	1.99	Saturated	Fully buried
Hist046 Hist047 Hist049	LB 5%	LB	1.67	4.76%	Fully buried
Hist051 Hist052 Hist053 Hist054 Hist055 Hist097 Hist098	STANAG saturated	STANAG	2.1	Saturated	Fully buried
Hist087 Hist089 Hist090 Hist096	LB 2.5%	LB	1.635	2.45%	Fully buried
Hist094 Hist095	LB side tamped	LB	1.635	2.45%	No overburden, soil flush with top surface of the charge
Hist101 Hist102	Water	Water	1.000	N/A	Fully buried

‡Moisture content is the geotechnical moisture content, that is the mass of water divided by the mass of solids

5.1 Structure of results

For each shot, the process outlined in Chapter 4 is applied. The following section presents an example of the results generated at each stage of the analysis, with the full set included in Appendix A and figures for each series included in the results and discussion section below. The labelling convention used for the different data channels is as discussed in § 3.1.1, iincluded again below for clarity in Figure 5.1. With each radial distance assigned a letter designation, and each radial direction a numerical one[1].

[1]e.g. all the "A" bars are at the same radial distance (100 mm) and all the "1" bars form a radial line.

5.1.1 Pressure and specific impulse data

Figure 5.2 shows a typical pressure trace recorded from the Hopkinson bars during this work, this data is from Shot014, a test in carbonate sand at 5% moisture content. The five signals correspond to the data from one of the radial lines and the central bar. The varying arrival times for the signals demonstrates how the loading reaches the central region first and then spreads out over the target plate. As is to be expected, the delay between the central bar and the 25 mm bar is small as the charge extends radially to the 25 mm bars (as shown in Figure 3.1). The shape of the pressure pulse approximately resembles that of an explosive air shock, with a rapid rise to peak pressure and rapid decay, which is in agreement with previous work on dry sand by Taylor et al. (2008) and Clarke et al. (2020). As the radius of the measurement point increases, the shape of the pressure trace has less resemblance to an an air shock with the loading over a longer duration.

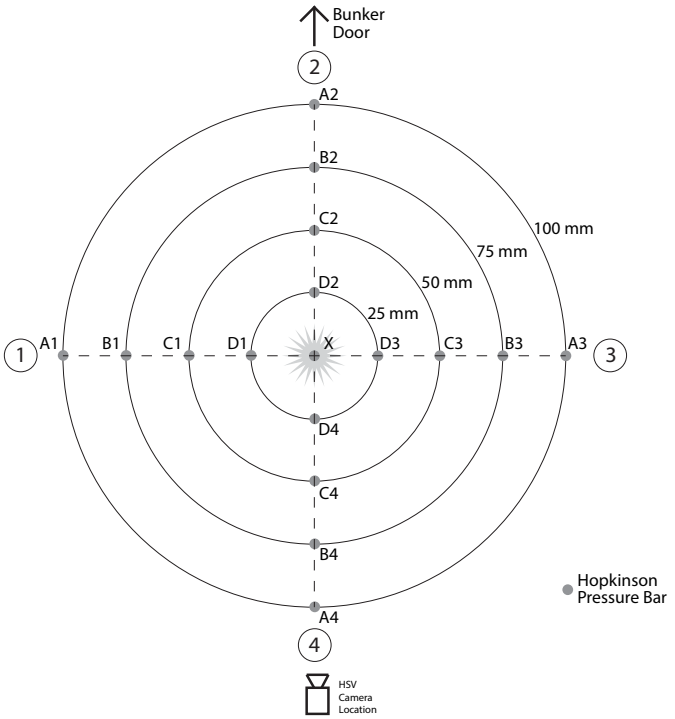

Figure 5.1: Diagram showing the naming convention used for the CoBL apparatus in this work.

Figure 5.3 show a comparison between the central reading and the output from Blast.m (Rigby and Tyas (2014)) for spherical free air charges at the same stand off distance[2]

[2]This is used for comparison of the shape of the pressure trace, not tool to predict the loading.

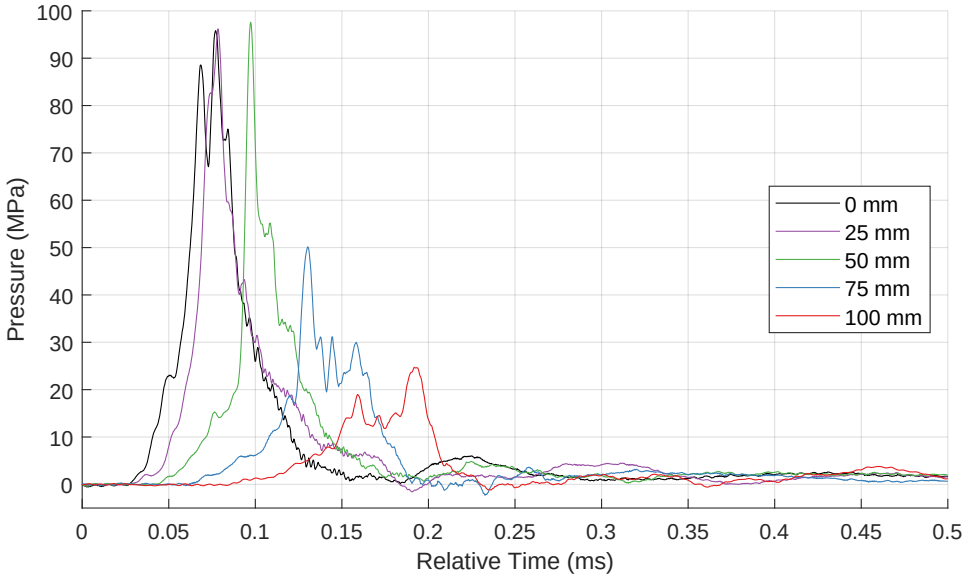

Figure 5.2: Pressure time history for five bars in a single test (other traces excluded for clarity).

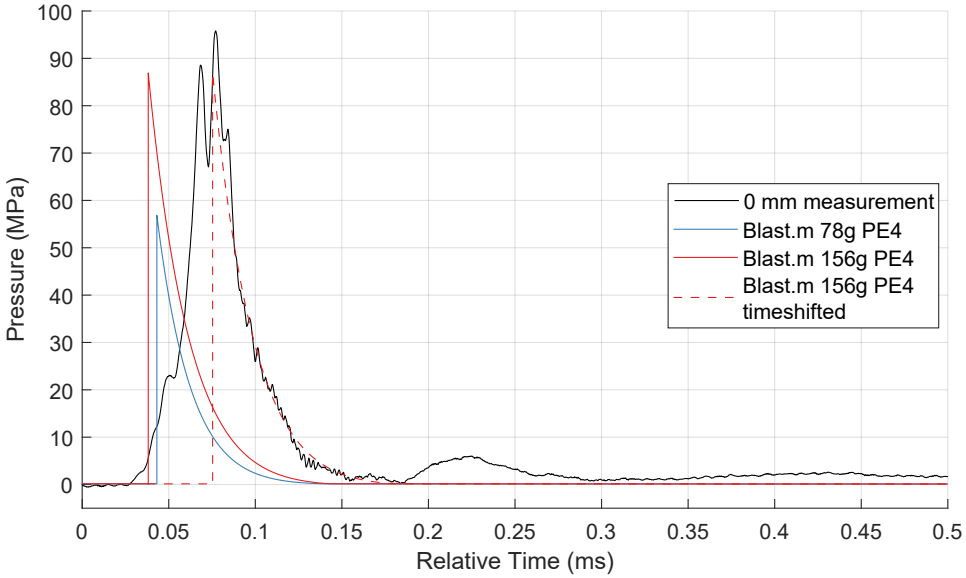

Figure 5.3: Pressure time history for the central bar compared to the output of the empirical free air blast pressure predictor, Blast.m (Rigby and Tyas (2014)).

Three comparisons have been included which show the following:

- **78g PE4** — Showing how the pressure measured from the buried charge is significantly higher than for an equal sized free air spherical charge. This is inline with findings of Westine et al. (1985) and Ehrgott et al. (2011).
- **156g PE4** — Showing that the magnitude of the pressure is comparable to a bare chargee of approximately double the mass, with the loading beginning at a similar time.
- **Timeshifted 156g PE4** — Showing that the decay from peak pressure is of a similar form to that of an air shock, but the onset of pressure is over a larger time period.

For each test, charts have been produced as shown in Figure 5.4 with the full details in §A.1. The left hand column shows the pressure time history for each bar in the given test. The right hand column shows the cumulative specific impulse for each bar, in each radial distance. The vertical dashed lines on the cumulative specific impulse show the time at which the signal was truncated, as per the description in §4.1.3 and the corresponding Y value is the specific impulse value for the given measurement point. The horizontal dashed line shows the average specific impulse for the central (r=0) bar and the horizontal dashed line shows the average specific impulse for all the measurements at the same radial distance

Once the specific impulse for each bar is calculated, the average specific impulse for each bar at a given radius is calculated and plotted to show how this changes as the radius increases, as shown in Figure 5.5. The shaded area represents the standard error on the mean, defined as $\frac{\sigma}{\sqrt{n}}$ where σ is the standard deviation and n is the number of samples. By averaging the specific impulse values at the same radius in nominally identical tests, a more statistically robust average can be found[3].

[3] i.e. in a single test, there are four data points for each radius (only one for r=0 mm) but by combining three nominally identical tests this is increased to 12 data points.

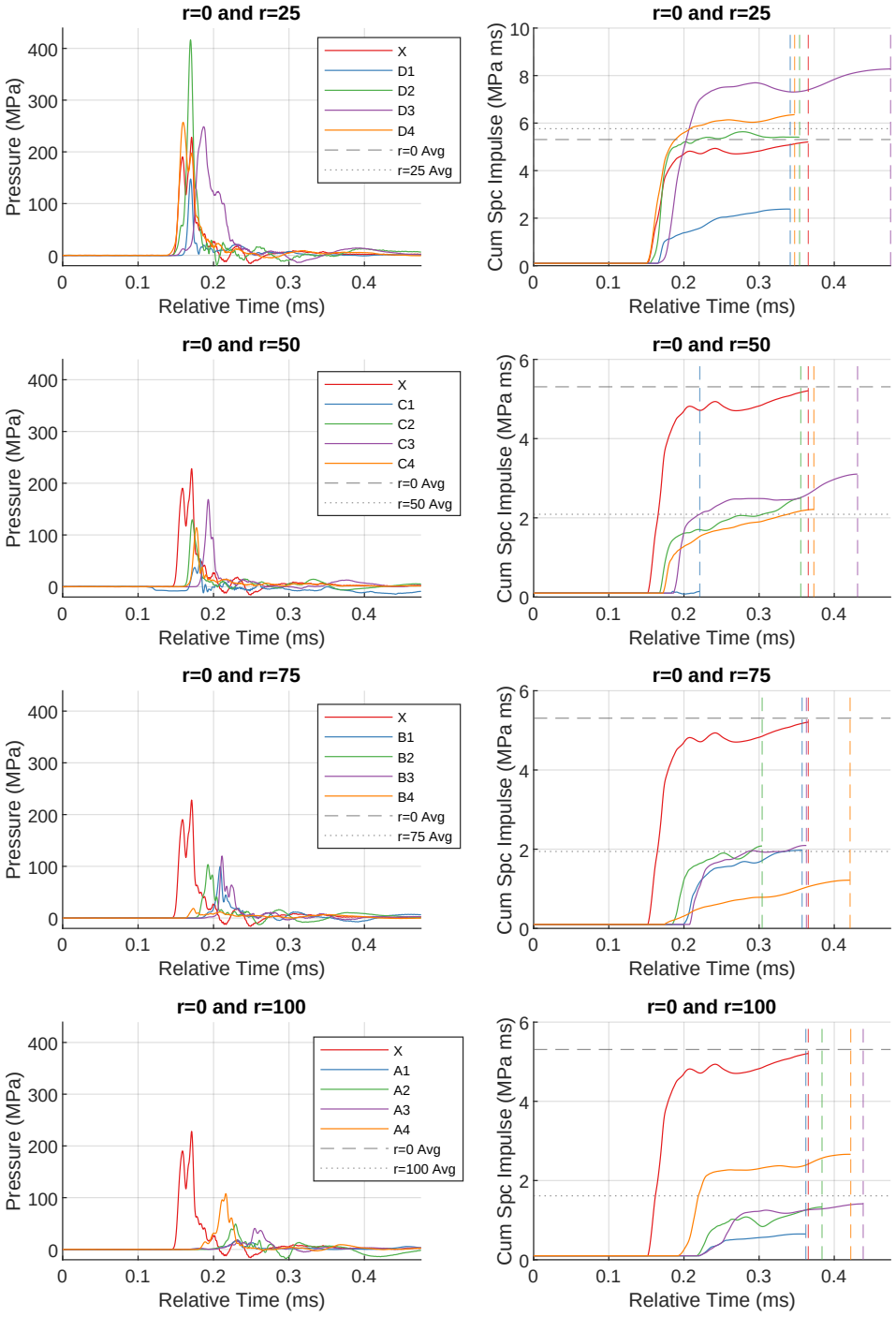

Figure 5.4: Shot 025 pressure (left) and cumulative specific impulse (right) plots for each radial distance. The dashed lines on the cumulative specific impulse plots indicate the time at which the traces have been truncated.

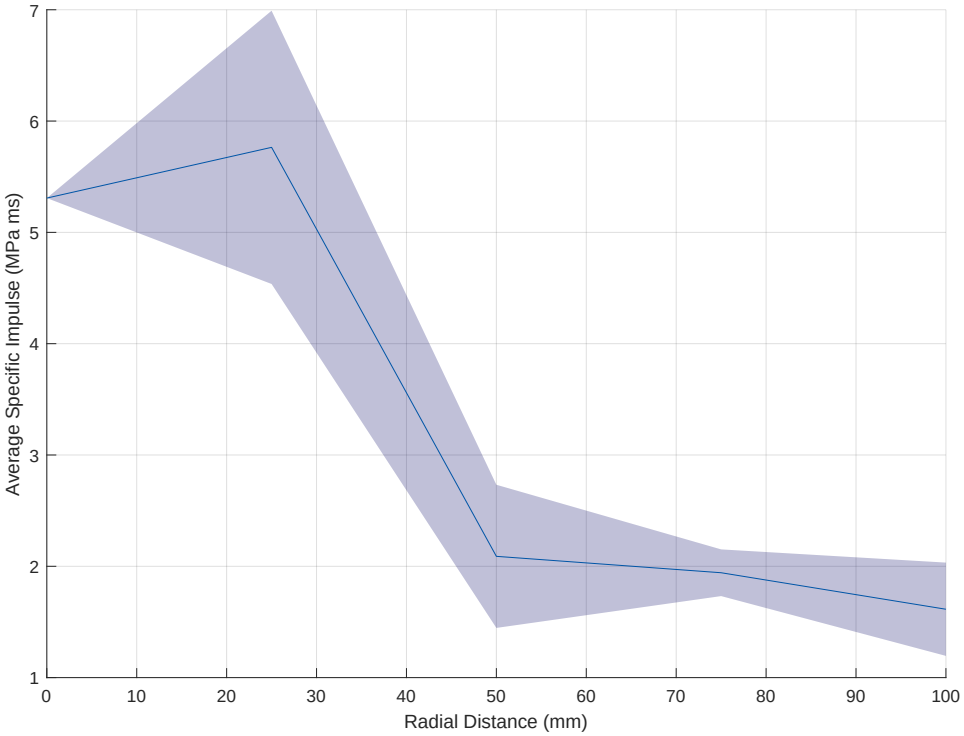

Figure 5.5: Plot showing the average specific impulse measured at each radial distance. The shaded area represents the standard error on the mean.

5.1.2 2D interpolated specific impulse data

Having applied the 2D interpolation discussed in § 4.1.5.2, it is possible to produce a plot of the cumulative impulse as a function of time, the peak of which gives the total impulse. Due to this being based on the 2D interpolation, it is possible to produce plots highlighting which radial bars are giving the largest contribution at each point. An example of such a plot is included in Figure 5.6, which shows how the cumulative specific impulse is first dominated by the lower radii HPBs until approximately 250 μs where the lower radii bars begin to dominate again. This information can be compared to high speed video footage to attempt to understand what is causing the loading (i.e. are there two distinct loading events visible in the video such as a pressure wave preceding the impact of soil particles?).

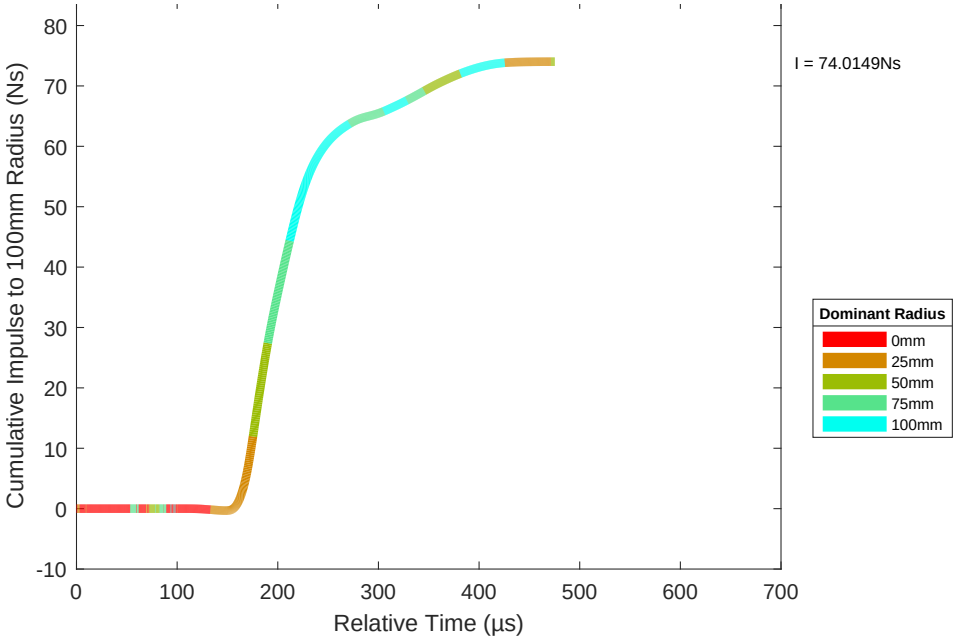

Figure 5.6: Plot showing the cumulative impulse for Shot 025 as a function of time.

5.1.3 High speed video

As detailed in §4.2.2, for each test where high speed video was recorded, image analysis has been performed in MATLAB to track the shape and progression of the resultant shock wave and ejecta cloud. Examples are included in Figures 4.14, 5.7 and 5.8. These examples show that for the given tests (all tests with frozen material below the charge) there is a good degree of consistency in the shape and temporal evolution of the both the shockwave and the ejecta cloud. It can also be seen that the ejecta cloud is relativly uniform with no significant indication of directional effects.

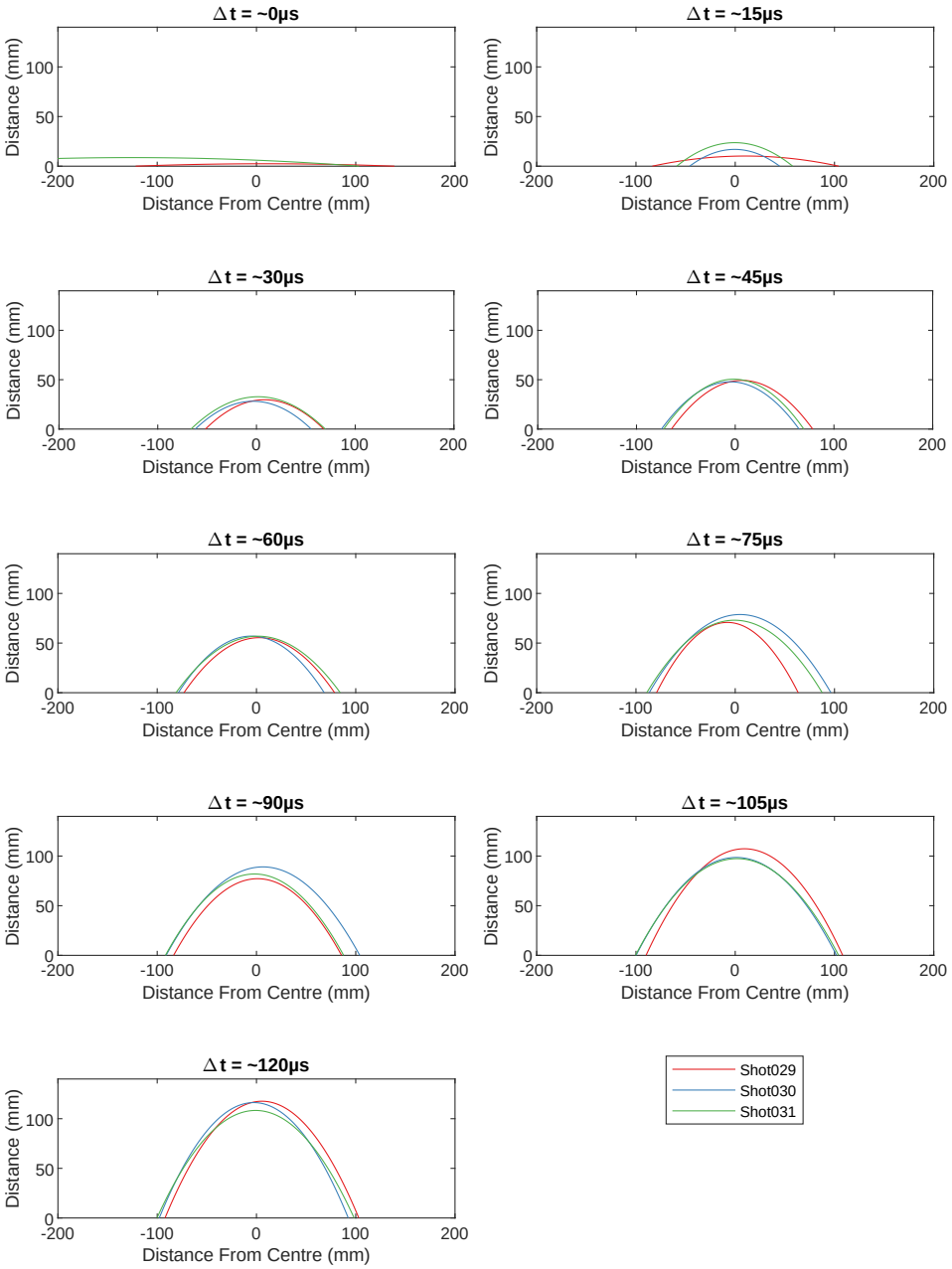

Figure 5.7: HSV tracking showing the detected shockwave for three nominally identical tests.

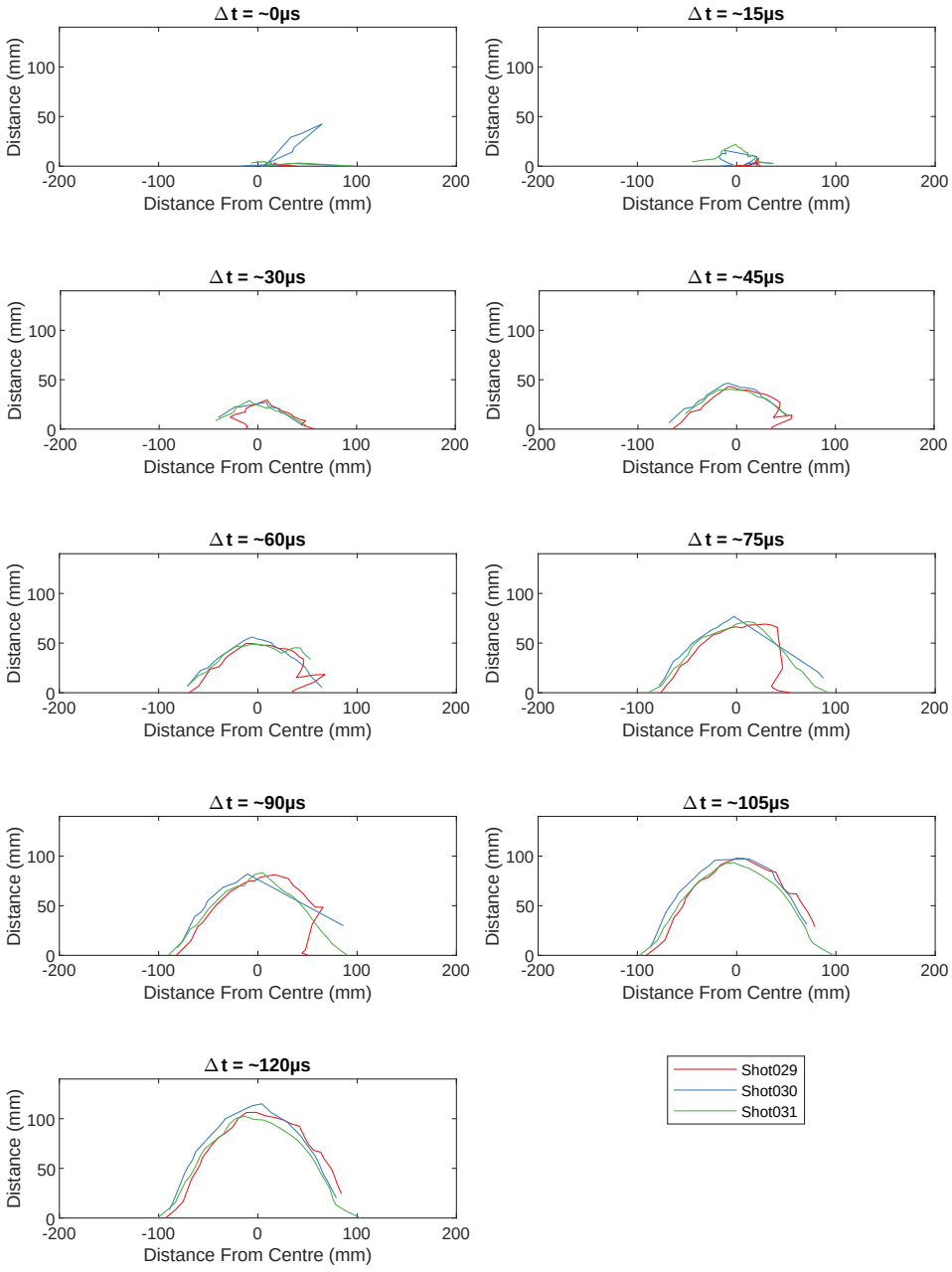

Figure 5.8: HSV tracking showing the detected ejecta clouds for three nominally identical tests.

Chapter 6

Frozen Soils

This chapter investigates the effect burying a charge in frozen ground has on the explosive output generated. Initial work was done to ensure that sub-zero temperatures have no adverse effect on the function of the high-explosives utilised. Methods for freezing samples are also discussed along with the relevant literature.

6.1 Hypotheses and predictions

Frozen Hypothesis 1 — The ice within the frozen soil will absorb energy as it melts, acting as an energy sink and reducing the loading.

Frozen Hypothesis 2 — Frozen soil has a higher shear strength and is less compressible than unfrozen soil, so will provide additional confinement to a buried charge, leading to an increased loading directly above the charge.

Exploring hypothesis 1 further, estimates can be made as to how much frozen material can be heated/melted with the available energy from the explosive. The heat energy Q [J] required to increase the temperature of an object of mass, m [kg], and specific heat capacity, c [Jkg^{-1}K^{-1}], by a ΔT [°K] is given by:

$$Q = mc\Delta T \tag{6.1}$$

The heat energy Q [J] required for an object of mass m [kg], and specific latent heat L [kJkg^{-1}] to undergo a phase transition (e.g. melting or vaporising) is given by:

$$Q = mL \tag{6.2}$$

Therefore, if all the energy from the detonation of 1 g of PE4 went into melting and vaporising water ice, it could heat, melt and vaporise 1.47 g of ice from -20 °C to +101 °C. Alternatively, it would take all the energy of 0.7 g of PE4 to melt and vaporise 1 g of water ice. If the ice is taken from -20 °C to water at 0 °C, this would require the available energy of 0.08 g of PE4 per gram of ice. This is based on the following properties:

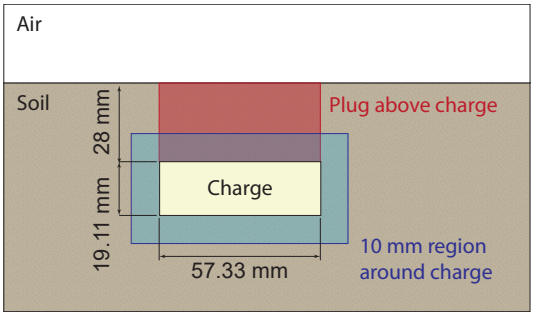

Figure 6.1: Diagram showing the experimental charge geometry and surrounding material.

- Specific heat capacity of water -4.187 $Jg^{-1}K^{-1}$
- Specific heat capacity of ice -2.108 $Jg^{-1}K^{-1}$
- Latent heat of fusion 334 Jg^{-1}
- Latent head of vaporisation 2256 Jg^{-1}
- Heat of detonation of PE4 of 4.5 kJg^{-1}

Taking the proposed test geometry into account (as per Figure 6.1), the volume of material directly above the charge is 7.23×10^{-5} m^3, giving a mass of 72 g of ice, or 120 g of soil (of which 5.7 g is water assuming $w = 5\%$). Similarly, there is 123 g of ice and 224 g of soil (of which 10.7 g is ice) in a nominal region of 10 mm surrounding the charge. In these examples, the ice present in the testing with frozen soil has the potential to neutralise 5.1% and 9.6% of the available energy from the explosive charge to vaporise the ice, which would lead to a significant reduction in the loading recorded. If a significant difference is detected during the testing, then this will be explored further.

It is anticipated that this effect will not be observed as the calculations above do not take into account the time taken for heat transfer to occur. This can be estimated from first principles using Fourier's heat transfer law Fourier (1822) which is defined as:

$$\frac{Q}{\Delta t} = -kA\frac{\Delta T}{\Delta x} \tag{6.3}$$

where: Q [J] is the heat energy transfer; Δt [s] is the duration; k [$Wm^{-1}C^{-1}$]is the thermal conductivity of the material; A [m^2] is the area of the heat emitting surface; ΔT [°C] is the difference in temperature between the hot and cold bodies; and Δx is the thickness of material that is conducting the heat. For the example above of a 10 mm shell around the charge, taking the thermal conductivity of the material to be that of ice (2.2 $Wm^{-1}C^{-1}$), the heat transfer rate Δt as a function of the temperature is plotted in Figure 6.2. This shows that for an event lasting less than a microsecond, the temperature difference

required to affect the required heat flow is above 1,000,000°C which is none physical in the context of this work.

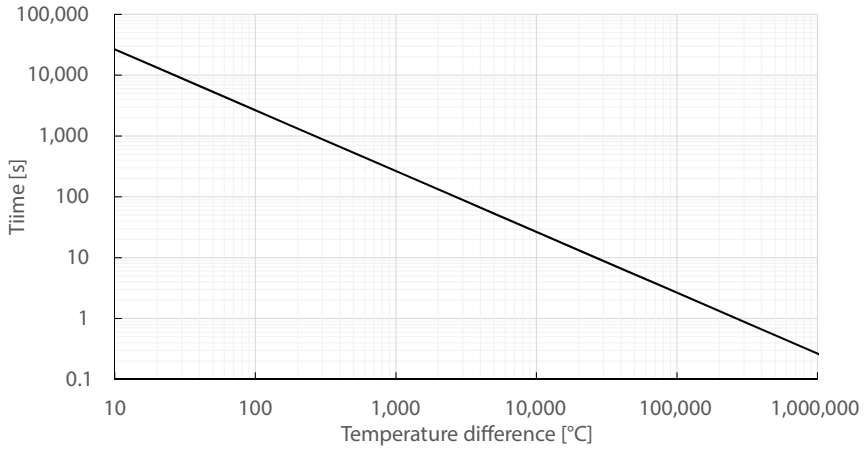

Figure 6.2: Plot showing how the heat transfer time varies as a function of the temperature difference of the bodies.

6.2 Methodology

> The strength and deformation properties of frozen soil samples are known to be affected by sublimation, evaporation, and thermal disturbance. Their effect is in the redistribution and ultimate loss of moisture from the specimen as the result of a temperature gradient or low humidity environment or both. Loss of moisture reduces the cohesion between soil particles and may reduce the strength (which is dependent on temperature) (Baker 1976).

Baker (1976)'s work, *Transportation, Preparation, and Storage of Frozen Soil Samples for Laboratory Testing*, presented a methodology for preparing and storing lab scale[1] artificially frozen samples alongside procedures for extracting in situ frozen samples. A summary of the method for lab frozen samples is as follows, with further discussion of how each step could be applied to this work in the following sections:

1. Construct a mould for the soil;
2. Add soil into the mould in a number of layers, compacting each to the desired level before adding further layers;
3. Add water to saturate the soil to the desired level;
4. Freeze the soil; and
5. Remove the sample from the mould.

[1] Samples of the order 1 kg.

6.2.1 Use of a soil mould

Baker's process is designed to work with soil samples of different shapes as required for particular tests (e.g. dumbbell-shaped). They suggest split moulds be used to facilitate the removal of the sample for subsequent testing. For the purposes of this work, the samples are predominantly tested inside a steel container rather than being removed, to replicate results of previous buried charge testing by Clarke et al. (2020). Therefore, split moulds are not possible. For the previous work of Clarke et al. (2015a), the soil containers were designed such that they would be large enough that the boundary of the container would not influence the loading. As an additional verification of this, a test with the frozen soils can be conducted without the soil container to understand if there is a significant contribution due to the confinement.

6.2.2 Addition of soil

Baker's procedures for adding and compacting the sample in smaller lifts are in line with § 3.1.3, which details the approach taken for this work. Therefore, there should be no significant issues applying this same technique to the frozen samples.

6.2.3 Freezing direction

Baker suggests that moulds be constructed of insulating material to facilitate unidirectional freezing. This is to ensure the sample has a uniform moisture content throughout. Baker (1976) proposes techniques for making lab scale frozen soil samples but notes that, "*it is not known whether it is possible to produce large uniform samples using existing freezing techniques*". A number of factors relating to how the sample is frozen are identified by Baker as potentially affecting the sample's material properties. These are outlined below.

Baker's preferred technique for freezing lab scale soil samples is using a thermoelectric cooling plate on the base of an insulated mould[2]. This results in unidirectional freezing which the authors suggest is preferable when aiming to prepare a uniform sample. However, the compressive strength results of Tsytovich and Sumgin (1959) indicate that samples frozen with an omnidirectional technique showed no significant difference to those that were frozen unidirectionally.

[2]Thermoelectric cooling plates are not cost effective when scaled up to the size required for this work

6.2.4 Freezing temperature/duration

The temperature of the freezing is linked to the duration it takes to freeze, with faster freezing times resulting in a reduction in the amount of moisture redistribution that can occur (Baker 1976).

Vyalov et al. (1966) investigated how the temperature at which samples are frozen changes the structure of the sample. They reported that samples frozen at temperatures below -30 °C resulted in a uniform structure without ice lenses, whereas freezing at -6 °C and above resulted in a layered lens structure. Warder and Andersland (1971) found that when freezing samples at -18 °C for 48 hours, this resulted in water migration to the surface creating an ice cap that required sanding off prior to testing. The layer of ice on the surface was proof that the soil sample was non-uniform after freezing. One way to avoid this non-uniformity is to freeze the ice unidirectionally and provide a supply of free water to the distal end of the sample to replenish water that is drawn towards the freezing face (Baker 1976). These techniques are much more applicable to lab scale samples in a controlled environment; for larger scale (≈100 kg soil plus 50 kg steel container) samples this may not prove viable. Instead, focus was placed on what equipment was available for freezing samples. Ultimately, this drove the technique used. For this work, a large refrigerated shipping container was used for freezing multiple samples at once. The internal temperature was set to the minimum achievable (set point of -20 °CC).

6.2.5 Volume changes

The expansion of water when it freezes is a widely reported phenomenon with values of the volumetric increase of around 9% (Liu et al. 2019). However, this is due to the molecular structure of water and does not hold for most other materials. Liu et al. (2019) investigated the change in volume of silty clay undergoing freeze thaw cycling and found that soils with a higher saturation level expanded, whereas those with a saturation level below 70% contracted when frozen. Figure 6.3 shows the change in void ratio after a number of freeze thaw cycles. In all cases, the largest change was during the first freeze cycle and even in the worse case, the increase in the void ratio was around 4% corresponding to a volumetric increase of the sample of $\ll 4\%$[3].

For a sample with a fixed height, a 4% increase in volume results in an approximately 2% increase in the radius. At the proposed experimental scale for this work, this corresponds to an increase of approximately 5 mm in the sample radius which is within the accepted range of experimental error for this work.

[3] As the void ratio is the volume of voids divided by the volume of solids, a 4% increase in the void ratio must correspond to a volumetric expansion of $\ll 4\%$.

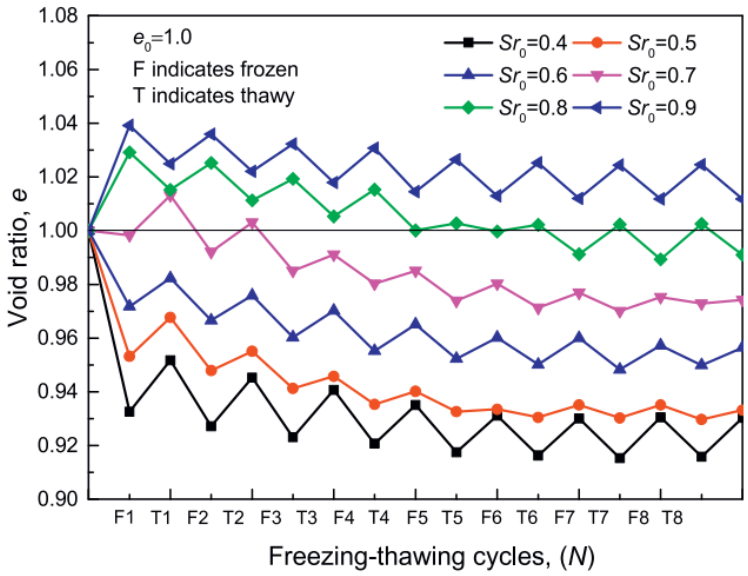

Figure 6.3: Plot showing how the void ratio changes after multiple freeze (F) and thaw (T) cycles for silty clay at different pre-freezing saturation levels (Liu et al. 2019).

6.2.6 Verification the sample is frozen

If the temperature of a sample is recorded during freezing (e.g. via embedded thermocouples), then a plot of temperature versus time should indicate if the sample is fully frozen. During the freezing phase, the temperature of the sample will remain constant due to the enthalpy of fusion. This effect was observed by Lackner et al. (2005), as illustrated in Figure 6.4 which shows three periods: firstly when the sample temperature is falling to the freezing point; secondly when the sample is undergoing freezing and the temperature remains constant; and finally once the sample is frozen the temperature falls further to match the environment. Employing a similar technique, multiple embedded thermocouples can be used to verify if a sample is frozen by recording the change in temperature at different points. This data can also be used to measure the time taken for the sample to freeze which, as discussed above in section 6.2.4, is important when trying to control moisture migration.

In the current work, the use of thermocouples was attempted for multiple batches. Additional issues were introduced with the refrigerated container being an external space, leading to the data recorded either being exposed to the elements externally or housed within the container at sub-zero temperatures. Each time the data recorder failed to record data either due to exposure to the weather or due to battery failure in cold temperature inside.

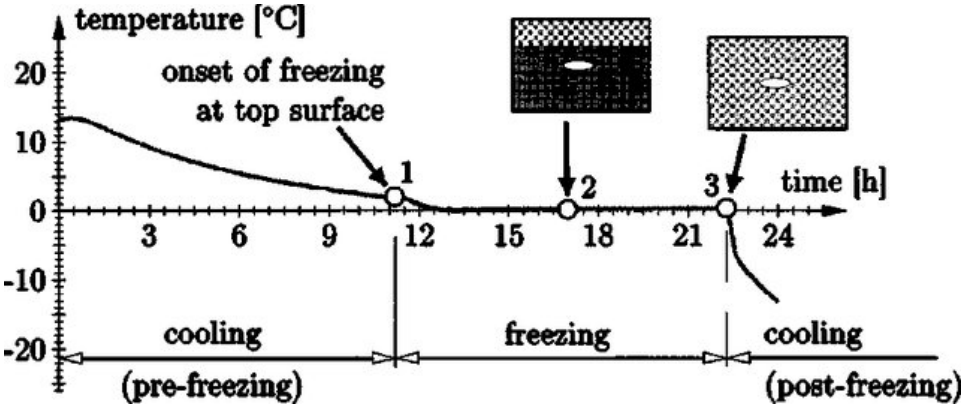

Figure 6.4: Plot showing how the temperature within a soil sample changes as it undergoes freezing (Lackner et al. 2005).

6.2.7 Logistical considerations for freezing a soil target

Following the same process described in § 3.1.3 and § 3.1.4 for preparing a soil bin and placing a charge poses a potential logistical issue for frozen samples depending on when the freezing takes place. A number of approaches are discussed below along with the advantages and disadvantages of each.

1) Freeze the whole bin once the charge is placed

The soil bin is prepared as outlined in § 3.1.3 and frozen once the charge is placed and the material tamped back down to give a level surface (i.e. frozen after image (f) in Figure 3.5). This approach is the most representative of a frozen buried charge but does however, require a full soil bin to be frozen with a charge and detonator in place which poses both safety and security issues, as once a detonator and charge are combined they cannot be left unattended.

2) Freeze the bin once the charge cavity has been formed then again after backfilling

The soil bin is prepared as discussed above and frozen once the charge cavity is created (after image (c) in Figure 3.5). Once the bulk of the bin is frozen, the process is resumed and the charge is placed before the material is backfilled. The whole bin is then placed back in a freezer to ensure the backfilled material is frozen prior to testing. This method has the advantage over method 1 in that the freezing time with a detonator in place is significantly reduced, thereby reducing (but not eliminating) the safety risk. However, this comes at the cost of introducing a discontinuity within the soil sample, namely in a ring around the charge.

3) Freeze the bin once the charge cavity has been formed then insert a precast section as the backfill

The soil bin is prepared as discussed above in method 2 until the charge is placed. At this point, a precast section is used in place of the backfill to negate the need to refreeze the whole soil sample. This has the advantage that the sample does not need to be frozen with charge and detonator in place, greatly reducing the risk. It does, however, pose a potential problem in that the precast "plug" is not bonded to the bulk of the soil sample and may respond differently. This could be partially resolved if water is injected into the gap and allowed to freeze due to the low temperature of the surrounding material, however, this would still result in the discontinuity discussed above in method 2.

4) Create the soil sample in two slabs and sandwich the charge between them

The soil bin is prepared up to the depth of the charge before being frozen. A second soil sample that is the correct size to fill the bin is then prepared to the same geotechnical conditions and frozen. A cavity is then cut into one of the two frozen slabs for the charge/detonator before the top slab is added onto the base section, sandwiching the charge between the two. This has the advantage over methods 2 and 3 in that the discontinuity in the sand bin is below the charge, rather than above/surrounding it in a ring. As with method 3, this method removes the need to freeze the soil bin with the charge in place, greatly reducing the risk.

6.3 Preliminary frozen charge tests

Prior to conducting any tests using the CoBL rig, a number of lower complexity tests were conducted to understand both the performance and logistical impact of freezing a buried explosive charge and to validate the methodological concerns in § 6.2. Two types of preliminary tests were conducted to this effect:

- baseline performance of PE4 at reduced temperatures to allow this to be accounted for in the CoBL results; and
- determine the finalised methodology for producing frozen soil samples with a charge in situ.

The first set of preliminary tests conducted measured the relative performance of frozen PE4 with respect to PE4 at ambient conditions. This was conducted using a similar methodology as that used by Rigby and Sielicki (2014) which was used to measure the TNT equivalence. That is, measuring the reflected pressure on a large wall due to a 250 g hemispherical charge detonated at a known distance from the gauge. Tests for this work were scheduled to coincide with testing being undertaken on the EPSRC-funded Mechanisms and Characterisation of Explosions (MaCE) project, where the charges were detonated between two instrumented walls, allowing two separate reflected pressure measurements

to be taken during each test. The wider data set from this set of tests, not including the frozen PE4 charges conducted for this thesis, are reported by Farrimond et al. (2024a). For the current work, the results of four ambient and two frozen PE4 tests are considered. Each test was conducted with a 250 g PE4 hemisphere placed at the centre point, 5 m from two walls with reflective gauges installed at the base. Two Kulite HKM 375 pressure gauges were used with the data recorded on a TiePie HandyScope HS4 USB oscilloscope. The experimental setup is shown in Figure 6.5.

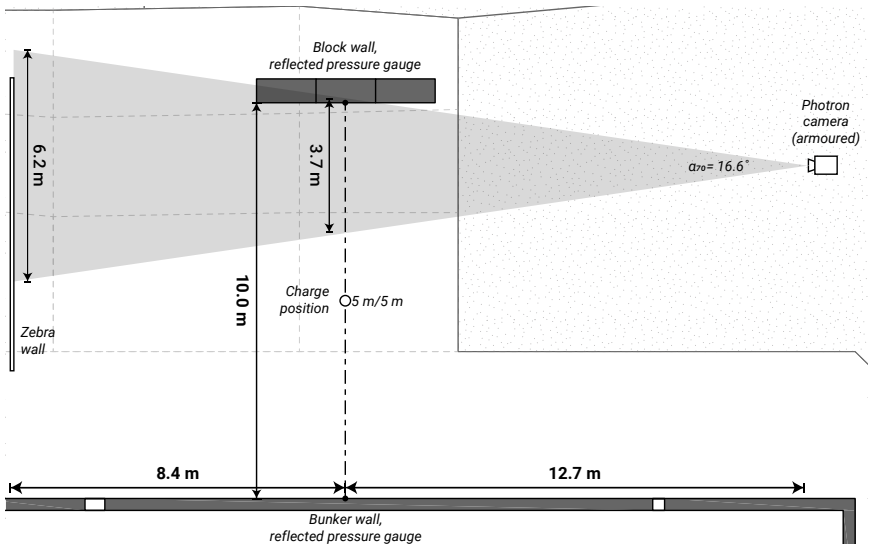

Figure 6.5: Schematic showing the test arrangement for the frozen PE4 characterisation tests Farrimond et al. (2024a).

For this series of tests, the charges were hand stemmed into hemispherical 3D printed moulds and then stored in a laboratory freezer at -30 °C until testing. Charges were removed from the freezer and detonated as quick as reasonably practical to avoid them warming up. Prior to detonation, the external temperature of the charge was recorded using an IR thermometer to ensure it had not significantly increased. For the two tests reported, the temperature prior to testing remained below -20 °C The tests were conducted over two subsequent days with similar weather conditions, as detailed in Table 6.1.

Table 6.1: Summary of weather conditions during PE4 performance tests.

Series name	Air temperature [°C]	Air pressure [mbar]
Ambient PE4	6.7	1026.5
Frozen PE4	8.0	1025.3

Figure 6.6 shows the pressure traces from the four ambient (grey) and two frozen (red) tests. The results show that there is no significant difference between the output from a PE4 charge at ambient or sub zero temperatures. Therefore, for testing charges buried in frozen ground, the results are not expected to vary based on the temperature of the charge alone.

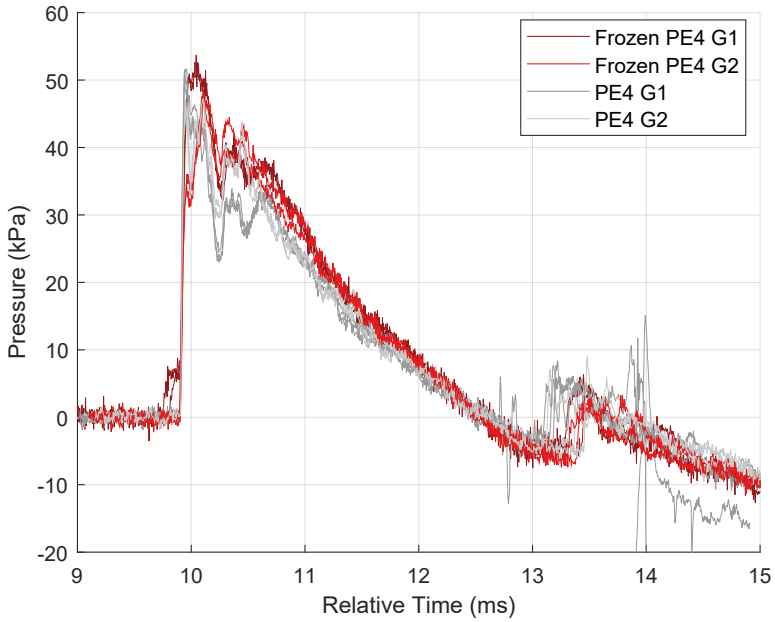

Figure 6.6: Pressure traces comparing the loading from 250 g frozen (red) and non-frozen (grey) hemispherical PE4 charges. Results include two frozen and four non-frozen tests, with two traces per test from separate reflective pressure gauges (G1 and G2), each 5 m away from the charge.

6.4 Preliminary ice block tests

To determine which freeing method to use (as detailed in § 6.2.7), a series of simplified tests were conducted to investigate the difference in failure mechanisms of ice blocks created by different methods. Ice was formed into geometries representing the methods outlined, detonated and recorded using high speed video (HSV). If the HSV results showed each arrangement failed in a similar way, then the method with the lowest logistical burden was used. If, however, there was a difference (e.g. the precast plug was ejected as if fired from a cannon, or the sandwiched ice blocks separate from each other rather than shattering), an assessment was made between the logistical burden and the effect on the experimental results. The potential configurations are sketched in Figure 6.7. Arrangement (a) is the idealised solution, aiming to represent the case of a charge frozen in a monolithic block. There are no inherent weaknesses

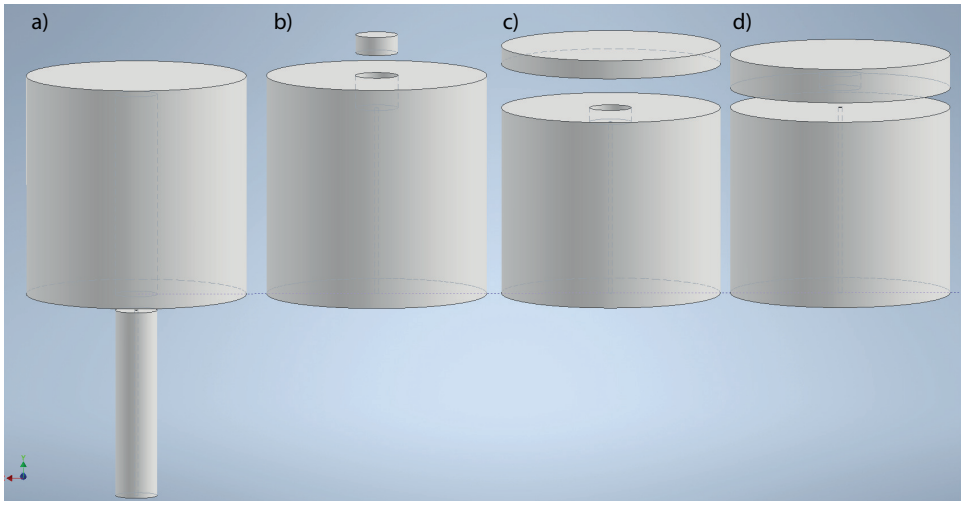

Figure 6.7: Sketches showing four potential arrangements for a charge encased within a block of ice: a) a block with the charge inserted via a cavity underneath which is subsequently blocked with an ice plug; b) a block with the charge inserted via a cavity above which is subsequently blocked with an ice plug; c) a charge that is placed inside a void with a capping slab placed on top; and d) a charge that is placed inside a void in the capping slab which is then placed on top of the base.

built into the ice block above the charge and so represents method 1 in § 6.2.7 but without the need to freeze the whole system with a detonator and charge in situ. It is, however, not a practical solution for the full scale testing as it would either require the soil bins to be redesigned (making the tests inconsistent with previous work) or require the bulk of the soil sample to be moved around once frozen. Arrangement (b) represents sand bin preparation method 3 above and arrangements (c) and (d) are two variations on method 4.

6.4.1 Results

Figure 6.8 shows a photo of the arrangement used in the preliminary testing using a cylindrical charge of 24 g of PE4 within a block of ice arranged as per 6.7(c). This geometry was tested as attempts to form arrangement (a) in Figure 6.7 proved problematic and it was deemed to be more representative than arrangement (b). Multiple ice blocks were made using different containers to assess if it was possible to control the freezing direction on samples of this size with the available equipment. Each was visually inspected to see if internal faults or cracks could be seen and none were detected. For these tests, the water container was sized to allow the largest block to be made using a small scale freezer (prior to the purchase of the refrigerated ISO container), reducing the amount of airflow and insulation between the container wall and the freezer walls.

Figure 6.8: Image of an ice block pre-test. The block is supported on two timber stands, with the detonator (yellow tube) and a camera trigger wire (orange) inserted through a long hole to the charge from the lower face (indicated by the dashed lines).

The ice block was frozen in a domestic chest freezer for one week prior to testing. It was then cut in half using a wire saw to produce two sections. Initial attempts found that it was difficult to produce thin slabs via this method as there was a tendency for them to crack or split during cutting. Producing a flat and level cut was difficult as the wire saw was hard to control. The wire saw also had a tendency to become stuck with the removed ice refreezing and blocking the cut. Because of these issues, it was decided for the soil-based tests it would be beneficial to produce the top and bottom sections separately instead of trying to cut them from a single block.

For the preliminary test, a 6 mm hole was drilled through the base of the block to insert the detonator, and a cylindrical pocket drilled out to hold the charge. Prior to testing, the detonator and break wire were inserted though the 6 mm hole until they protruded into the charge pocket. Once in position, cold water was added to freeze them in place. The charge was then stemmed into the void and the top ice block placed on immediately prior to testing. Again, a small amount of cold water was added to allow the top and bottom blocks to freeze together.

The ice block was tested unconfined and high speed video was used to determine if there was a vertical separation of the two blocks or signifiant lateral venting of

the explosive products along the seam. Figure 6.9 shows stills from high speed video of the test.

Immediately after the flash from the detonation has subsided, it can be seen that the ice block is fractured throughout and is effectively inertially confined granular fragments of ice. The later frames show no significant deviation caused by the construction method of the ice block and therefore it was deemed a suitable technique for preparing the frozen soil samples for testing. Also noteworthy is that the timescales over which the ice begins to displace (approx. 0.15 ms), which are similar to those for the pressure arrival at the measurement device on CoBL (i.e. as the arrival time in 5.2), are significantly longer than the internal shattering ($<$0.07 ms), indicating that the ice arriving at the target plate is likely to be granular instead of monolithic large fragments. This preliminary test was repeated to ensure the findings were consistent. Based on these results, it was decided to proceed with a similar charge configuration method for the full test series.

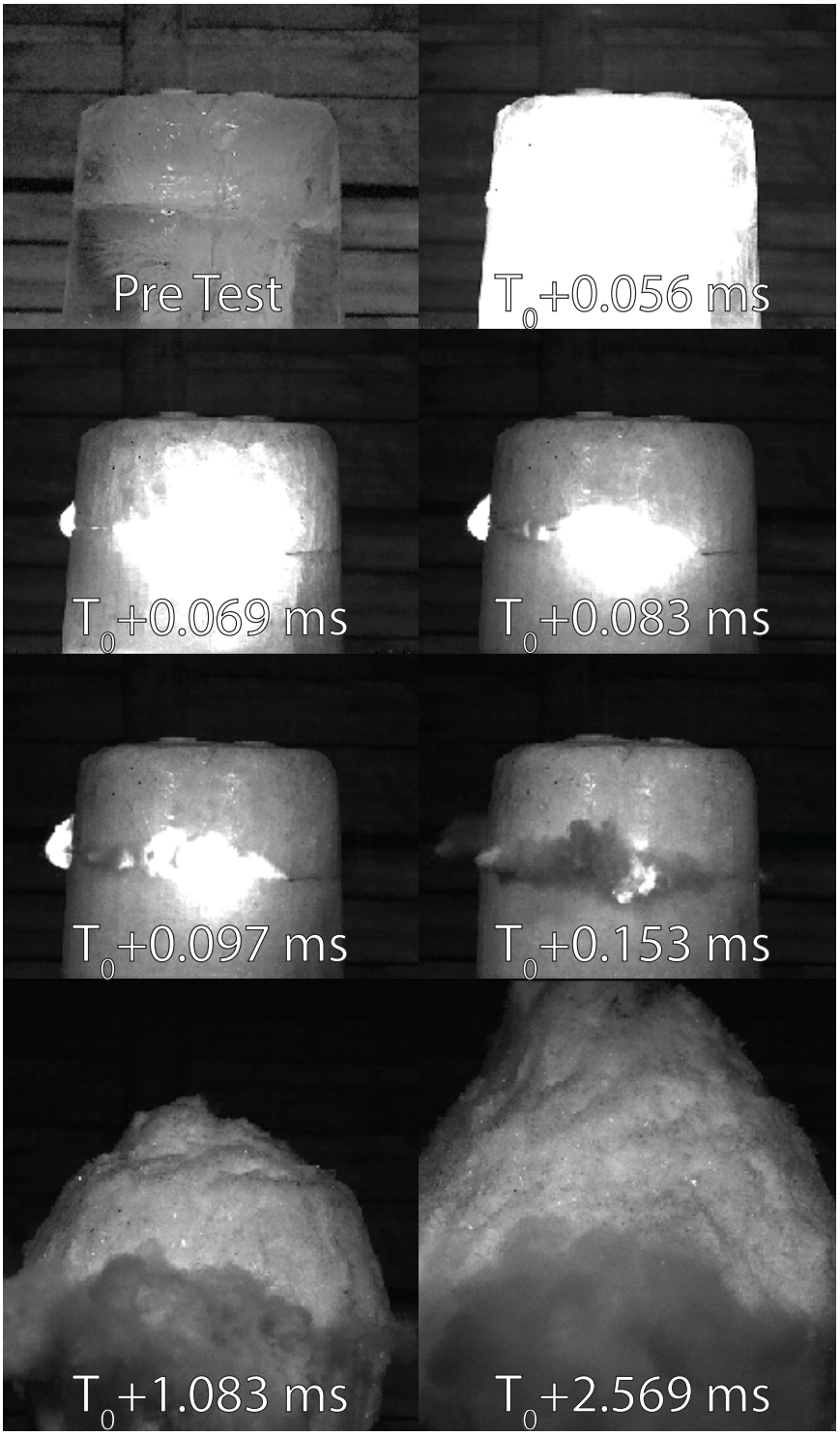

Figure 6.9: Still from high speed images of a 24 g PE4 charge contained within a block of ice, showing the failure mechanism of the ice is due to the shockwave propagation, shattering the ice, which remains inertially confined.

6.5 Soil freezing and charge placement method development

Once the ice sample methodology was decided, additional preliminary tests were conducted to verify the the technique would work for a soil sample. Due to the increased size of the samples for the CoBL testing, an industrial ISO container freezer unit was used, which allowed multiple soil containers to be prepared and frozen at the same time. As discussed previously, it was determined that producing the top and bottom sections of the samples separately was more effective than producing monolithic samples and cutting them to size. The bottom elements were prepared as in § 3.1.3 before being placed in the freezer. The top sections were prepared on steel plates with a cardboard cylindrical liner to form the shape. The liners were made from tubular cardboard concrete forms of diameter matching the soil containers.

It was found that the top section of the soil samples were fragile due to their thinness. To combat this, the charge recess was cut into the underside of the top section, instead of into the upper side of the lower section. This allowed the top sections to be 19 mm thicker (giving a total thickness of 47 mm) which were more robust but still subject to breakage. Therefore, it was determined to make the top sections oversized (100 mm thick) and then remove the extra material prior to testing. In addition to the increased mechanical strength during processing, this also resulted in a flat top surface free of imperfections caused by separating the slab from the steel plate it was frozen on (e.g. it compensated for any material that remained frozen to the steel plate).

The final charge placement technique was based on that described in § 3.1.4 and detailed in Figure 6.10. This process took place inside the industrial freezer to minimise the risk of the temperature increasing prior to testing.

1. The cardboard liner was removed from the top section and a void was made in the underside to house the charge. A charge case with inert fill was used to confirm the correct sizing of the void (Figure 6.10a).
2. The charge was prepared in the mould, with the detonator attached and taped in place (Figure 6.10b).
3. A slot was carved out of the bottom section to allow for the detonator and shock tube to be positioned (Figure 6.10c).
4. The excavated sand was repacked around the detonator and shocktube to fill the voids, and the top surface misted with water to allow it to re-freeze (Figure 6.10d).
5. The top section was added, aligning the charge with the pre-formed hole in the underside.
6. The surface of the top section was scraped off with a steel plate to leave the soil surface level with the top edge of the soil container.

Figure 6.10: Modification to the charge placement procedure required for the frozen tests.

For the tests using solid ice, the process detailed above had to be further modified to account for the significant expansion during freezing. As discussed in § 6.2.5, ice expands by approximately 9% when freezing whereas no expansion was expected (or observed) for the soil samples. In addition to the increased volume, the expansion of the ice samples proved problematic due to the directional freezing caused by the more efficient heat transfer from the steel soil containers than the free air surface, resulting in freezing inwards from the sides and base. This resulted in the ice freezing and cracking in the centre and on the top due to heave. To address this, the samples were frozen and allowed to directionally freeze. Once fully frozen the cracked sections were removed using a hammer and chisel. This removal continued until solid, unbreakable ice was found after which the created void was filled with fresh water and frozen again. This method allowed for all the soil bins to be frozen in the industrial freezer at once. As the degree of vertical expansion was difficult to predict accurately

Figure 6.11: Photo of the soil container filled with ice prior to the test, showing the charge in the centre (white disc in orange charge case).

prior to freezing, the samples were all made oversized and then carved down to size using a stiff wire wheel attachment on an angle grinder, before final shaping was undertaken with a flat steel edge. Similar to with the soil tests, the top sections of the ice tests were made oversized and scraped down to size prior to testing. Figure 6.11 shows a soil bin prior an ice test; in the centre of the image the charge can be seen as a white disc contained in an orange charge casing.

6.6 Results

Table 6.2 details the tests conducted and the historic data re-analysed for this section.

Table 6.2: Table outlining the data generated and analysed for the frozen soil section.

Shot name	**Series name**	**Soil type**	**Bulk density**† **(Mg/m^3)**	**Moisture content**	**Burial conditions**
Shot022	Frozen top and bottom unconfined	LB	1.600	2.50%	LB sand frozen above and below charge (no radial confinement during the test)
Shot023 Shot024 Shot028	Frozen top and bottom	LB	1.604 1.620 1.592	5.00% 5.00% 5.00%	LB sand frozen above and below charge
Shot025 Shot026 Shot027 Shot037 Shot038	Ice	Ice	1.000	N/A	Water ice
Shot029 Shot030 Shot031	Frozen bottom	LB	1.660 1.629 1.616	5.00% 5.00% 5.00%	LB sand frozen below charge
Shot032 Shot033 Shot034	Frozen top	LB	1.645 1.593 1.589	5.00% 5.00% 5.00%	LB sand frozen above charge
Hist046‡ Hist047‡ Hist049‡	LB 5%	LB	1.670	4.76%	Fully buried
Hist101‡ Hist102‡	Water	LB	1.000	NA	Fully submerged

†Bulk density is taken prior to freezing for the frozen samples.
‡Clarke et al. (2020) data has been re-analysed and processed for this work.

6.6.1 Pressure data

As discussed in § 5.1.1, Figure 6.12 shows a typical pressure trace recorded from the Hopkinson pressure bars during these tests. Full pressure time histories for all of the current testing can can be found in Appendix A and have not been included in the main body of the thesis, instead the integrated results are discussed.

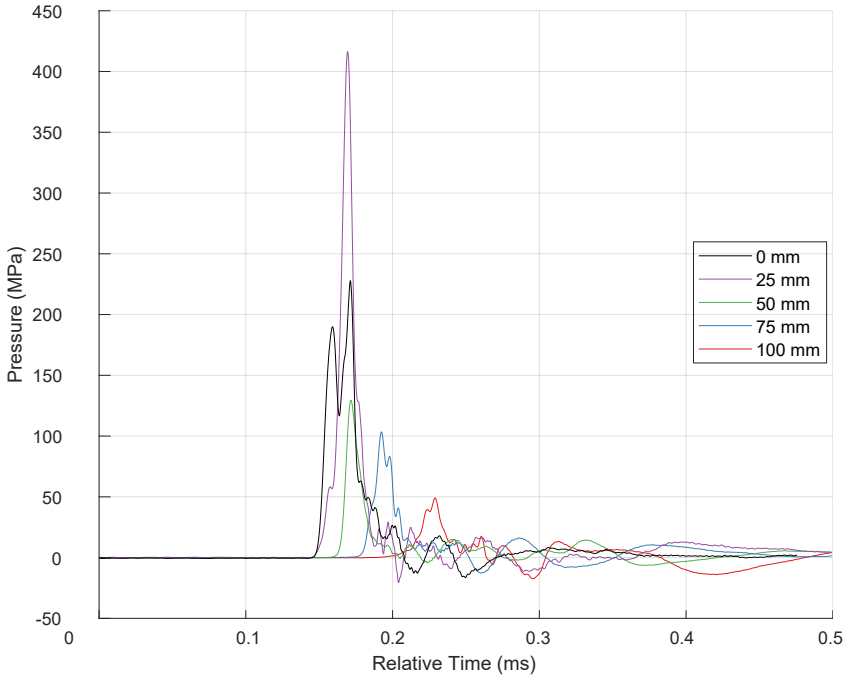

Figure 6.12: Pressure time history for a single array of 5 bars in Shot 025, with the charge buried in ice (other traces excluded for clarity).

6.6.2 Frozen soil

Figures 6.13, 6.14 & 6.15 show the specific impulse distribution for the tests with the top section frozen, the bottom section frozen and all soil frozen respectively. It can be seen that when the top section of the sample is frozen (Figures 6.13 & 6.14), there is a significant increase in the variability. This is evident by the large error bounds on the aggregated data plots. In contrast, the tests with just the material below the charge frozen and the material above not, show less variability. However, there is still a larger degree of variability when compared to the historic testing with non-frozen LB sand (Figure 6.16).

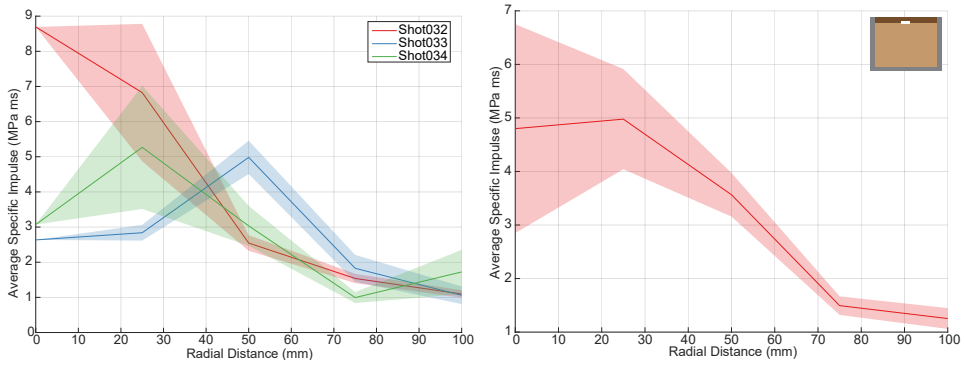

(a) Individual test data **(b)** Aggregated data across all tests

Figure 6.13: Average specific impulse as a function of radial distance for all the tests with the material above and to the sides of the charge frozen.

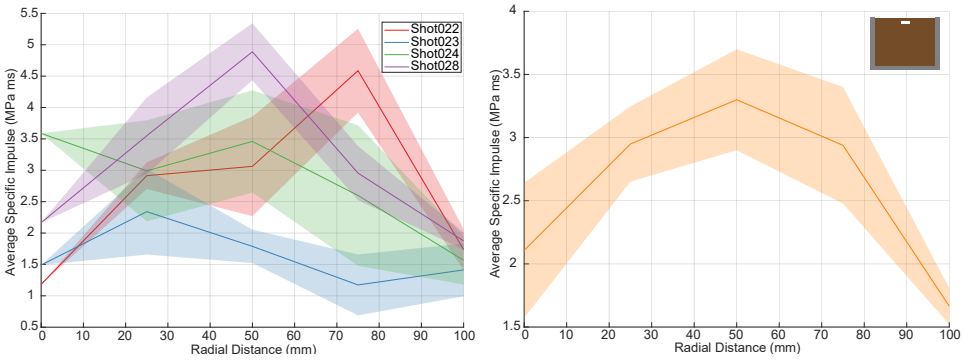

(a) Individual test data **(b)** Aggregated data across all tests

Figure 6.14: Average specific impulse as a function of radial distance for all the tests with all the material frozen.

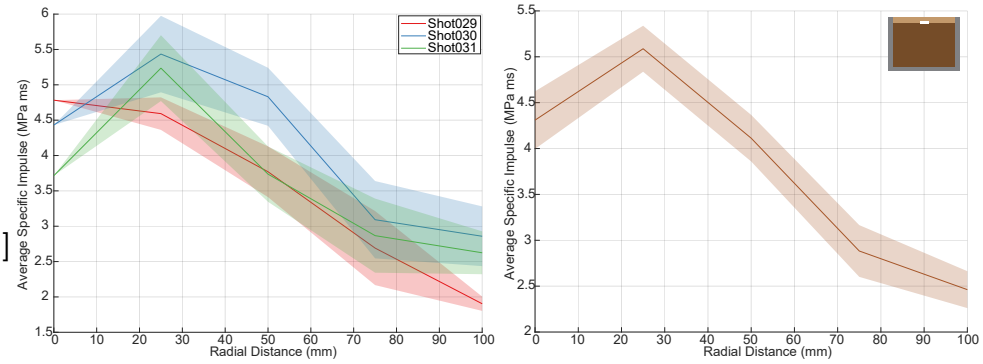

(a) Individual test data **(b)** Aggregated data across all tests

Figure 6.15: Average specific impulse as a function of radial distance for all the tests with the material below the charge frozen.

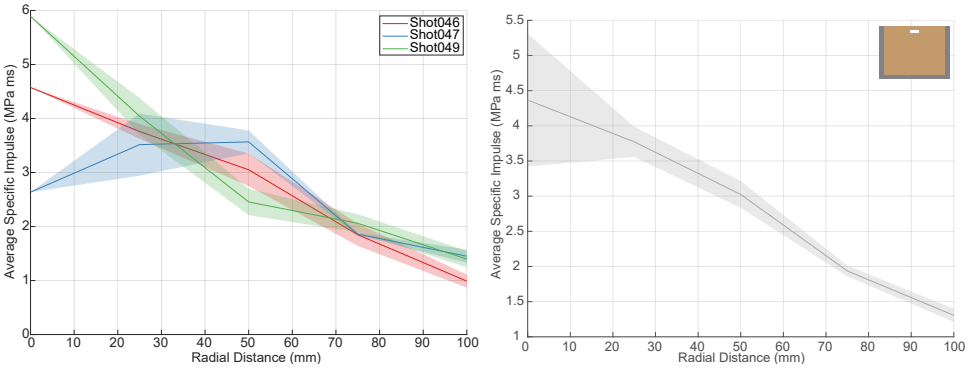

(a) Individual test data **(b)** Aggregated data across all tests

Figure 6.16: Average specific impulse as a function of radial distance for the historic tests with LB at 5% moisture content.

Figure 6.14b shows a different loading distribution to the other tests, with a lower loading in the central region and an increased loading further out. When compared to the other series (as in Figure 6.19), this different profile is clearly evident. It is difficult to suggest a mechanism that could explain this change in loading that shouldn't also result in a similar loading profile for either the frozen top or frozen bottom series. It is, therefore, assumed that the unusual profile of the specific impulse data is due to variability of the individual test results (as seen in Figure 6.14a), where the four tests conducted show little similarity in their profiles. This is further evident in Figure 6.20c, which again shows inconsistent results across the four tests conducted. This indicates a potential issue with the experimental setup where both the top and bottom sections of the soil container were frozen as any imperfections in either may dislodge the charge, making it's surface none-parallel with the target plate. Constructing a soil container with two frozen sections may also lead to poor contact between the two sections creating a weakness, however, as shown in Figure 6.17 showing the unconfined test, the joint between the two sections was well aligned with no gaps.

(a) Pre test **(b)** Post test

Figure 6.17: Photos showing the unconfined frozen soil sample before and after testing in Shot 022.

Figure 6.14a shows that the specific impulse distribution from the unconfined test, Shot 022, shows a similar pattern to the tests in the steel soil bins, indicating that the confinement offered by the soil bin does not affect the loading significantly. However, it is clear there is a high degree of variability in these results. One potential mechanism for high variability is that of particle strikes (as discussed by Waddoups et al. (2023)) from clumps of frozen soil. However, inspection of the post test soil condition indicate that there were no frozen clumps post test, as demonstrated in Figure 6.17 which shows the soil before and after the unconfined test. In the post test state, the soil was predominately granular with a small amount of clumping, indicating no clumps were formed or thrown during the test. This is further confirmed by photos taken after the tests with frozen and unfrozen sands, as shown in Figure 6.18, where both tests show a similar degree of soil clumping after the test, which is independent of the freezing.

(a) Post test photo from Shot003, testing with unfrozen LB sand in § 7

(b) Post test photo from Shot024 with frozen LB sand

Figure 6.18: Photos showing the soil after unfrozen (6.18a) and frozen (6.18b) tests. Both tests show a similar amount of clumping of the sand post test with a small number of clumps on the surface approximately 5 mm in diameter.

Figure 6.19 compares the aggregated average specific impulse for each series. It can be seen that the tests with only the material below the charge frozen differ significantly from the historic baseline. This is in contrast to the findings of Clarke et al. (2020), who found that the degree of back tamping for a buried charge was not a significant factor in determining the loading. However, this result should be interpreted in the overall context of results in Figures 6.13 to 6.19 which show that the frozen soil shows considerably higher variation between nominally identical tests.

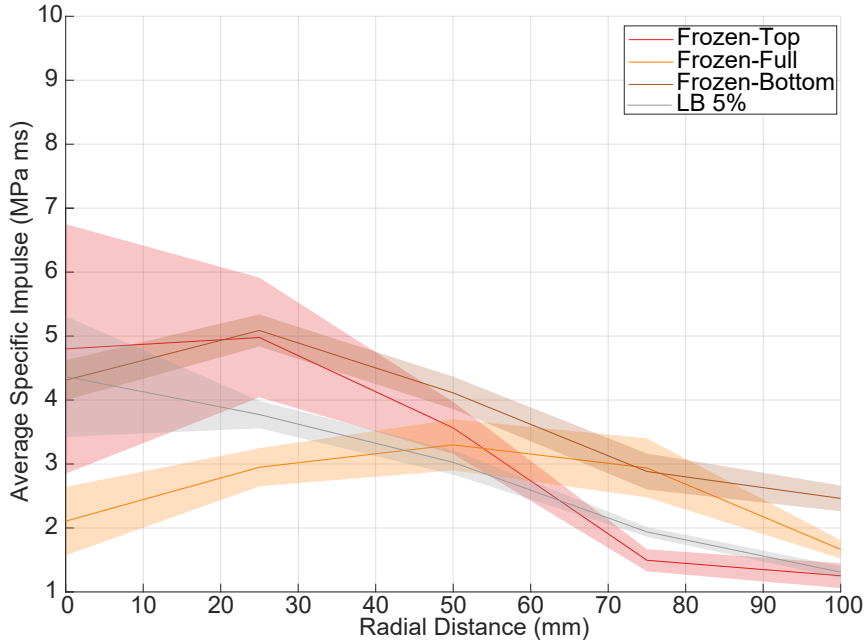

Figure 6.19: Average specific impulse distribution for each of the three frozen sand series compared to each other and to the historic 5% LB data.

Figure 6.20 shows the temporal evolution of total impulse for each of the frozen sand series. It can be seen that the tests with frozen material above the charge (Figures 6.20a & 6.20c) show a lower level of repeatability than those with no frozen material above (Figures 6.20b & 6.20d). This is especially the case with the fully frozen tests (Figure 6.20c) where one test shows a significant deviation from the others, resulting in a loading 50% lower. There are no known experimental differences between this and the other nominally identical tests. When comparing the pressure traces (included in Appendix A) the results for Shot 023 are different to the other comparable tests Shots 022, 024 and 025) but do not show signs of data corruption or instrumentation failure. Therefore, the results are assumed to be an accurate record of a test that did not proceed as planned (e.g. a true recording of the loading event caused by an experiment where there was an unexpected error in the setup).

Figure 6.21 shows the total interpolated impulse within the 100 mm instrumented region for all the frozen tests. This confirms the conclusion that the back tamping provided by the frozen soil increases the loading measured on the target plate with both the fully frozen, and bottom frozen series giving higher results than the top frozen and unfrozen LB tests.

A potential explanation for the effect of back tamping increasing the impulse is that back tamping increases the confinement behind the charge, preventing the immediate release of explosive energy and redirecting more force into the surrounding material.

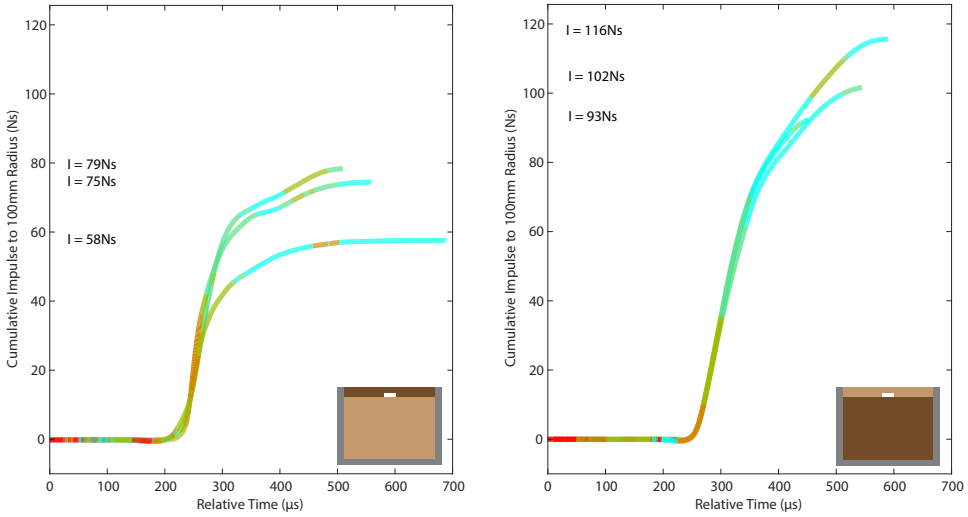

(a) Soil above and side of the charge frozen

(b) Soil below the charge frozen

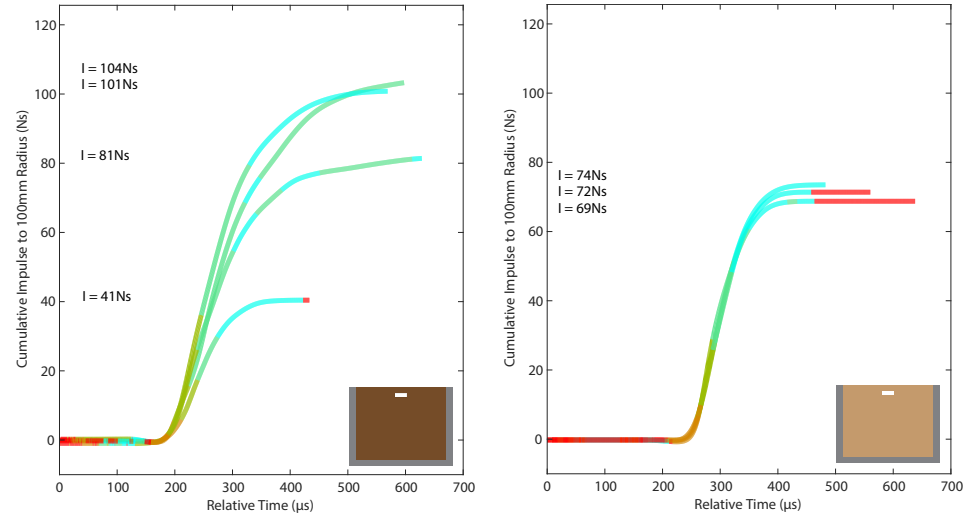

(c) All soil frozen

(d) Historic tests with 5% LB

Figure 6.20: Evolution of the cumulative impulse as a function of time for the four series considered; each plot shows the results for the repeat tests within the given series and demonstrates the repeatability of the data.

This confinement effect can result in:

- Higher Pressure and Impulse: The tamping limits venting, which increases the pressure exerted on the material, resulting in higher impulse values.
- Higher Shock Speed: The added confinement amplifies the shock wave's intensity, often increasing the shock speed through the material as the energy is concentrated and more effectively transferred.

These mechanisms explain why back-tamped charges can produce stronger results than untamped charges in similar conditions.

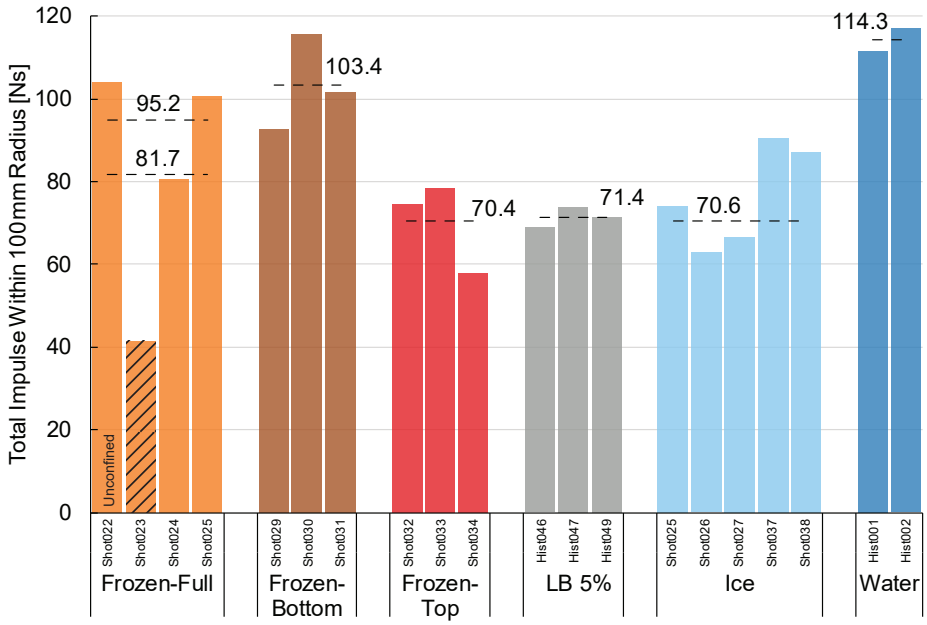

Figure 6.21: Total interpolated impulse within the 100 mm instrumented region for each test, with the average for each series overlaid as a dashed line. For the frozen full series, the average has been plotted both including (81.7 Ns) and excluding (95.2 Ns) the anomalous result.

Figure 6.22 shows a comparison of the shape of the ejecta cloud for typical results of the different test series with frozen material, and Figure 6.23 shows the shot to shot consistency for the fully frozen and frozen bottom tests. It can be seen that the tests with frozen material above the charge repeatedly produce ejecta clouds with a more chaotic shape compared to the ones with no frozen material above the charge. As discussed above in § 2, Westine et al. (1985) and Ehrgott et al. (2011) found that the loading from a buried charge is primarily due to the particles striking a target and not from the air shock. Therefore, the degree of non uniformity of the loading and shot to shot variability observed in the high speed images matches the variability observed in the measured specific impulse.

Figure 6.24 shows the results of tracing the shock wave in the high speed imagery. The results show that the shock wave from the tests with frozen material above the charge travel faster than than those that have passed through unfrozen soil. This can be attributed to the increased stiffness of the frozen material leading to a higher wave speed.

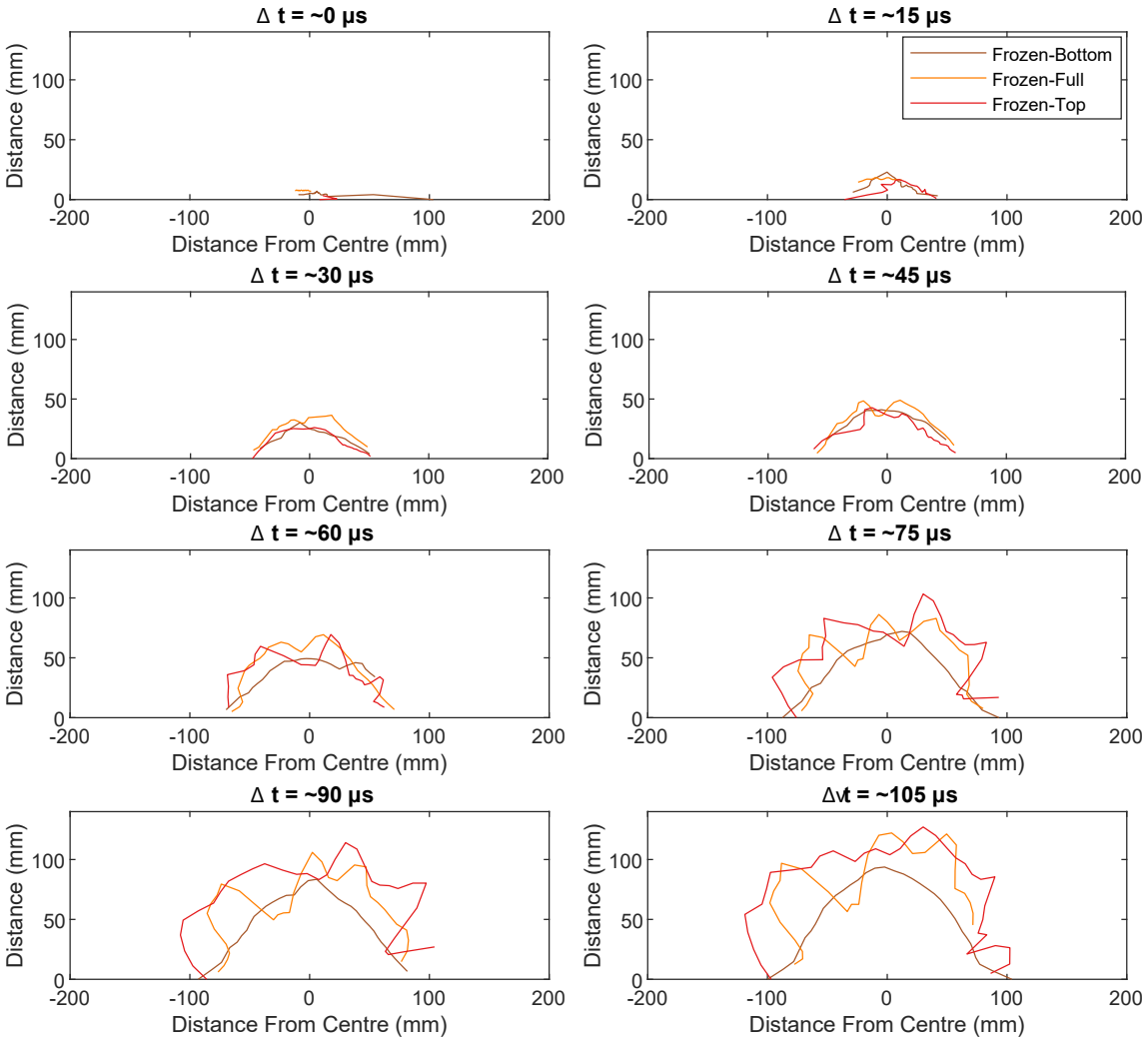

Figure 6.22: Output from the high speed video tracking of the ejecta cloud for typical tests from the different frozen arrangements.

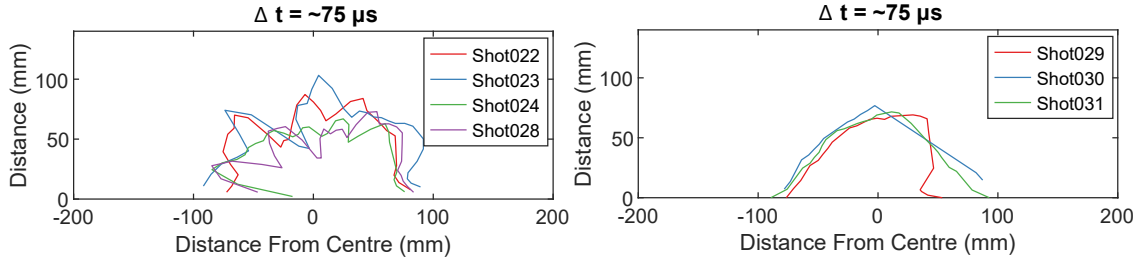

Figure 6.23: Single time step output from the high speed video tracking of the ejecta cloud for tests with the frozen material above the charge (left) produce significantly more chaotic clouds of ejecta than the ones with non frozen material above (right).

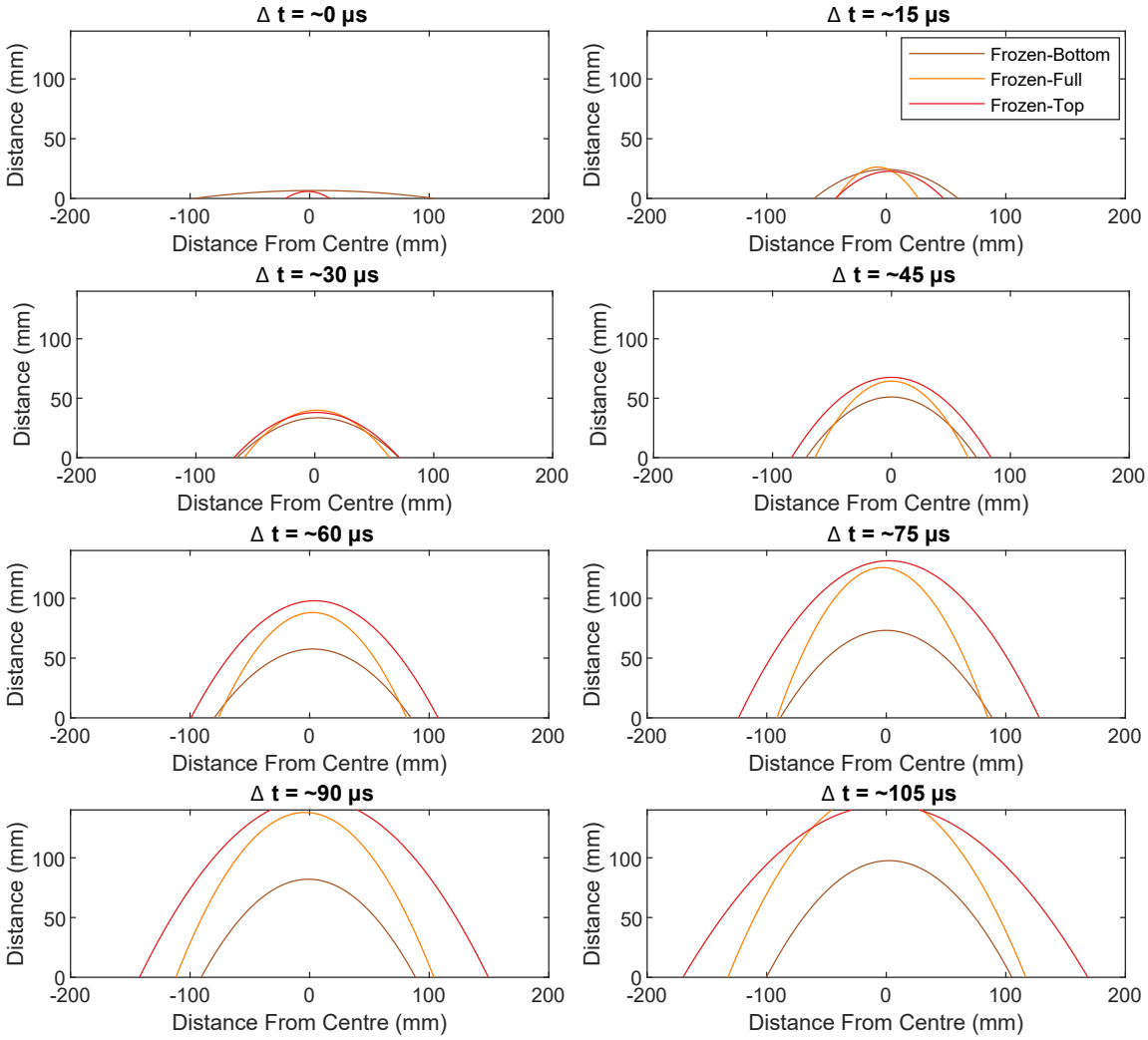

Figure 6.24: Output from the high speed video tracking of the shock wave for typical tests from the different frozen arrangements.

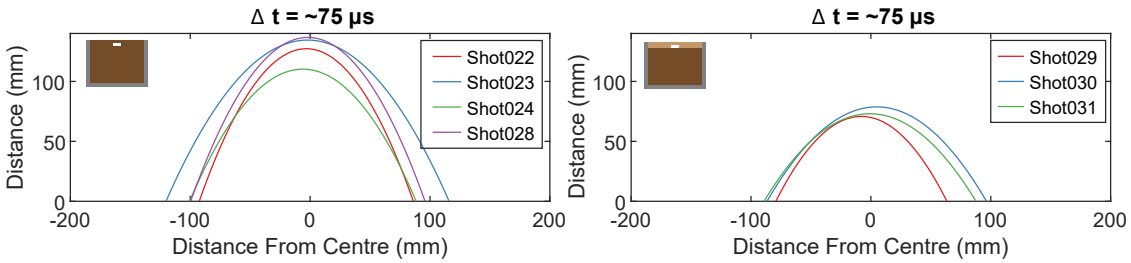

Figure 6.25: Single time-step output from the high speed video tracking of the shock wave. Both series of tests produce consistent shot to shot shock waves.

6.6.3 Ice

Figures 6.26 & 6.27 show the specific impulse distribution for the tests with ice and water respectively. The aggregated results are then compared to that of LB sand in Figure 6.29, which shows that the testing in ice resulted in a more centralised loading than the water testing, with the loading at larger radial distances tending towards that of LB. It is clear from these results, that the ice produces a different loading (both in terms of shape and magnitude) than water. As discussed above, a potential mechanism for this could be that of discrete particle strikes (as per Waddoups et al. (2023)). Figure 6.28 shows photos of the ice within the soil bin post test. It can be seen from the insert of Figure 6.28a that the ice is pulverised into approximately 10mm pieces post testing. This pulverisation was observed throughout the whole soil containers as seen in Figure 6.28b, which shows a hole dug to the base of the bin post test. This total pulverisation of the ice is in line with the findings of the preliminary testing discussed above. It was also observed that post testing the ice was dry and frozen with no evidence of melting.

Figure 6.30 shows the temporal evolution of the total impulse. As with the soils, testing with frozen material above the charge resulted in significant variability in the measured loading. In contrast, the two historic tests with water appear to show a higher level of consistency. The total impulse in the instrumented region is included in Figure 6.21 above, which shows that the total impulse from tests in ice are more comparable to those for LB than they are for tests with water.

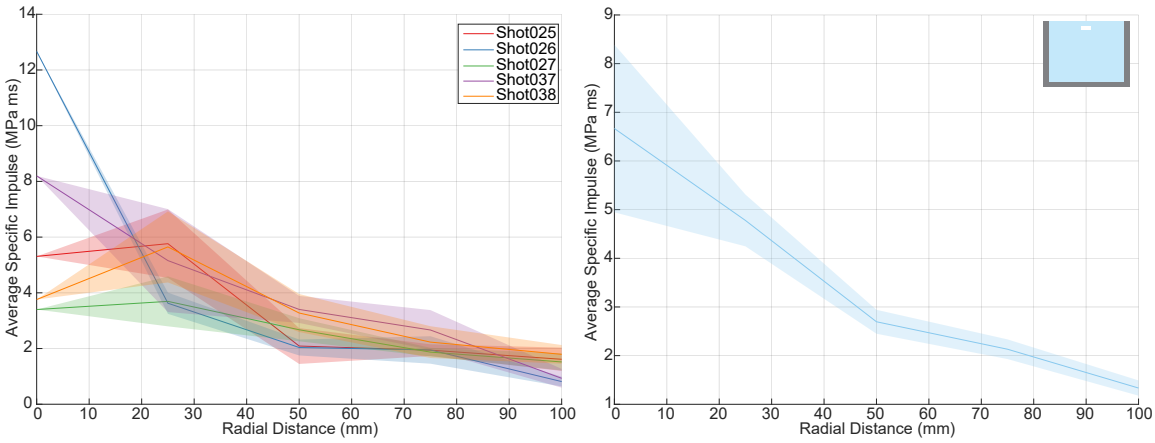

(a) Individual test data **(b)** Aggregated data across all tests

Figure 6.26: Average specific impulse as a function of radial distance for all the tests with ice.

The test to test variability is also present in the high speed imagery, as shown in Figure 6.31 where both the chaotic shape and shot to shot variability of the ice ejecta cloud is evident. Due to the water tests being historic data using different previous generations of high speed video equipment, the data is not of

sufficient quality to perform the ejecta tracking and so comparisons cannot be made. However, Figure 6.30b shows the data from the two tests have similar, consistent results.

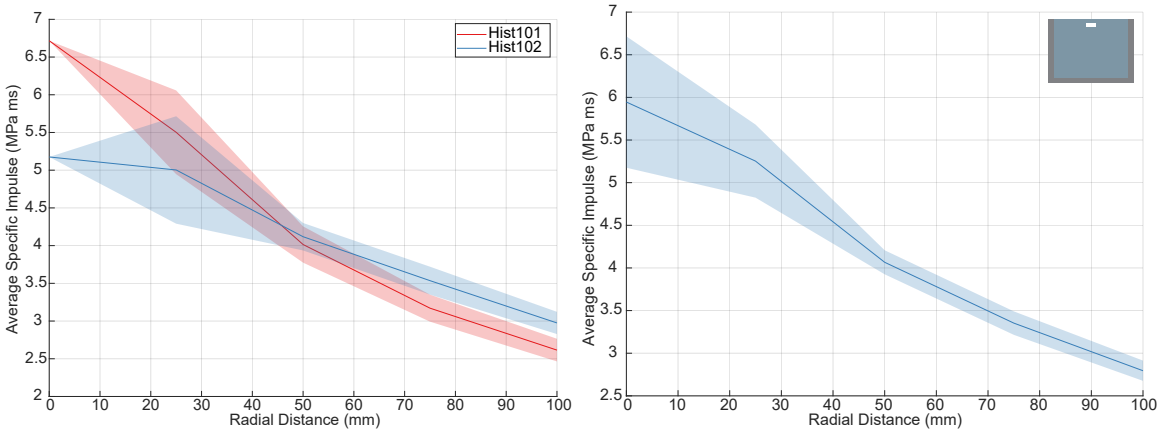

(a) Individual test data

(b) Aggregated data across all tests

Figure 6.27: Average specific impulse as a function of radial distance for the historic tests with water.

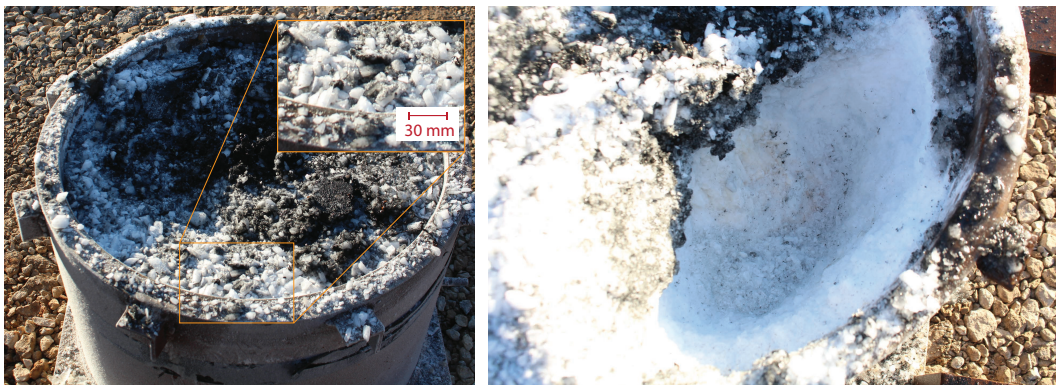

(a) Post test surface

(b) Post test with a hole excavated in the bin

Figure 6.28: Photos showing the soil container full of ice after Shot 025. It can be seen that the ice has fractured into pieces approximately 10 mm in size throughout the whole container to the base.

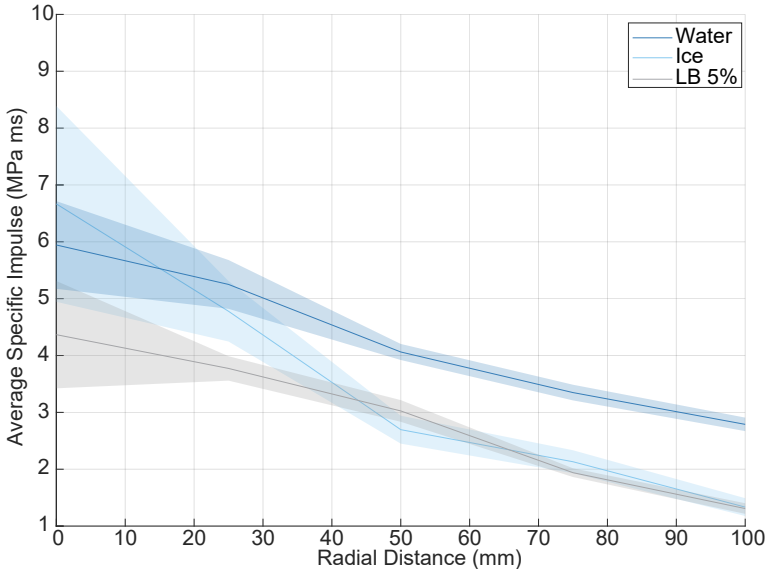

Figure 6.29: Average specific impulse distribution for the ice and water series compared to each other and the historic 5% LB data.

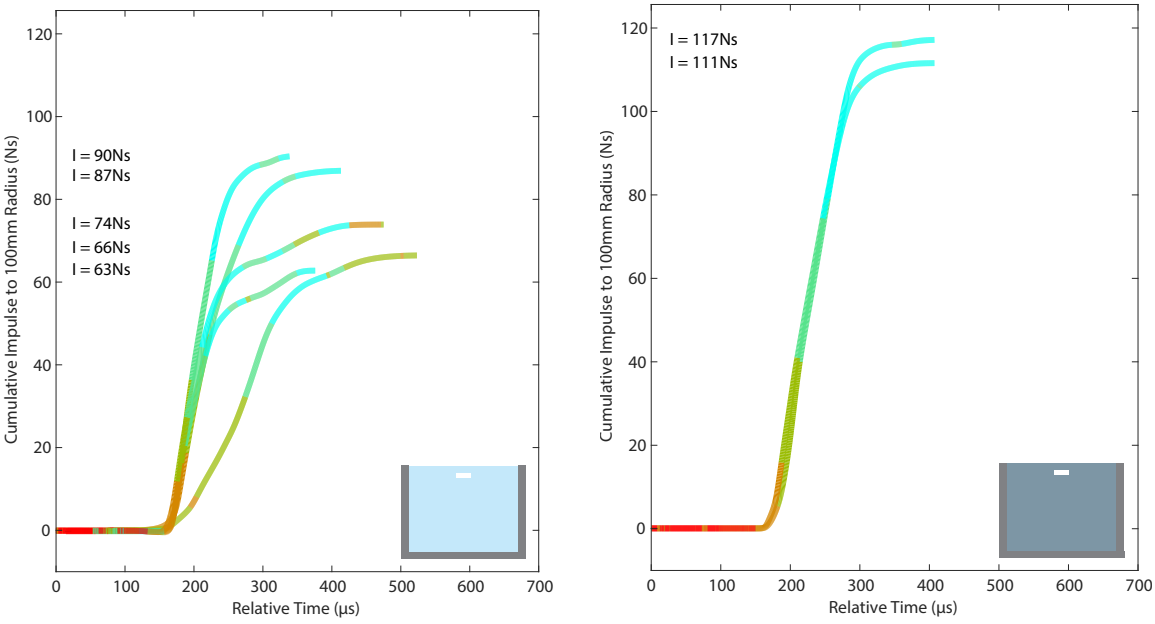

(a) Cumulative impulse as a function of time for the tests with ice

(b) Cumulative impulse as a function of time for the historic tests with water

Figure 6.30: Evolution of the cumulative impulse for the series considered; each plot shows the results for the repeat tests within the given series and demonstrates the repeatability of the data.

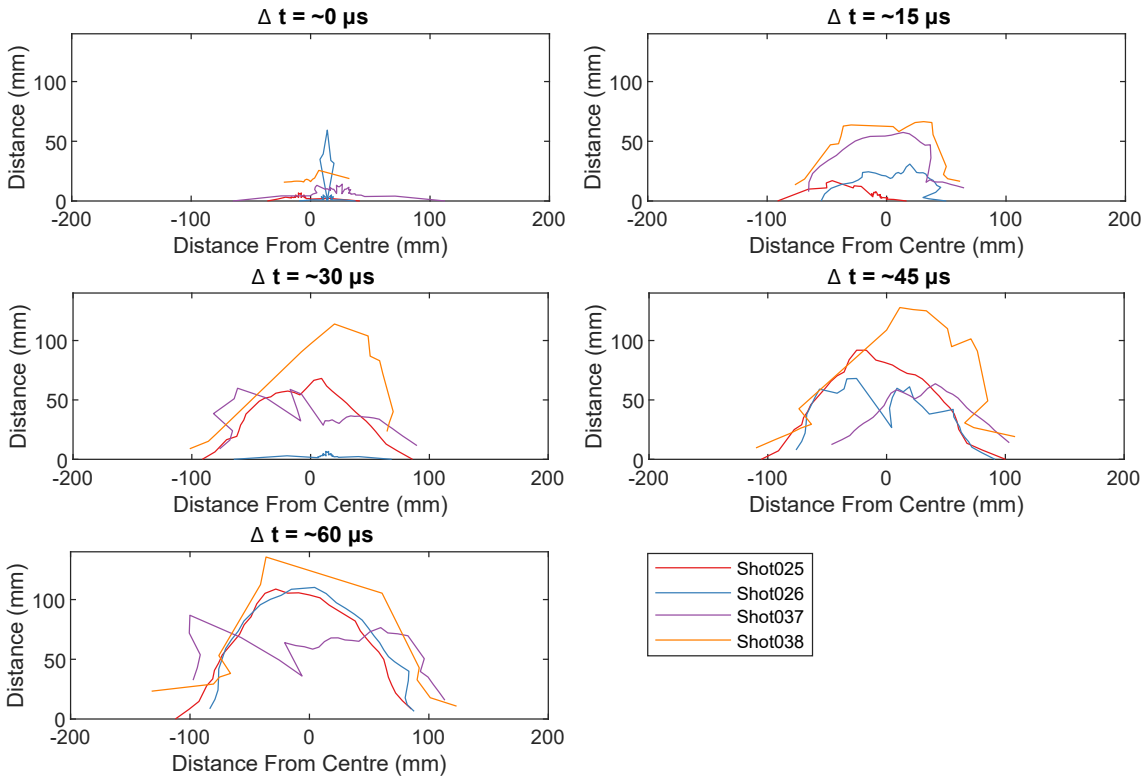

Figure 6.31: Output from the high speed video tracking of the ejecta cloud for tests with the ice, showing chaotic behaviour as with the sand.

6.7 Discussion

Tests with frozen soil surrounding the charge have shown a significant deviation from testing with unfrozen material. One potential explanation for this is to consider the effect of discrete particle strikes. Figure 6.32 shows how historic data with STANAG soil (which contains large gravel particles) compares with the frozen tests. The data for the tests with STANAG show little in common with the frozen tests, with both the shape and magnitude of the loading being dissimilar. The same is found when comparing the total impulse, as in Figure 6.33, where the total impulse is approximately double that recorded in the tests reported on in this work.

Also shown in Figure 6.32 for comparison is Series C of Clarke et al. (2020), which was where the material directly above the charge was removed, resulting in a partial burial condition. This series shows remarkable agreement with the frozen top series, however, it is difficult to determine a mechanism that could justify this. Had the frozen soil been prepared with a loose plug above the charge (as per Figure 6.7b), this could be explained as the material above the charge providing a lower resistance path for the detonation products and ejecta to preferentially expand. Another potential, but invalid, explanation could be the increased lateral confinement around the charge, but this effect should also be observed in the fully frozen test series and wasn't. In the absence of additional testing to validate this similarity, it is prudent to assume this is a coincidence and not a physical relation.

6.7.1 Hypothesis discussion

Hypothesis 1 (recap) — The ice within the frozen soil will absorb energy as it melts, acting as an energy sink and reducing the loading.

The data gathered does not support this hypothesis. Testing with frozen sand in a number of different configurations showed no decrease in loading when compared to tests with unfrozen sand. In two out of the three series (frozen full and frozen bottom) an increase in loading compared to the unfrozen sand was observed. Also, post testing the sand samples were found to be still frozen and dry further indicating the material had not been melted by the detonation products. Recent work that has yet to be published has shown that the timescales over which heat transfer effect the pressure from an explosive charge do not take effect until approximately 0.5 ms, which compares with the loading durations of this work which are of the order 0.1 ms. This work is a continuation of the experiments discussed in Farrimond et al. (2024b), and will be published in due course by the same authors.

Hypothesis 2 (recap) — Frozen soil has a higher shear strength and is less compressible than thawed soil, so will provide additional confinement to a buried charge, leading to an increased loading.

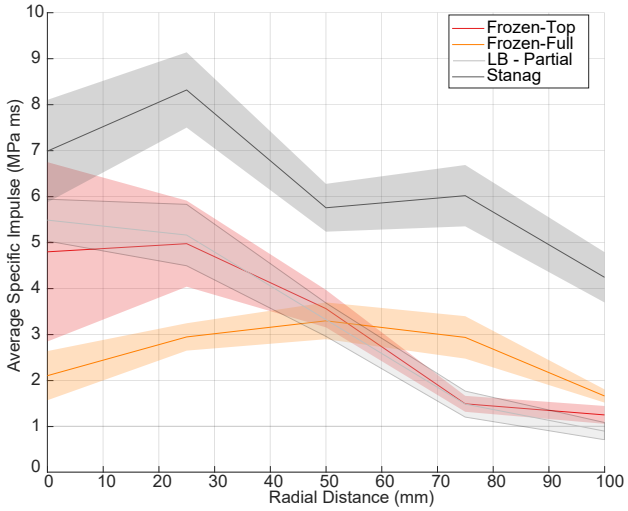

Figure 6.32: Average specific impulse distribution for each of the three frozen sand series compared to each other and to the historic 5% LB data.

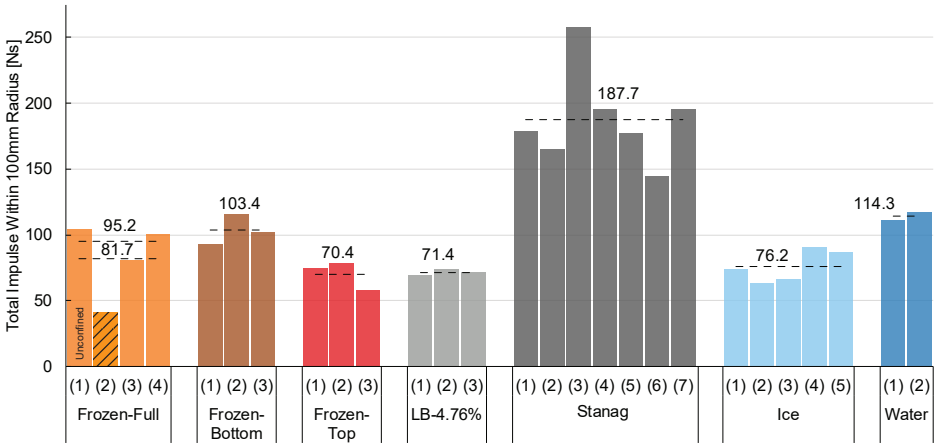

Figure 6.33: Total impulse comparisons to historic STANAG tests, showing significant differences in tests-to-test results, and also substantial differences compared to the new testing of this work.

The gathered data is inconclusive with respect to this hypothesis. The fully frozen and frozen base tests show an increase in loading compared to the baseline case of unfrozen LB sand. This is likely caused by the rigid reflecting surface below the charge, in contrast to the findings of Clarke et al. (2020) who did not observe an effect on the loading due to changes in back tamping. The work of Curry and Langdon (2021) also showed a significant increase in the impulse transferred (up to 5×increase) from a rigidly backed charge compared to a free air one. So the results of the discrepancy between the results of the current work and those of Clarke et al. (2020) require further investigations. This apparent discrepancy may be explained by the difference in strength between the frozen soil back tamping and the unfrozen soil back tamping, with the frozen soil closer to the solid steel backing used by Curry and Langdon (2021).

Regarding the lateral confinement, it can be concluded that the frozen soil did not result in additional loading due to the lateral confinement as, were this the case, an increased loading would be evident in both the fully frozen and frozen top test series, but not the frozen bottom series.

6.7.2 Conclusions

- Techniques for preparation and testing of charges buried in frozen material have been developed and implemented.
- Testing on charges buried in frozen soils and ice have shown the loading profile to be significantly more variable than equivalent testing of unfrozen samples.
- Frozen soils and ice do not undergo melting/vaporisation over the timescales of detonation.
- Frozen soils and ice do not form clumps when exposed to explosive events on the scales examined.

Chapter 7

Littoral Zone

This chapter aims to understand the effect of non uniformities within the soil due to variations in the water table, within and above the soil surface. This was achieved by compacting the soil samples to the same dry density then adjusting the position of the water table by saturating the samples from the base, utilising an external standpipe to indicate the water level achieved.

Littoral Hypothesis 1 — The degree of back tamping (i.e. the density/rigidity of the underlying material) below a buried charge will not affect the measured output.

Littoral Hypothesis 2 — Increasing the water table to saturate the soil above the level of the charge will increase the measured loading.

Littoral Hypothesis 3 — Water above the soil surface will significantly increase the loading for the same soil surface to target distance.

The above three hypotheses outline what is expected to be found in this testing series. Hypothesis 1 is based on the findings of Clarke et al. (2020) who observed that a charge back-tamped with soil (series B of Clarke et al. (2020)) produced the same output as that of a charge suspended in air (series A of Clarke et al. (2020)). Extending this logic, it is hypothesised that testing with a discontinuity in the soil,, with the soil saturated to be level with the base of the charge and 'dry' above, will produce the same loading as a charge buried entirely in dry soil. This hypothesis is in contradiction to the findings of the previous chapter of this work, which found that frozen soil below the charge yielded an increased impulse measurement. Therefore expanding the testing to cover another scenario where there is a discontinuity in material properties (density, stiffness etc.) above and below will allow the finding's of Clarke et al. (2020) to be further examined.

Hypothesis 2 aims to explore this further, by saturating the material below and around the charge, but not the material above. It is hypothesised that this will produce an increase in loading compared to the dry case, but lower than the fully saturated case.

Finally, hypothesis 3 aims to verify that having water above the surface of the soil, for example as encountered when a vehicle is fording a river, increases the loading due to a buried charge. This is anticipated to be the case as the

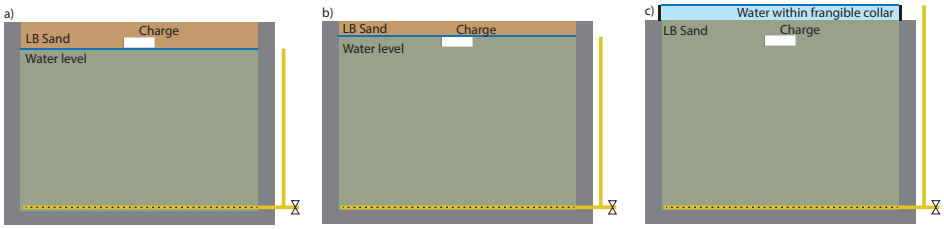

Figure 7.1: Diagrams showing the different test arrangements: a) saturated sand up to the base of the charge; b) saturated sand up to to the top of the charge; and c)fFully saturated sand with standing water on the surface.

incompressible water will, in effect, replace some of the compressible air between the soil surface and target. This, along with the increased mass of the water should lead to a significant increase in the loading measured.

7.1 Methodology

For these tests, the methodology of Clarke et al. (2014) was modified. As shown in Figure 3.4 on page 52, a buried perforated hose placed in the bottom of the sand bins allowed the bins to saturate from the base up at a low flow rate. For this testing a similar approach was used, however, in addition to the buried hose, an extra hose was added to the outside of the soil bin that could be used to set the height of water within the soil. Physically, this has the same effect as placing a hole in the side of the soil bin at the required height, hence allowing the water level to be set during the test instead of in advance. Therefore, all the soil bins could be prepared equally with the final water height determined at the time of testing. Figure 7.1 shows diagrams of the three water levels tested in this section, a) with the water level with the base of the charge, b) level with the top of the charge and c) 35 mm above the surface of the soil. Figure 7.2 shows pre-test photos with the water level set to different heights via the tube on the outside of the bin; on the left the water level is at the base of the charge, and on the right the water is above the surface of the soil contained within a frangible plastic collar.

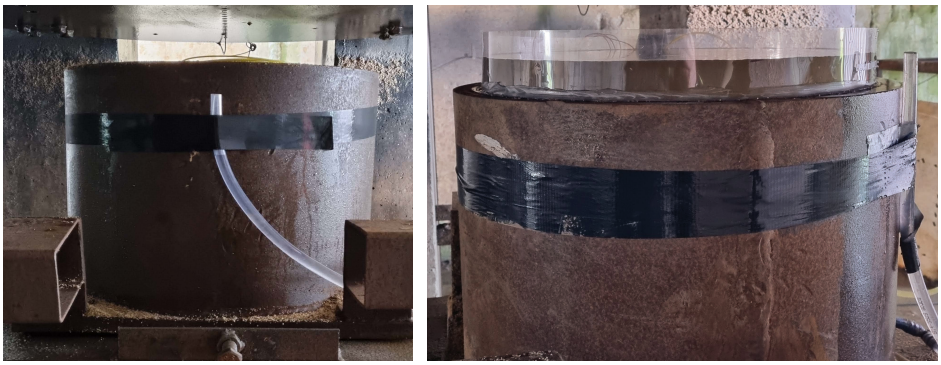

Figure 7.2: Photos showing the soil containers prior to testing for two of the test series. Left shows the water level with the base of the charge, and right shows the test series with 35 mm of standing water on the soil surface. In both images, the clear tube used to set the water level is visible, attached to the side of the soil bin.

7.2 Results

Table 7.1 outlines the data generated and analysed for this section, including the historical data from Clarke et al. (2020) that has been re-analysed to make comparisons with the new data. Figures 7.3a, 7.4a & 7.5a show the specific impulse distribution for the three test series with the water above the soil surface, level with the top of the charge and level with the base of the charge respectively. The results show that each of the test series has a similar degree of consistency, as shown by the similar width of the traces on the aggregated plots. It is also evident from Figure 7.8, which plots the aggregated data for each series, that increasing the water table within the soil increases the loading.

Figure 7.9 plots the total impulse for each series, and Figures 7.10 & 7.11 show the temporal evolution of the impulse. Figures 7.10 shows that for the newly gathered data, there is good consistency in the early stages of the loading for each series, with the gradients of the charts matching closely. However, there loading profile for both the top saturated (Figure 7.10b) and (Figure 7.10c) shows inconsistencies around 300 ms. In contrast, both the tests with water above the charge ((Figure 7.10a) and historic data (Figure 7.11) shows good test to test repeatability. It can also be seen that in both of the tests with saturated sand above the charge ((Figures 7.10a & 7.10a), the loading is over a longer period than the others tests considered here.

Table 7.1: Table outlining the data generated and analysed for this section.

Shot name	**Series name**	**Soil type**	**Bulk density**† **(Mg/m^3)**	**Moisture content**†	**Saturation conditions**
Shot003	Base	LB	1.622	2.50%	Soil saturated to the base of the charge
Shot004			1.634	2.50%	
Shot005			1.574	2.68%	
Shot009	Top	LB	1.566	2.55%	Soil saturated to the top of the charge
Shot010			1.558	2.56%	
Shot011			1.558	2.59%	
Shot012			1.576	2.49%	
Shot006	Above	LB	1.609	2.62%	35 mm of water above the surface of the soil
Shot007			1.565	2.51%	
Shot008			1.561	2.50%	
Hist041‡	LB saturated	LB	1.67	Saturated	Fully saturated
Hist042‡					
Hist043‡					
Hist044‡					
Hist045‡					
Hist087‡	LB 2.5%	LB	1.635	2.45%	Uniform moisture content
Hist089‡					
Hist090‡					
Hist096‡					

†Bulk density and moisture content is taken prior to saturation.

‡Clarke et al. (2020) data has been re-analysed and processed for this work.

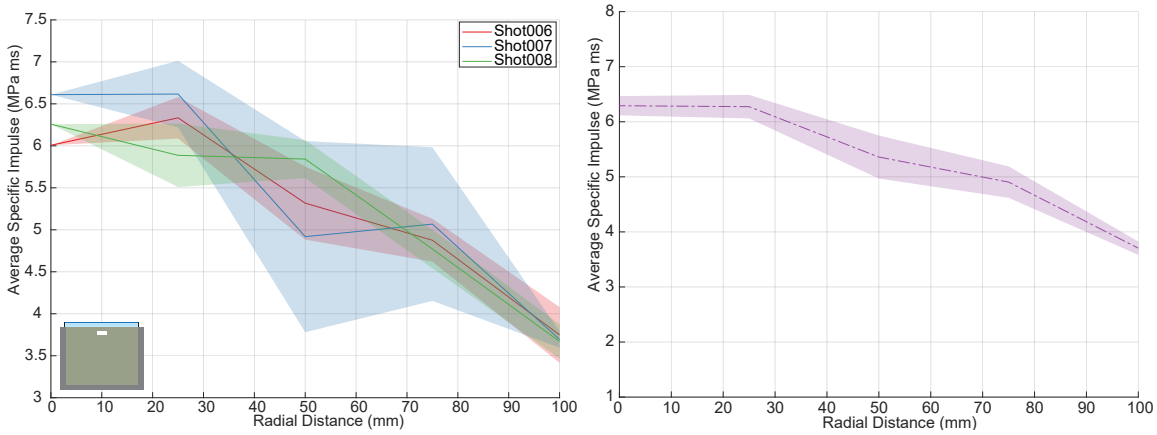

(a) Individual test data **(b)** Aggregated data across all tests

Figure 7.3: Specific impulse as a function of radial distance for the three tests with water 35 mm above the soil surface.

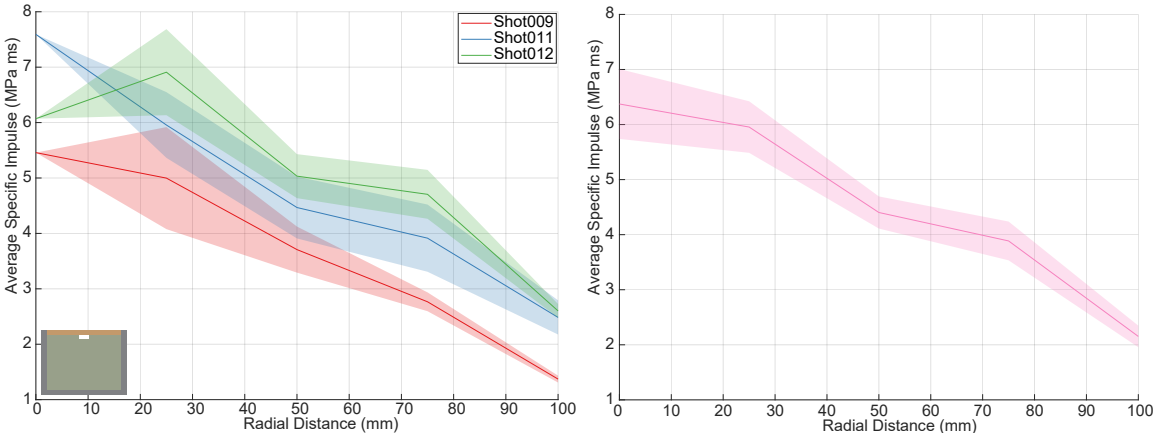

(a) Individual test data **(b)** Aggregated data across all tests

Figure 7.4: Specific impulse as a function of radial distance for the three tests with water at the top of the charge.

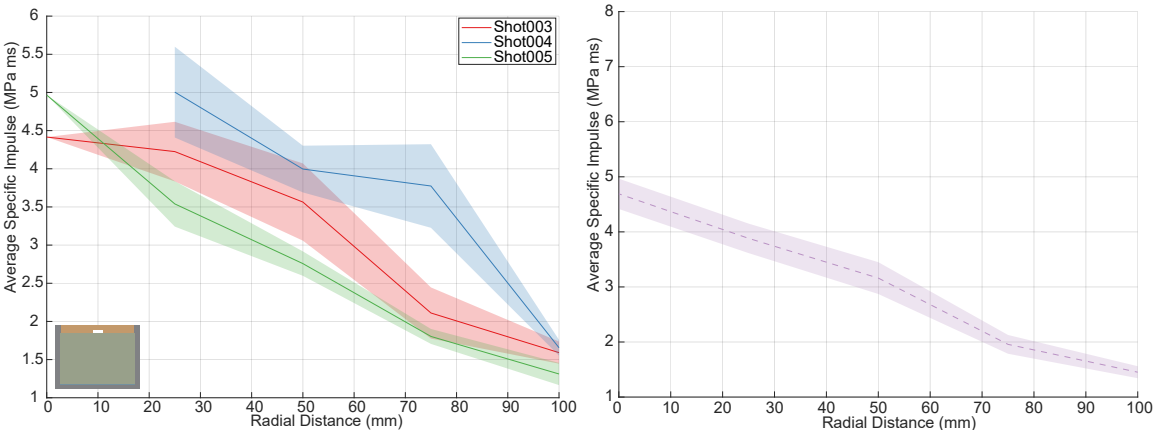

(a) Individual test data **(b)** Aggregated data across all tests

Figure 7.5: Specific impulse as a function of radial distance for the three tests with water at the base of the charge. Note for Shot004 there was no R=0 data captured due to an equipment failure.

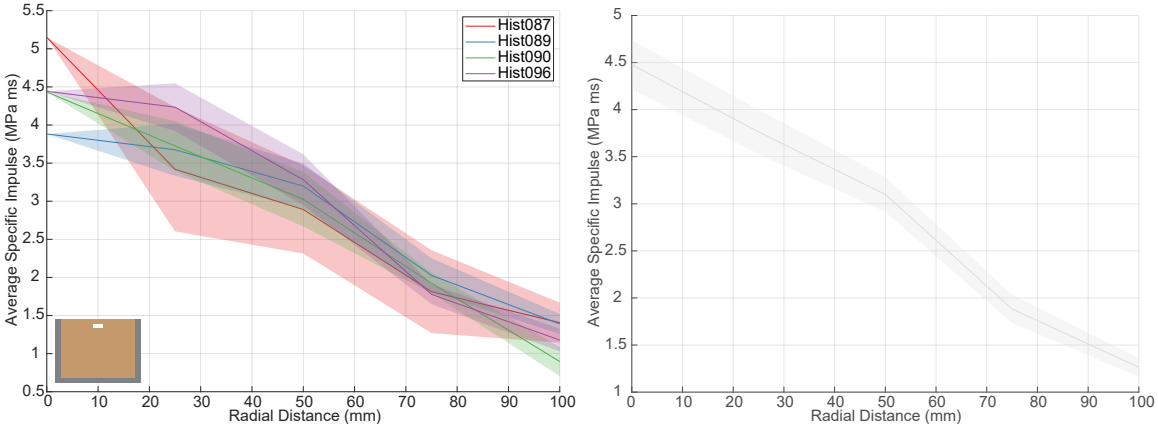

(a) Individual test data **(b)** Aggregated data across all tests

Figure 7.6: Specific impulse as a function of radial distance for the historic tests with LB at 2.5% moisture content.

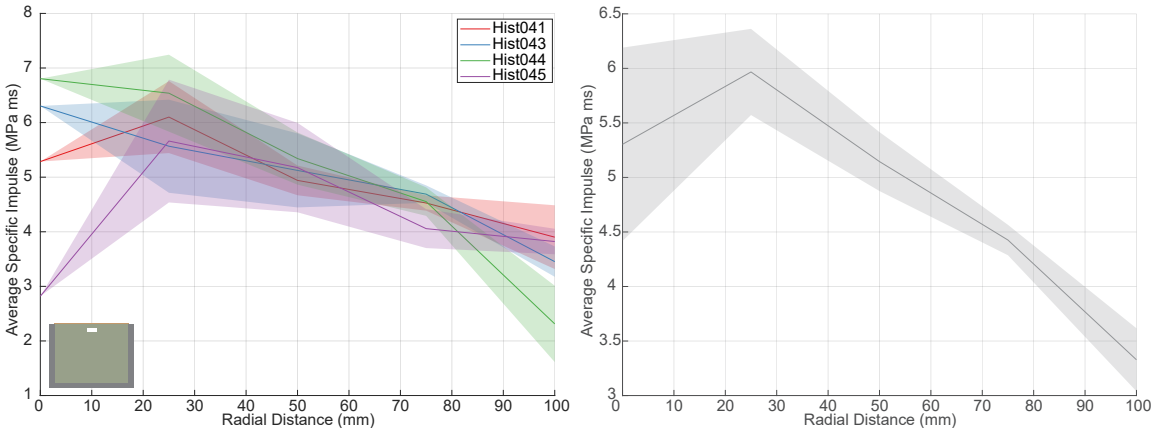

(a) Individual test data

(b) Aggregated data across all tests

Figure 7.7: Specific impulse as a function of radial distance for historic tests with saturated LB.

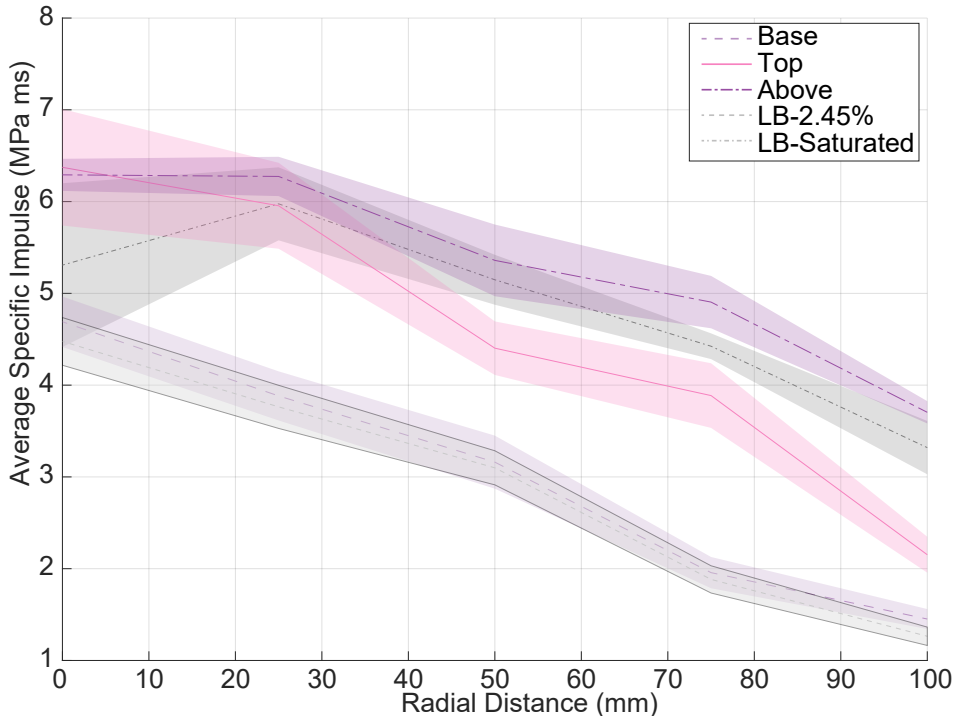

Figure 7.8: Plots showing the average specific impulse as a function of radial distance for the three series of tests conducted compared to the historic data.

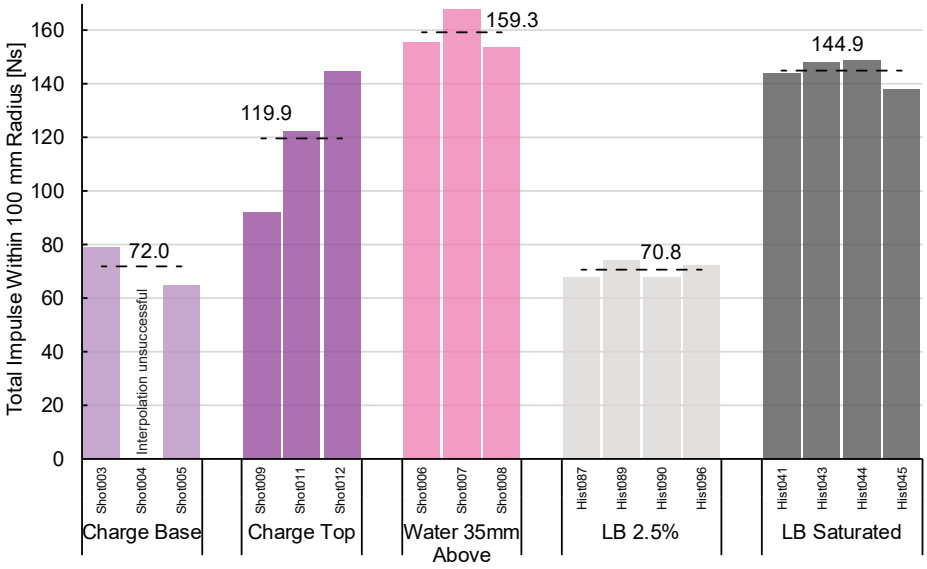

Figure 7.9: Plots showing the total impulse for the tests conducted.

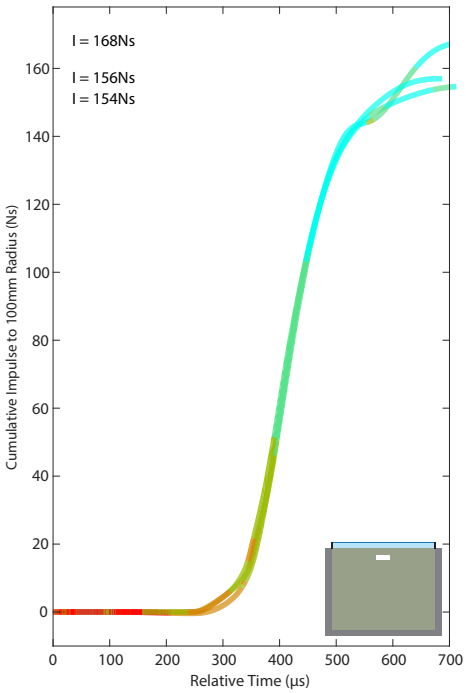

(a) Water 35 mm above surface of the soil

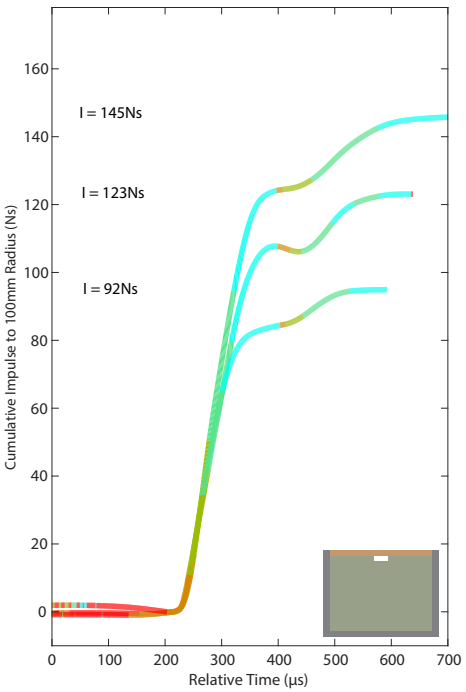

(b) Water level with the top of the charge

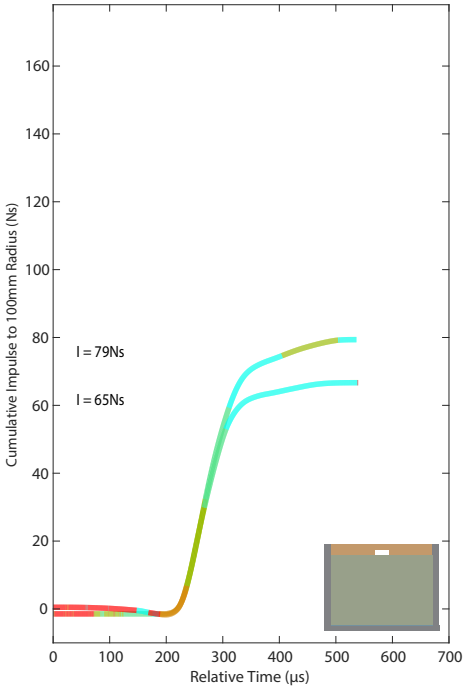

(c) Water level with the base of the charge

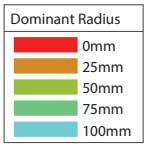

Figure 7.10: Evolution of the cumulative impulse for the four series considered; each plot shows the results for the repeat tests within the given series and demonstrates the repeatability of the data.

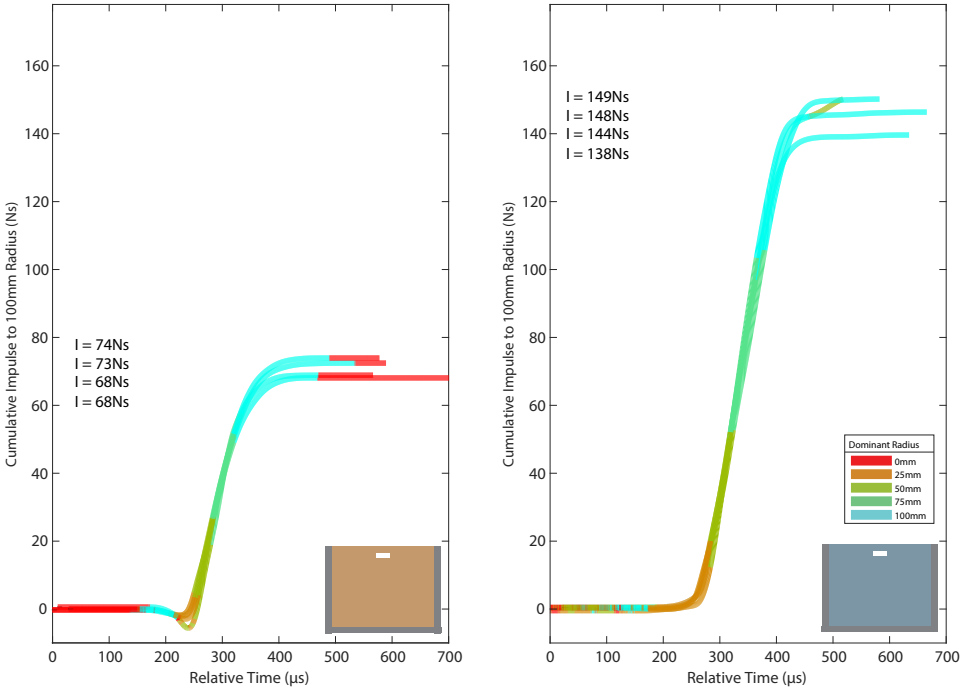

(a) Cumulative impulse as a function of time for historic tests with LB at 2.5% moisture content

(b) Cumulative impulse as a function of time for the historic tests with saturated LB

Figure 7.11: Evolution of the cumulative impulse for the four series considered; each plot shows the results for the repeat tests within the given series and demonstrates the repeatability of the data.

7.3 Discussion

Hypothesis 1 (recap)— The degree of back tamping of a charge within a buried charge will not affect the output.

Figure 7.8 shows that the tests with the soil saturated to the base of the charge show a high level of agreement with the historic testing of LB sand at 2.5% moisture content. This is in agreement with the findings of Clarke et al. (2020), who found back tamping of a buried charged did not significantly affect the loading when compared with a free air charge. Therefore, it is to be expected that the case where the soil is saturated up to the base of the charge yields a similar output to tests with unsaturated soil. This finding is, however, in contrast with the results of the testing conducted for this work with frozen soils, as discussed in § 6.7.1, which found that back tamping with frozen material did affect the loading. The work of Curry and Langdon (2021) also showed a significant increase in the impulse transferred (up to 5×increase) from a rigidly backed charge compared to a free air one. The work Curry and Langdon (2021) was conducted at a scaled distance of $Z = 0.16[mkg^{-\frac{1}{3}}]$ whereas the work of Clarke et al. (2020) and the current work is at a scaled distance of $Z = 0.33[mkg^{-\frac{1}{3}}]$. Therefore, additional work back tamping the charge with a stiff material is an area where further study is required as results from different tests are not in agreement.

Hypothesis 2 (recap)— Increasing the water table to partially saturate the soil to the level of the top of the charge will increase the measured loading.

Figure 7.9 shows that saturation of the soil up to the top surface of the charge resulted in an average 70% increase in the total impulse compared to LB at 2.5% moisture content. Compared to fully saturated LB, the loading for the top of the charge tests is 17% lower. This result is in line with expectations that the top saturated case will produce an output between the 'dry' and fully saturated cases. Figure 7.8 shows there is more variability in the loading with the top saturated case compared to the fully saturated case and a more varied radial load distribution.

Hypothesis 3 (recap)— Water above the soil surface will significantly increase the loading for the same soil to target distance.

Figure 7.10a shows that the tests conducted with water above the surface of the soil showed a good degree of consistency in the interpolated loading, which is in agreement with the consistency of the specific impulse profiles in Figure 7.3a. As expected, when compared to historic testing, the loading in the case with water above the surface of the charge is higher than the case where the soil is fully saturated but with no free water on the surface. The addition of 35 mm of water above the charge, occupying 25% of the space between the soil surface and the target plate, resulted in an approximately 10% increase in the measured total impulse. In the simplified model used for the analysis in

§ 2.5.4, Figure 2.28 shows that for a fixed stand-off distance, the total impulse as a function of the air gap is non-linear. Therefore, additional testing would be required to understand at what rate the loading continues to increase as the water level rises. It would be expected that if the air gap were replaced entirely with water, then the loading transferred would be significantly higher as this would constitute an underwater explosion not a buried charge explosion, and is beyond the scope of this work.

7.3.1 Conclusions

- Techniques for preparation and testing of charges with a varying water table have been developed and implemented.
- Testing on charges buried in soils with different water tables have shown:
  - The level of the water table in a soil sample can impact on the above surface impulse from a buried charge.
  - No increase was measured when the water table was level with the base of the charge, therefore, it can be said the effect is only observed when the water level is at least as high as the charge.
- Testing on charges buried in soils with water above the surface of the soil (reducing the air gap) significantly increases the transferred impulse.

Chapter 8

Carbonate Sand

This chapter investigates the effect burying a charge in carbonate sand has on the explosive output generated. This was done with the aim of investigating the effect of particle mineralogy on the loading but utilising a soil with similar particle sizes but different mineral composition and particle morphology.

Carbonate Hypothesis— Energy lost to soil particle breakage during the detonation of a shallow buried charge will reduce the energy available to be imparted on a target, resulting in a lower overall loading.

8.1 Methodology

As discussed in § 3.2.2, to investigate the effect of soil particle morphology and mineralogy, carbonate sand was chosen as it is predominantly made up of plate-like particles, in stark contrast to the more spherical quartz-based sands tested previously by Clarke et al. (2015a), Rigby et al. (2015), Clarke et al. (2016b) and Clarke et al. (2020). To recap, for this study we define carbonate sand as having greater than 50% calcium carbonate content. Soils with less than 50% calcium carbonate are known as calcareous soils.

8.1.1 Soil details

Figure 8.1 shows electron microscopy and Figure 8.2 colour photography of both the carbonate and quartz sands used in this work at different levels of magnification. The difference in particle shape is clearly visible between the two soils. This is in agreement with the work of Bowman et al. (2001) discussed in § 3.2.2 and summarised in Figure 3.9, where the carbonate-based sand was shown to be more angular, elongated, and more asymmetric than the generally rounded quartz sand whilst maintaining a comparable level of variability of shape and size.

Previous work by Clarke et al. (2017) involved testing on three sizes of quartz-based Leighton Buzzard sand. The three sizes used were fraction B (range

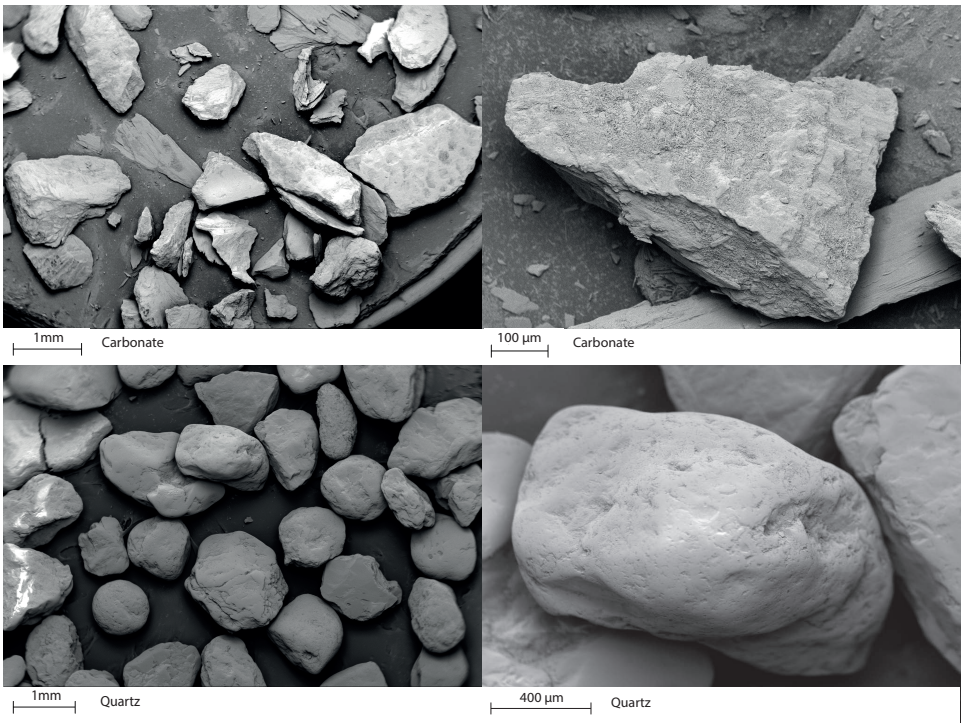

Figure 8.1: Electron microscope images of the two types of sand tested. The left hand images show the difference in particle shapes and the right hand images show the difference in surface texture of the particles.

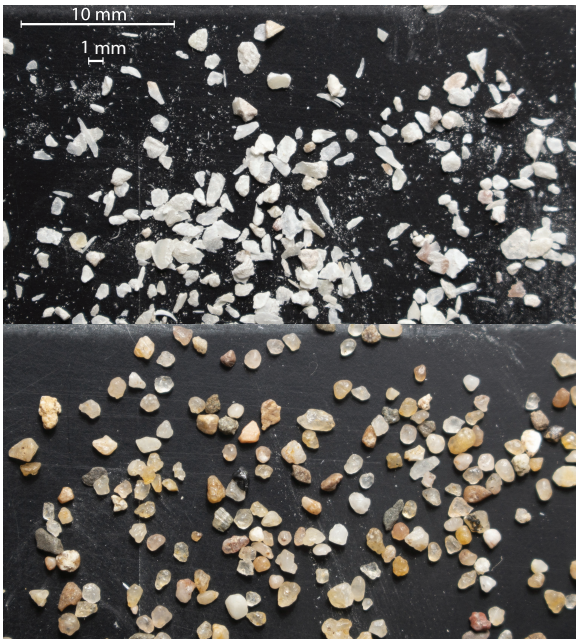

Figure 8.2: Colour photography of the sand samples; top) carbonate sand and bottom) quartz sand.

0.6–1.18 mm, D_{50}=0.87 mm) referred to in this work as LB, 2LB (range 1.18–2.8 mm, D_{50}=1.76 mm) which is approximately double the size of fraction B, and LBF (range 0.2–2.8 mm, D_{50}=1.27 mm) which had a wider range of particle sizes overlapping LB and 2LB. Clarke et al. (2017) found that small changes of particle size between LB and 2LB did not result in differences in total impulse, therefore any changes in loading observed in the current work with sand of similar size can be attributed to other factors.

Due to the large quantities of sand required for blast testing, a sustainable source of sand of the correct particle size distribution (and mineralogy) was required. The material used was aquarium sand manufactured from sea washed shells (calcium carbonate) produced by Tropical Marine Centre. Tropical Marine Centre's 'EcoSand Fine' was found to be the most suitable as it has a particle size distribution between fractions of Leighton Buzzard sand used in previous testing that were shown to have a no notable effect on impulse Clarke et al. (2017). The particle size distribution for the carbonate sand used was measured (D_{50}=0.87 mm), and is presented in Figure 8.3 alongside LB and that for a widely studied natural carbonate sand from Dog's Bay, Ireland (White 2003). The particle size distribution of the carbonate sand shows there is a higher amount of fine sand than in LB, but less than in LBF. This is also observable in Figure 8.2, where additional fines are visible against the black background. Hence, based on particle size distribution alone there would not be any expected variation between testing conducted with the carbonate sand or LB.

The bulk density of the carbonate sand was measured to be 1.27 Mg/m^3 (w=5%), which is considerably lower than the density of 1.67 Mg/m^3 (w=5%) measured for LB. It is well known the intraparticle voids play a large role in the reduced bulk densities seen in carbonate sands, leading to an expected range of 1.15–1.5 Mg/m^3 (Golightly 1988). The minimum and maximum measured densities were 1.04 and 1.31 Mg/m^3 respectively, giving a relative density, D_r=85%. Relative density is defined in Equation 8.1 (as per (Hatanakai and Feng 2006)), and gives a measure of the degree of compaction of a soil sample. The specific gravity for carbonate was measured to be 2.73, being slightly higher than for LB. The properties for both sands are tabulated in Table 8.1.

$$D_r = \frac{\rho_{\text{max}}(\rho_{\text{bulk}} - \rho_{\text{min}})}{\rho_{\text{bulk}}(\rho_{\text{max}} - \rho_{\text{min}})} \tag{8.1}$$

8.1.2 Sample preparation

The process for sample preparation is as discussed in § 3.1.3. The degree of compaction for the carbonate sands was determined to be the highest level of compaction that could be repeatably achieved when applying the same process as used for the LB sand.

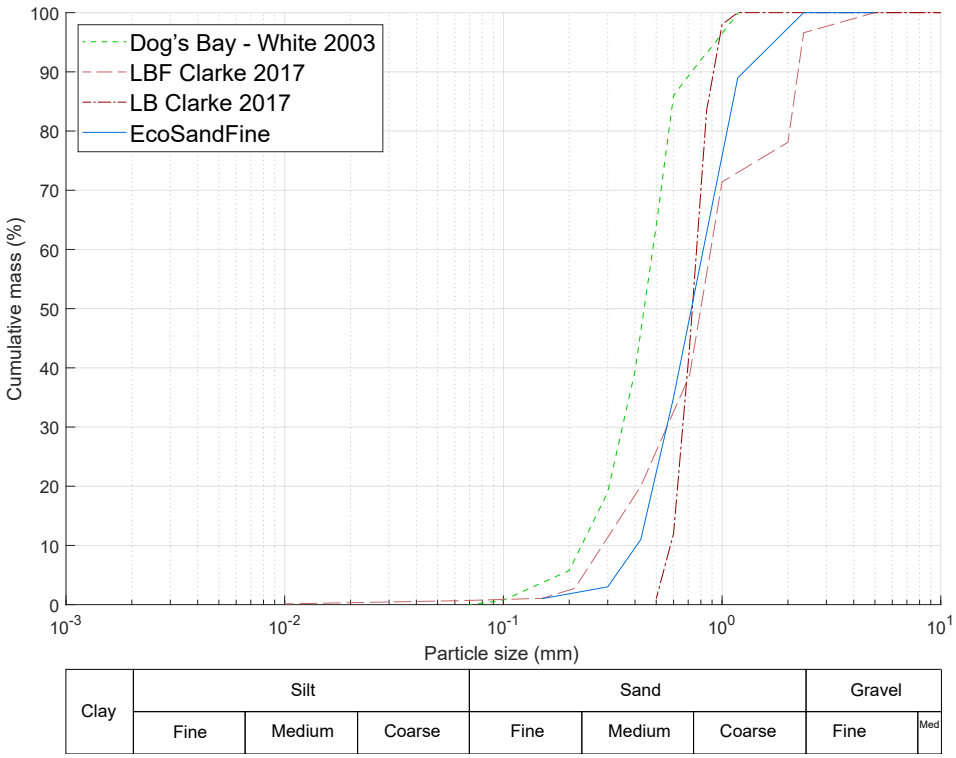

Figure 8.3: Particle size distribution for the carbonate sand used for this work, compared to the quartz sands of Clarke et al. (2017) and carbonate sand of White (2003).

Table 8.1: Table summarising the properties of the carbonate sand and LB.

Property	**LB**	**Carbonate**	
Bulk density	1.67	1.27	Mg/m^3
Minimum density	1.48	1.04	Mg/m^3
Maximum density	1.74	1.31	Mg/m^3
Relative density	73	85	%
Specific gravity	2.65	2.73	

8.2 Impulse prediction

It has been shown in previous work that increasing bulk density leads to an increased measured impulse, but that moisture content had a greater effect in increasing impulse than the added mass alone would suggest (Clarke et al. (2015a)). As discussed in § 2.4, this led to the development of a modification factor, I_{mod}, to be applied to the output from the Westine model to determine the loading from a buried charge by (Clarke et al. 2017). Equation 2.7 is repeated below for ease of discussion (Equation 8.2) and gives the factor I_{mod}, which determines the impulse relative to a baseline condition of dry (w=0%) quartz sand at a bulk density of 1.6 Mg/m^3. In the previous work, a lower bound on bulk density of 1.23 Mg/m^3 was deemed acceptable due to the minimum densities achievable in quartz-based soils.

$$I_{mod} = 0.9 - 0.096w + 0.033\rho + 0.078w\rho \tag{8.2}$$

where w is the gravimetric moisture content (%) and ρ is the soil bulk density (Mg/m^3).

This model predicts that for two soils with the same moisture content and comparable particle size distribution to the baseline, the one with a higher bulk density will result in a larger loading. In addition, it predicts that for soils with a bulk density above 1.23 Mg/m^3, increasing the moisture content also increases the loading. Below this density, the empirical nature of the model means the outputs are non-physical.

Figure 8.4 shows the expected increase in loading compared to the baseline used in the Clarke et al. model. For the carbonate sand density achieved in the current work, testing at 2.5% moisture content with all other factors consistent, an 8.4% reduction in loading compared to dry quartz sand would be expected. Any variation in impulse measured from carbonate sands is likely caused by other geotechnical factors not included in the original I_{mod} formulation. This predicted reduction in impulse is purely a factor of the reduced bulk density, with additional reductions also anticipated due to particle breakage.

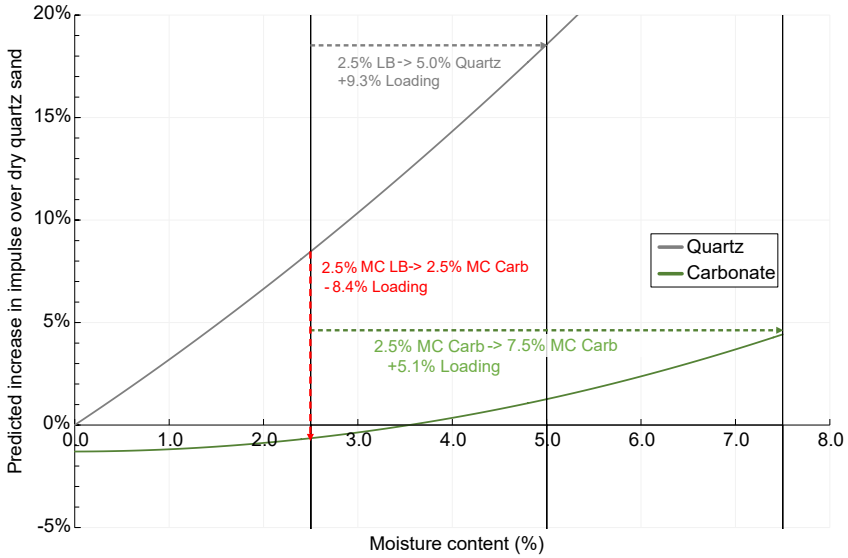

Figure 8.4: Plot showing the I_{mod} predicted increase in impulse for variations in moisture content and density.

8.3 Results

Table 8.2 summarises the new experiments performed and historic data analysed in this section. In total, nine tests were conducted on carbonate sands, yielding 153 pressure-time traces which were combined with data from seven historic tests (a further 102 traces).

8.3.1 Pressure data

As discussed in § 5.1.1, Figure 8.5 shows a typical pressure trace recorded from the Hopkinson pressure bars during these tests. Full pressure time histories for all of the current testing can can be found in Appendix A and have not been included in the main body of the thesis, instead the integrated results are discussed.

8.3.2 Particle breakage

To quantify the degree of particle breakage, samples from before and after testing were evaluated with a laser diffraction particle size analyser (Malvern Mastersizer 3000) to determine the particle size distribution (PSD). It was found that the small sample size (approx 5 g) required for the laser diffraction analysis was very sensitive to small quantities of dust and soot in the post-blast test samples. Therefore sieve analysis was conducted using larger samples (>100 g)

Table 8.2: Table outlining the data generated and analysed for this section.

Shot name	Series name	Soil type	Bulk density (Mg/m^3)	Moisture content	Burial conditions
Shot013	Carb 2.5%	Carbonate	1.290	2.15%	Carbonate sand at 2.5% moisture content
Shot015			1.247	2.39%	
Shot016			1.240	2.40%	
Shot014	Carb 5%	Carbonate	1.281	4.95%	Carbonate sand at 5% moisture content
Shot017			1.252	4.80%	
Shot018			1.263	4.80%	
Shot019	Carb 7.5%	Carbonate	1.335	7.50%	Carbonate sand at 7.5% moisture content
Shot020			1.285	7.49%	
Shot021			1.295	7.48%	
Hist087†	LB 2.5%	LB	1.635	2.45%	Fully buried
Hist089†					
Hist090†					
Hist096†					
Hist046†	LB 5%	LB	1.67	4.76%	Fully buried
Hist047†					
Hist049†					

†Clarke et al. (2020) data has been re-analysed and processed for this work.

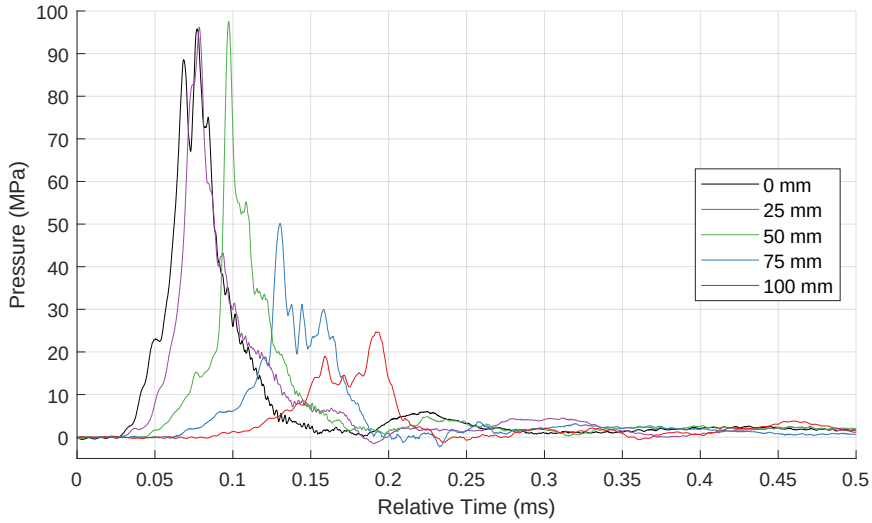

Figure 8.5: Pressure time history for a single array of five bars in Shot 014, Carb 5% (other traces excluded for clarity).

Table 8.3: Summary of particle size distribution parameters for both soil types before and after testing (all values in mm unless otherwise specified).

Sand	Pre			Post			B_t
	D_{10}	D_{50}	C_u	D_{10}	D_{50}	C_u	Total breakage
Quartz	0.686	0.970	1.494	0.440	0.938	2.264	7.3%
Carbonate	0.491	0.742	1.672	0.335	0.734	2.433	4.2%

to rule out any sampling errors. The results of the PSD analysis are presented in Figure 8.6, which shows qualitatively that there is a larger degree of particle breakage in the quartz sand than the carbonate sand. This is further apparent when comparing the D_{10}, D_{50}, C_u and B_t factors (summarised in Table 8.3) which are the sizes above which 10% and 50% of the measured diameters fall, the coefficient of uniformity, and the total breakage factor defined by Hardin (1985) respectively. The total breakage factor (B_t) represents the change in the integral of the particle size distribution curve, and attempts to quantify the overall degree of particle breakage in the sample:

$$B_t = \int_0^1 (b_{po} - b_{pl}) df \tag{8.3}$$

in which b_{po} = the original values of b_p; and b_{pl} = the values of b_p after loading. b_p is the potential for breakage of a particle of a given size, D, and may be represented by:

$$b_p = \log_{10}\left[\frac{D \text{ in mm}}{0.074 \text{ mm}}\right] \text{ for } D \geq 0.074 \text{ mm} \qquad \& \qquad b_p = 0 \text{ for } D < 0.074 \text{ mm} \tag{8.4}$$

The quartz sand samples consistently show a higher degree of breakage than the carbonate sand, however, the overall change is still small (e.g. a 3.3% reduction in the median particle size, and breakage factor of 7.4% for quartz sand). Figure 8.6 and Table 8.3 show that there is no substantial increase in particle breakage for the carbonate sand. In fact the results show a lower degree of breakage than in the quartz sand, contrary to previous findings of Coop et al. (2004). The lack of *substantial* difference in breakage of the carbonate sand would therefore predict that the loading follows the trend outlined in Figure 8.4 and Equation 2.7.

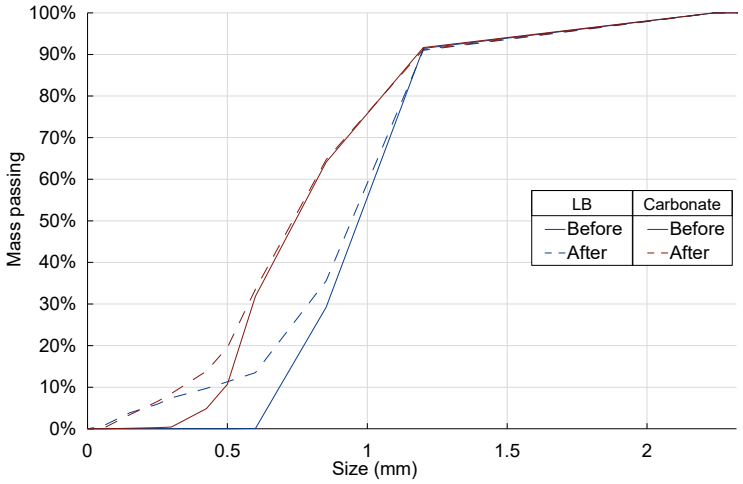

Figure 8.6: Particle size distribution of LB (quartz) and carbonate sand before and after blast testing using sieve analysis.

8.3.3 Specific impulse distribution

Figure 8.7 plots the average specific impulse for each test in each series as a function of radial distance. The shaded region indicates the standard error on the mean within a given test (based on the four measurements for each radius, and one for the central bar). It can be seen that there is good test to test consistency for measurements at radii of 25 mm and above. The variation in the loading at the central measurement point is to be expected, as there is a single measurement point that is highly sensitive to small variations in the charge position. Figures 8.7a, 8.7c and 8.7e show the effect of increasing moisture content on the pressure distributions. As expected, at low moisture contents there is no phenomenological difference in the distributions and the increase in total impulse (from the integrated signals discussed later) shows a minimal increase with increasing moisture content. Figures 8.7a and 8.7b show the specific impulse distributions for the carbonate and LB tests at the same moisture contents. LB historically has been identified as a soil which generated very repeatable loading Clarke et al. (2015a), especially in comparison with well-graded soils. The carbonate test results show a tighter spread on impulse distributions, thus making this an exceptionally repeatable test condition. The impact of this will be discussed later in the total impulse calculations.

Figure 8.8 plots the specific impulse as a function of radial distance, averaged across all measurement points in a given series (i.e. the average of the results from multiple measurement points in all the nominally identical tests shown in Figure 8.7). It can be seen in Figure 8.8a that as the moisture content of the carbonate sand increases, there is a small increase in the measured loading. This is in agreement with previous results of Clarke et al. (2020), who investigated the

effects of moisture content in quartz-based sands. Figures 8.8b and 8.8c show that both the magnitude and spatial distribution of the loading for carbonate and quartz sand is comparable, and again highlights the level of repeatability achievable with careful control over the soil preparation.

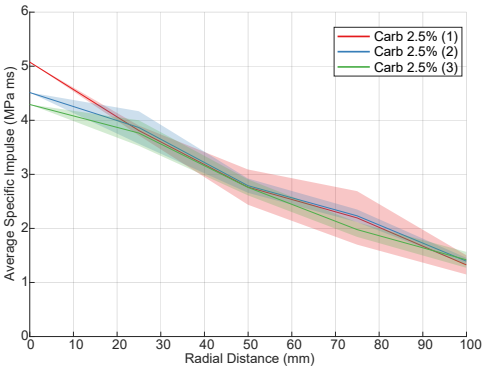

(a) Carbonate 2.5% moisture content

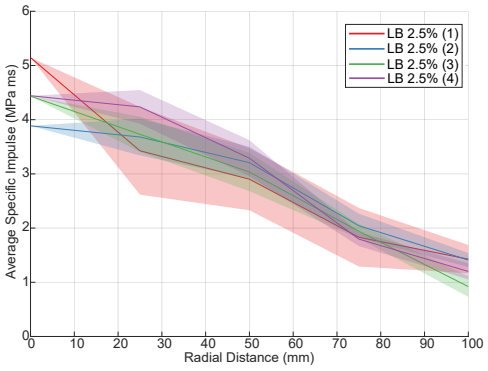

(b) Quartz 2.5% moisture content

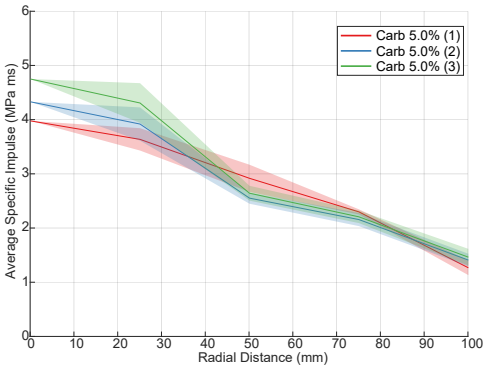

(c) Carbonate 5.0% moisture content

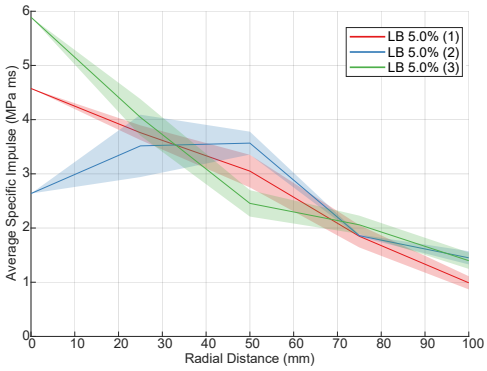

(d) Quartz 5.0% moisture content

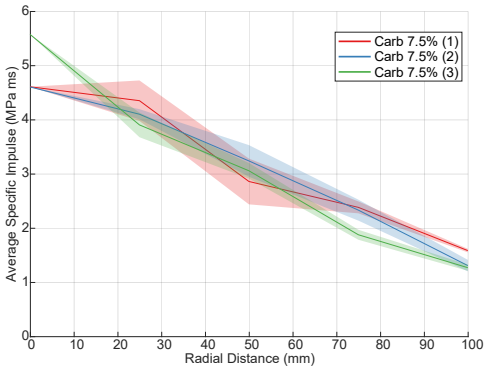

(e) Carbonate 7.5% moisture content

Figure 8.7: Specific impulse distribution for the five series considered; each plot shows the results for the repeat tests within the given series and demonstrates the repeatability of the data.

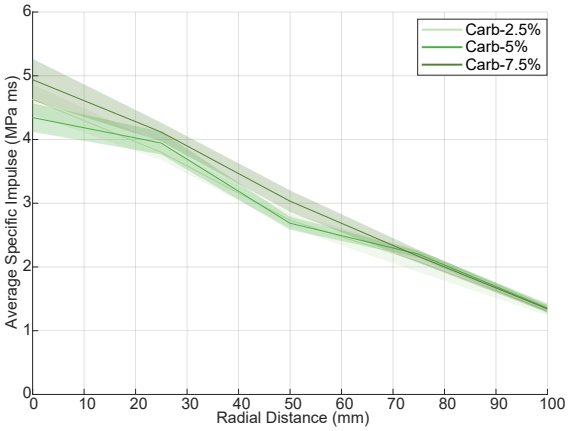

(a) Carbonate sand at 2.5%, 5.0% and 7.5% moisture content

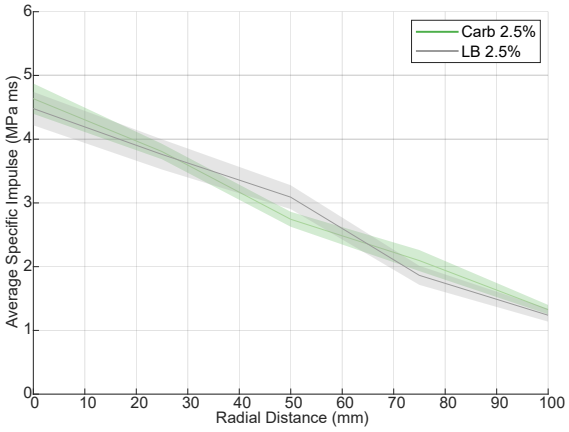

(b) Quartz and Carbonate sand at 2.5% moisture content

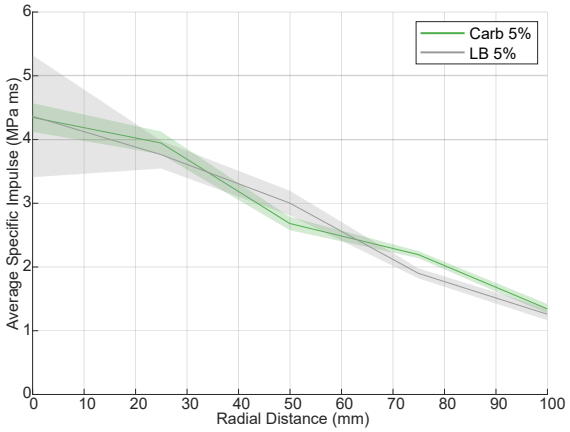

(c) Quartz and Carbonate sand at 5% moisture content

Figure 8.8: Average specific impulse distributions comparing the sand types at varying moisture contents.

8.3.4 Total impulse

As well as an absolute value of total impulse, the development of the total impulse with time can also be plotted allowing a deeper analysis of how the loading is delivered to the target, as shown in Figure 8.9. Each bar's contribution to the overall loading is coloured in the plots to show when the loading at a specific radius is dominant. As expected, the soil ejecta engages each set of bars from 0–100 mm in order. For the historic quartz tests (Figures 8.9b & 8.9d) there is very little contribution to impulse past 400 μs, in contrast with all of the carbonate plots which show a longer duration contribution lasting up to 700 μs. The time of arrival in the carbonate testing is also shorter than in the quartz tests, though this could also be a product of changes in the timing of

the breakwire when comparing the current work with the historical data. The maximum total impulse is also given in each sub figure for each test, which are collated into Figure 8.10.

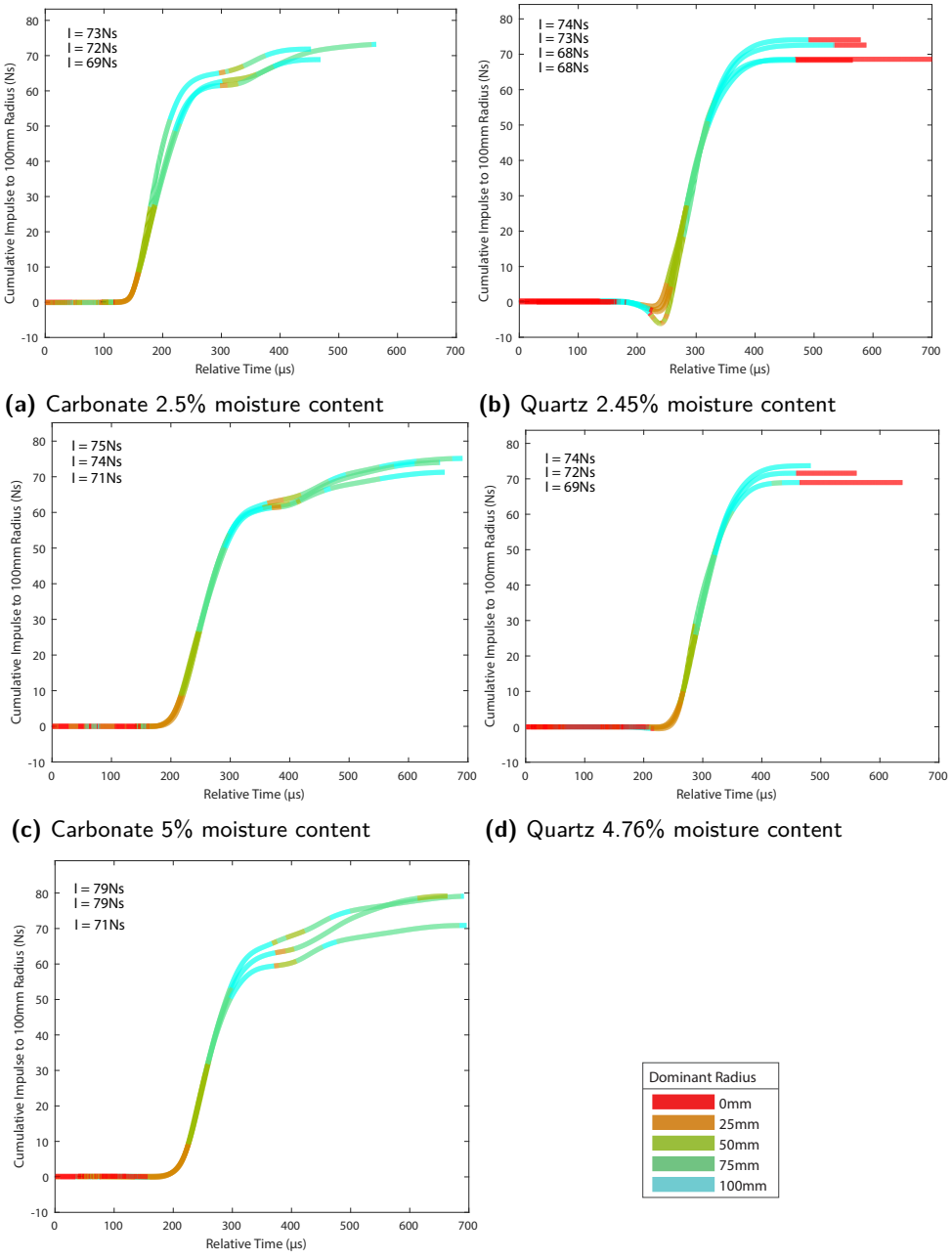

(a) Carbonate 2.5% moisture content

(b) Quartz 2.45% moisture content

(c) Carbonate 5% moisture content

(d) Quartz 4.76% moisture content

(e) Carbonate 7.5% moisture content

Figure 8.9: Evolution of the cumulative impulse for the five series considered; each plot shows the results for the repeat tests within the given series and demonstrates the repeatability of the data.

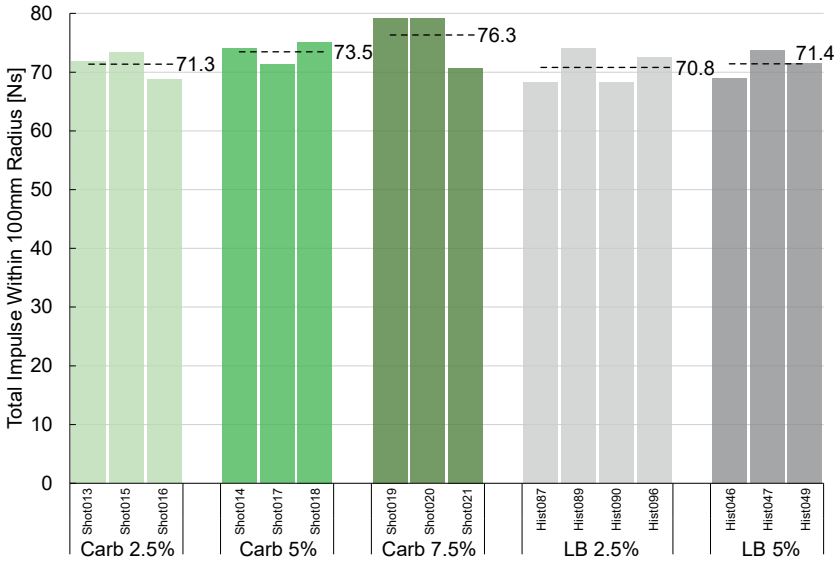

Figure 8.10: Total interpolated impulse within the 100 mm instrumented region for each test, with the average for each series overlaid as a dashed line.

Figure 8.10 shows the total interpolated impulse over the 100 mm radius instrumented region for each test, along with the average value for each series. It can be seen that as the moisture content of the carbonate sand increases, the total impulse increases (Figures 8.8a & 8.10), as is expected based on historic work Clarke et al. (2017). It can also be seen that the carbonate sands at all moisture contents result in a similar loading to the comparable quartz sand tests. This is contrary to what would be expected for a sand with lower bulk density, indicating that bulk density may be of a lower priority in governing blast events than previous models have predicted.

8.3.5 High speed video

Figures 8.11 and 8.12 show the shape of the ejecta cloud and shock wave respectively from two tests each of LB and carbonate sand. The form of the shockwave and ejecta cloud shape is similar for all four tests, with the most apparent difference being the increased speed of the shockwave and ejecta for the carbonate sand. This is to be expected from a kinetic energy point of view, with the lower density material travelling faster, and matches the time of arrival trends shown in Figure 8.9.

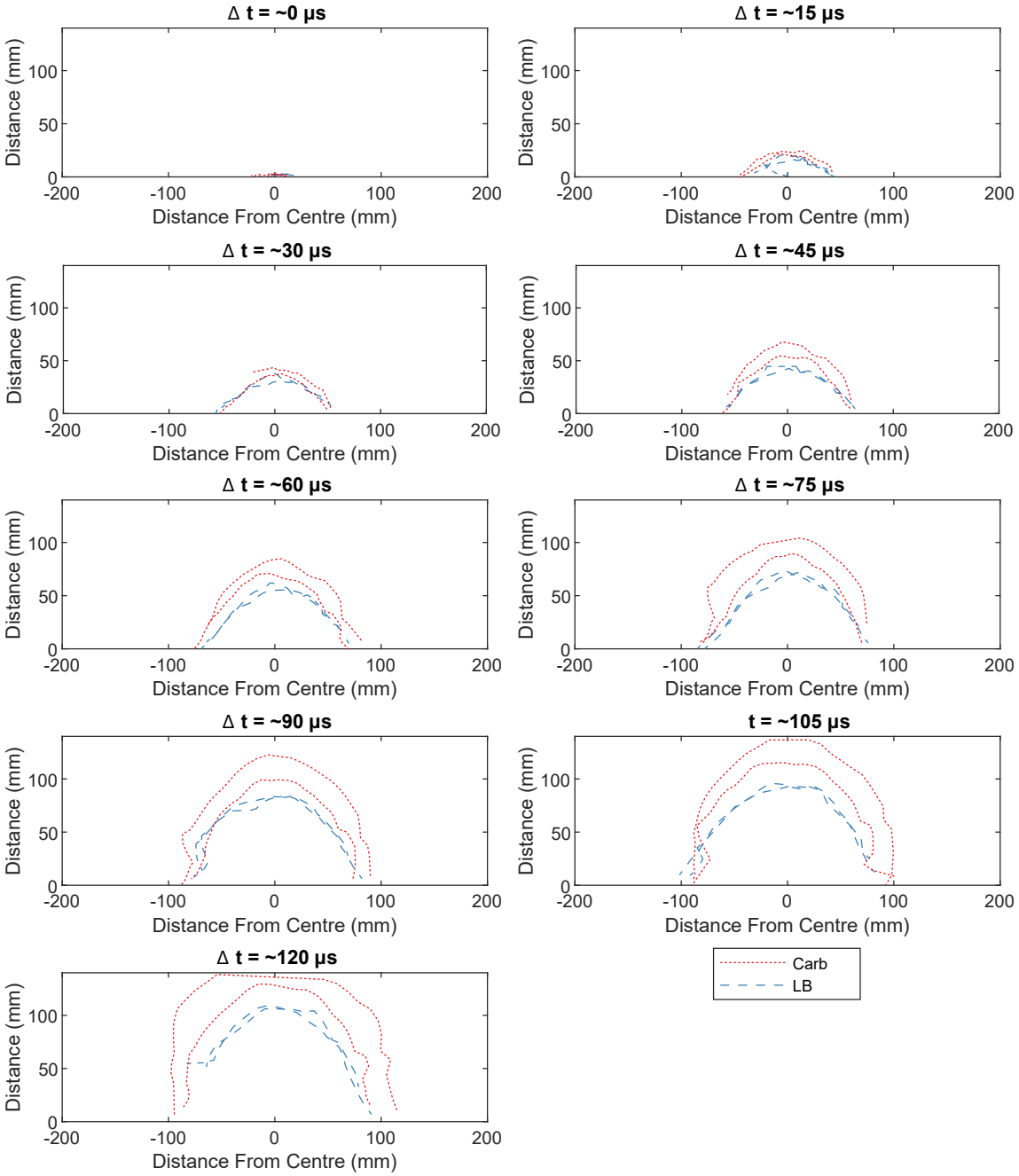

Figure 8.11: Output from the high speed video tracking of the ejecta cloud for two tests on carbonate and two tests on LB sand at 2.5% moisture content.

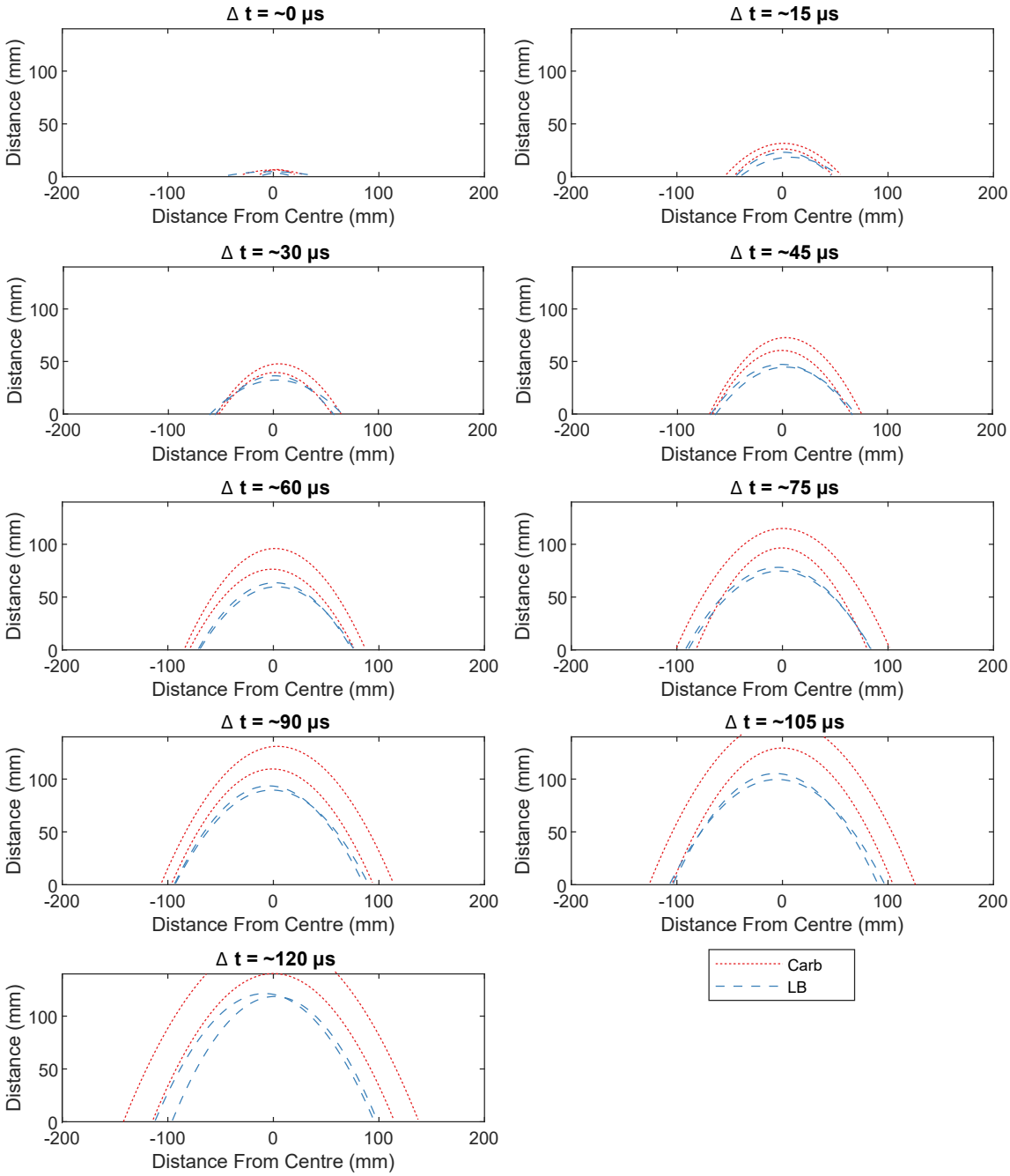

Figure 8.12: Output from the high speed video tracking of the shockwave for two tests of carbonate and two tests of LB sand at 2.5% moisture content.

8.4 Discussion

Table 8.4 summarises both the experimental results and the output from the empirical models of Westine et al. (1985) and Clarke et al. (2017). As shown previously in Figure 8.4, relative to the 2.5% moisture content quartz sand, carbonate sand is predicted to produce lower loading due to the lower bulk density. In contrast, the experimental results show an increase over the quartz sand baseline. Combining the measured increase, and the predicted decrease, this indicates that the balance of factors affecting the loading is incorrect in the previous models. In the case of carbonate sand at 7.5% moisture content, this additional factor accounts for an 11.6% increase over what is predicted from previous work of Clarke et al. (2017), indicating that there is an overdependence on the role of bulk density in previous models. This assumption is supported by work done on explosives buried in materials other than soils. Clarke et al. (2020) reported experiments where charges submerged in water showed no decrease in impulse and Fourney et al. (2005) reported on experiments within saturated lead shot where again, despite the increased bulk density, the impulse measured was comparable to that in saturated sand.

In addition to the predicted decrease in loading due to the change in bulk density between LB and carbonate sand, Equation 2.7 can also be used to predict the change in loading due to increasing the moisture content of the sand, as originally proposed by Clarke et al. (2017). Figure 8.4 shows that for the carbonate sand used in these tests, when increasing the moisture content from 2.5% to 7.5% there is expected to be an increase in the loading of 5.1%. Table 8.5 summarises the three repeat tests for each moisture content along with the prediction for each measurement. It can be seen that the result of applying Equation 2.7 to the 2.5% moisture content total impulse measurements (76.3 ±2.8 Ns) is in agreement with the measured total impulse (76.3 ±2.8 Ns) for the 7.5% moisture content sand.

Table 8.4: Difference in measured and predicted total impulse relative to the 2.5% LB series.

Series	Measured	Westine prediction	I_{mod} prediction
LB 2.5%	Baseline	Baseline	Baseline
LB 5.0%	0.8%	1.1%	9.31%
Carb 2.5%	0.7%	-12.2%	-8.4%
Carb 5.0%	3.8%	-12.0%	-6.6%
Carb 7.5%	7.8%	-10.6%	-3.7%

Table 8.5: Difference in measured and predicted total impulse between 2.5% and 7.5% moisture content carbonate tests.

	Measured total impulse [Ns] w **=2.5%**	w **=7.5%**	**Predicted total impulse [Ns]** w **=7.5%**
Test 1	72.0	79.2	75.6
Test 2	73.3	79.1	77.1
Test 3	68.8	70.7	72.3
Mean	71.3 ±1.4	76.3 ±2.8	75.0 ±1.4

8.4.1 Conclusions

Particle mineralogy and hence the role of particle breakage have not previously been investigated. The low degree of breakage seen can be explained to a certain degree by Xiao et al. (2019), who found that the extent of particle breakage was higher under quasi-static loading than under dynamic loading conditions at the same stress. The quartz-based sands in this paper were more friable than the similarly sized carbonate sands; this is in contrast to the published literature but is possibly a product of the artificial nature of the sand tested and that the quartz sand was more uniform (Coop et al. 2004).

Hypothesis (recap) — Soil particle breakage during the detonation of a shallow buried charge will reduce the energy available to be imparted on a target, resulting in a lower loading.

As per the stated hypothesis, the results do suggest that the reduction in particle breakage could have an impact on the overall impulse delivered to the target, with the lower degree of particle breakage in the carbonate sands correlating with the increase in impulse over the quartz sands. However, this is very much likely to be a second order process due to the small variations observed. The dynamic compaction response of the two sands could also be a cause for variations in impulse.

8.5 Further results and discussion

8.5.1 Stiffness

Testing by Weckert and Resnyansky (2022) has shown in dynamic testing the stiffness of carbonate sand is lower than that of the quartz sands, and that this is also a product of the moisture content of the sand as seen previously (Barr et al. 2016a). It is known that the plate-like particles of carbonate sands likely produce soils with greater shear strength at low stresses (Coop et al. (2004) and Golightly (1988)). At higher stresses, Weckert and Resnyansky (2022) indicate

little difference between the two soils at higher degrees of compression. Whether this behaviour has an impact at the high stresses seen in blast events is as yet unknown, but should be the focus of future research.

Oedometer testing was undertaken for both the carbonate and quartz sands in their dry state (0.3% moisture content) to investigate the stiffness and compaction. As per ISO17892-5:2017 (International Organization for Standardization 2017), the loading was applied in discrete steps, with time allowed for the sample to achieve equilibrium before proceeding to the subsequent loading. The stages applied are identified in Figure 8.13, which shows that a steady state is achieved rapidly after each change in applied stress.

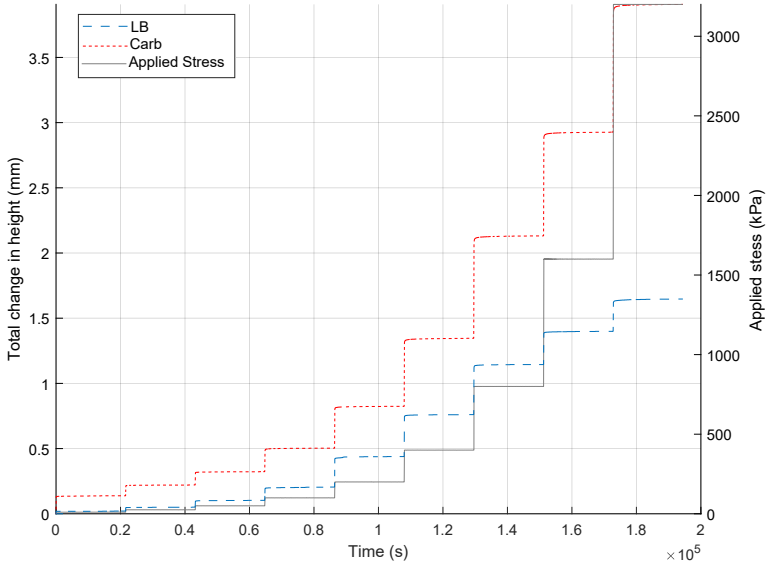

Figure 8.13: Results from oedometer testing for both soils at low moisture contents to investigate their compaction response, showing the compaction and the applied load as a function of time.

The void radio, e, defined as the volume of voids, V_v, per volume of solids, V_s can be calculated as follows (Bache et al. 2008):

$$e = \frac{V_v}{V_s} \tag{8.5}$$

The volume of the voids can also be expressed in terms of total volume, V and volume of solids:

$$V_v = V - V_s \tag{8.6}$$

$$e = \frac{V - V_s}{V_s} \quad = \frac{V}{V_s} - 1 \tag{8.7}$$

Using the phase relationships, volume can also be expressed in terms of total mass, M, and the mass of the solids, M_s, with use of the specific gravity, G_s.

$$V_s = \frac{M_s}{G_s \cdot \rho_w} \tag{8.8}$$

$$\begin{aligned} M_s &= M - M_w \\ &= M - (M_s \cdot w) \end{aligned} \tag{8.9}$$

$$\begin{aligned} &\implies M = (1 + w) \cdot M_s \\ &\implies M_s = \frac{M}{1 + w} \end{aligned} \tag{8.10}$$

$$\begin{aligned} \therefore V_s &= \frac{\frac{M}{1+w}}{G_s \cdot \rho_w} \\ &= \frac{M}{(1 + w) \cdot (G_s \cdot \rho_w)} \end{aligned} \tag{8.11}$$

Within the oedometer test, the area of the sample remains constant as the height changes, so rewriting volume in terms of height and area aids the analysis.

$$V = \text{Area} \cdot \text{Height} \tag{8.12}$$

$$\therefore e = \frac{\text{Area} \cdot \text{Height} \cdot G_s \cdot \rho_w \cdot (1 + w)}{M} - 1 \tag{8.13}$$

where:
$\rho_w = 1$ Mg/m^3
$w =$ Geotechnical moisture content, M_w/M_s
Area = The area of the oedometer
Height = The height of the sample being tested (this is the measurement taken in Figure 8.13).

For a given soil V, ρ, w and G_s are known/measurable parameters. This means the results obtained from the oedometer testing shown in Figure 8.13 can be plotted as the void ratio as a function of the applied stress, as shown in Figure 8.14. Plotting the void ratio as a function of the applied stress, allows a comparison of both the total voids present (magnitude of e) and the bulk compressibility of the soil from the negative gradient of the compression line. Figure 8.14 shows that the carbonate sand has a higher compressibility than the quartz-based sand up to 2.5 MPa.

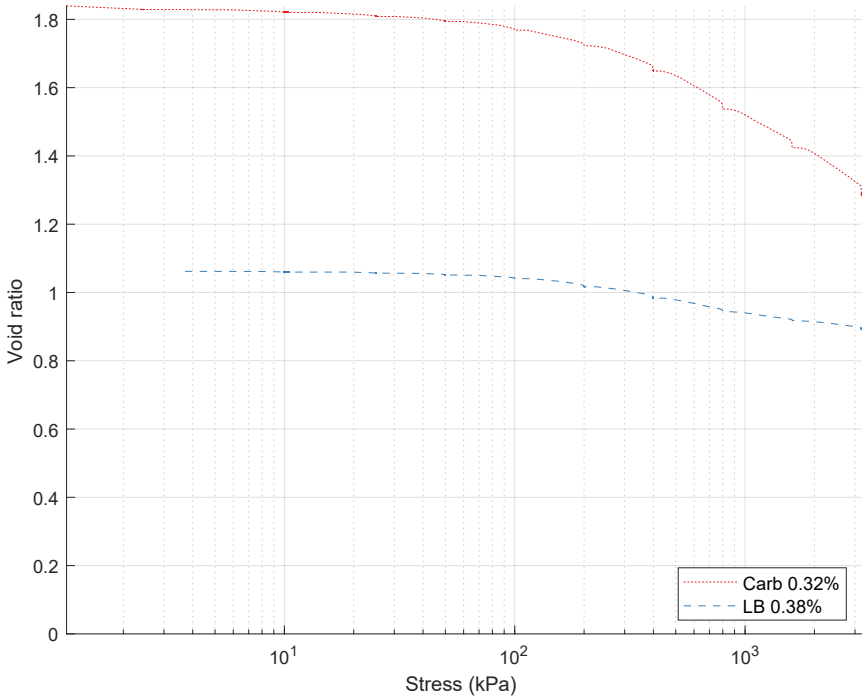

Figure 8.14: Results from oedometer testing for both soils at low moisture contents to investigate their compaction response, showing the void ratio as a function of applied stress.

8.5.2 Shear angle

Another possible source for the discrepancy in loading, other than compressibility, is the shear angle/strength of the soil. Given that both soils are cohesionless the critical angle may be useful as a way to gauge the area of the surface breakout from a buried charge, and hence how much focussing of the blast the soil enables.

Rankine (1857) determined that the load on a retaining wall from a cohesionless soil with a friction angle, ϕ, would form a slip plane at an angle of $45° + \frac{\phi}{2}$ to the horizontal. This approach can be used to approximate the volume of soil that will respond to the blast from a buried charge. The top row in Figure 8.15 shows how the Rankine criteria, and changing the friction angle affects the force bearing on a retaining wall. The bottom row shows how this same approach can be applied to the failure of the soil plug above the charge (and hence indicating the possible initial width of the surface breakout). With a finite load applied upward on the lower face, there is a section of soil that does not contribute to the vertical loading due to the formation of a slip plane. Logically, it follows that for the same stimulus (e.g. the same size buried charge), a smaller breakout area will mean a more focussed load onto the target plate. The critical angles for both Leighton Buzzard and carbonate sands have been well researched, with

Jamiolkowski et al. (2003) providing values of 34° and 40° at relative densities similar to the soils tested in the current work.

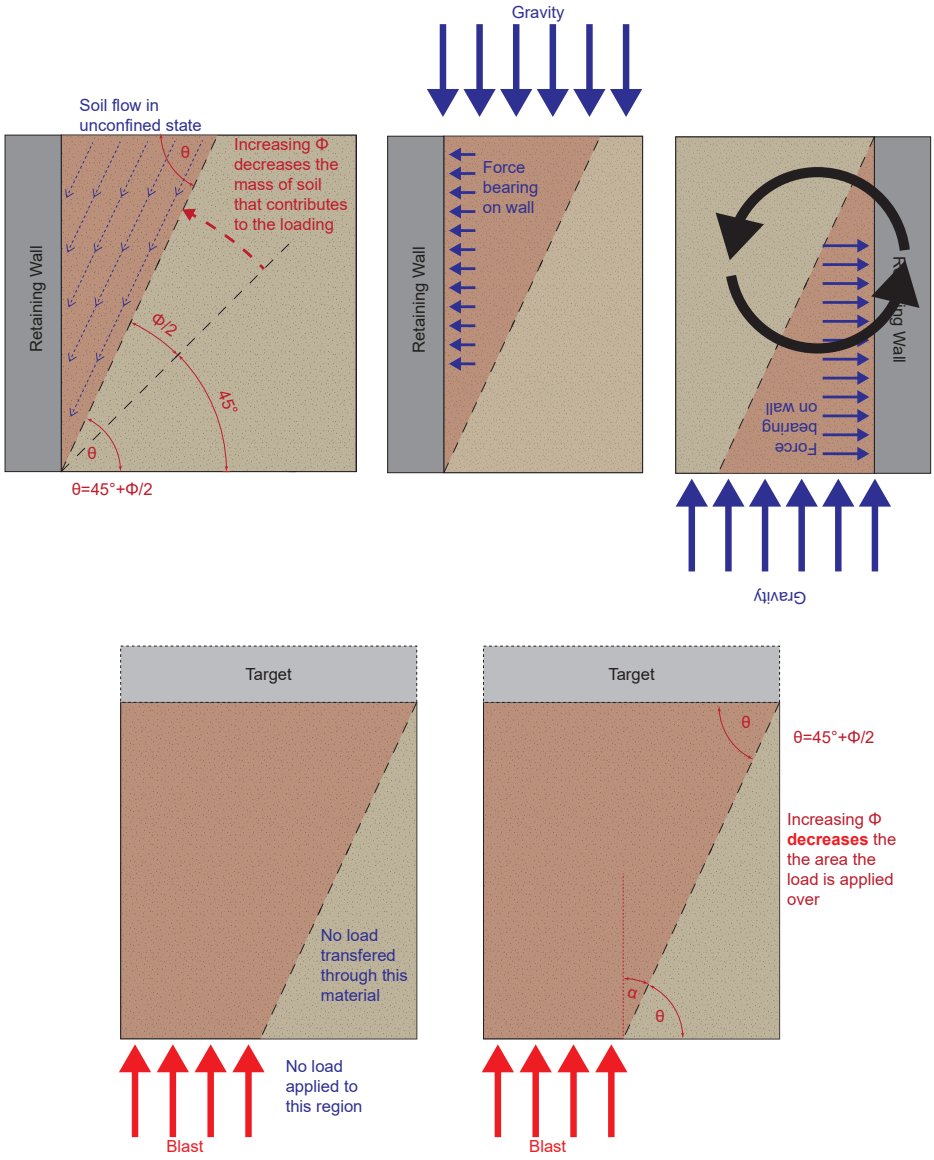

Figure 8.15: Diagrammatic representation of how the Rankine criteria for the formation of a slip plane in soil against a retaining wall can be used to infer the degree of spread from a buried charge.

Safinus et al. (2013) identified issues when applying standard Rankine load calculations from silica-based sediments to carbonate-based sediments. They state that the discrepancies can be significant, especially in high stress environments. Their work looked at understanding the loading conditions encountered

by spudcan foundations for offshore structures. They conducted scaled testing with both silica and carbonate sand to determine the difference between the two sand types. Figure 8.16 shows the soil deformation profiles from tests with carbonate and silica sand, and highlights the different observed loading angles, α, for the two soil types.

Figure 8.17 shows the loading angle for both carbonate (red) and quartz (blue) sands, using the results of Safinus et al. (2013) on the left and using the Rankine criteria on the right. It can be seen that both approaches indicate the loading in carbonate sand is expected to be applied over a smaller area. The area over which the loading is distributed for the carbonate sand compared to the quartz sand is 8.2% lower using the Rankine criteria approach, and 27.6% lower using the results of Safinus et al. (2013). The reduction in area has been computed at the sand surface as, above this point, the sand is free to expand laterally without further confinement. This concentration of the loading may go some way towards the observed discrepancy between the carbonate results and the prediction based on previous work, as discussed in § 8.4.

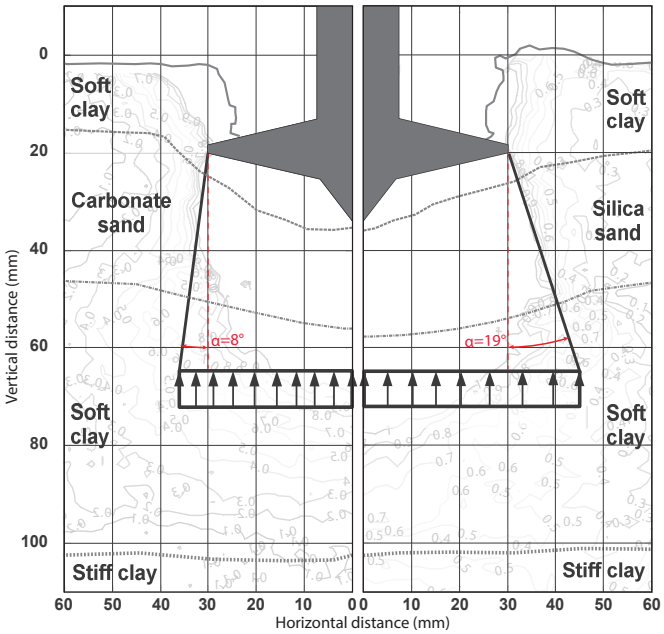

Figure 8.16: Results from scaled spudcan testing of Safinus et al., which found carbonate and quartz sand to have load spread angles of 8° and 19° respectively. The contours show the normalised soil flow velocity, where 1 equates to the soil moving at the same rate as the penetrating spudcan (modified from Figure 5 of Safinus et al. (2013)).

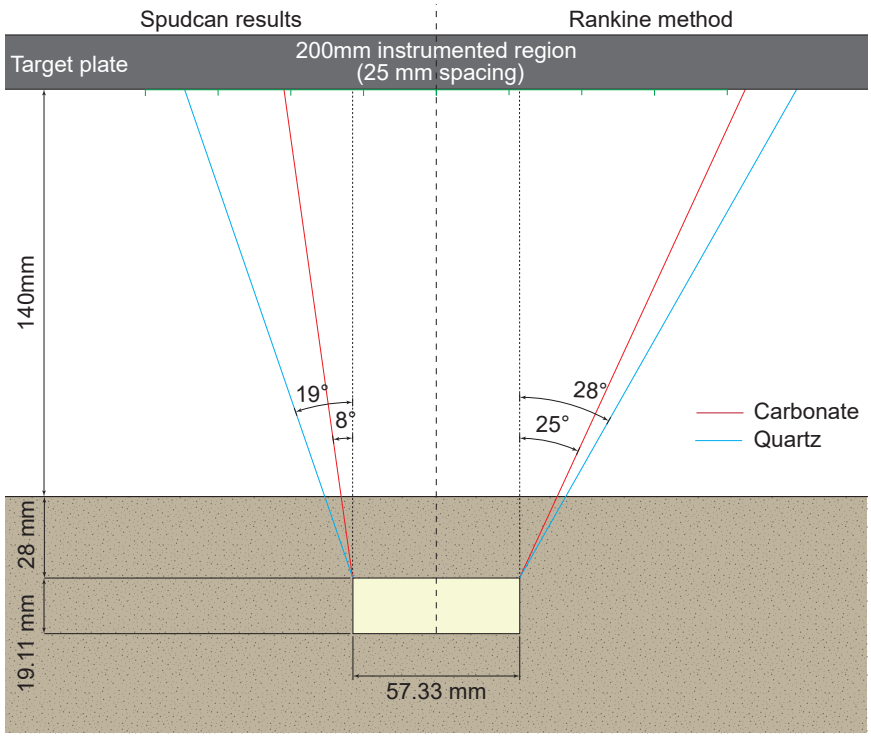

Figure 8.17: Diagram showing of the two different load spread angles for each sand type.

Chapter 9

Summary conclusions

Aims – recap This work aimed to investigate the risk posed by buried charges in both littoral and subarctic environments, areas which had previously not been studied. The data collected was to be combined with existing data (from both previous University of Sheffield testing and from the literature) to widen knowledge on the effect geotechnical conditions have on the loading from a buried charge.

Objectives – recap

1. Undertake experiments to investigate buried charges in the littoral environment by varying: the water level within a soil; and the presence of water above the soil surface.
2. Undertake experiments to investigate buried charges in soil with a different mineralogy but comparable particle size distribution to previous data.
3. Develop a system to undertake testing of frozen soil with an emplaced buried charge.
4. Undertake experiments to investigate buried charges in the subarctic environment by conducting tests in solid ice, frozen soil and partially frozen soil.

In this work, 38 buried charge tests have been conducted across 10 different test series to gather data and further the understanding on the factors which effect the loading from a shallow buried charge. In addition to the generation of new experimental data, a number of new analytical methods have been developed for this work including:

- A method for producing impulse vs time histories that are synced with high speed video to understand the loading events (§ 4.2.1)
- A method for analysing high speed video to track shockwave and ejecta from a burried charge (§ 4.2.2)
- A revised method for automating the analysis of large volumes of data from buried charge testing to produce consistent results from a disparate range of tests

The newly generated data has been compared to historic data from 23 tests in 6 different series, of Clarke et al. (2020). The newly gathered and historic data have been analysed and processed using the same analysis techniques developed for this work to produce a consistent set of results from which conclusions can be drawn. The results have been presented and discussed in three themed sections above, Chapter 6 covering frozen soils, Chapter 7 covering soils in the littoral zone and Chapter 8 covering carbonate based soils. Within each theme, the findings have been discussed in detail and are summarised again below.

- Objective 1: Data on charges buried in the littoral environment.
  - The level of the water table in a soil sample can impact on the above surface impulse from a buried charge.
  - No increase was measured when the water table was level with the base of the charge, therefore, it can be said the effect is only observed when the water level is at least as high as the charge.
  - Water above the surface of the soil (reducing the air gap) significantly increases the loading.
    - However, it is unclear whether this was primarily due to (1) the presence of water above the charge or (2) the reduction in stand-off distance between the surface and the target.
- Objective 2: Data on charges buried in carbonate sand.
  - Low density carbonate sands do not follow the trends predicted by previous results of Clarke et al. (2017) when considering density based effects alone.
  - Carbonate sands do not undergo significantly more particle breakage than quartz based sands
    - Albeit this is for carbonate soils manufactured from washed sea shells, rather than naturally produced carbonate sand due to the lack of availability of sufficient quantities of naturally occurring material.
  - Carbonate sands produce results with a marginally higher level of test to test repeatability than quartz based sand.
- Objective 3: Testing methodology for frozen charges.
  - Techniques for preparation and testing of charges buried in frozen material have been developed and implemented.
  - Techniques to combine Hopkinson pressure bar results and high speed imaging have been developed and used to compare the output from shallow buried charges.
- Objective 4: Data on charges buried in frozen soil.
  - Testing on charges buried in frozen soils and ice demonstrate a loading profile which is significantly more variable than equivalent testing of unfrozen samples.
  - Frozen soils and ice do not undergo melting/vaporisation over the timescales of detonation.
  - Frozen soils and ice do not form clumps when exposed to explosive events on the scales examined.

  - Charges buried in frozen soils do not show an increase in lateral confinement compared to unfrozen soils.
  - Charges buried in frozen soils produce upto 10% higher impulse than those in unfrozen soils.
  - Charges buried in ice produce lower impulse than charges submerged in water.

Figure 9.1 shows the total impulse for all tests conducted alongside the analysed historic data. It can be seen from the previous findings that saturated soils produce a higher impulse, and this trend can now be extended to include tests where the charge is surrounded by saturated soil with dry soil above. It can also be seen that while carbonate sand produced loadings higher than predicted, the results are comparable to those for LB sand at the same moisture content. Finally, it has been shown that frozen soils produce a loading that is more variable than, and up to 10% higher impulse than unfrozen soils.

9.0.1 Application

The overall context of this work is to better understand the risk posed by shallow buried charges, such as landmines and other historic remnants of war in different regions around the world. When viewed in this frame of reference, the results show:

- a vehicle or system designed to resist the loading for dry quartz sands is likely to also resist the loading from carbonate based sands;
- a vehicle or system designed to resist the loading for saturated sands is likely to also resist the loading encountered in both littoral and sub arctic environments;
- a vehicle or system designed to resist the loading for STANAG soils is likely to also to resist the loading encountered in both littoral and sub arctic environments;
- STANAG soil poses a significantly higher risk than the other materials considered, so can be used to conservatively assess survivability in a wider range of environments.
  - designing with STANAG soil threat scenario may result in 'over protection' and subsequent reductions in capability. Wider considerations into the efficiency of vehicle design compared to survivability is beyond the scope of this work.

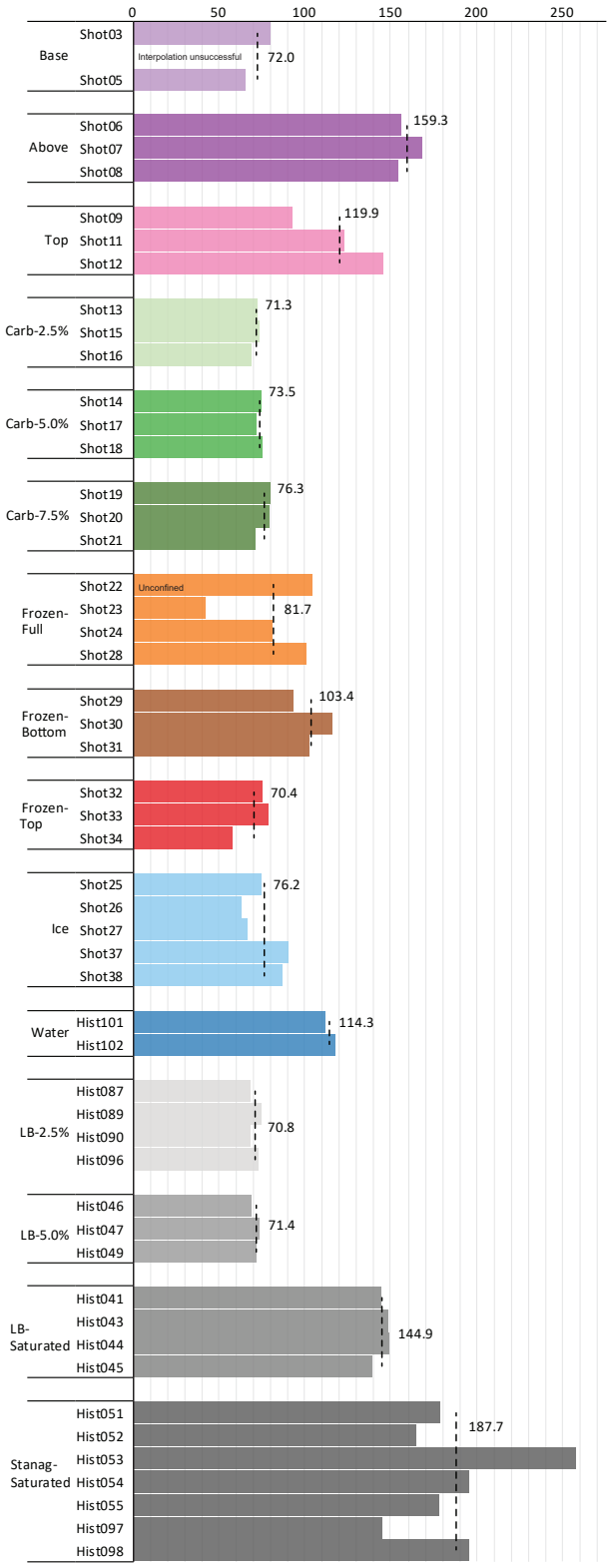

Figure 9.1: Plots showing the total impulse for the tests conducted.

9.0.2 Future work

This work has successfully addressed the aims and objectives, however the field could benefit from additional work in the following areas:

- A detailed study into the properties of the strain rate effects of carbonate soil both of natural origin (e.g. dogs bay sand) and artificial (e.g. the material used for this work). This would compare well with the work of Barr (2016b) to ensure that the trends identified in this work are fully understood.
- A meta analysis of the data contained within the existing literature, scaling to a common baseline and combining to determine if additional trends can be observed when utilising data from disparate sources. Currently the published results from different researchers are hard to compare direcrtly due to differences in materials used, burial conditions and experimental measurement techniques.
- Research into the links between above ground effects from a buried charge with then below ground effects. A detailed understanding of the two would enabled modelling of a wider range of scenarios to be undertaken.
- Undertake tests to investigate if the proportion of water ice in a soil changes the impulse transferred in a similar way to moisture content for unfrozen soils.

Bibliography

Allaby, M. (2010), *A Dictionary of Ecology*, Oxford University Press.

Anderson, C. E., Behner, T. and Weiss, C. E. (2011), 'Mine blast loading experiments', *International Journal of Impact Engineering* **38**, 697–706.
URL: *http://dx.doi.org/10.1016/j.ijimpeng.2011.04.005*

Anderson, C. E., Behner, T., Weiss, C. E., Bigger, R. and Chocron, S. (2010), Mine blast loading: Experiments and simulations, Technical Report 18.12544/011, Southwest Research Institute.

Bache, B. W., Chesworth, W., Chesworth, W., Gessa, C. and Lewis, D. T. (2008), *Encyclopedia of Soil Science*, Springer Netherlands.

Baker, T. (1976), *Transportation, Preparation, and Storage of Frozen Soil Samples for Laboratory Testing*, American Society for Testing and Materials, pp. 88–88–25.
URL: *http://www.astm.org/doiLink.cgi?STP39077S*

Baker, W. E., Cox, P. A., Kulesz, J. J., Strehlow, R. A. and Westine, P. S. (2012), *Explosion hazards and evaluation*, Vol. 5, Elsevier.

Barr, A. D. (2016b), Strain rate effects in quartz sand, PhD thesis, University of Sheffield.

Barr, A. D., Clarke, S. D., Petkovski, M., Tyas, A., Rigby, S. E., Warren, J. and Kerr, S. (2016a), 'Effects of strain rate and moisture content on the behaviour of sand under one-dimensional compression', *Experimental Mechanics* **56**, 1625–1639.
URL: *http://dx.doi.org/10.1007/s11340-016-0200-z*

Barr, A., Rigby, S. and Clayton, M. (2020), 'Correction of higher mode pochhammer–chree dispersion in experimental blast loading measurements', *International Journal of Impact Engineering* **139**, 103526.
URL: *https://www.sciencedirect.com/science/article/pii/S0734743X19306220*

Bergeron, D. and Tremblay, J. (2000), 'Canadian research to characterize mine blast output', *Military Aspects of Blast and Shock 16 (MABS16)* pp. 501–511.

Bergeron, D., Walker, R. and Coffey, C. (1998), Detonation of 100-gram anti-personnal mine surrogate charges in sand, Technical Report 668, Defence Research Establishment Suffield.

Bowman, E. T., Soga, K. and Drummond, W. (2001), 'Particle shape characterisation using fourier descriptor analysis', *Géotechnique* **51**, 545–554.
URL: *http://www.atypon-link.com/TELF/doi/abs/10.1680/geot.51.6.545.40465*

British Standards Institution (2015), 'BS 5930:2015. code of practice for ground investigations'.
URL: *https://knowledge.bsigroup.com/products/code-of-practice-for-ground-investigations*

Carter, S., Ned, A., Chivers, J. and Bemis, A. (2016), 'Selecting piezoresistive vs. piezoelectric pressure transducers', *Kulite Semiconductor Products, Inc* pp. 1–25.

Clarke, S. D., Fay, S. D., Rigby, S. E., Tyas, A., Warren, J. A., Reay, J. J., Fuller, B. J., Gant, M. T. and Elgy, I. D. (2016b), 'Blast quantification using hopkinson pressure bars', *Journal of Visualized Experiments* **2016**, 1–11.

Clarke, S. D., Fay, S. D., Warren, J. A., Tyas, A., Rigby, S. E. and Elgy, I. (2015), 'A large scale experimental approach to the measurement of spatially and temporally localised loading from the detonation of shallow-buried explosives', *Measurement Science and Technology* **26**.

Clarke, S. D., Fay, S. D., Warren, J. A., Tyas, A., Rigby, S. E., Reay, J. J., Livesey, R. and Elgy, I. (2017), 'Predicting the role of geotechnical parameters on the output from shallow buried explosives', *International Journal of Impact Engineering* **102**, 117–128.
URL: *http://dx.doi.org/10.1016/j.ijimpeng.2016.12.006*

Clarke, S. D., Rigby, S. E., Tyas, A., Fay, S. D., Reay, J. J., Warren, J. A., Gant, M. and Elgy, I. (2016a), 'Reflected pressures from explosives buried in idealised cohesive soils', *24th Military Aspects of Blast and Shock* **2016**, 8.

Clarke, S., Fay, S. and Tyas, A. (2014), 'Repeatability of buried charge testing', *Proceedings of the 23rd International Symposium on Military Aspects of Blast and Shock.* pp. 1–8.
URL: *http://eprints.whiterose.ac.uk/80754/*

Clarke, S., Rigby, S., Barr, A., Tyas, A., Warren, J. and Elgy, I. (2018), Characterisation of sandy-gravel across the scales, Technical report, University of Sheffield.

Clarke, S., Rigby, S., Fay, S., Barr, A., Tyas, A., Gant, M. and Elgy, I. (2020), 'Characterisation of buried blast loading', *Proceedings of the Royal Society A: Mathematical, Physical and Engineering Sciences* **476**(2236), 20190791.
URL: *https://royalsocietypublishing.org/doi/abs/10.1098/rspa.2019.0791*

Clarke, S., Warren, J. and Tyas, A. (2011), 'The influence of soil density and moisture content on the impulse from shallow buried explosive charges', *14th International Symposium on the Interaction of the Effects of Munitions with Structures (ISIEMS)* pp. 19–23.
URL: *http://eprints.whiterose.ac.uk/75931/*

Coop, M. R., Sorensen, K. K., Freitas, T. B. and Georgoutsos, G. (2004), 'Particle breakage during shearing of a carbonate sand', *Geotechnique* **54**, 157–163.

Cooper, P. (1996), *Explosives Engineering*, 1 edn, Wiley.

Cranz, C. (1926), 'Lehrbuch der ballistik', **26**.
URL: *https://doi.org/10.1007/BF01999484*

Curry, R. (2017), Response of plates subjected to air-blast and buried explosions, PhD thesis, University of Cape Town.

Curry, R. and Langdon, G. (2021), 'The effect of explosive charge backing in close-proximity air-blast loading', *International Journal of Impact Engineering* **151**, 103822.
URL: *https://www.sciencedirect.com/science/article/pii/S0734743X21000099*

Davies, R. M. (1948), 'A critical study of the hopkinson pressure bar', *Philosophical Transactions of the Royal Society of London. Series A, Mathematical and Physical Sciences* **240**, 375–457.
URL: *https://royalsocietypublishing.org/doi/10.1098/rsta.1948.0001*

Denefeld, V., Heider, N. and Holzwarth, A. (2017), 'Measurement of the spatial specific impulse distribution due to buried high explosive charge detonation', *Defence Technology* **13**, 219–227.
URL: *http://dx.doi.org/10.1016/j.dt.2017.03.002*

Dobratz, B. M. and Crawford, P. C. (1985), 'LLNL explosives handbook', *Properties of Chemical Explosives and Explosive Simulants* p. 208.

Ehrgott, J. Q., Akers, S. A., Windham, J. E., Rickman, D. D. and Danielson, K. T. (2011), 'The influence of soil parameters on the impulse and airblast overpressure loading above surface-laid and shallow-buried explosives', *Shock and Vibration* **18**, 857–874.

Farrimond, D. G. (2023), Characterisation of Blast Loading from Ideal and Non-Ideal Explosives, PhD thesis, University of Sheffield.

Farrimond, D. G., Rigby, S. E., Clarke, S. D. and Tyas, A. (2022), 'Time of arrival as a diagnostic for far-field high explosive blast waves', *International Journal of Protective Structures* **13**, 379–402.

Farrimond, D. G., Woolford, S., Barr, A. D., Lodge, T., Tyas, A., Waddoups, R., Clarke, S. D., Rigby, S. E., Hobbs, M. J., Willmott, J. R., Whittaker, M., Pope, D. J. and Handy, M. (2024b), 'Experimental studies of confined

detonations of plasticized high explosives in inert and reactive atmospheres', *Proceedings of the Royal Society A: Mathematical, Physical and Engineering Sciences* **480**(2294), 20240061.
URL: *https://royalsocietypublishing.org/doi/abs/10.1098/rspa.2024.0061*

Farrimond, D. G., Woolford, S., Tyas, A., Rigby, S. E., Clarke, S. D., Barr, A., Whittaker, M. and Pope, D. J. (2024a), 'Far-field positive phase blast parameter characterisation of RDX and PETN based explosives', *International Journal of Protective Structures* **15**(1), 141–165.
URL: *https://doi.org/10.1177/20414196221149752*

Fay, S., Clarke, S., Warren, J., Tyas, A., Bennett, T., Reay, J., Elgy, I. and Gant, M. (2013), 'Capturing the spatial and temporal variations in impulse from shallow buried charges', *15th International Symposium on the Interaction of the Effects of Munitions with Structures (ISIEMS)* .

Fay, S. D. (2020), Characterisation of blast loading for shallow buried explosives, PhD thesis, University of Sheffield.

Fourier, J. B. J. (1822), *Théorie analytique de la chaleur*, F. Didot.

Fourney, W. L., Leiste, H. U., Hauch, A. and Jung, D. (2010), 'Distribution of specific impulse on vehicles subjected to ied's', *Proceedings of the IMPLAST 2010 Conference* .

Fourney, W., Leiste, U., Bonenberger, R. and Goodings, D. (2005), 'Mechanism of loading on plates due to explosive detonation', *Fragblast* **9**, 205–217.

Fox, D. M., Akers, S. A., Leiste, U. H., Fourney, W. L., Windham, J. E., Lee, J. S., Ehrgott, J. Q. and Taylor, L. C. (2014), 'The effects of air filled voids and water content on the momentum transferred from a shallow buried explosive to a rigid target', *International Journal of Impact Engineering* **69**, 182–193.
URL: *http://dx.doi.org/10.1016/j.ijimpeng.2014.02.019*

Friedlander, F. G. and Taylor, G. I. (1946), 'The diffraction of sound pulses i. diffraction by a semi-infinite plane', *Proceedings of the Royal Society of London. Series A. Mathematical and Physical Sciences* **186**(1006), 322–344.
URL: *https://royalsocietypublishing.org/doi/abs/10.1098/rspa.1946.0046*

Fuller, B., Rigby, S., Tyas, A., Clarke, S., Fay, S., Reay, J. and Warren, J. (2015), 'Effect of spatial variation of blast loading on response of plates', *The First International Conference on Structural Safety under Fire and Blast (CONFAB 2015)* .

Garcia-Castellanos, D. and Lombardo, U. (2007), 'Poles of inaccessibility: A calculation algorithm for the remotest places on earth', *Scottish Geographical Journal* **123**, 227–233.

Genson, K. (2006), Vehicle shaping for mine blast damage reduction, PhD thesis, University of Maryland.

Goel, M. D., Matsagar, V. A., Gupta, A. K. and Marburg, S. (2012), 'An abridged review of blast wave parameters', *Defence Science Journal* **62**, 300–306.

Golightly, C. R. (1988), The Engineering Properties of Carbonate Sands, PhD thesis, University of Bradford.

Grujicic, M., Pandurangan, B., Huang, Y., Cheeseman, B. A., Roy, W. N. and Skaggs, R. R. (2007), 'Impulse loading resulting from shallow buried explosives in water-saturated sand', *Proceedings of the Institution of Mechanical Engineers, Part L: Journal of Materials: Design and Applications* **221**, 21–35.

Hardin, B. O. (1985), 'Crushing of soil particles', *Journal of Geotechnical Engineering* **111**, 1177–1192.

Hatanakai, M. and Feng, L. (2006), 'Estimating relative density of sandy soils', *Soils and Foundations* **46**, 299–313.

Heider, N., Denefeld, V., Steinbrenner, A. and Holzwarth, A. (2016), 'Engineering tool for the evaluation of global ied effects', *Defence Technology* **12**(2), 214–221. 2016 International Symposium on Ballistics.
URL: *https://www.sciencedirect.com/science/article/pii/S2214914715000811*

Held, M. (2009), 'Blast load diagnostic', *Propellants, Explosives, Pyrotechnics* **34**, 194–209.

Hlady, S. (2004), 'Effect of soil parameters on land mine blast', *18th Military Aspects of Blast and Shock (MABS)* .

Hoffmann, K. (1974), *Applying the wheatstone bridge circuit*, HBM Darmstadt, Germany.

Hopkinson, B. (1914), 'A method of measuring the pressure produced in the detonation of high explosives or by the impact of bullets', *Philosophical Transactions of the Royal Society of London. Series A, Containing Papers of a Mathematical or Physical Character* **89**, 411–413.
URL: *https://royalsocietypublishing.org/doi/10.1098/rsta.1914.0010*

Hopkinson, B. (1915), 'British ordnance board minutes. 13565'.

International Organization for Standardization (2017), 'ISO17892-5:2017: Geotechnical investigation and testing: Laboratory testing of soil. part 5: Incremental loading oedometer test'.
URL: *https://www.iso.org/standard/55247.html*

International Permafrost Association Standing Committee on Data Information and Communication (2003), 'Circumpolar active-layer permafrost system (caps), version 1'.

Jamiolkowski, M., Lo Presti, D. and Manassero, M. (2003), 'Evaluation of relative density and shear strength of sands from CPT and DMT', *Geotechnical Special Publication* pp. 201–238.

Lackner, R., Amon, A. and Lagger, H. (2005), 'Artificial ground freezing of fully saturated soil: Thermal problem', *Journal of Engineering Mechanics* **131**(2), 211–220.
URL: *https://doi.org/10.1061/(ASCE)0733-9399(2005)131:2(211)*

Leiste, H. U. (2012), Experimental Studies to Investigate Pressure Loading on Target Plates, PhD thesis, University of Maryland.

Liu, Z., Liu, J., Li, X. and Fang, J. (2019), 'Experimental study on the volume and strength change of an unsaturated silty clay upon freezing', *Cold Regions Science and Technology* **157**, 1–12.

Lodge, T., Clarke, S., Waddoups, R., Rigby, S., Gant, M. and Elgy, I. (2023), 'The effect of soil mineralogy and particle breakage on the impulse generated from shallow buried charges', *Applied Sciences* **13**, 5628.
URL: *https://www.mdpi.com/2076-3417/13/9/5628*

Lodge, T., Clarke, S., Waddoups, R., Rigby, S., Gant, M. and Elgy, I. (2024), 'Blast testing of explosive charges buried in frozen soil'.

Luijendijk, A., Hagenaars, G., Ranasinghe, R., Baart, F., Donchyts, G. and Aarninkhof, S. (2018), 'The state of the world's beaches', *Scientific Reports* **8**, 1–11.

Merriam-Webster (n.d.), 'Subarctic. in merriam-webster.com dictionary'.
URL: *https://www.merriam-webster.com/dictionary/subarctic*

Ministry of Defence (2017), 'JDP 0-10 UK maritime power joint doctrine publication 0-10'.

Nansteel, M. W., Veldman, R. L., Chen, C. C. T. and Lawrence, W. (2013), 'Impulse plug measurements of blast reflected impulse at close range', *Propellants, Explosives, Pyrotechnics* **38**, 120–128.

NATO (2014), 'AEP-55, procedures for evaluation the protection level of logistic and light armoured vehicles: Vol 2 mine threat', *Allied Engineering Publication* **2**, 12.

Neuberger, A., Peles, S. and Rittel, D. (2007), 'Scaling the response of circular plates subjected to large and close-range spherical explosions. part i: Air-blast loading', *International Journal of Impact Engineering* **34**(5), 859–873.

Pickering, E. G., Yuen, S. C. K., Nurick, G. N. and Haw, P. (2012), 'The response of quadrangular plates to buried charges', *International Journal of Impact Engineering* **49**, 103–114.
URL: *http://dx.doi.org/10.1016/j.ijimpeng.2012.05.007*

RAF (2020), 'F-35b short takeoff/vertical landing variant'.
URL: *https://www.raf.mod.uk/aircraft/f-35b-lightning/*

Rankine, W. J. M. (1857), 'II. on the stability of loose earth', *Philosophical Transactions of the Royal Society of London* **147**, 9–27.
URL: *https://royalsocietypublishing.org/doi/abs/10.1098/rstl.1857.0003*

Reise, K. (2012), *Tidal Flat Ecology: An Experimental Approach to Species Interactions*, Vol. 54, Springer Science and Business Media.

Rigby, S. E., Barr, A. D. and Clayton, M. (2018b), 'A review of pochhammer–chree dispersion in the hopkinson bar', *Proceedings of the Institution of Civil Engineers - Engineering and Computational Mechanics* **171**(1), 3–13.
URL: *https://doi.org/10.1680/jencm.16.00027*

Rigby, S. E., Fay, S. D., Clarke, S. D., Tyas, A., Reay, J. J., Warren, J. A., Gant, M. and Elgy, I. (2016), 'Measuring spatial pressure distribution from explosives buried in dry leighton buzzard sand', *International Journal of Impact Engineering* **96**, 89–104.

Rigby, S. E., Fay, S. D., Tyas, A., Clarke, S. D., Reay, J. J., Warren, J. A., Gant, M. and Elgy, I. (2018a), 'Influence of particle size distribution on the blast pressure profile from explosives buried in saturated soils', *Shock Waves* **28**, 613–626.

Rigby, S. E., Knighton, R., Clarke, S. D. and Tyas, A. (2020), 'Reflected near-field blast pressure measurements using high speed video', *Experimental Mechanics* **60**, 875–888.

Rigby, S. E. and Sielicki, P. W. (2014), 'An investigation of tnt equivalence of hemispherical pe4 charges', *Engineering Transactions* **62**, 423–435.

Rigby, S. E., Tyas, A., Clarke, S. D., Fay, S. D., Reay, J. J., Warren, J. A., Gant, M. and Elgy, I. (2015), 'Observations from preliminary experiments on spatial and temporal pressure measurements from near-field free air explosions', *International Journal of Protective Structures* **6**, 175–190.

Rigby, S. and Tyas, A. (2014), 'Blast.m'. © 2014 Rigby, S. and Tyas, A. This code is distributed freely for academic use, with the caveat that publications (including Undergraduate, MSc & PhD dissertations, conference and journal papers) using this work fully acknowledge its use.
URL: *https://eprints.whiterose.ac.uk/77858/*

Safinus, Hossain and Randolph (2013), 'Comparison of stress-strain behaviour of carbonate and silicate sediments', *Proc. 18th Int. Conf. on Soil Mechanics and Geotechnical Engineering* pp. 267–270.

Settles, G. S. and Hargather, M. J. (2017), 'A review of recent developments in schlieren and shadowgraph techniques', *Measurement Science and Technology* **28**(4), 042001.

Taylor, L. C., Fourney, W. L. and Leiste, U. (2008), Loading mechanisms from shallow buried explosives, Technical Report ISB 277-2008, University of Maryland.

The Editors of Encyclopaedia Britannica (2016), 'Continental subarctic climate'. **URL:** *https://www.britannica.com/science/continental-subarctic-climate*

The Editors of Encyclopaedia Britannica (2019), 'Littoral zone'. **URL:** *https://www.britannica.com/science/littoral-zone*

Tremblay, J. E. (1998), Impulse on blast deflectors from a landmine explosion, Technical Report DREV – TM – 9814, Defence Research Establishment, Centre de Recherches Pour La Defense, Valcartier, Quebec Canada.

Tsytovich, N. A. and Sumgin, M. I. (1959), *Principles of Mechanics of Frozen Ground*, U. S. Army Snow, Ice and Permafrost Research Establishment, Corps of Engineers. **URL:** *https://books.google.co.uk/books?id=l2KXGQAACAAJ*

United Nations (1994), 'Assistance in mine clearance: Report of the secretary-general', *United Nations* .

United States Navy (2019), 'MK45 - 5-Inch 54/62 Calibre Guns', *United States Navy Fact File* . **URL:** *https://www.navy.mil/Resources/Fact-Files/Display-FactFiles/Article/2167864/mk-45-5-inch-5462-caliber-guns/*

Vyalov, S. S., Gorodetskii, S. E., Ermakov, V. F., Zatsarnaya, A. G. and Pekarskaya, N. K. (1966), 'Methods of determining creep, long-term strength and compressibility characteristics of frozen soils', *State Committee Of The Council Of Ministers (USSR) For Construction* . Technical Translation by National Research Council of Canada. Number 1364.

Waddoups, R., Clarke, S., Tyas, A., Rigby, S., Gant, M. and Elgy, I. (2023), 'An approach to quantifying the influence of particle size distribution on buried blast loading', *Eng* **4**(1), 319–340. **URL:** *https://www.mdpi.com/2673-4117/4/1/20*

Warder, D. L. and Andersland, O. B. (1971), 'Soil–ice behavior in a model retaining structure', *Canadian Geotechnical Journal* **8**, 46–68.

Weckert, S. A. and Resnyansky, A. D. (2022), 'Experiments and modelling for characterisation and validation of a two-phase constitutive model for describing sands under explosive loading', *International Journal of Impact Engineering* **166**, 104234.

Westine, P. S., Morris, B. L., Cox, P. A. and Polch, E. Z. (1985), Development of computer program for floor plate response from land mine explosions, Technical Report 13045, Southwest Research Institute.

Wheatstone, C. (1843), 'Xiii. the bakerian lecture.—an account of several new instruments and processes for determining the constants of a voltaic circuit', *Philosophical Transactions of the Royal Society of London* **133**, 303–327.
URL: *https://royalsocietypublishing.org/doi/abs/10.1098/rstl.1843.0014*

White, D. J. (2003), 'Psd measurement using the single particle optical sizing (spos) method', *Géotechnique* **53**, 317–326.
URL: *http://www.icevirtuallibrary.com/doi/10.1680/geot.2003.53.3.317*

Xiao, Y., Yuan, Z., Chu, J., Liu, H., Huang, J., Luo, S. N., Wang, S. and Lin, J. (2019), 'Particle breakage and energy dissipation of carbonate sands under quasi-static and dynamic compression', *Acta Geotechnica* **14**, 1741–1755.
URL: *https://doi.org/10.1007/s11440-019-00790-1*

Åkerman, H. J. and Johansson, M. (2008), 'Thawing permafrost and thicker active layers in sub-arctic sweden', *Permafrost and Periglacial Processes* **19**, 279–292.
URL: *http://doi.wiley.com/10.1002/ppp.626*

Appendix A

Detailed Results

A.1 Pressure and Specific Impulse

As described is §5.1.1, the following charts show s the pressure time history for each bar in the given test on the left hand side and the cumulative specific impulse for each bar, in each radial distance on the right. These results have been aggregated (e.g. Figures 6.13 to 6.19 for frozen soil, Figures 6.27 to 6.29 for ice/water, Figures 7.3 to 7.8 for the littoral series and Figures 8.7 to 8.8 for the carbonate series)

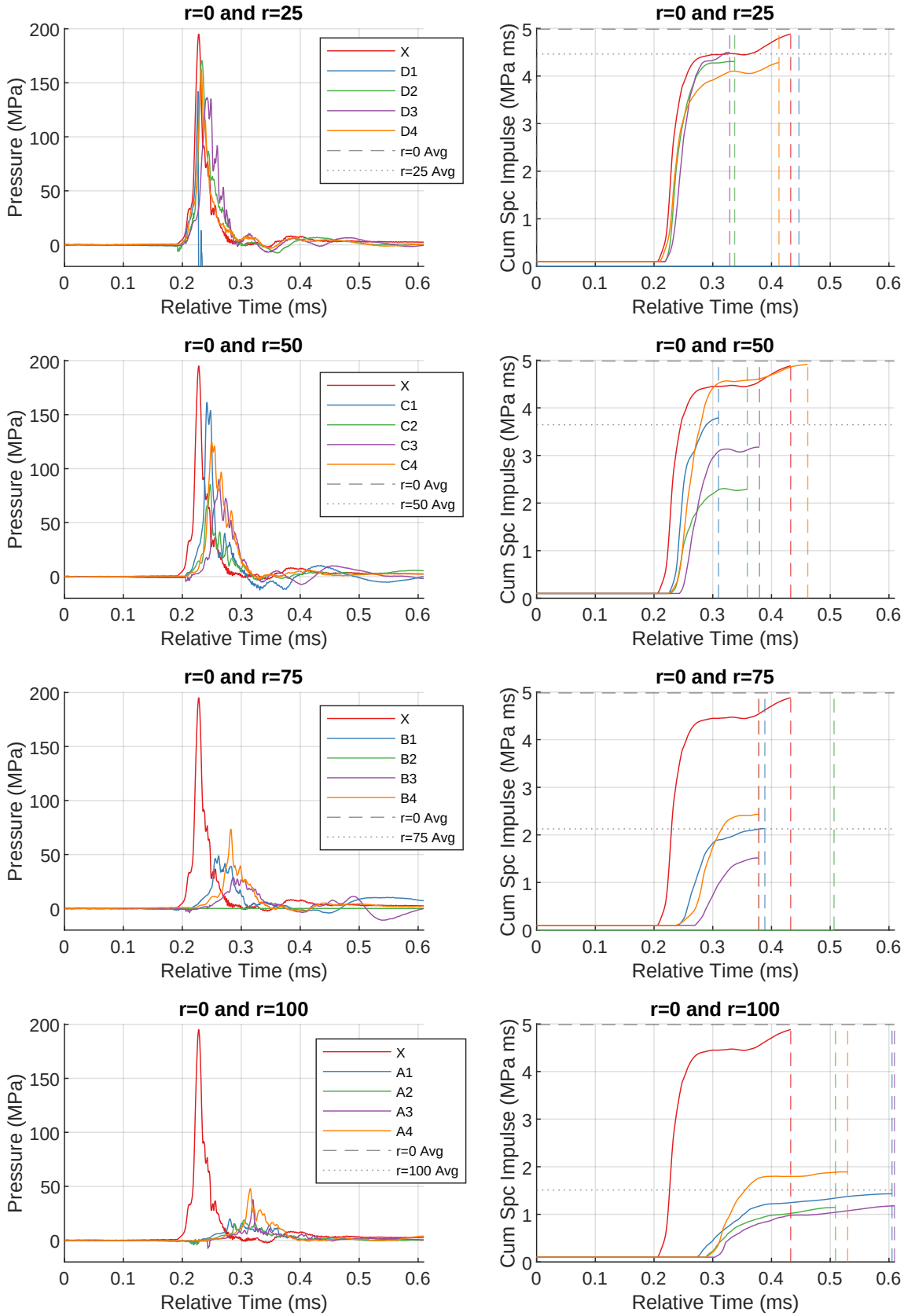

Figure A.1: Shot002pressure (left) and cumulative specific impulse (right) plots for each radial distance.

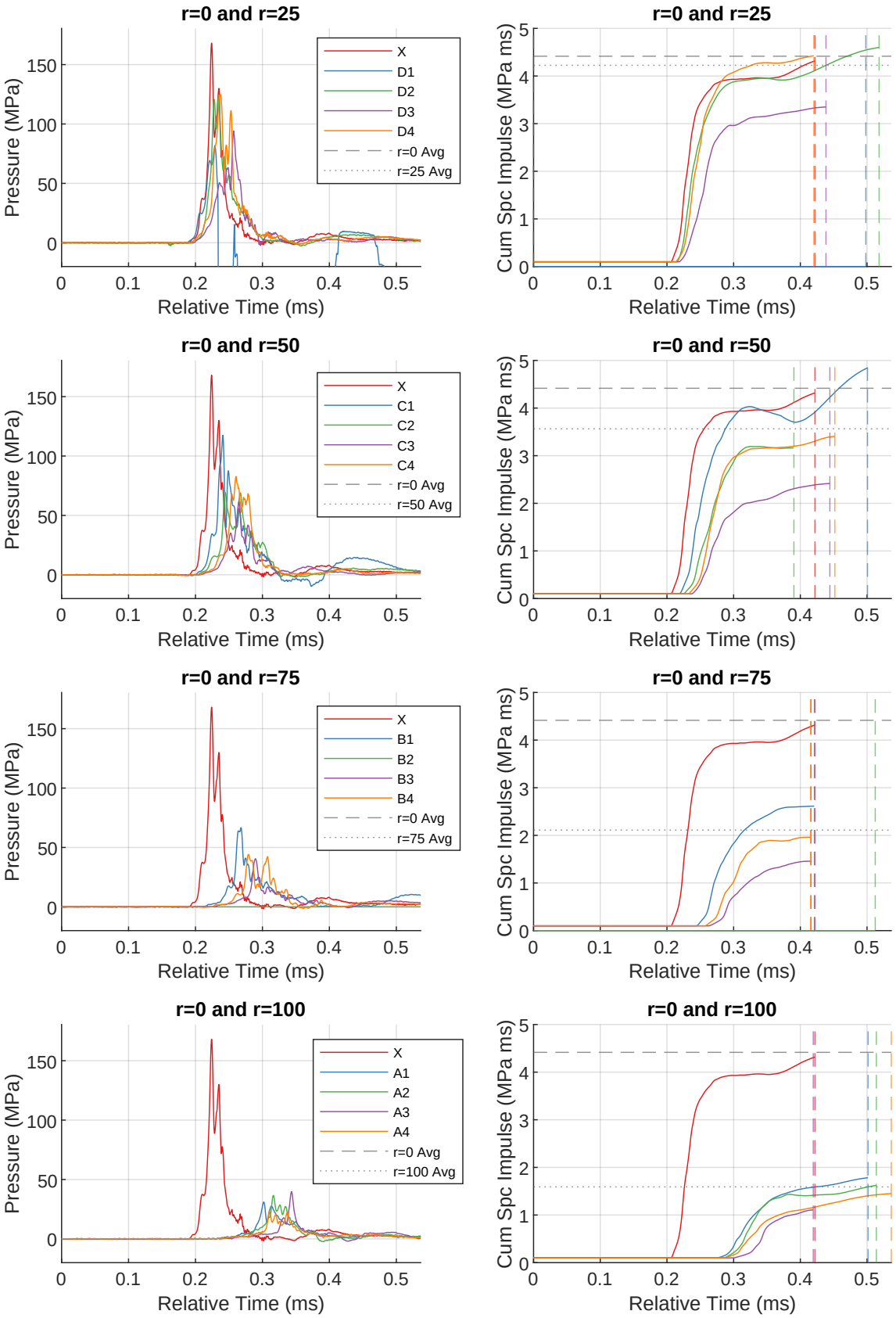

Figure A.2: Shot003pressure (left) and cumulative specific impulse (right) plots for each radial distance.

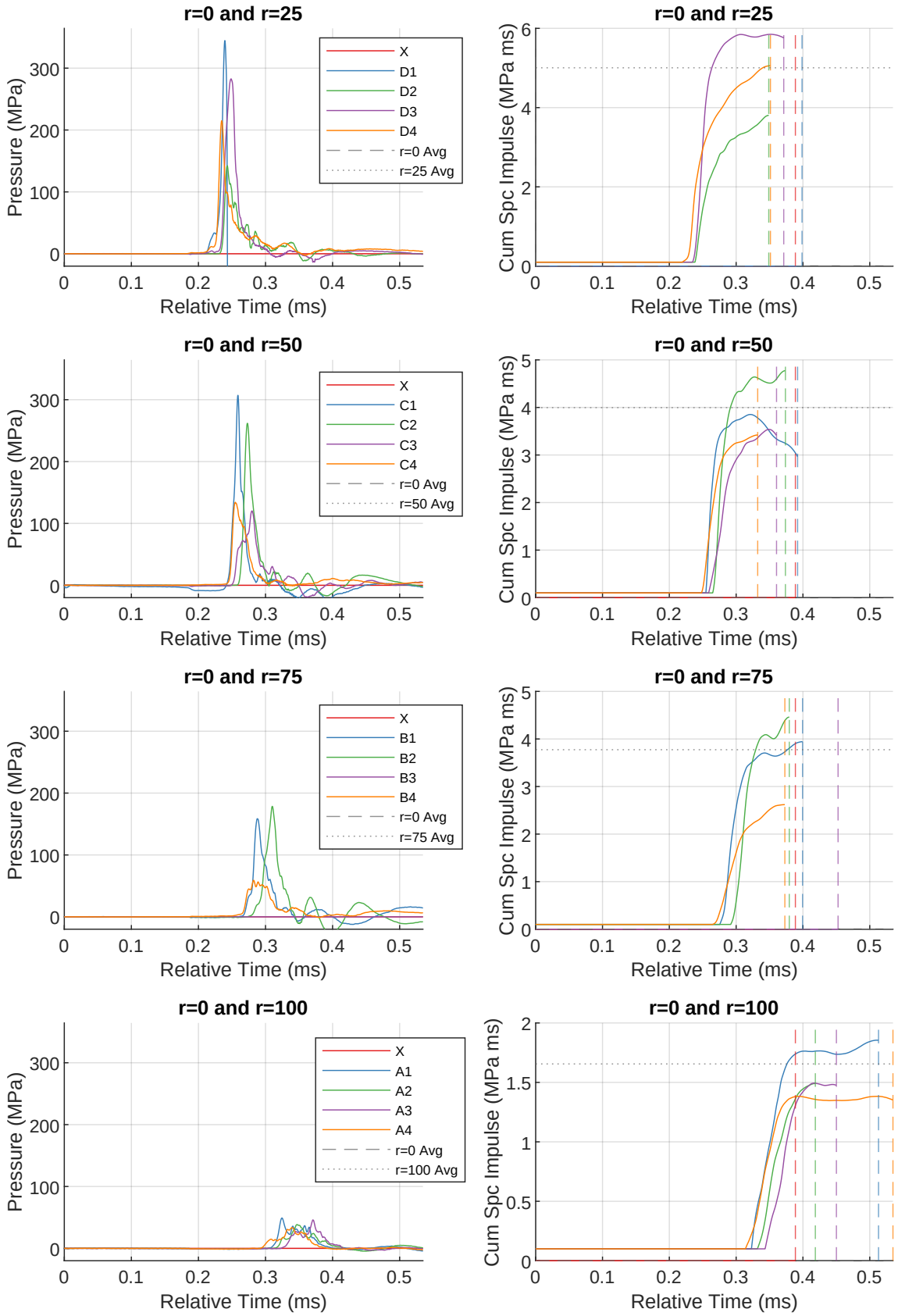

Figure A.3: Shot004pressure (left) and cumulative specific impulse (right) plots for each radial distance.

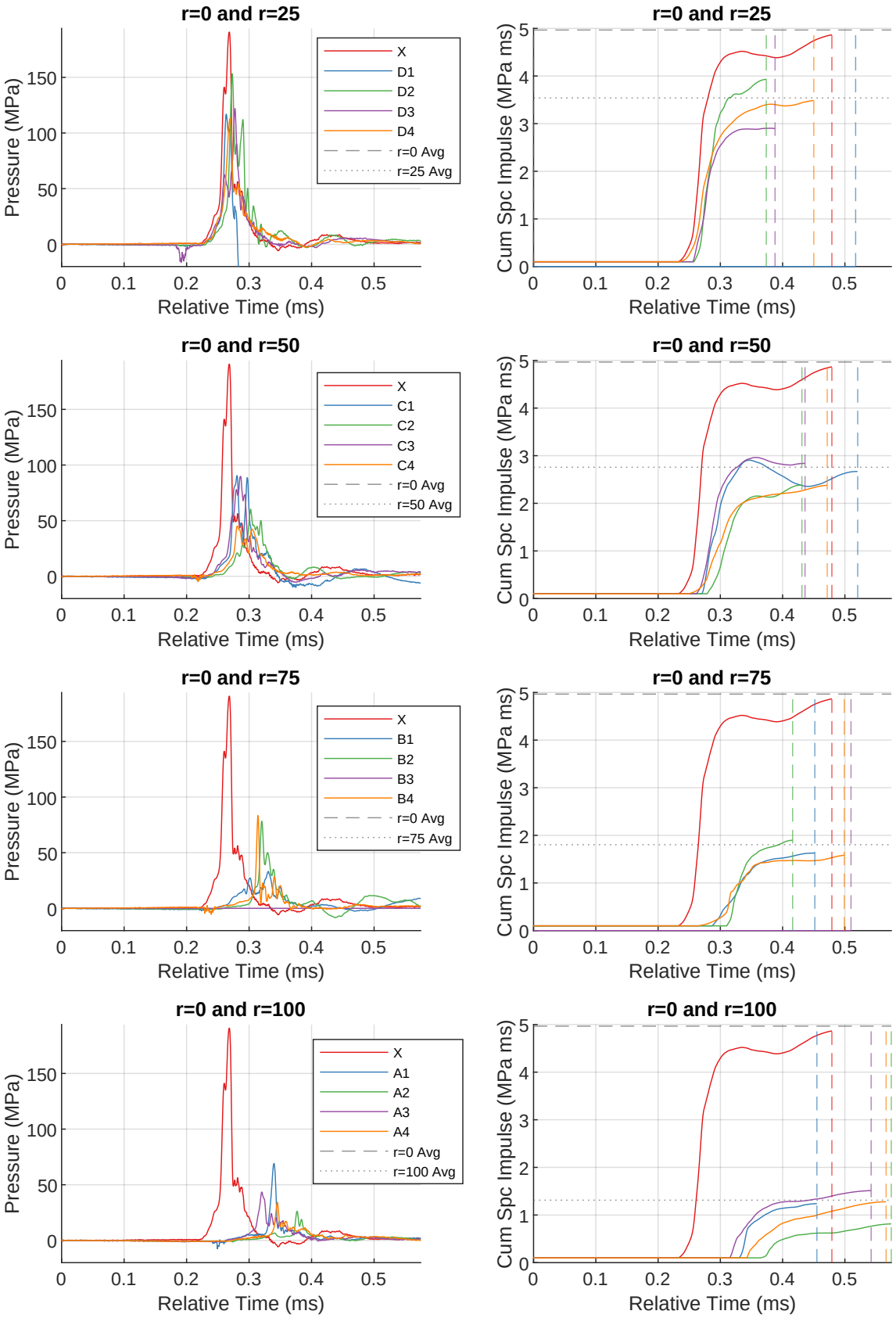

Figure A.4: Shot005pressure (left) and cumulative specific impulse (right) plots for each radial distance.

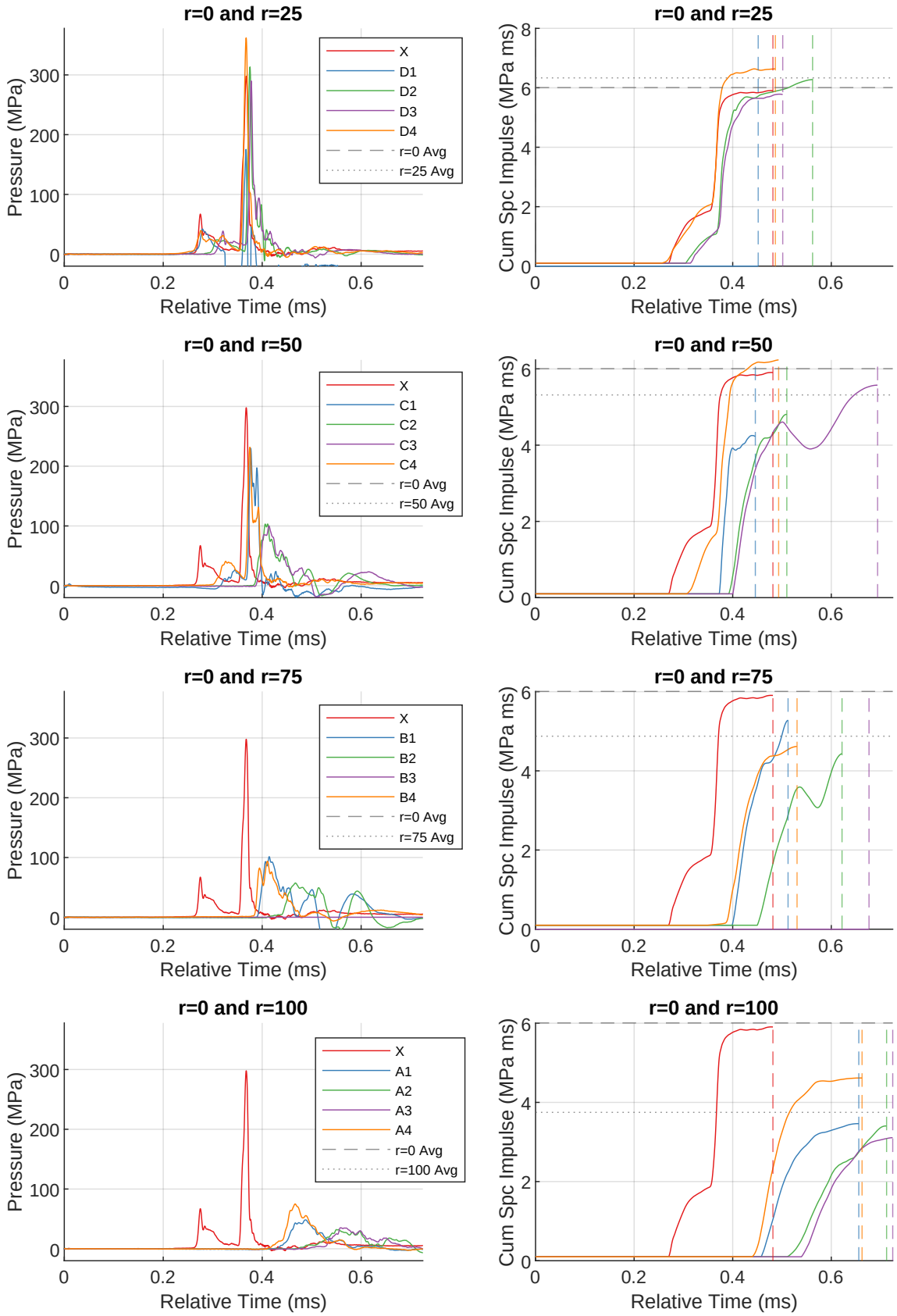

Figure A.5: Shot006pressure (left) and cumulative specific impulse (right) plots for each radial distance.

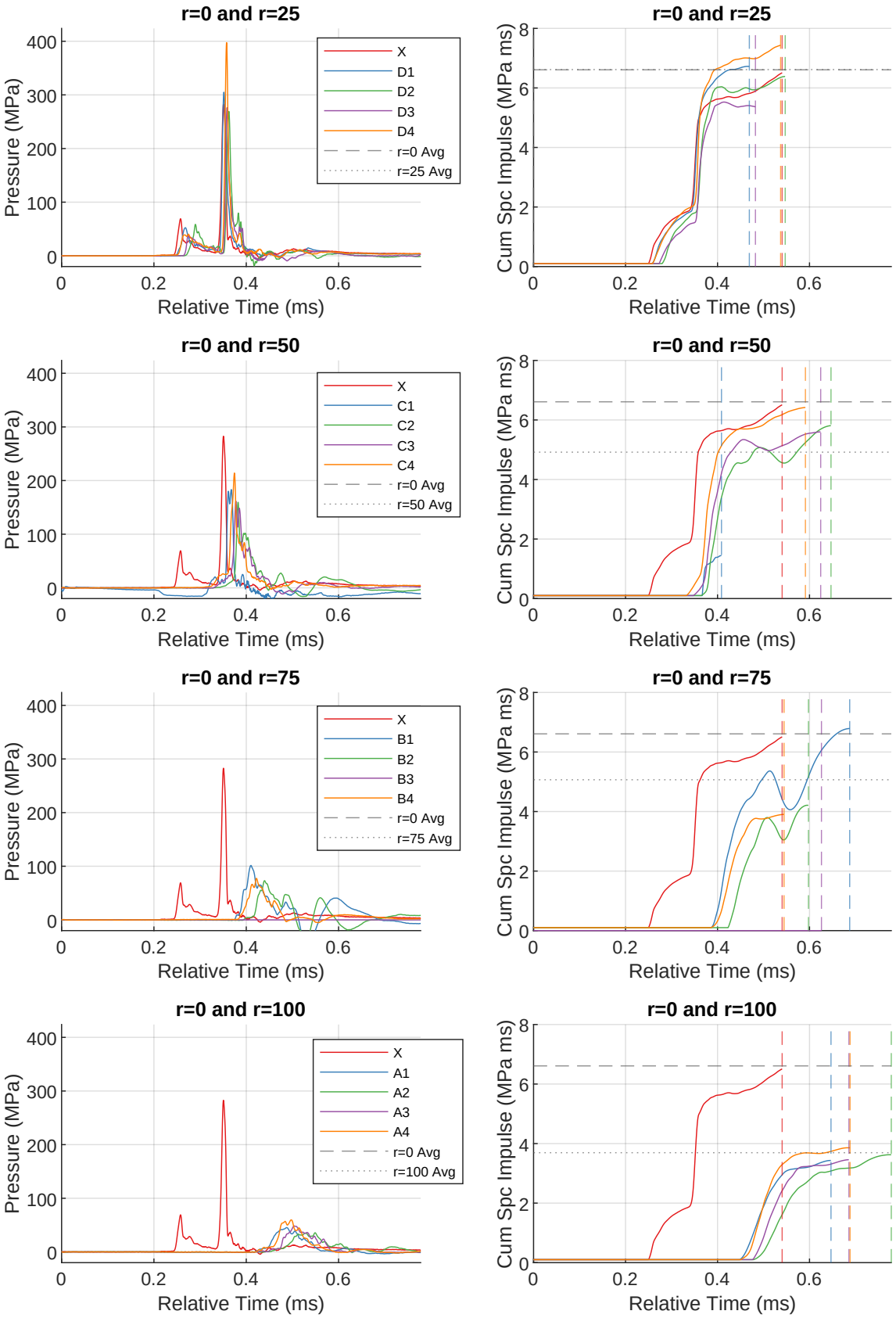

Figure A.6: Shot007pressure (left) and cumulative specific impulse (right) plots for each radial distance.

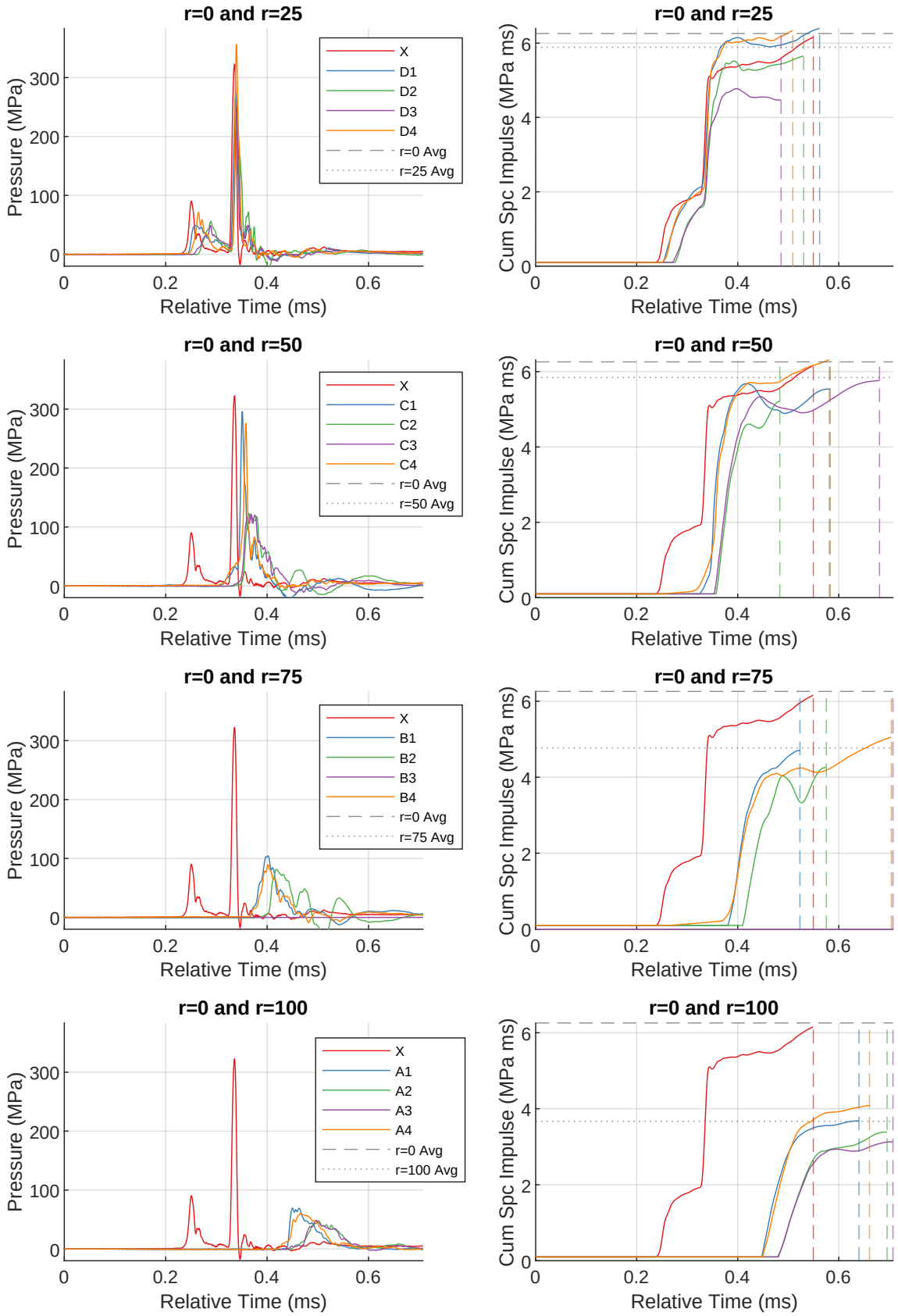

Figure A.7: Shot008pressure (left) and cumulative specific impulse (right) plots for each radial distance.

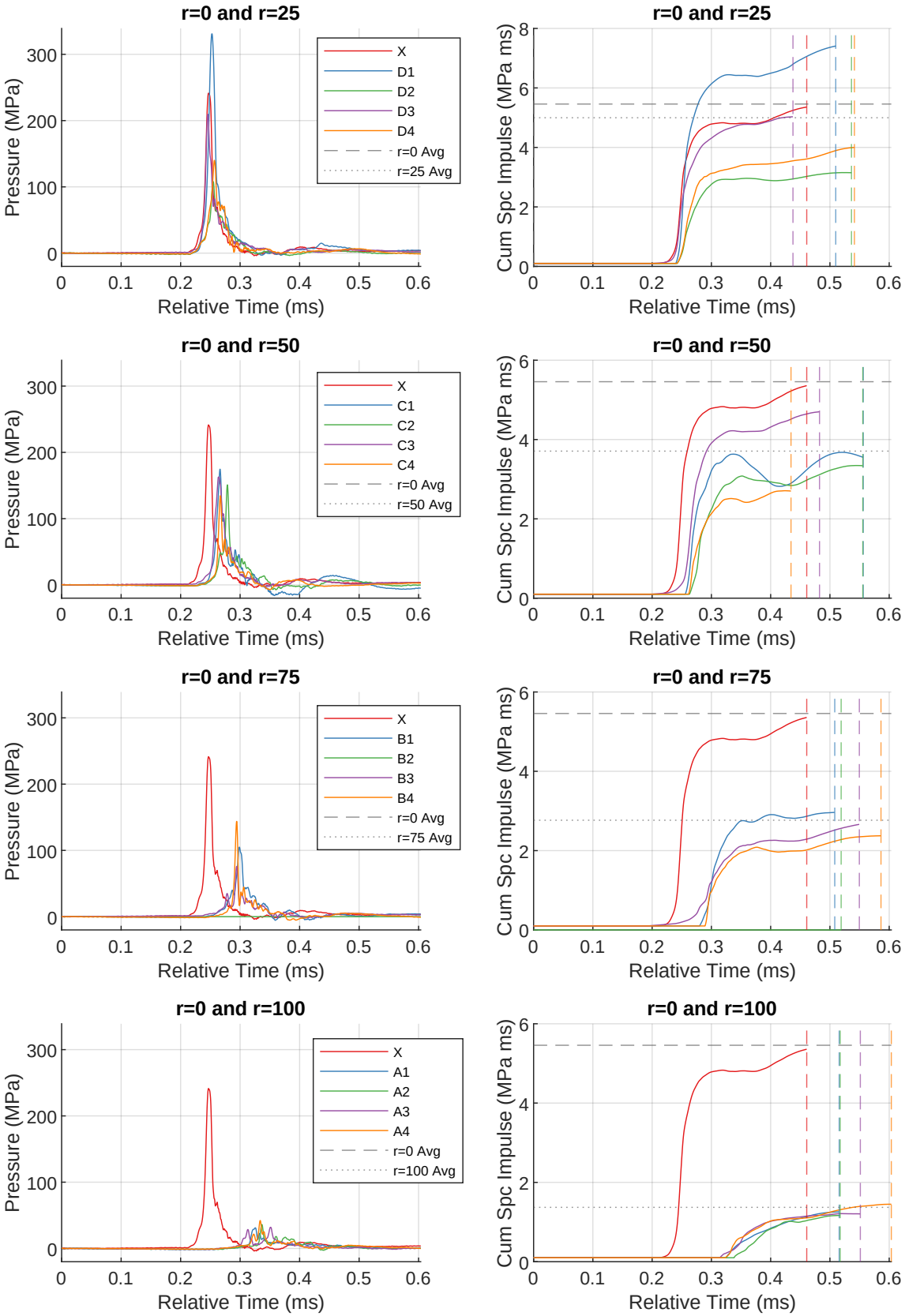

Figure A.8: Shot009pressure (left) and cumulative specific impulse (right) plots for each radial distance.

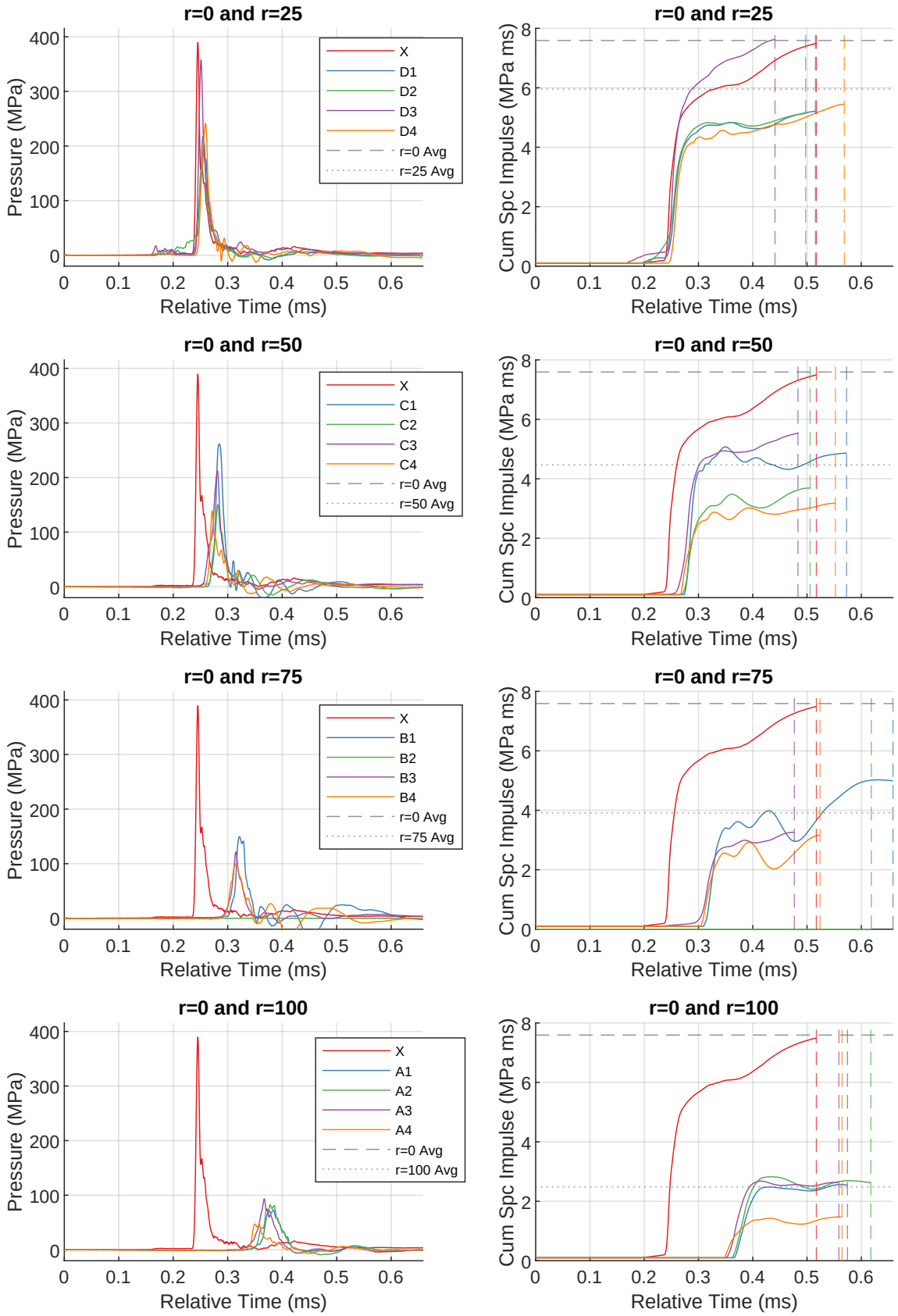

Figure A.9: Shot011pressure (left) and cumulative specific impulse (right) plots for each radial distance.

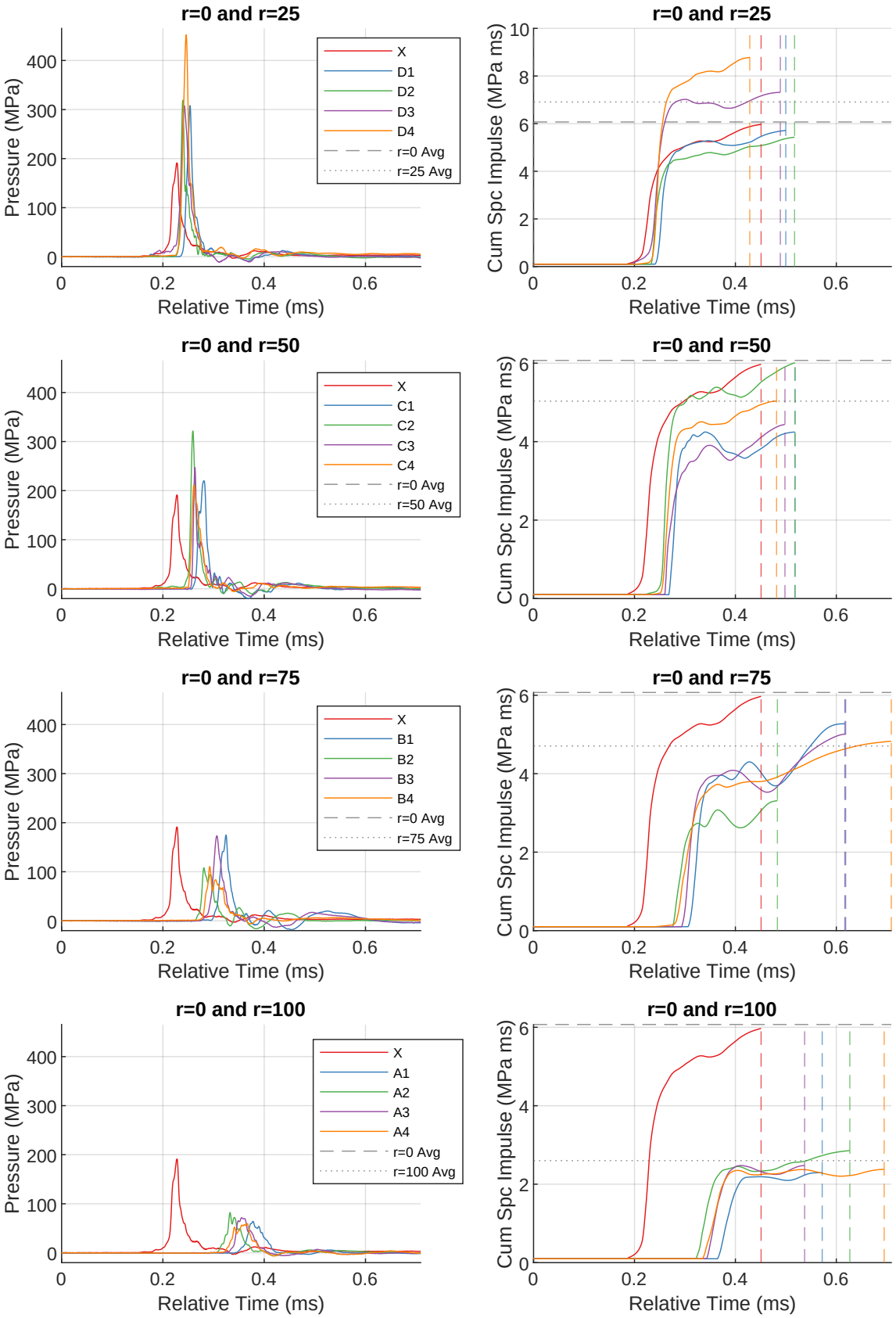

Figure A.10: Shot012pressure (left) and cumulative specific impulse (right) plots for each radial distance.

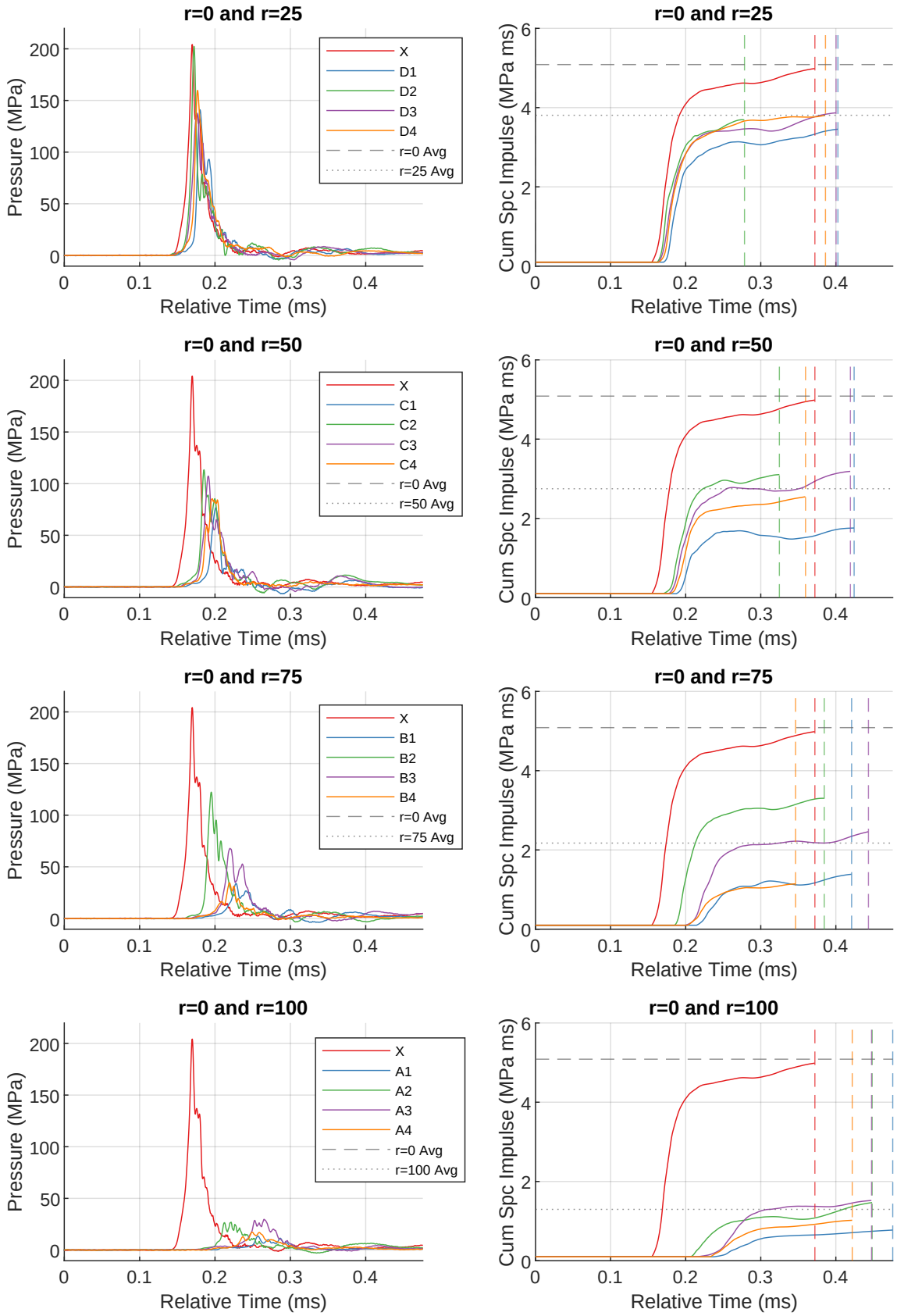

Figure A.11: Shot013pressure (left) and cumulative specific impulse (right) plots for each radial distance.

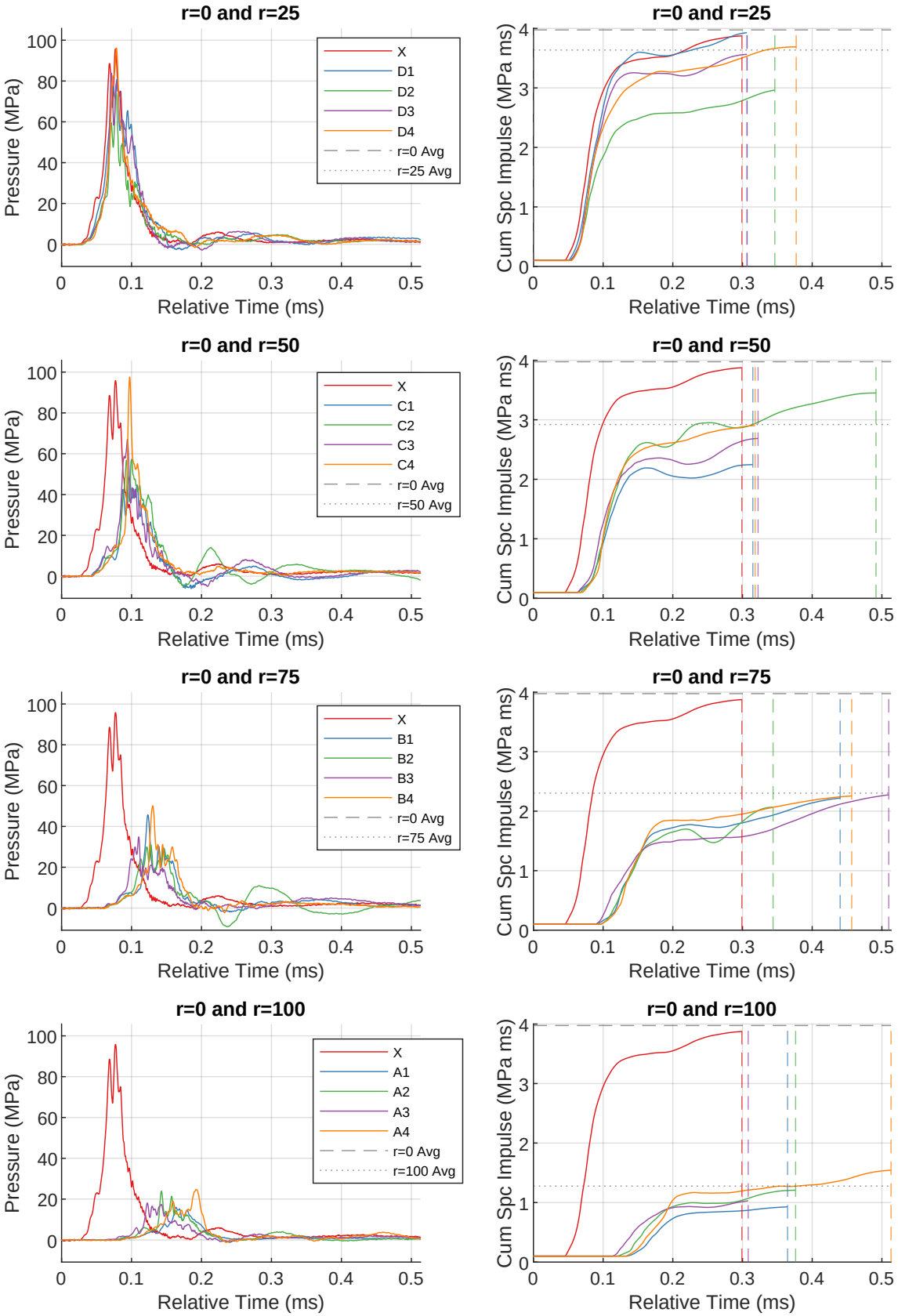

Figure A.12: Shot014pressure (left) and cumulative specific impulse (right) plots for each radial distance.

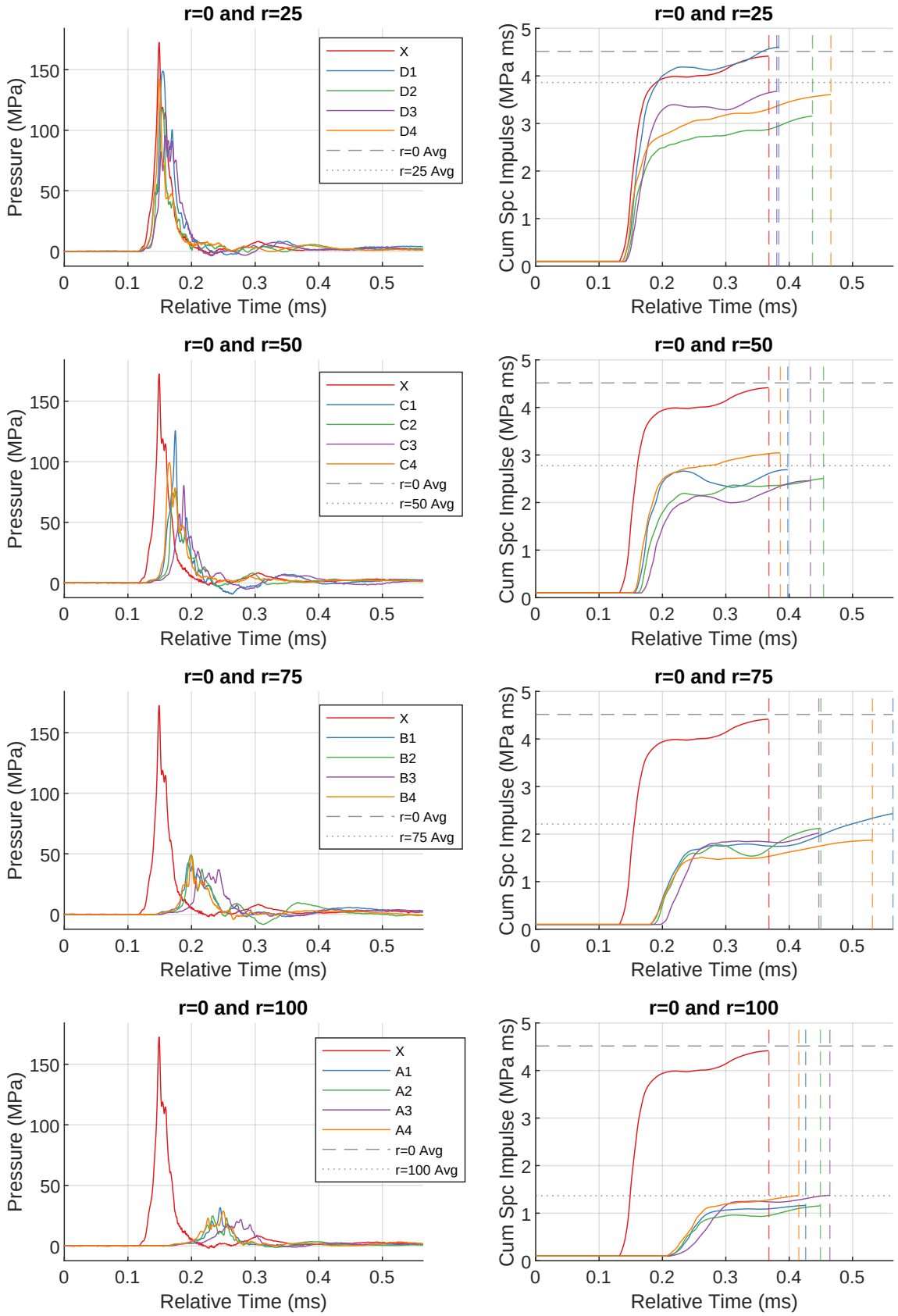

Figure A.13: Shot015pressure (left) and cumulative specific impulse (right) plots for each radial distance.

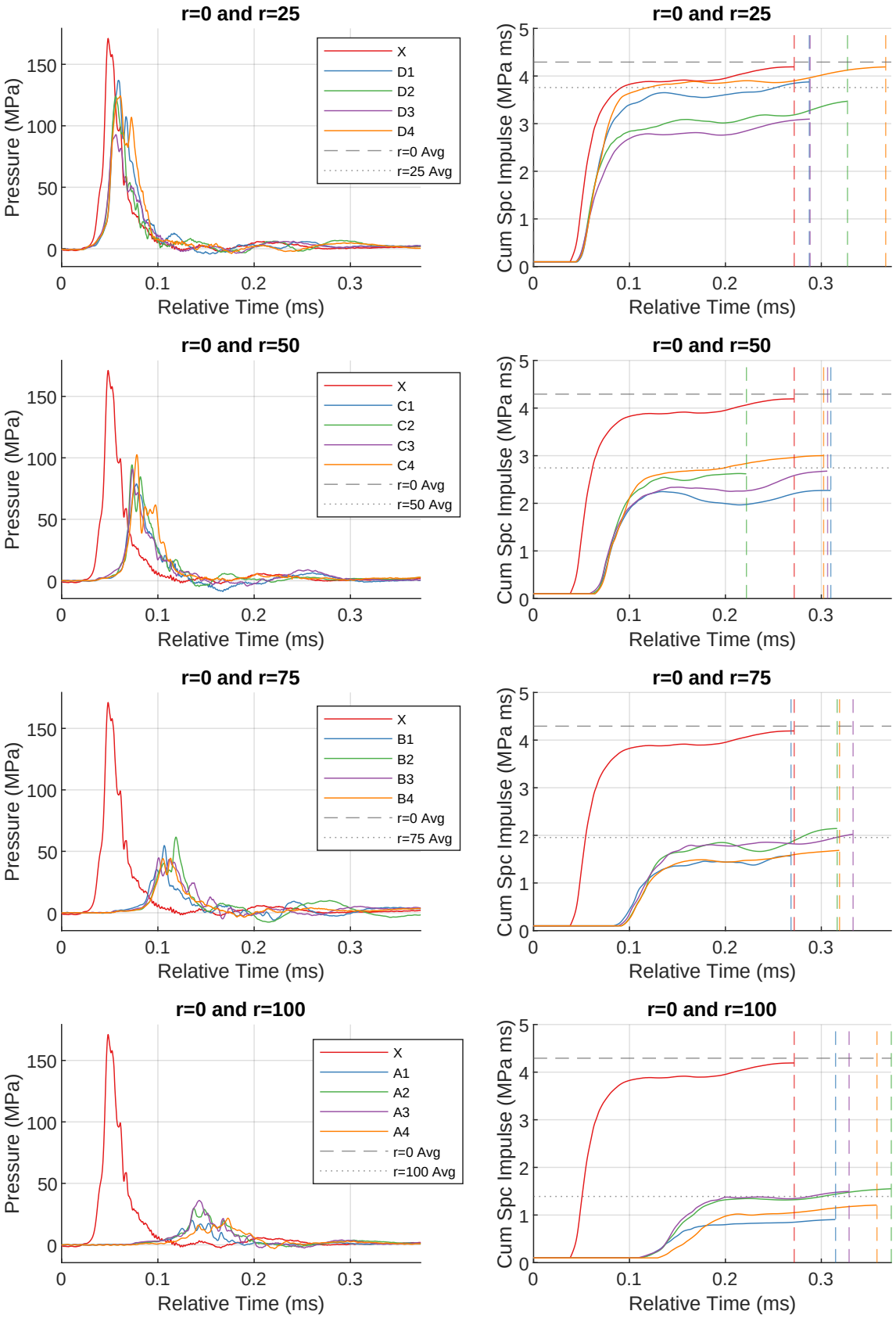

Figure A.14: Shot016pressure (left) and cumulative specific impulse (right) plots for each radial distance.

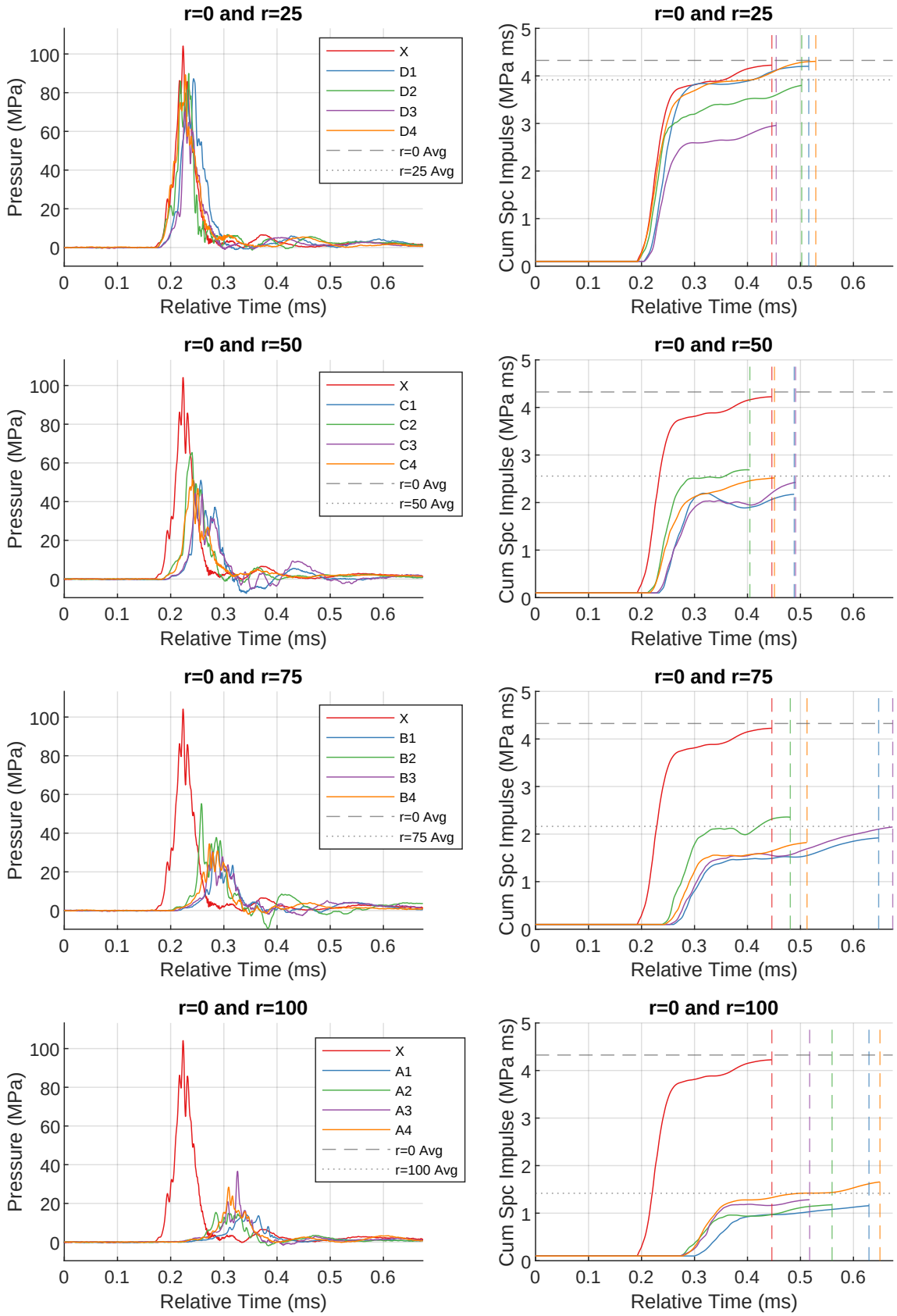

Figure A.15: Shot017pressure (left) and cumulative specific impulse (right) plots for each radial distance.

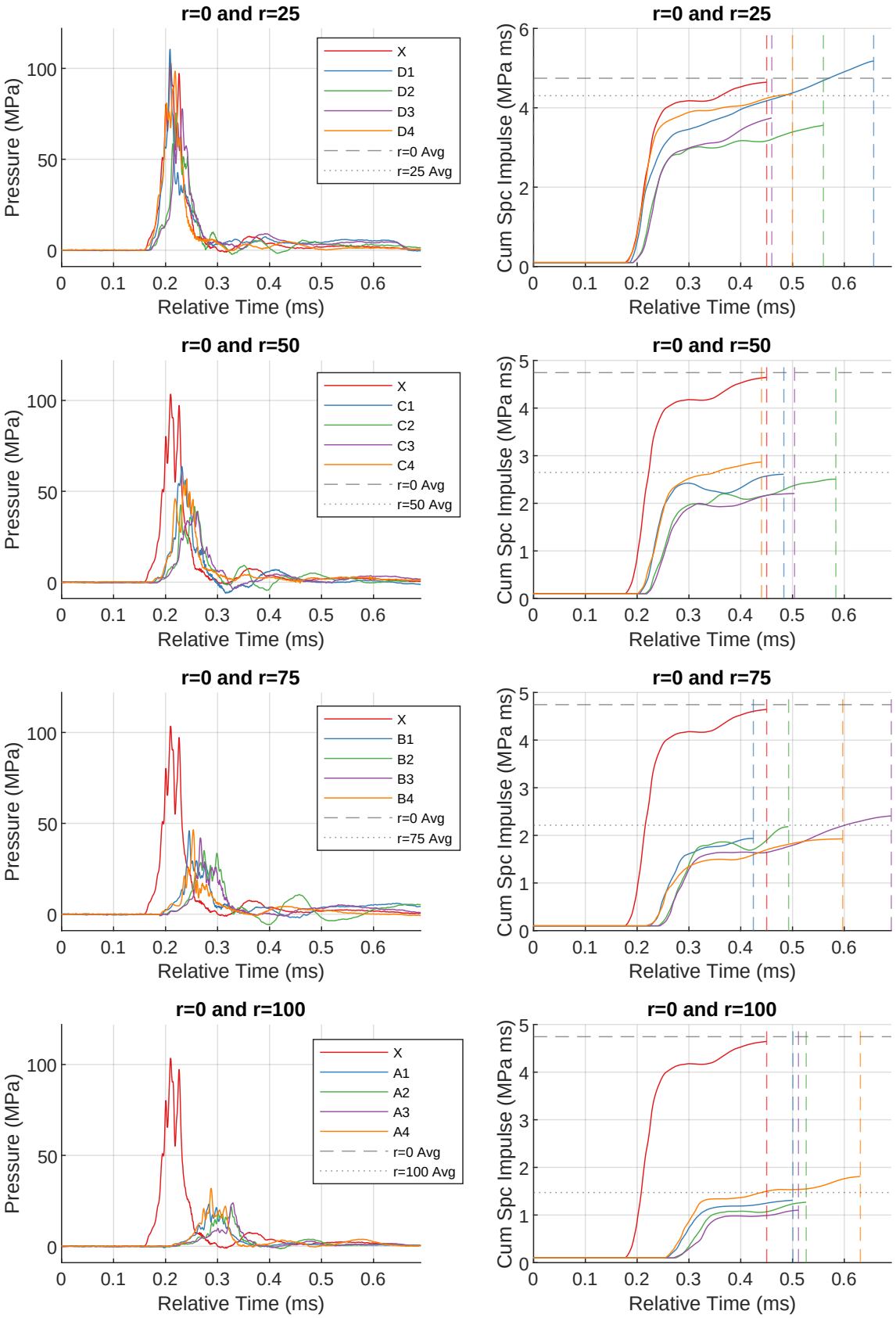

Figure A.16: Shot018pressure (left) and cumulative specific impulse (right) plots for each radial distance.

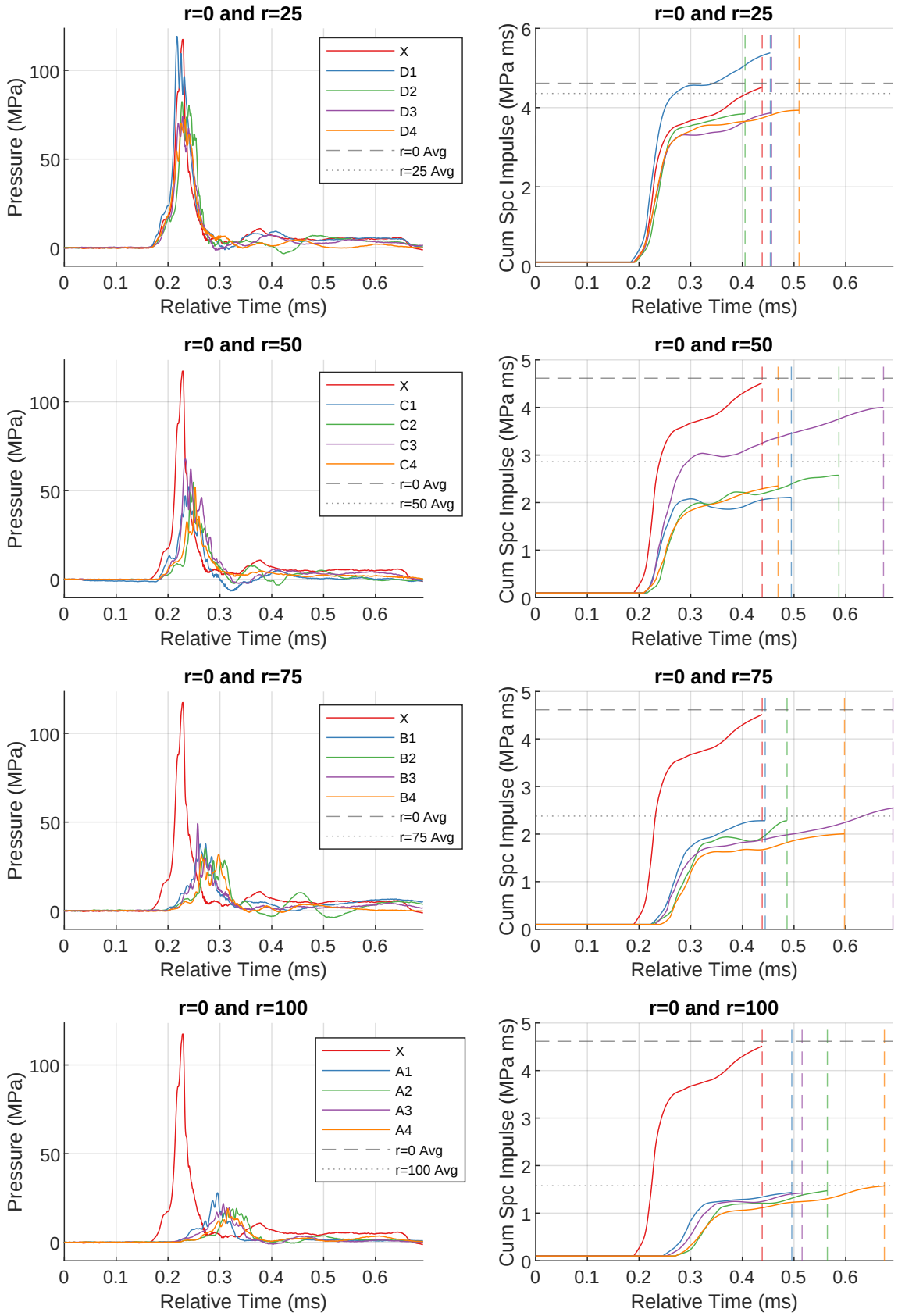

Figure A.17: Shot019pressure (left) and cumulative specific impulse (right) plots for each radial distance.

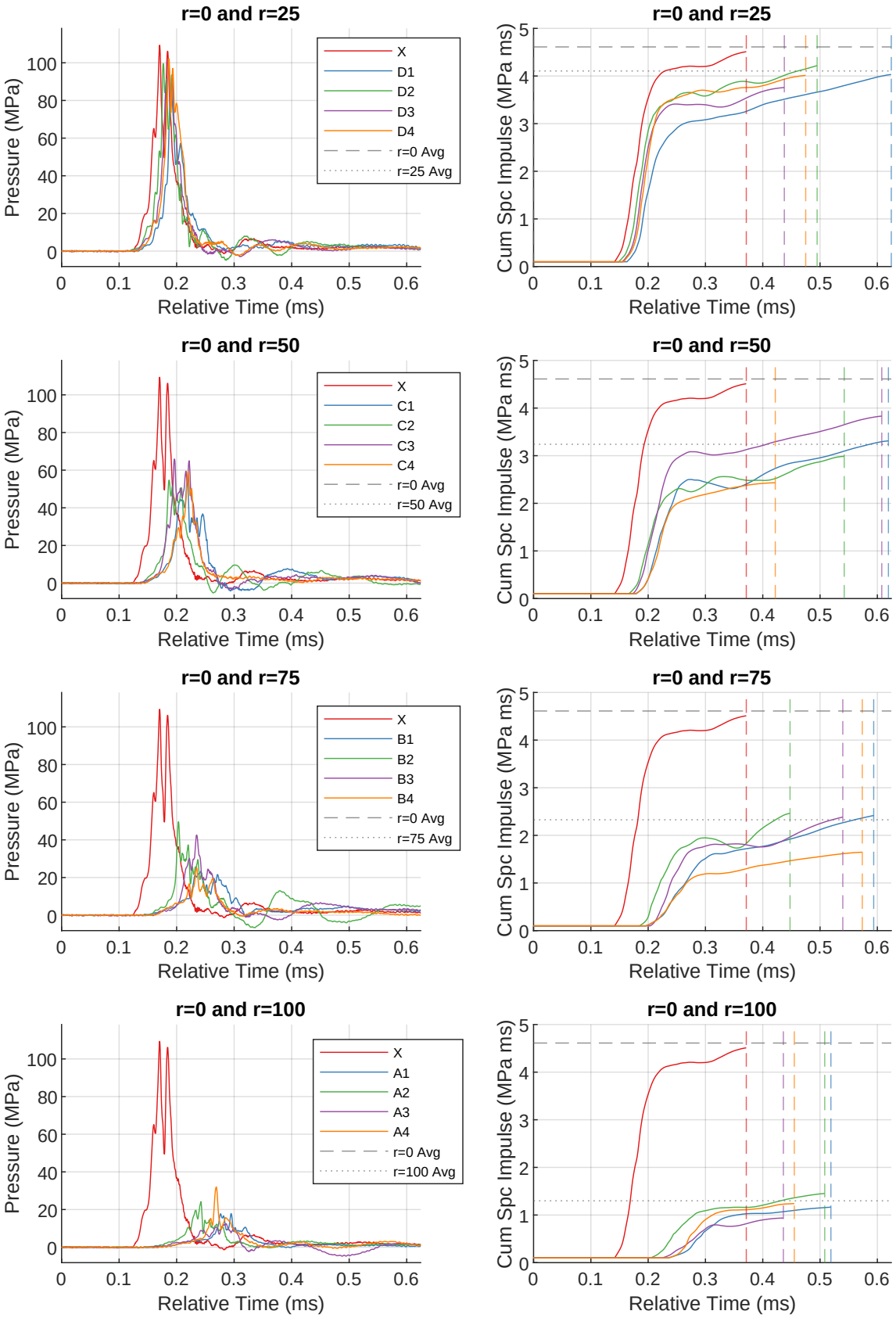

Figure A.18: Shot020pressure (left) and cumulative specific impulse (right) plots for each radial distance.

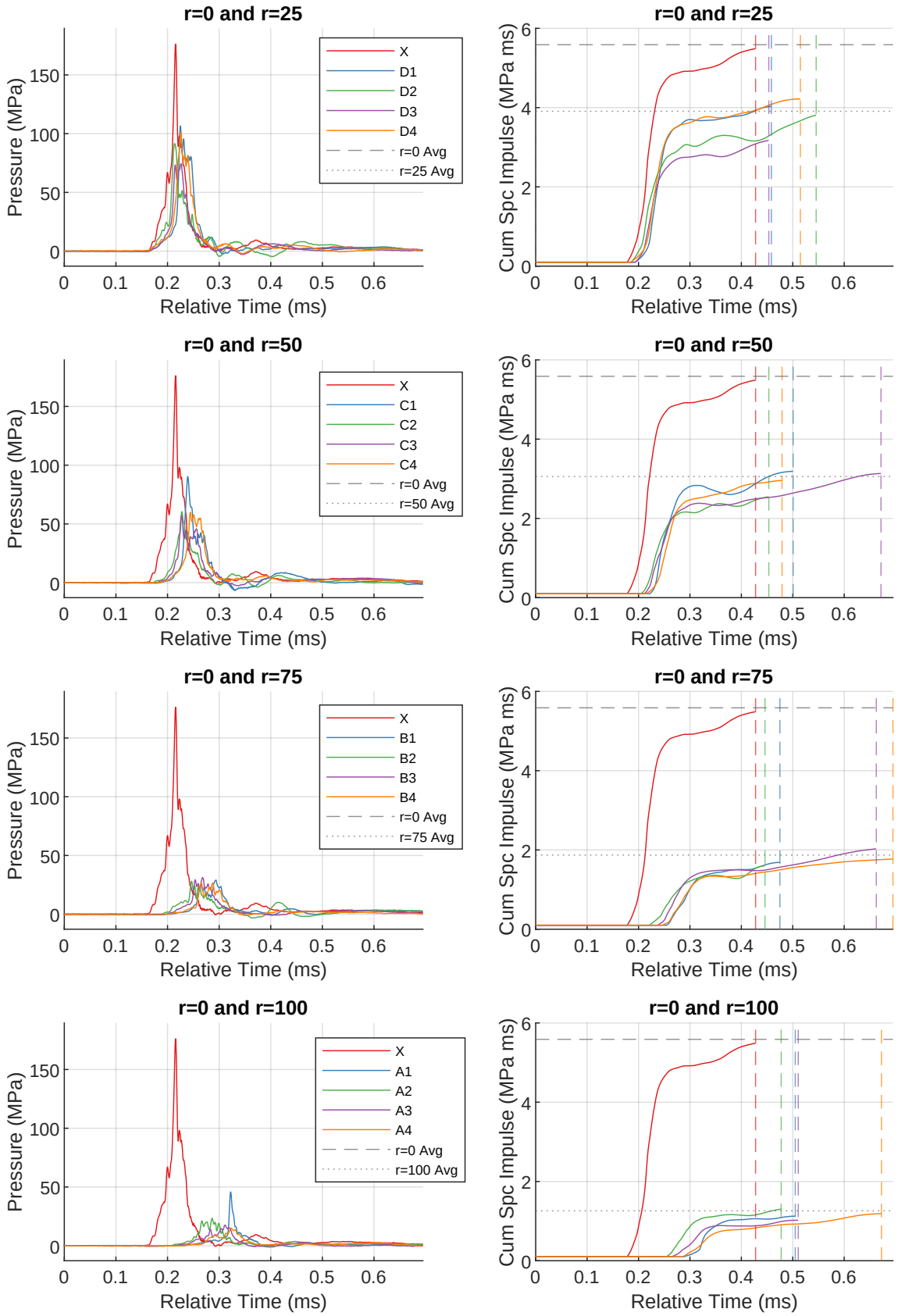

Figure A.19: Shot021pressure (left) and cumulative specific impulse (right) plots for each radial distance.

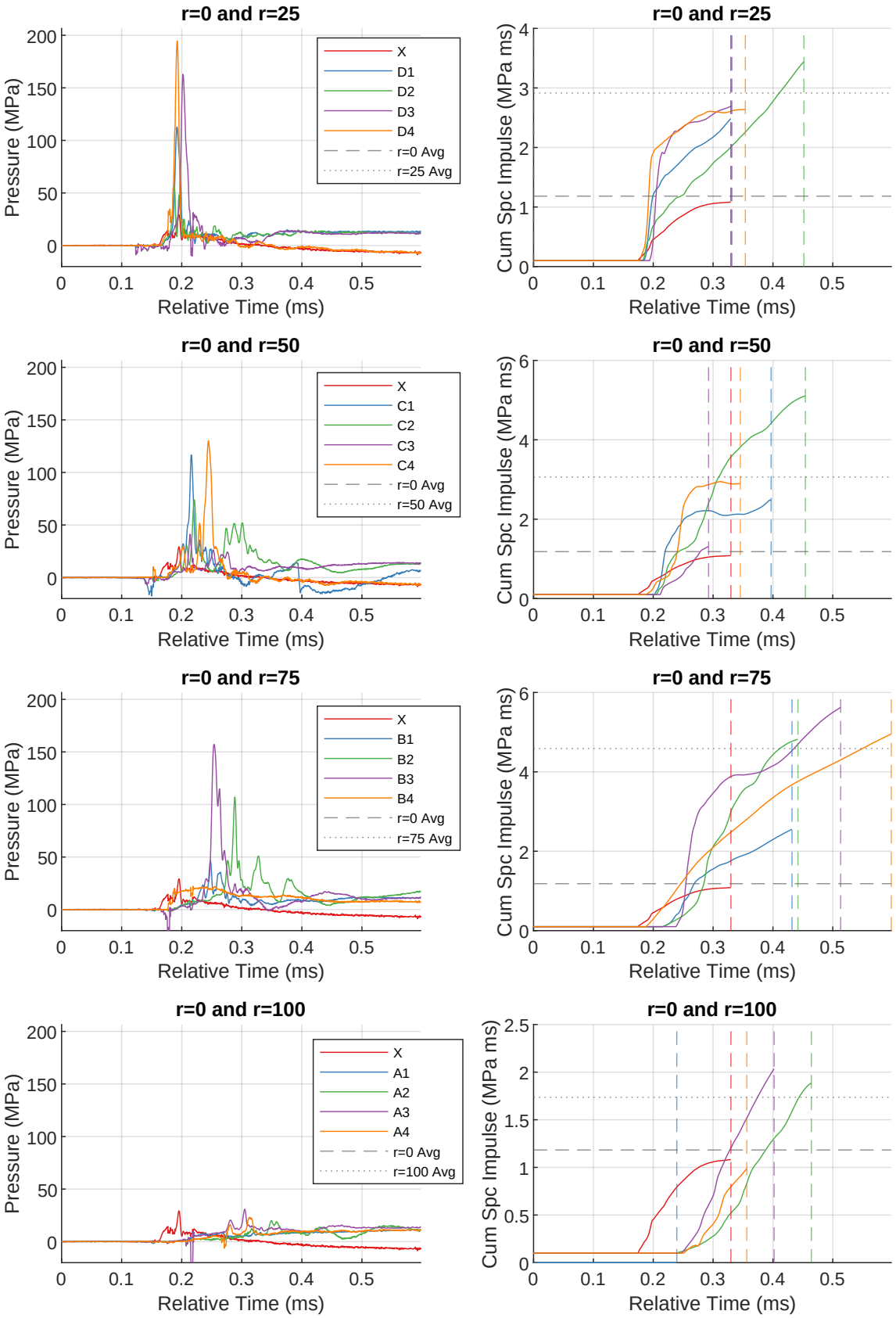

Figure A.20: Shot022pressure (left) and cumulative specific impulse (right) plots for each radial distance.

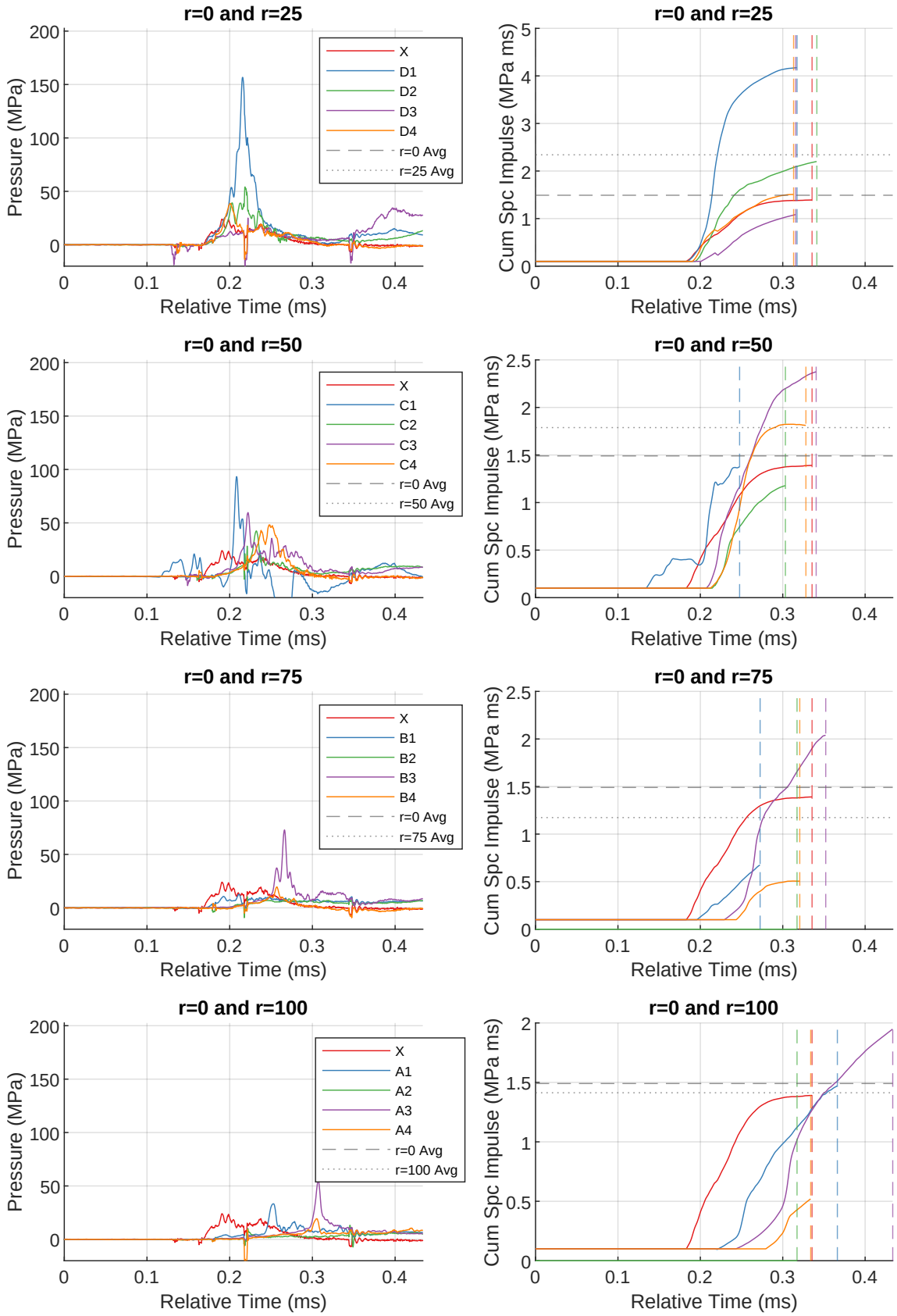

Figure A.21: Shot023pressure (left) and cumulative specific impulse (right) plots for each radial distance.

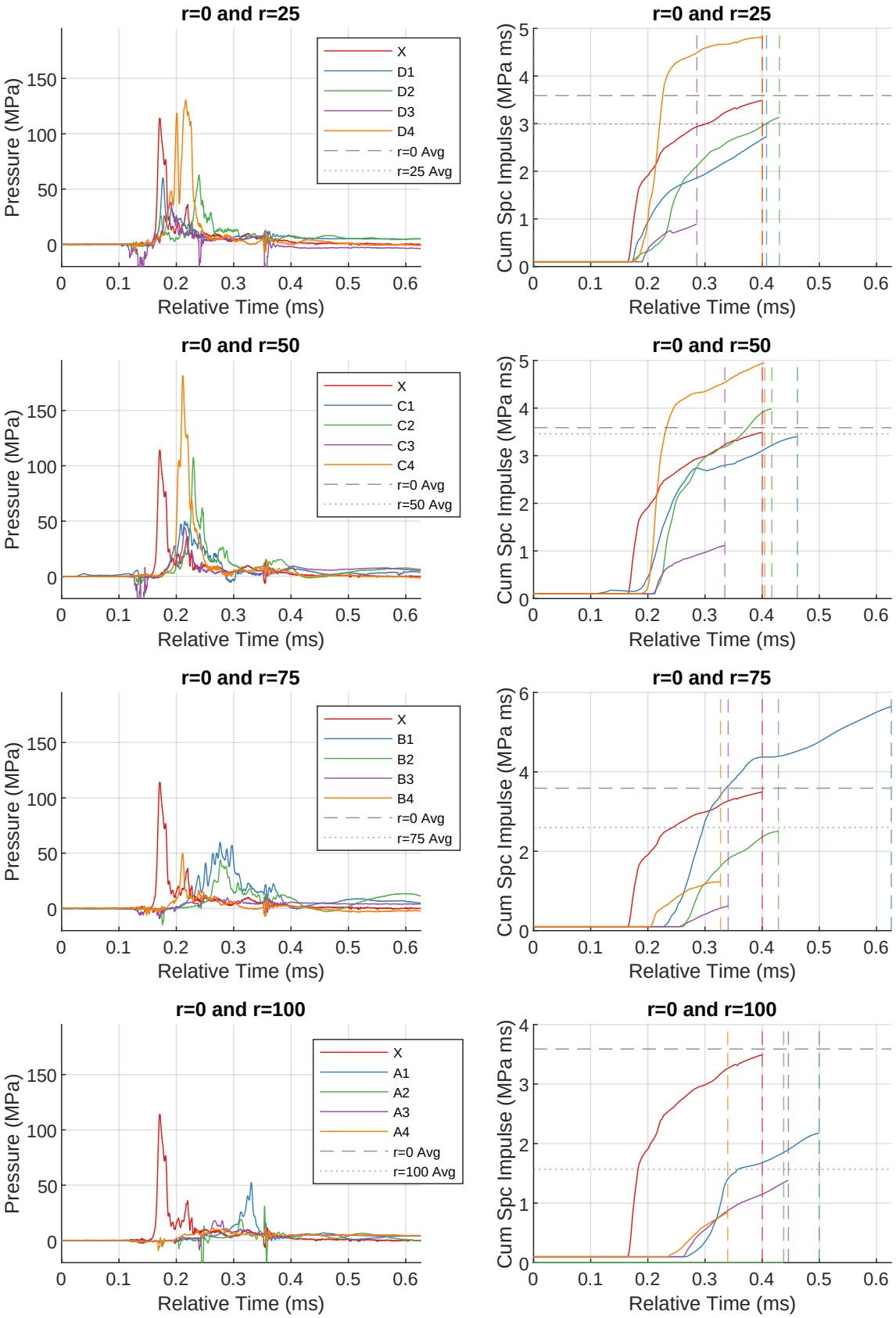

Figure A.22: Shot024pressure (left) and cumulative specific impulse (right) plots for each radial distance.

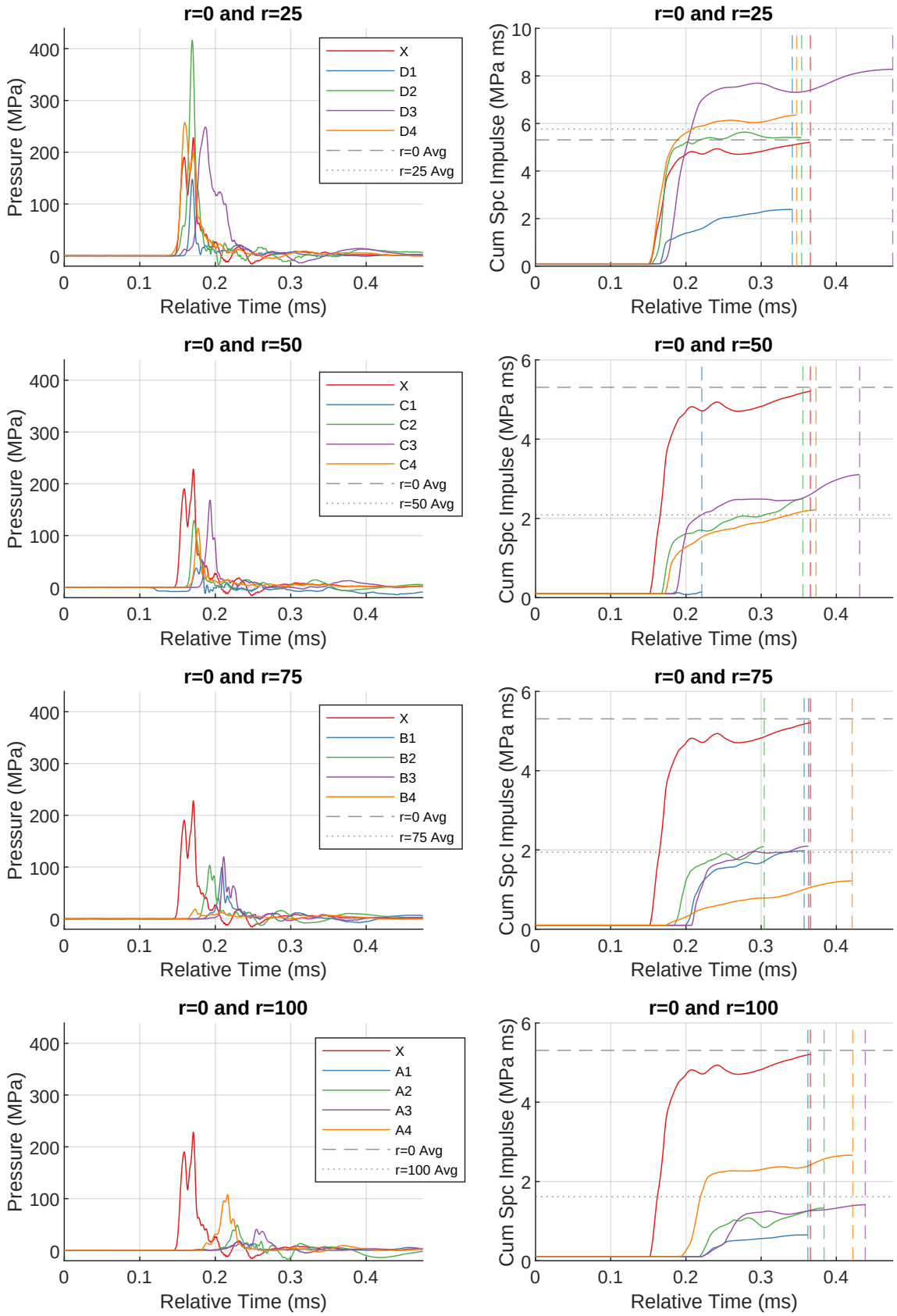

Figure A.23: Shot025pressure (left) and cumulative specific impulse (right) plots for each radial distance.

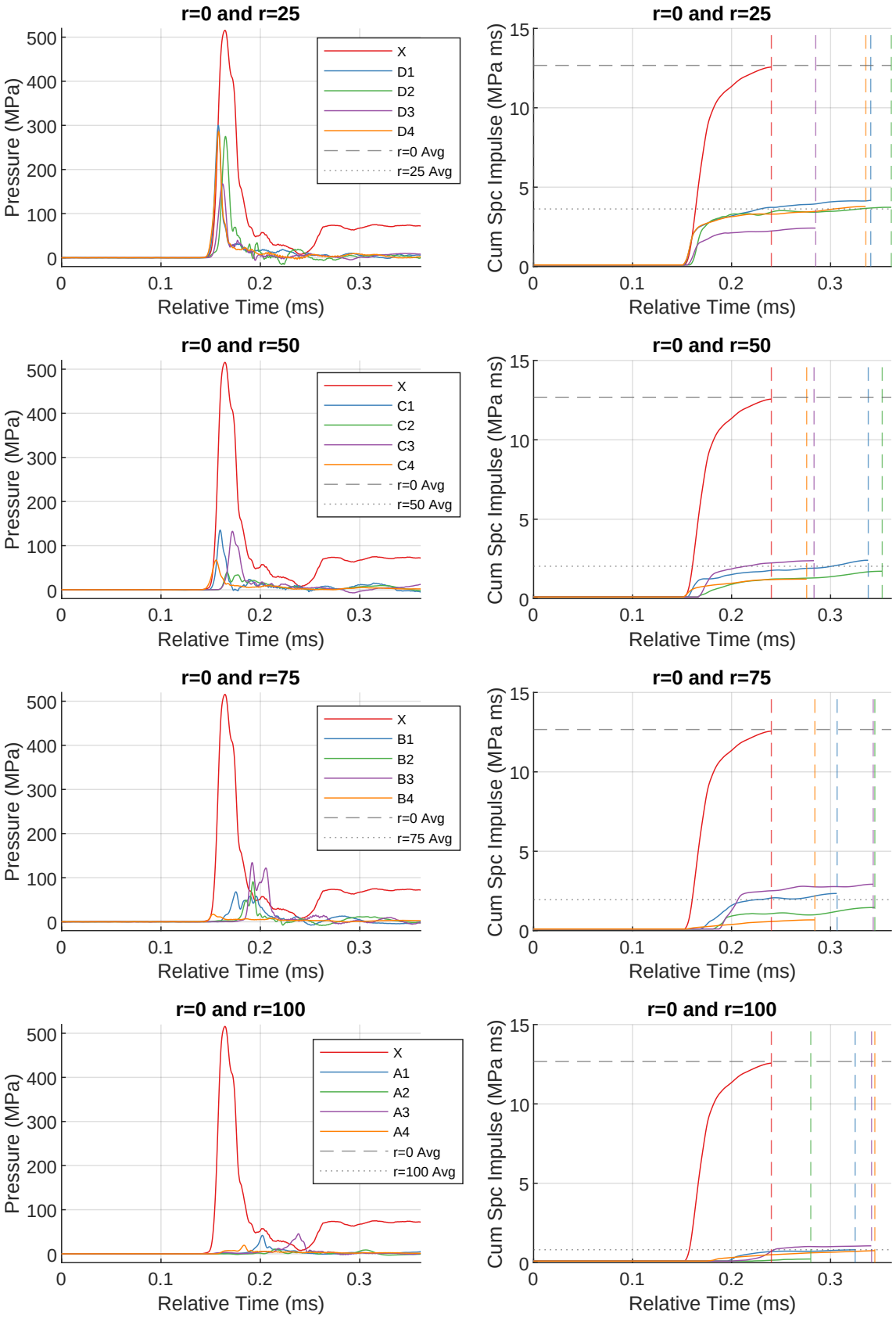

Figure A.24: Shot026pressure (left) and cumulative specific impulse (right) plots for each radial distance.

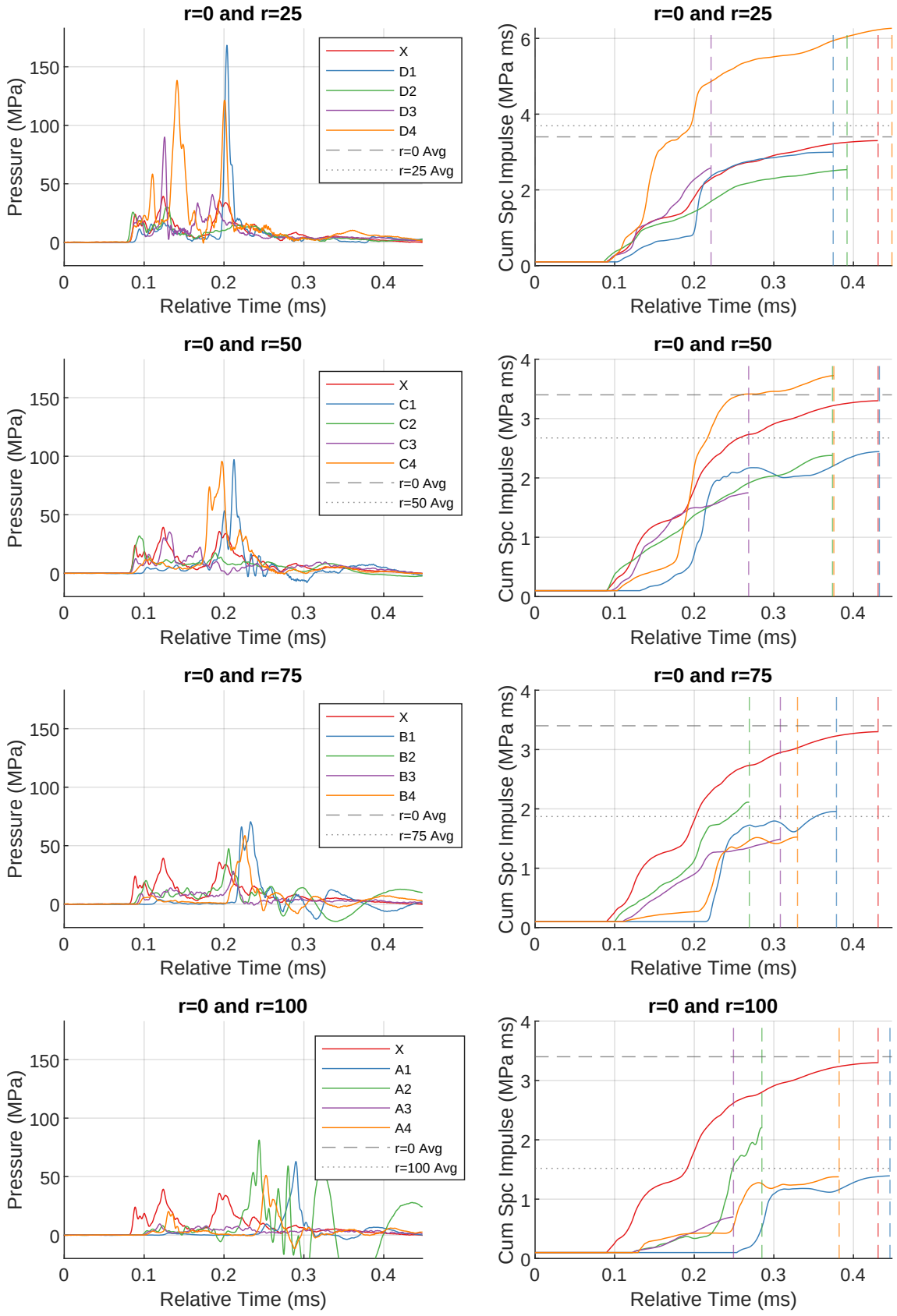

Figure A.25: Shot027pressure (left) and cumulative specific impulse (right) plots for each radial distance.

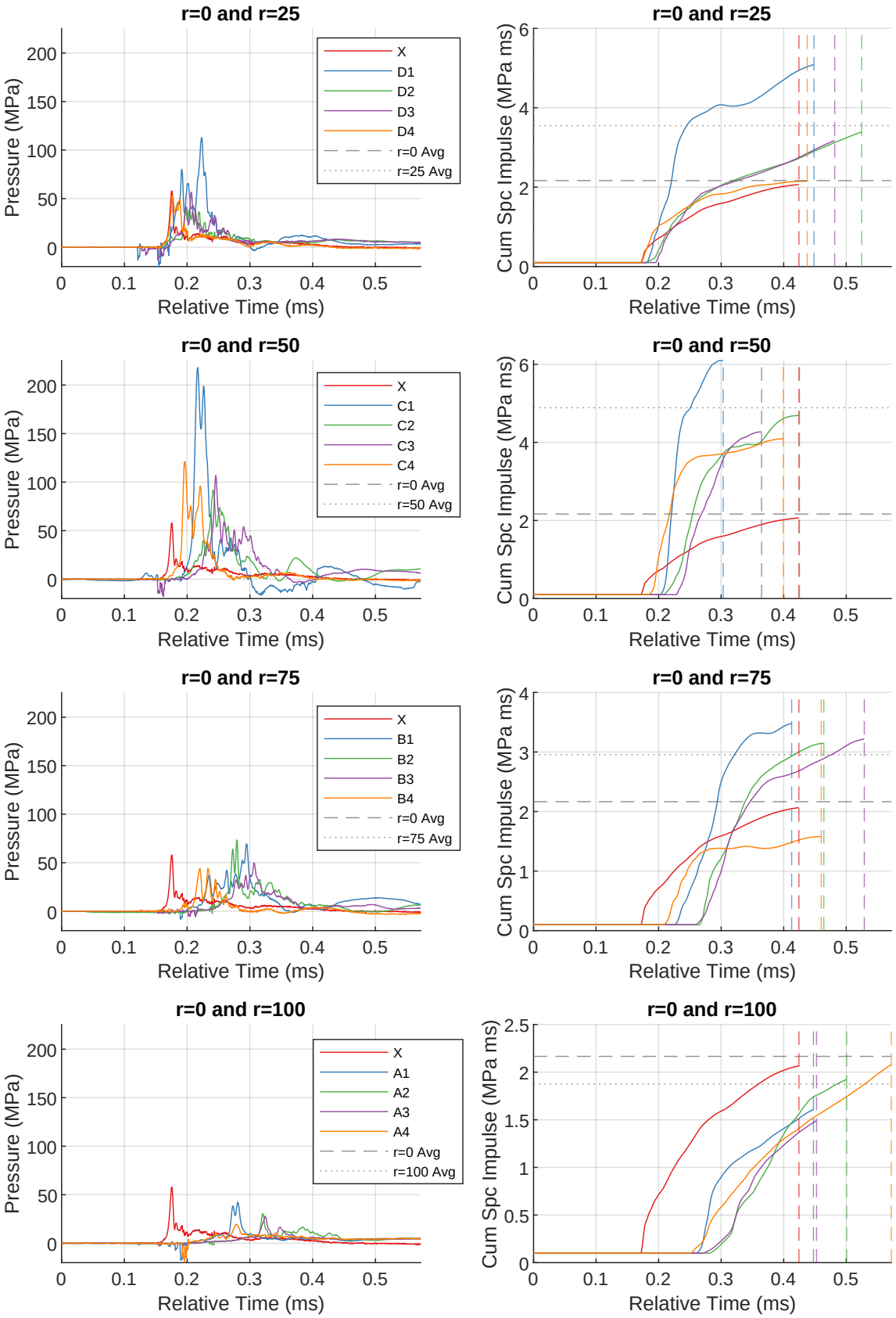

Figure A.26: Shot028pressure (left) and cumulative specific impulse (right) plots for each radial distance.

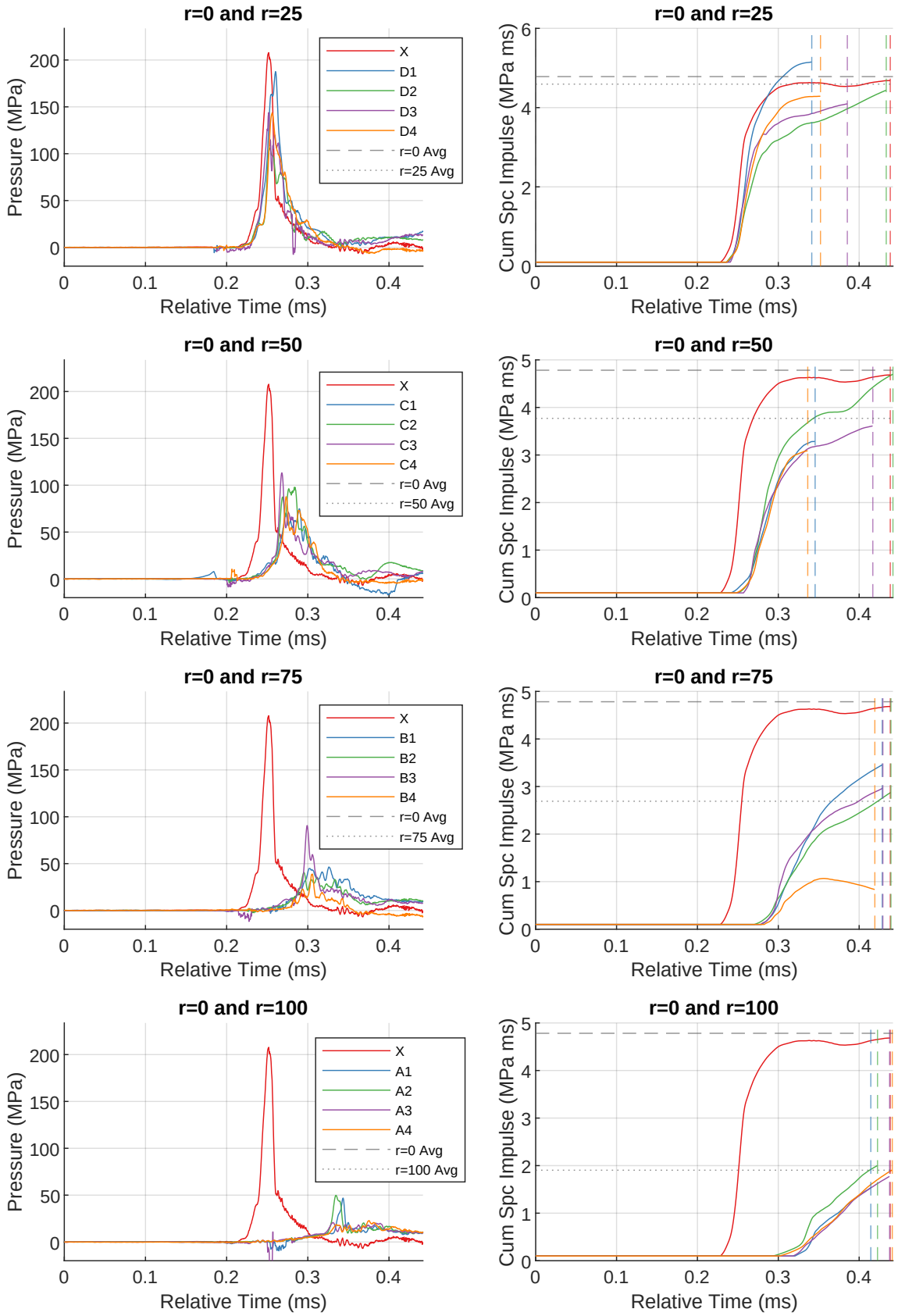

Figure A.27: Shot029pressure (left) and cumulative specific impulse (right) plots for each radial distance.

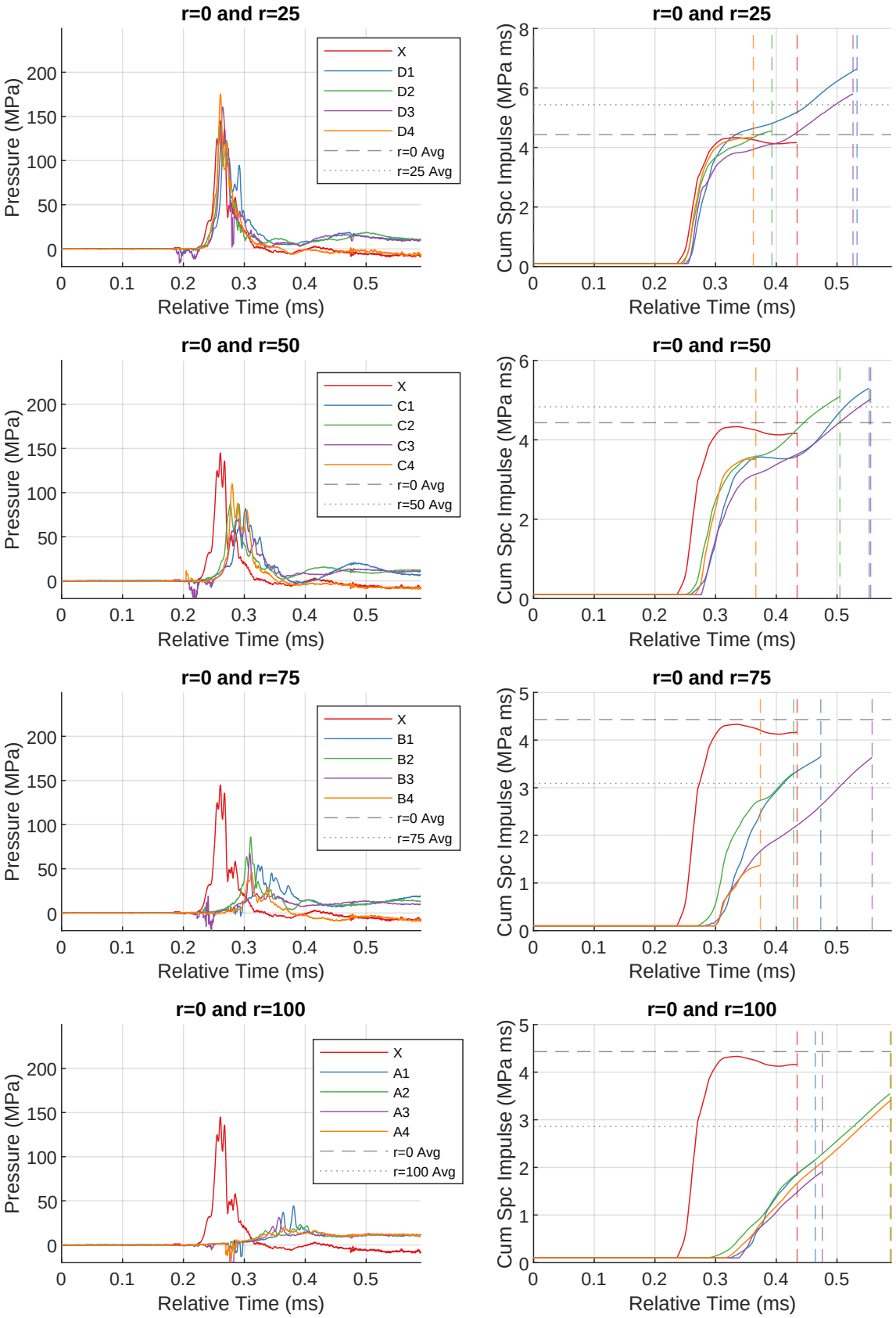

Figure A.28: Shot030pressure (left) and cumulative specific impulse (right) plots for each radial distance.

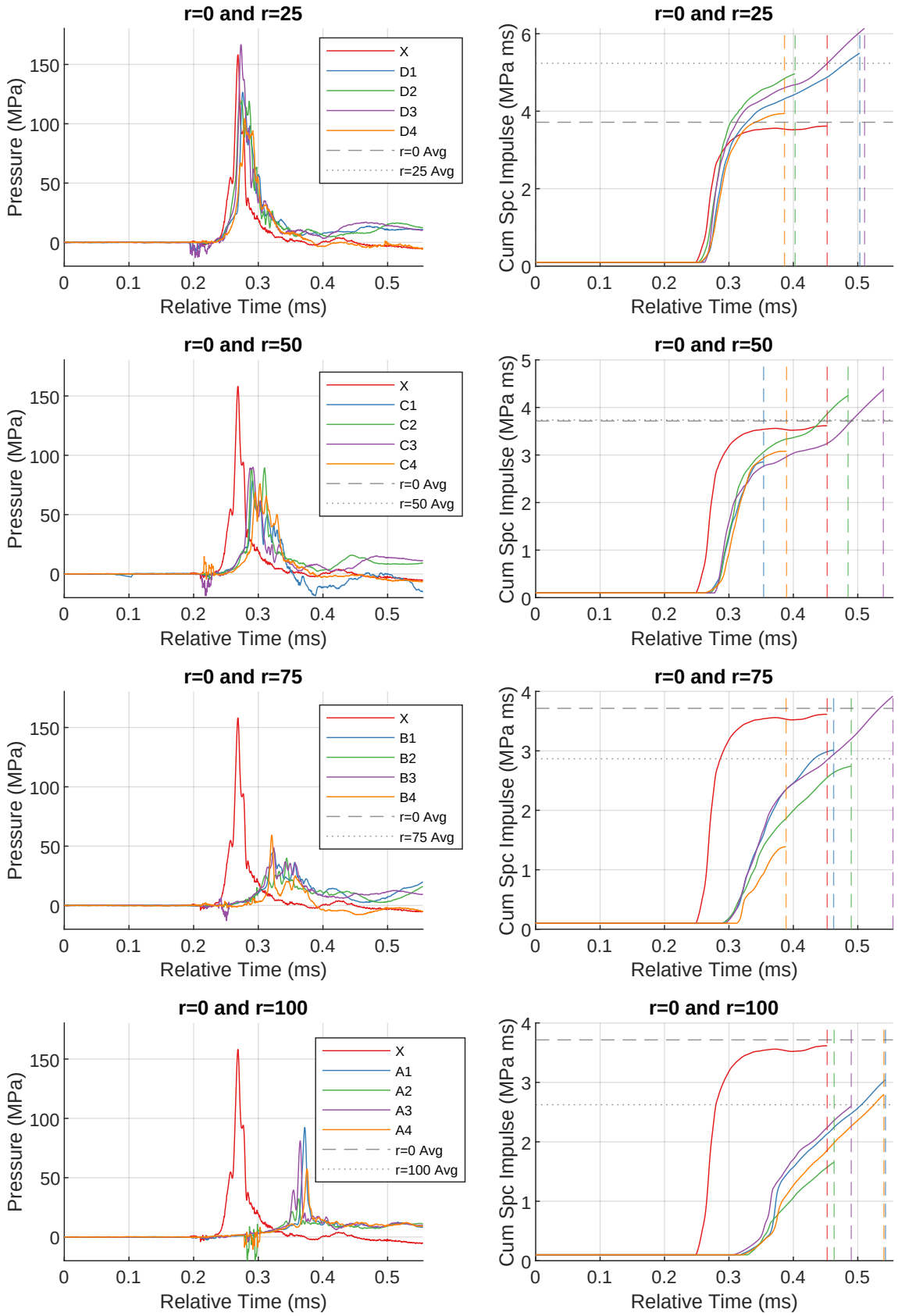

Figure A.29: Shot031pressure (left) and cumulative specific impulse (right) plots for each radial distance.

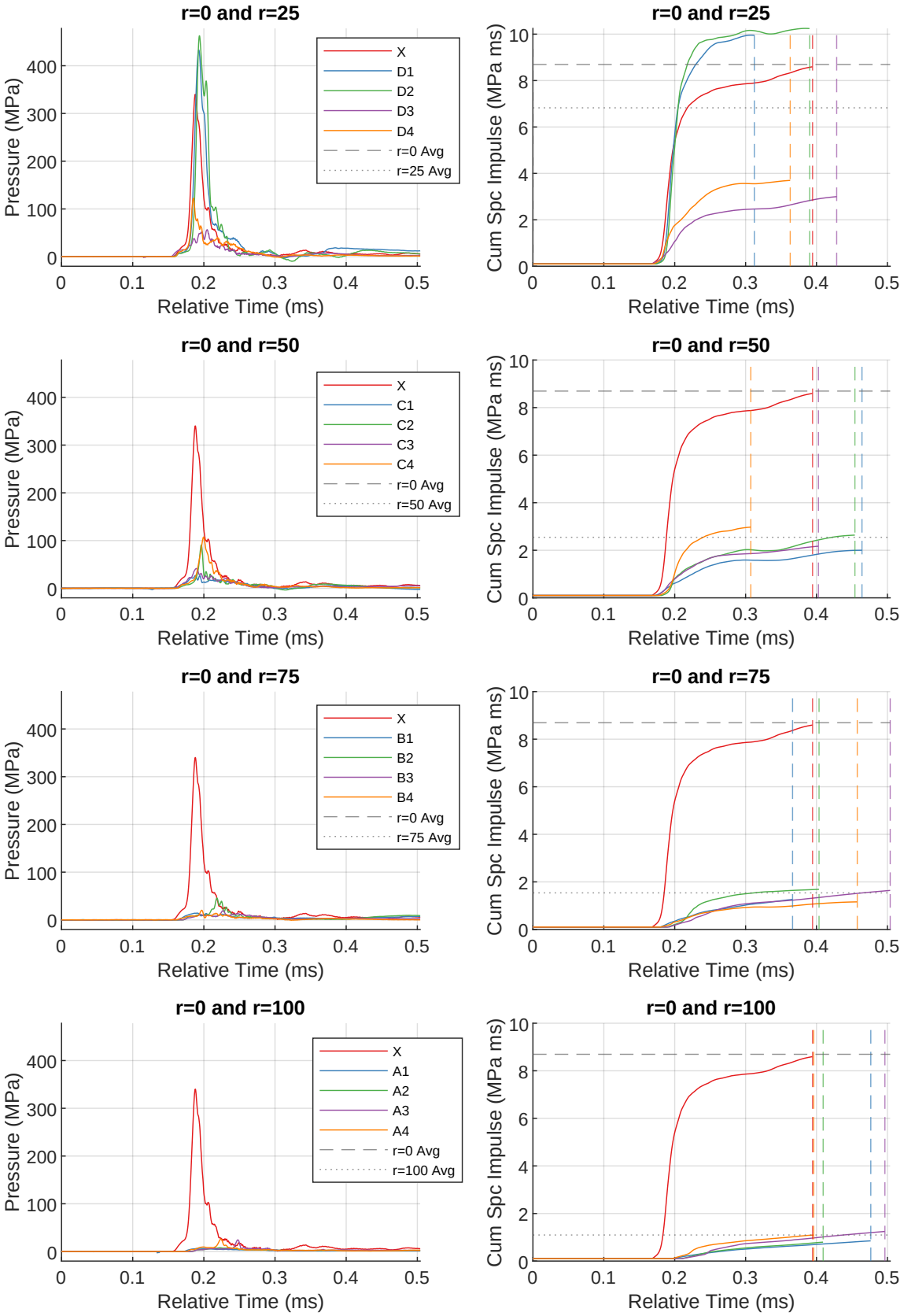

Figure A.30: Shot032pressure (left) and cumulative specific impulse (right) plots for each radial distance.

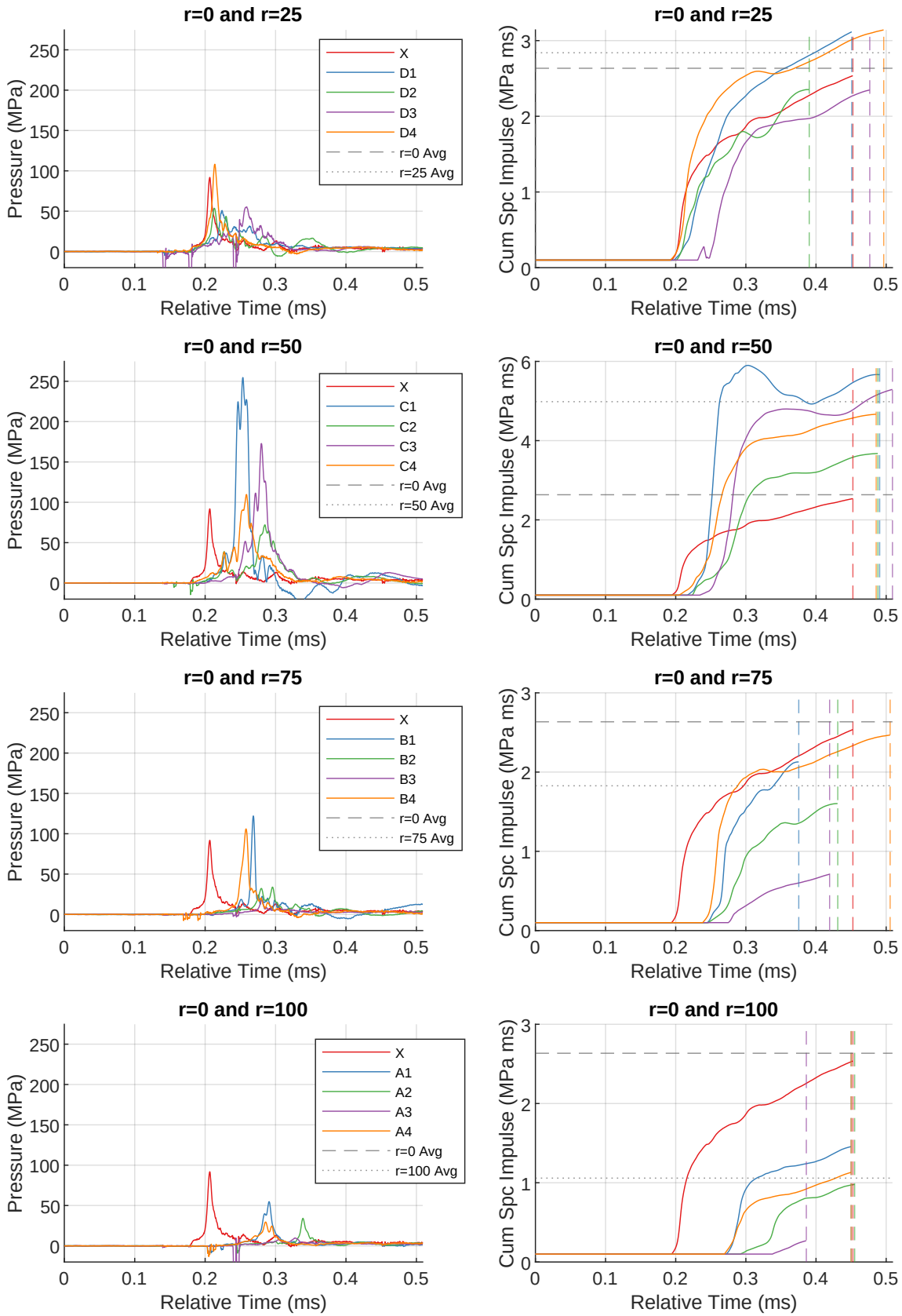

Figure A.31: Shot033pressure (left) and cumulative specific impulse (right) plots for each radial distance.

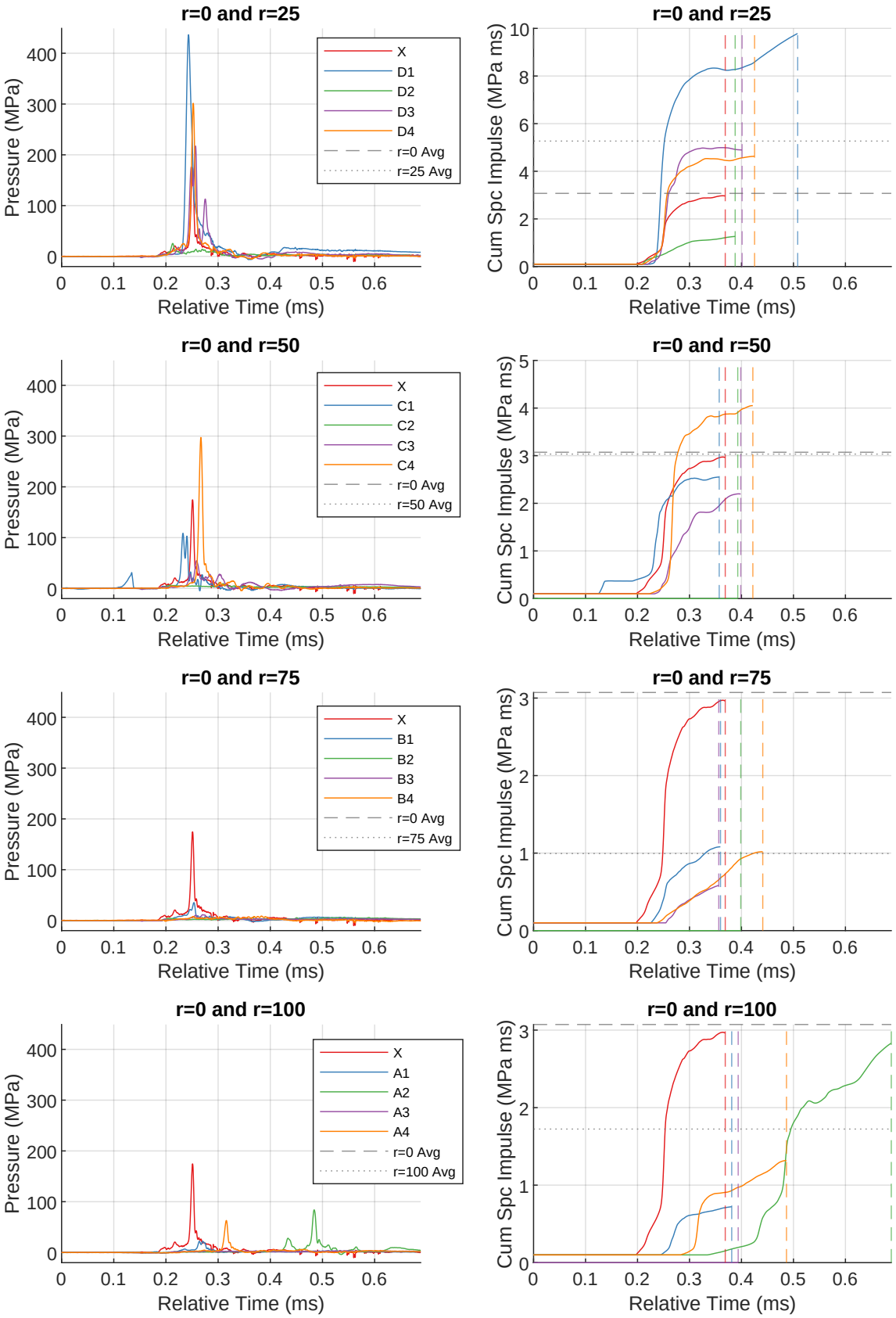

Figure A.32: Shot034pressure (left) and cumulative specific impulse (right) plots for each radial distance.

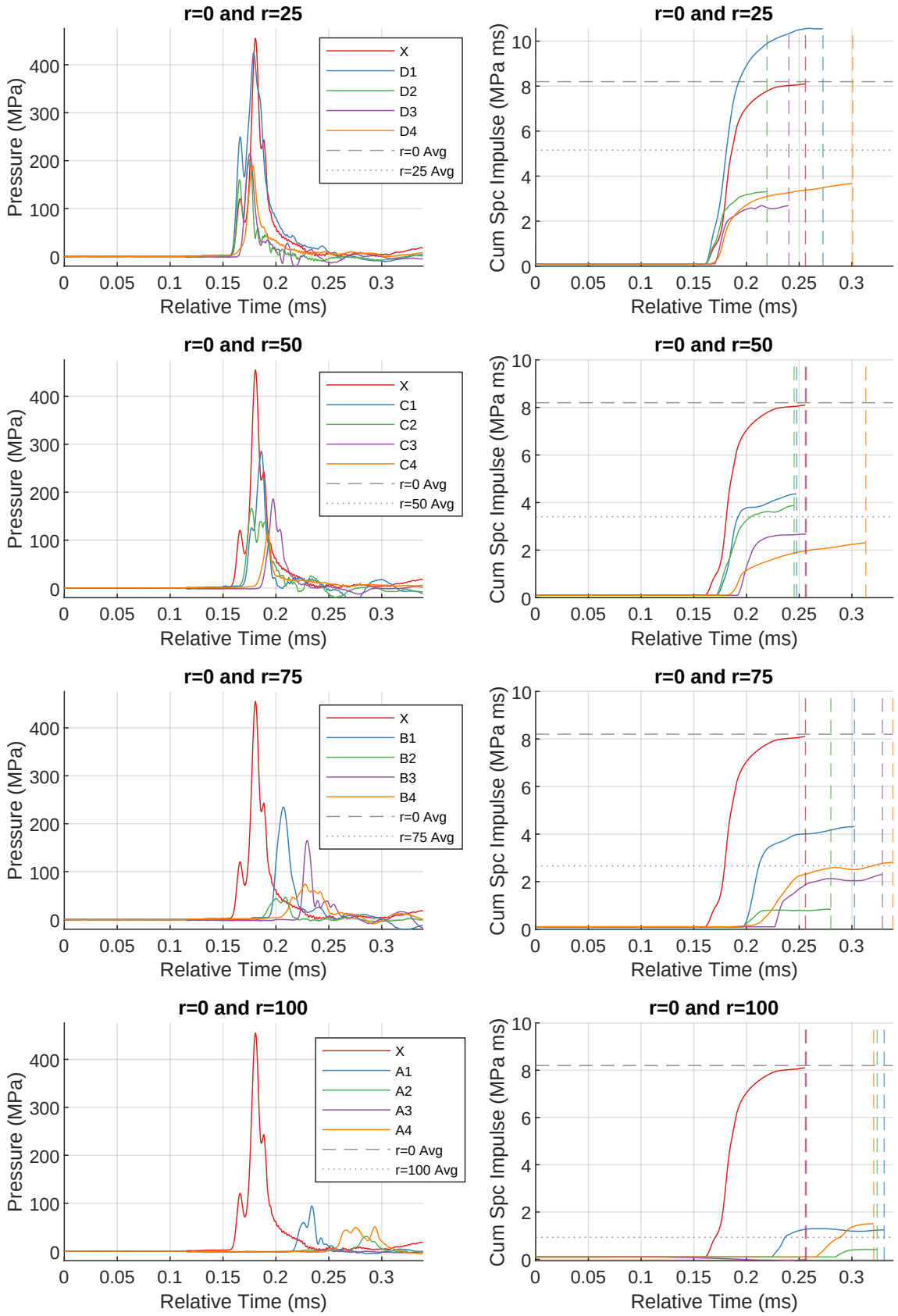

Figure A.33: Shot037pressure (left) and cumulative specific impulse (right) plots for each radial distance.

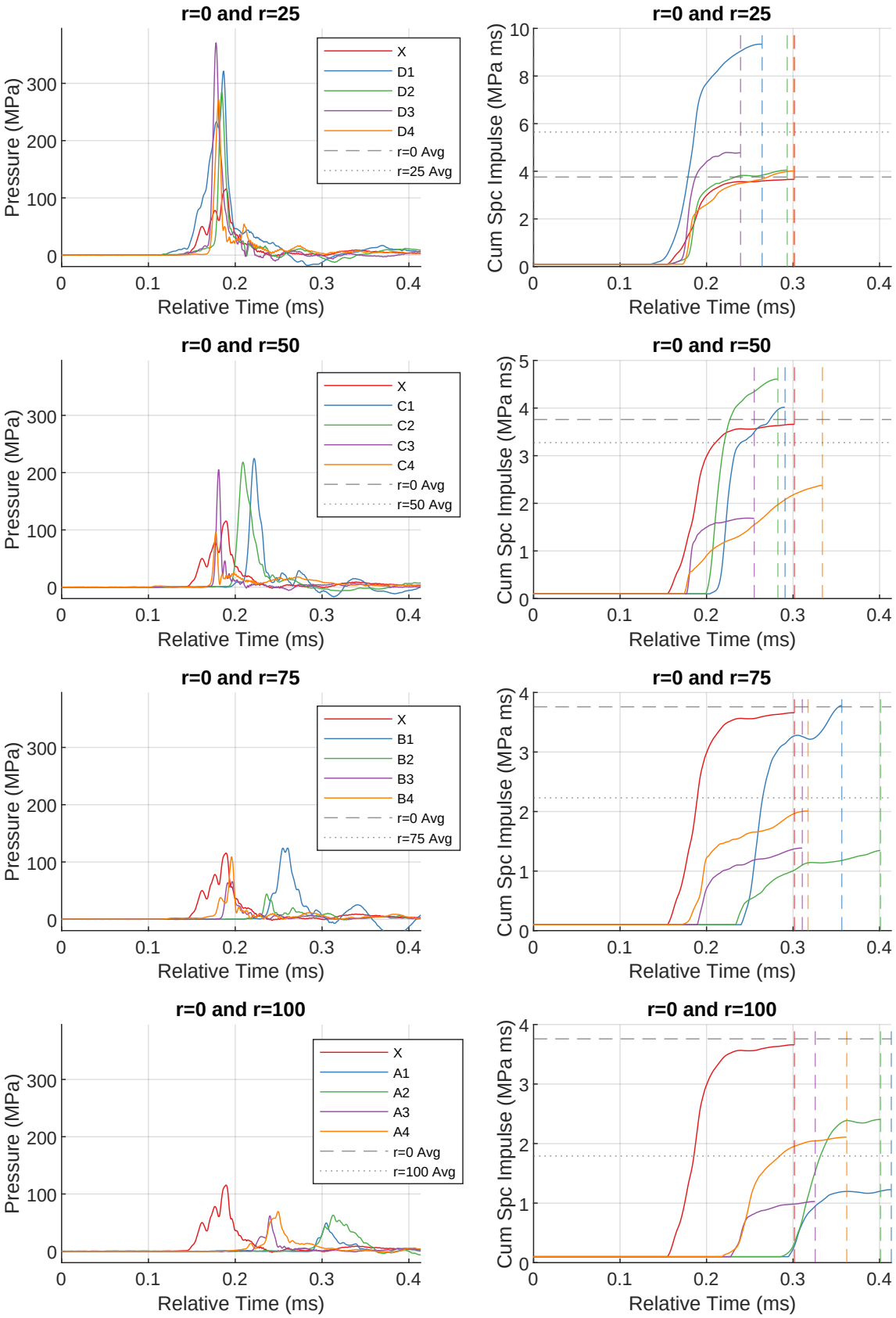

Figure A.34: Shot038pressure (left) and cumulative specific impulse (right) plots for each radial distance.

A.2 HSV tracking - Shock and Ejecta

As described in §4.2.2, the following plots show the shape of the shock wave and ejecta as determined from analysis of the high speed video. Comparisons between the different test series is made within the main body of the thesis, with the full results included here for reference

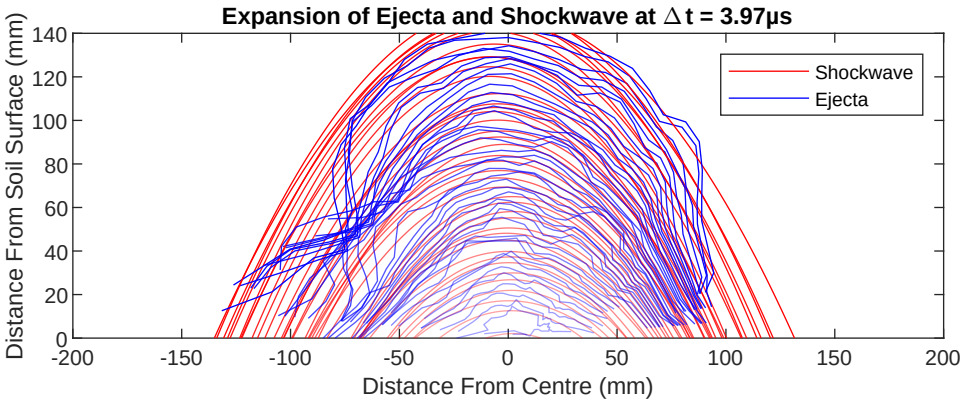

Figure A.35: Shot003HSV tracking showing the detected shockwave and ejecta clouds.

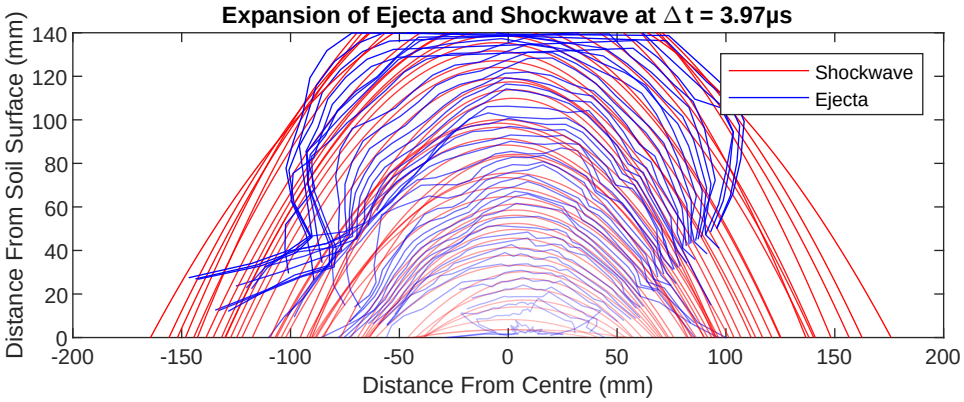

Figure A.36: Shot005HSV tracking showing the detected shockwave and ejecta clouds.

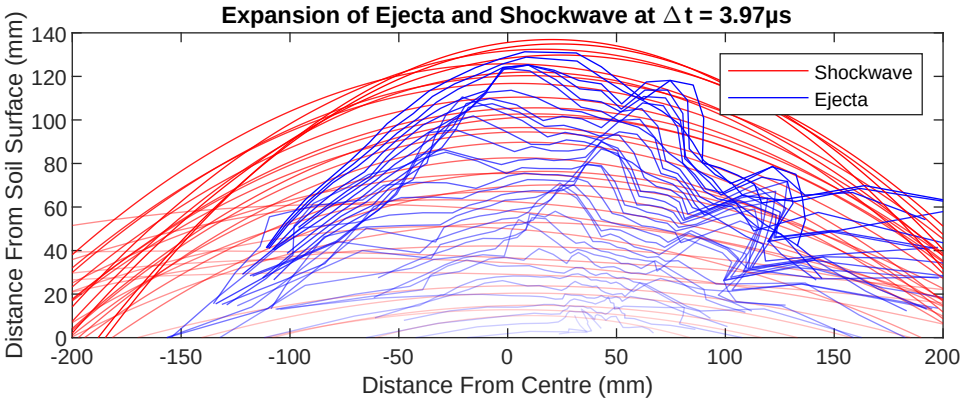

Figure A.37: Shot006HSV tracking showing the detected shockwave and ejecta clouds.

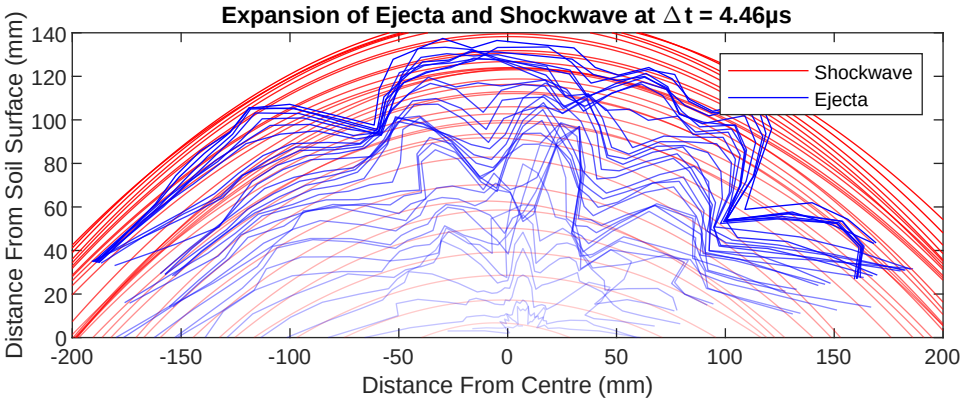

Figure A.38: Shot007HSV tracking showing the detected shockwave and ejecta clouds.

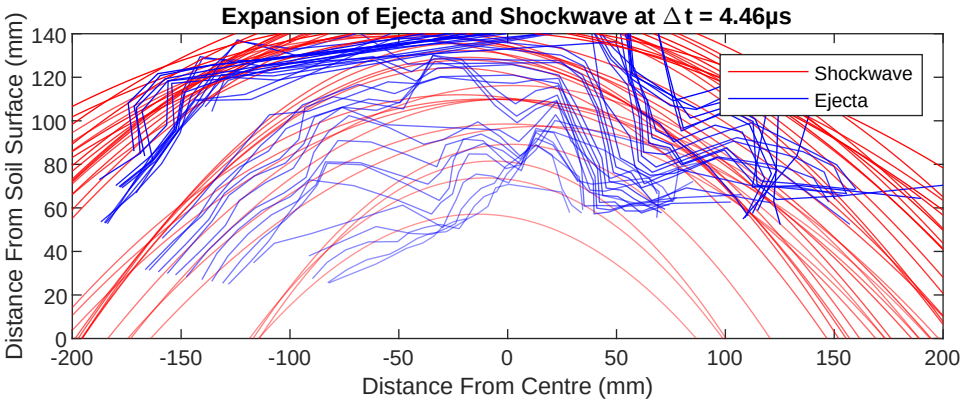

Figure A.39: Shot008HSV tracking showing the detected shockwave and ejecta clouds.

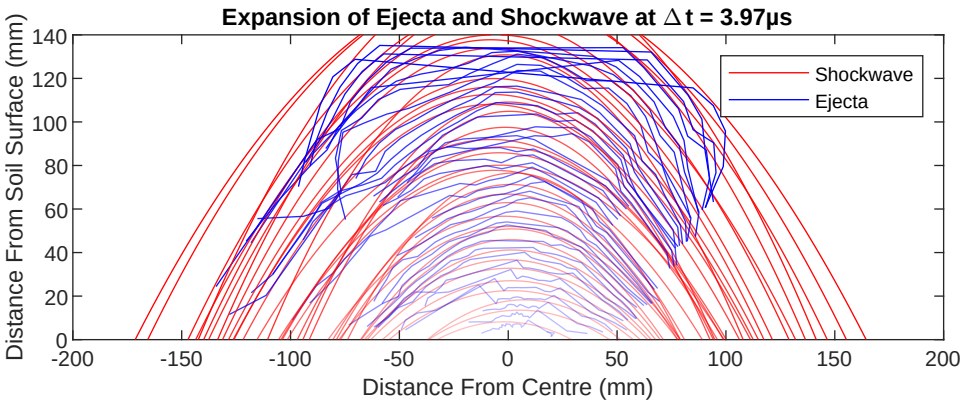

Figure A.40: Shot009HSV tracking showing the detected shockwave and ejecta clouds.

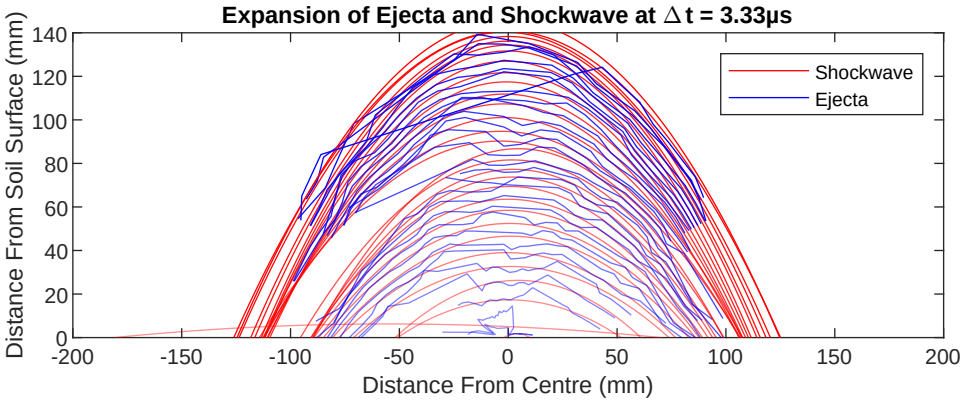

Figure A.41: Shot011HSV tracking showing the detected shockwave and ejecta clouds.

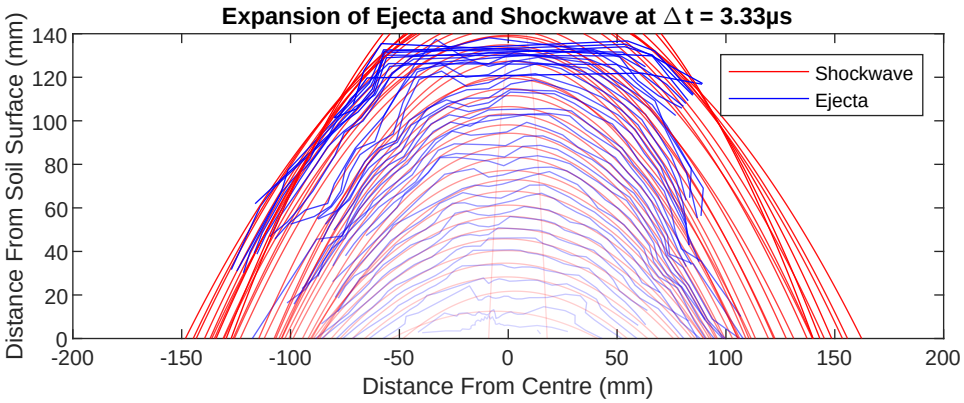

Figure A.42: Shot012HSV tracking showing the detected shockwave and ejecta clouds.

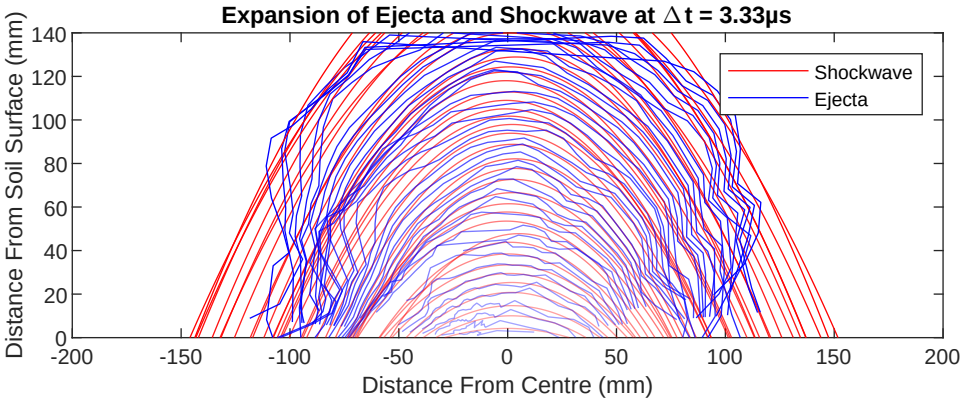

Figure A.43: Shot013HSV tracking showing the detected shockwave and ejecta clouds.

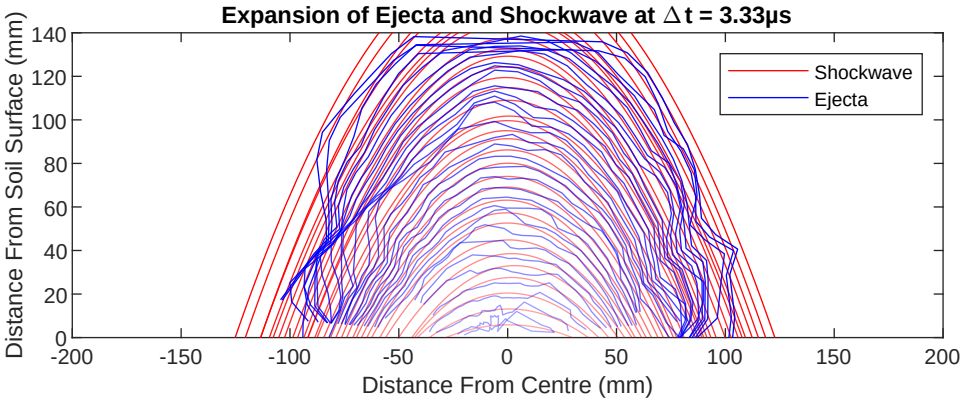

Figure A.44: Shot014HSV tracking showing the detected shockwave and ejecta clouds.

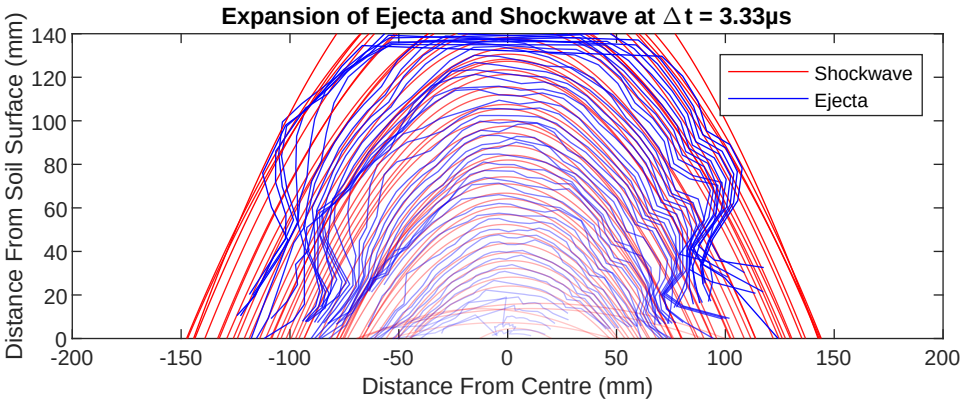

Figure A.45: Shot016HSV tracking showing the detected shockwave and ejecta clouds.

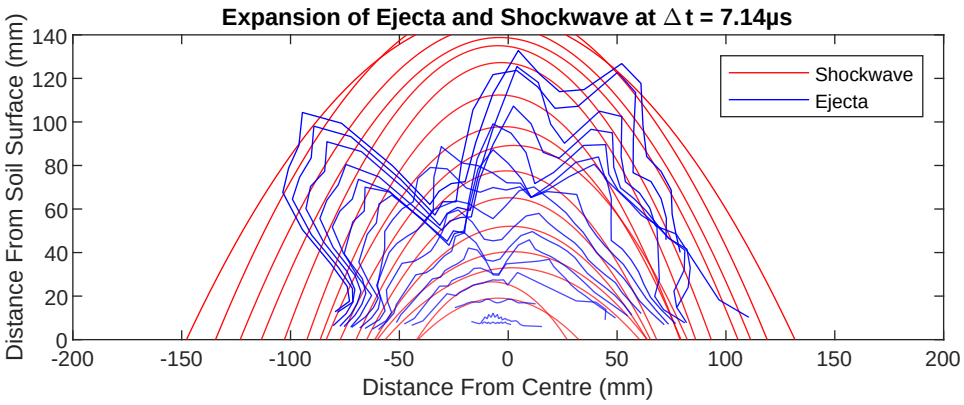

Figure A.46: Shot022HSV tracking showing the detected shockwave and ejecta clouds.

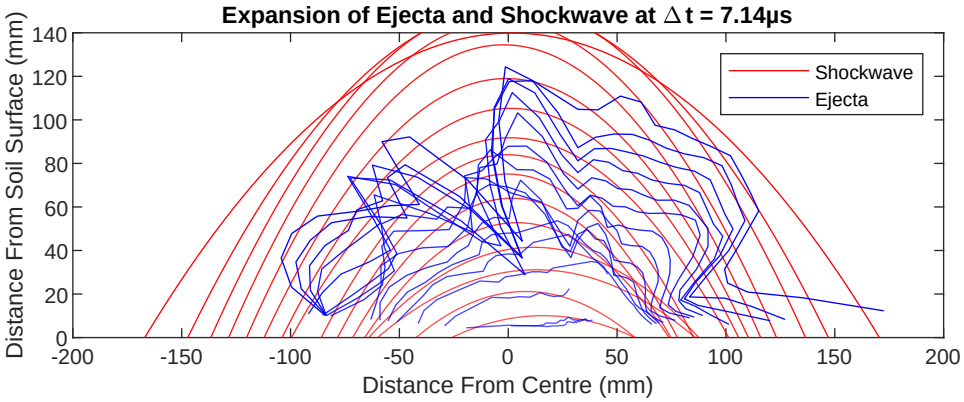

Figure A.47: Shot023HSV tracking showing the detected shockwave and ejecta clouds.

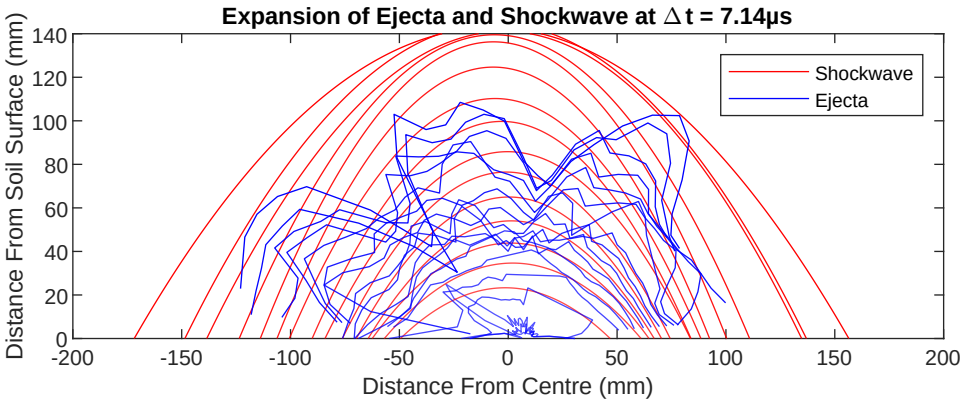

Figure A.48: Shot024HSV tracking showing the detected shockwave and ejecta clouds.

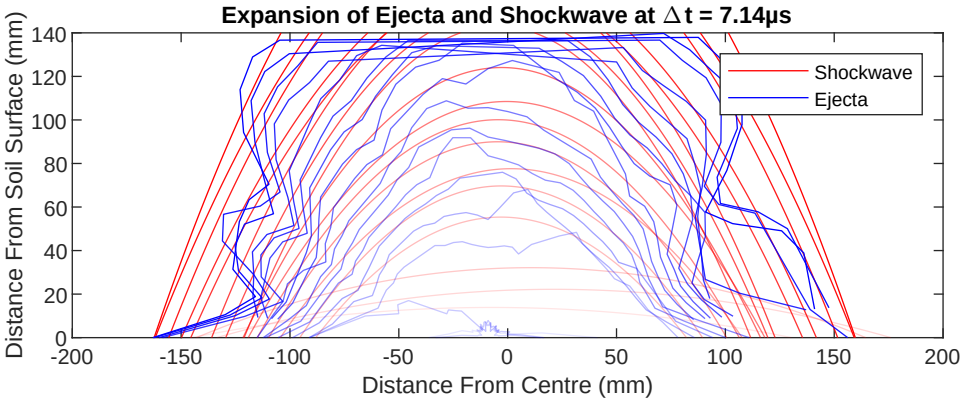

Figure A.49: Shot025HSV tracking showing the detected shockwave and ejecta clouds.

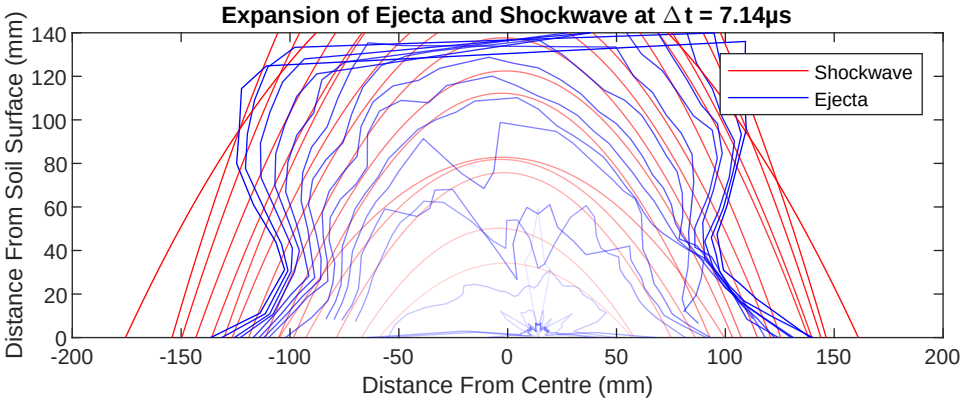

Figure A.50: Shot026HSV tracking showing the detected shockwave and ejecta clouds.

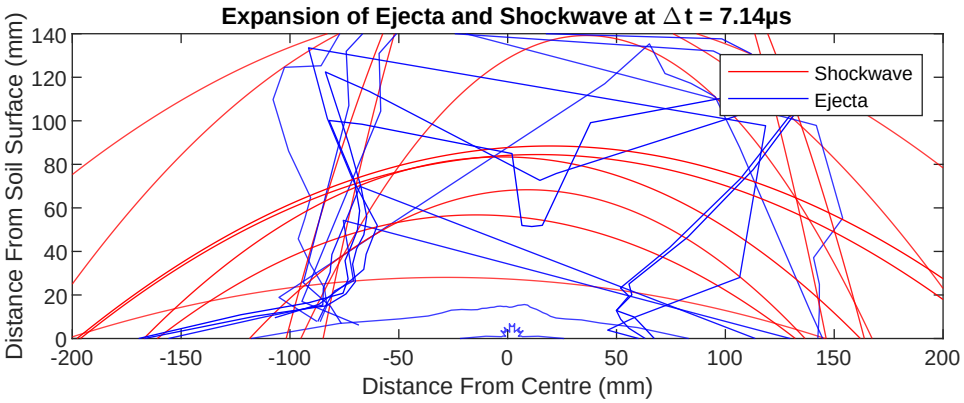

Figure A.51: Shot027HSV tracking showing the detected shockwave and ejecta clouds.

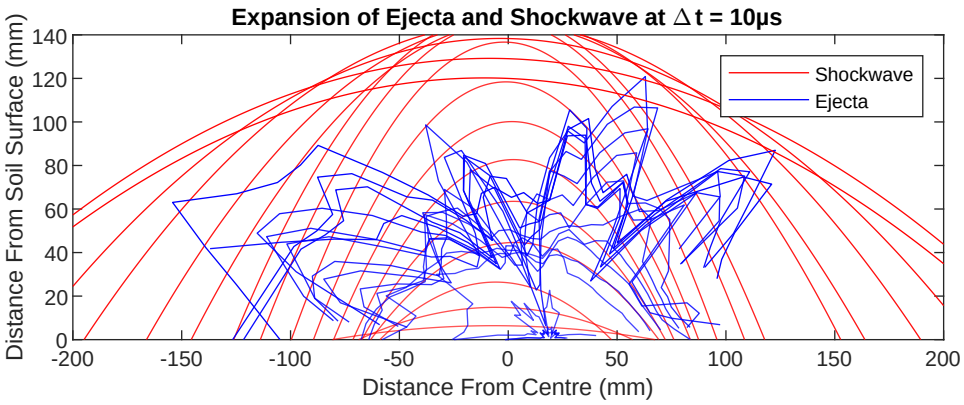

Figure A.52: Shot028HSV tracking showing the detected shockwave and ejecta clouds.

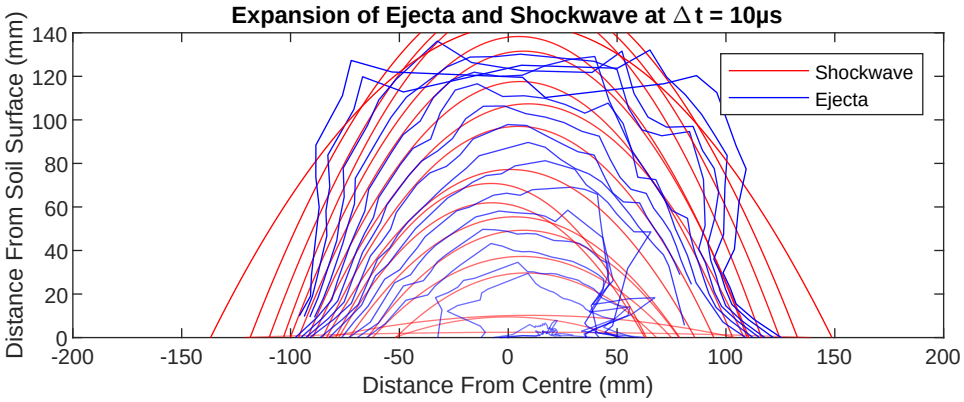

Figure A.53: Shot029HSV tracking showing the detected shockwave and ejecta clouds.

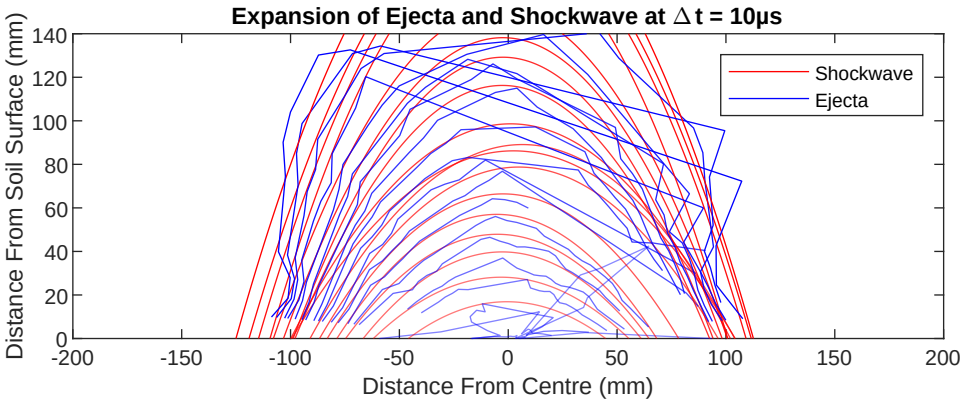

Figure A.54: Shot030HSV tracking showing the detected shockwave and ejecta clouds.

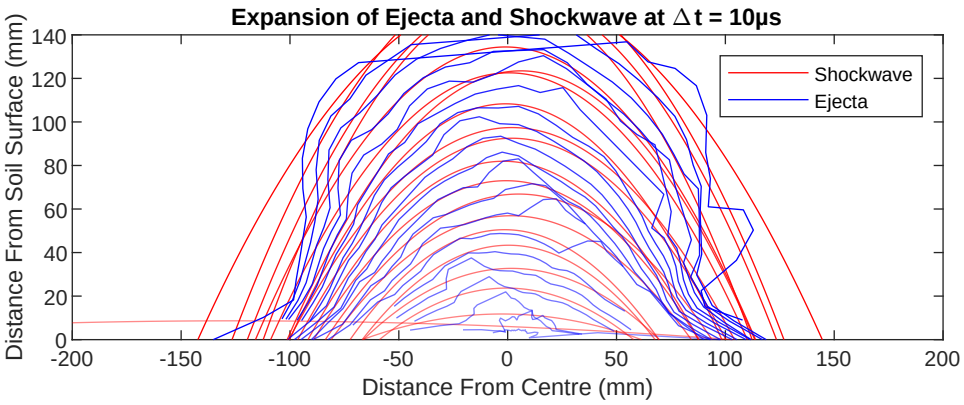

Figure A.55: Shot031HSV tracking showing the detected shockwave and ejecta clouds.

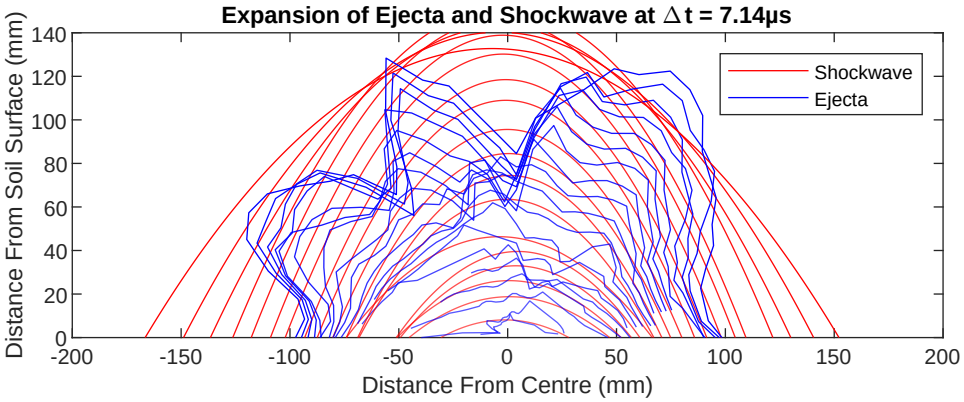

Figure A.56: Shot033HSV tracking showing the detected shockwave and ejecta clouds.

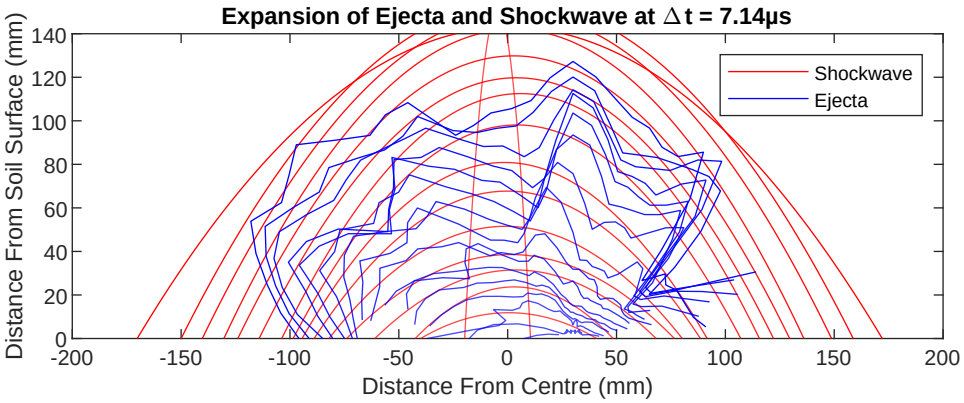

Figure A.57: Shot034HSV tracking showing the detected shockwave and ejecta clouds.

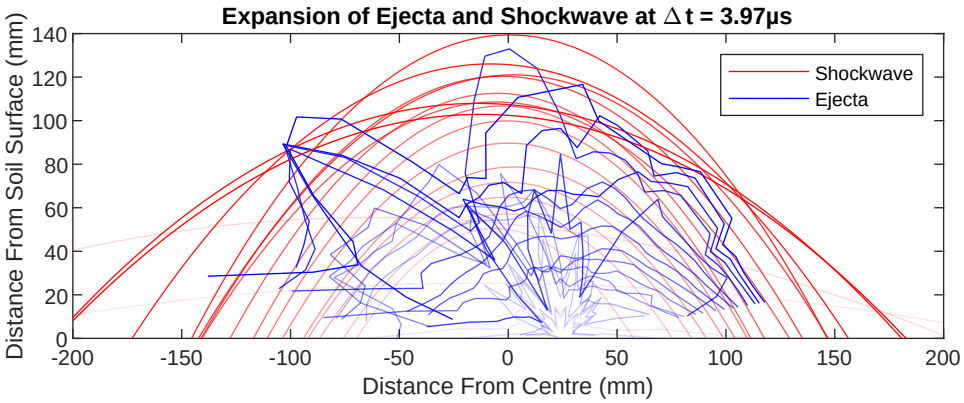

Figure A.58: Shot037HSV tracking showing the detected shockwave and ejecta clouds.

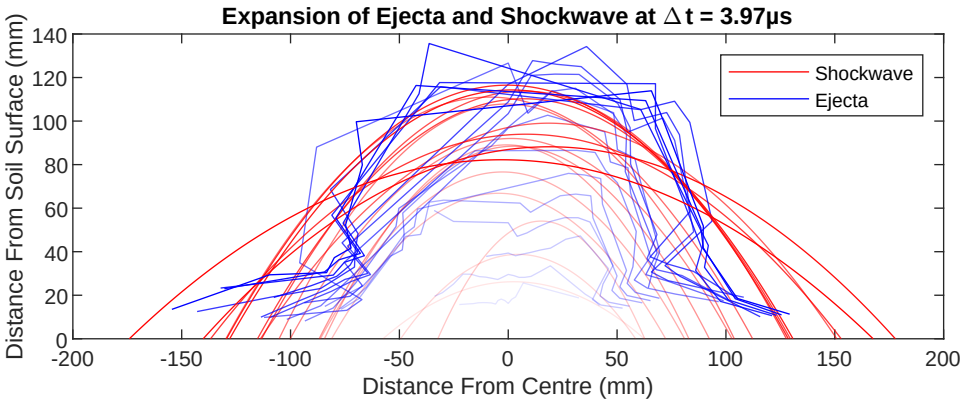

Figure A.59: Shot038HSV tracking showing the detected shockwave and ejecta clouds.